WASTE HEAT RECOVERY, THERMAL STORAGE, AND HEAT PUMPING IN DRYING PROCESSES

A Dissertation
Presented to
The Academic Faculty

by

Bachir El Fil

In Partial Fulfillment
of the Requirements for the Degree
Doctor of Philosophy in the
G. W. Woodruff School of Mechanical Engineering

Georgia Institute of Technology
May 2021

WASTE HEAT RECOVERY, THERMAL STORAGE, AND HEAT PUMPING IN DRYING PROCESSES

Approved by:

Dr. Srinivas Garimella, Chair
G.W. Woodruff School of Mechanical Engineering
Georgia Institute of Technology

Dr. William J. Koros
School of Chemical and Biomolecular Engineering
Georgia Institute of Technology

Dr. Samuel Graham
G.W. Woodruff School of Mechanical Engineering
Georgia Institute of Technology

Dr. Thomas F. Fuller
School of Chemical and Biomolecular Engineering
Georgia Institute of Technology

Dr. Sheldon M. Jeter
G.W. Woodruff School of Mechanical Engineering
Georgia Institute of Technology

Date Approved: [March 30, 2021]

To my father, mother, and sisters

ACKNOWLEDGEMENTS

I would to express my deepest gratitude to my advisor, Dr. Srinivas Garimella. He has generously supported me through my Ph.D. journey at the Georgia Tech, and he never failed in urging me to do my best and push the limits to excel in research, professional, and personal life. I am thankful for the leadership and mentorship he provided me with during my time at the Sustainable Thermal Systems Laboratory.

I would also like to thank my Ph.D. committee: Dr. William Koros, Dr. Samuel Graham, Dr. Sheldon M. Jeter, and Dr. Thomas F. Fuller. Their guidance has helped me significantly improve this dissertation and solve key practical engineering challenges.

The past and current members of the Sustainable Thermal Systems Laboratory have been an invaluable support network, both as friends and as technical advisors. While I have benefited greatly from the discussions and advice of every member of the lab, I would like to specifically thank Dr. Anurag Goyal, Dr. Allison J. Mahvi, Dr. Khoudor Keniar, Daniel B. Boman, Girish Kini, and Christy Green. The engaging conversations on my topic helped a lot to enhance the quality of my output.

Finally, I would like to express my deepest gratitude and appreciation to my back bone, my family. My father, my mother, and my sisters have been a constant source of support and provided me with all I need to stay motivated and never to shrink away from the end goal no matter how challenging it is. Without their unconditional love and support, this work would not have been possible. I would like to thank all my family and friends back home who always made my visits enjoyable and refreshing.

TABLE OF CONTENTS

LIST OF TABLES

LIST OF FIGURES

LIST OF SYMBOLS AND ABBREVIATIONS

A	Area (m^2)
A_w	wave amplitude (m)
c_p	specific heat capacity (kJ kg^{-1} K^{-1})
D	diffusion coefficient (m^2 s^{-1})
ΔH_{ads}	isosteric heat of adsorption (kJ kg_{ads}^{-1})
Δh_s	differential heat of sorption (kJ kg^{-1})
d	diameter (m)
E	energy (kJ)
F	force (N)
f	frequency (Hz)
g	gravity (m s^{-2})
H	enthalpy (kJ)
h_i^P	psychrometric enthalpy (kJ $kg_{moist\,air}^{-1}$)
h_c	heat transfer coefficient (kW m^{-2} K^{-1})
h_{fg}	enthalpy of vaporization (kJ kg^{-1})
h_m	mass transfer coefficient (m s^{-1})
j	mass flux (kg m^{-2} s^{-1})
K_{LDF}	LDF mass transfer coefficient (s^{-1})

k	thermal conductivity (W m^{-1} K^{-1})
L	length (m)
ℓ	liquid phase
m	mass (kg)
$\dot{m}$	mass flow rate (kg s^{-1})
$\dot{m}''$	mass flow rate per unit area (kg m^{-2} s^{-1})
$\dot{m}'''$	mass flow rate per unit volume (kg m^{-3} s^{-1})
MW	molar mass (kg mol^{-1})
n	number of moles (mol)
p	pressure (kPa)
Q	heat transferred (kJ)
q	water uptake ($kg_w kg_{ads}^{-1}$)
R	radius (m)
r	radial direction (m)
Re	Reynolds number ($\rho_a U d_p / \mu_a$)
RH	relative humidity (%)
S	saturation limit (-)
T	temperature (°C)
t	time (s)

U	overall heat transfer coefficient (kW m^{-2} K^{-1})
$\vec{U}$	axial velocity (m s^{-1})
v	velocity (m s^{-1})
V	volume (m^3)
$\dot{V}$	volumetric flow rate (m^3 s^{-1})
W	work (kJ)
x	axial direction (m)
X	moisture content (kg kg^{-1})
y_{RR}	recirculation ratio (-)

Greek Symbols

α_{cl}	water activity coefficient (-)
η_d	drying efficiency (%)
ω_f	angular frequency (Hz)
ω	humidity ratio (kg kg^{-1})
Δ	change (-)
θ	contact angle (rad)
ρ	density (kg m^{-3})
Ω_d	angular velocity speed (rad s^{-1})
σ	surface tension (N m^{-1})

γ	moles of excess air (mol)
ζ	moles of water moles (mol)
κ	permeability (m^{-2})
ε	porosity (-)
τ	tortuosity/correction factor (-)
μ	dynamic viscosity (kg m^{-1} s^{-1})

Subscripts

a	air
ads	adsorbent
amb	ambient
bed	sorption bed
C	cold
c	conversion/cooling
cl	cloth/textile
comb	combustor
d	drum
da	dry air
e	evaporation
eff	effective
eq	equilibrium

H	hot
fuel	fuel
g	gas phase
in	input
ma	moist air
ms	maximum saturation
out	output
p	product/pellet
s	solid
sf	shaft
v	vapor
w	water

Abbreviations

AAD	average absolute deviation
HHV	higher heating value
LHV	lower heating value
COP	coefficient of performance
ERD	electric resistance dryer
GFD	gas-fired dryer
HPD	heat pump dryer

MWD	microwave dryer
SMER	specific moisture extraction ratio
TED	thermoelectric dryer
TEHPD	thermoelectric heat pump dryer
TES	thermal energy storage
RHX	recuperative heat exchanger
AHP	adsorption heat pump
COP	coefficient of performance
EGR	exhaust gas recirculation

SUMMARY

Drying is a ubiquitous process in a wide range of applications and industries, including residential and commercial clothes dryers, agriculture, chemical processing, and pharmaceutical industry. Clothes dryers have become widespread in North American households and commerce. More than 80% of the households in the US have a washer and dryer. Thermal drying of textiles is a very energy-intensive process coupled with the complexities of several transport phenomena (mass, momentum, and energy) occurring simultaneously, and their influence on material properties. Dryers reject ~ 58% of the total input energy as waste heat or losses. While system efficiency can be improved by optimizing system design and operational parameters, there is also a significant opportunity in harnessing the energy from the exhaust stream of the dryer and storing it for use in future drying cycles.

In this work, a fundamental understanding of the heat and mass transfer processes in drying is sought with the goal of simultaneously reducing energy consumption and drying time. Transient thermodynamic, heat and mass transfer models are developed and validated experimentally. The validated models are used to optimize energy consumption and cycle time. Recirculation, waste heat recovery, thermal energy storage, and heat pumping are investigated as a means to achieve these goals. A commercial tumble dryer is used to implement these changes and demonstrate the effects of these enhancements. Implementation of these techniques is demonstrated to yield energy savings of up to 22% while simultaneously decreasing drying time by 23%. Adoption of these energy saving techniques in gas-fired tumble dryers across the U. S. market could reduce primary energy consumption by ~ 4.17×10^{7} GJ (11.6 billion kWh) annually.

CHAPTER 1. INTRODUCTION

1.1 Introduction

Increasing energy consumption and CO_2 emissions are a worldwide concern due to their impact on global climate change (Franke et al., 2019). The total U.S. primary energy consumption in 2019 was equal to 101.2 quadrillion BTU (1.067×10^8 TJ) of which 11.9% and 35.6% are consumed by the residential and commercial/industrial sectors, respectively (EIA, 2020). To reduce the use of natural gas and coal, renewable energy sources such as hydropower, solar, biomass, and geothermal energy are a promising solution for a safe and environmentally sustainable energy supply (Panwar et al., 2011; Kabir et al., 2018). The major challenge remains to retrofit or develop technologies that can make use of the available energy sources efficiently. Alongside the shift to more renewable energy generation methods, energy-saving designs and retrofits can reduce primary energy needs. Waste heat recovery, energy storage, and heat pumping can be used for this purpose (Little and Garimella, 2011; Rattner and Garimella, 2011) in a wide range of applications and industries, including residential and commercial clothes dryers, agriculture, chemical processing, and the pharmaceutical industry.

1.2 Motivation

Drying – or removing volatile substances from a solid – is one of the most energy intensive processes, accounting for 10-25% (Kudra, 2004; Mujumdar, 2014) of the US energy consumption in industrial processes, due primarily to the need to supply the latent of heat of vaporization to remove water. Drying is used for processing food, textiles, paper, wood, ceramics, and pharmaceuticals (Mujumdar, 2014). Although drying is one of the

oldest processes (Kerkhof and Coumans, 2002), current dryers, with typical lifetimes of a few decades, were not designed to cope with the present world energy demand.

More than 80% of US households have a washer and dryer. There are 89 million residential clothes dryers in the US (75% electrically driven, 25% gas-fired). In total, dryers now represent a $9 billion annual national energy bill, up to 6% of the overall household electricity consumption, and 2% of the natural gas consumption (Horowitz, 2011). In addition, there are more than 35,000 commercial dryer facilities in the US, in hotels, hospitals, resorts, prisons, and stand-alone laundry services. Commercial tumble dryers for clothes use a significant amount of energy and remain in service almost 24 hours per day. These units consume ~53 billion kWh of primary energy. Dryers (12% electrically driven and 88% natural gas-fired) in hotels, prisons and resorts can be responsible for as much as 90% of their overall energy bill (EIA, 2015). Thermal drying of clothes is very energy intensive, coupled with the complexities of several transport phenomena (mass, momentum, and energy) occurring simultaneously, and their influence on material properties. While efficiency can be improved by optimizing system design and operational parameters, there is also a significant opportunity in harnessing and storing energy from the exhaust stream of the dryer for future cycles.

Currently, dryers reject ~ 58% of the total input energy as waste heat or losses as depicted by Figure 1.1 (Lambert et al., 1991). A third of the input energy is rejected in the exhaust air stream. According to the Natural Resource Defense Council (NRDC), if all installed dryers in the US operated in an energy efficient mode (drying efficiency > 50%),

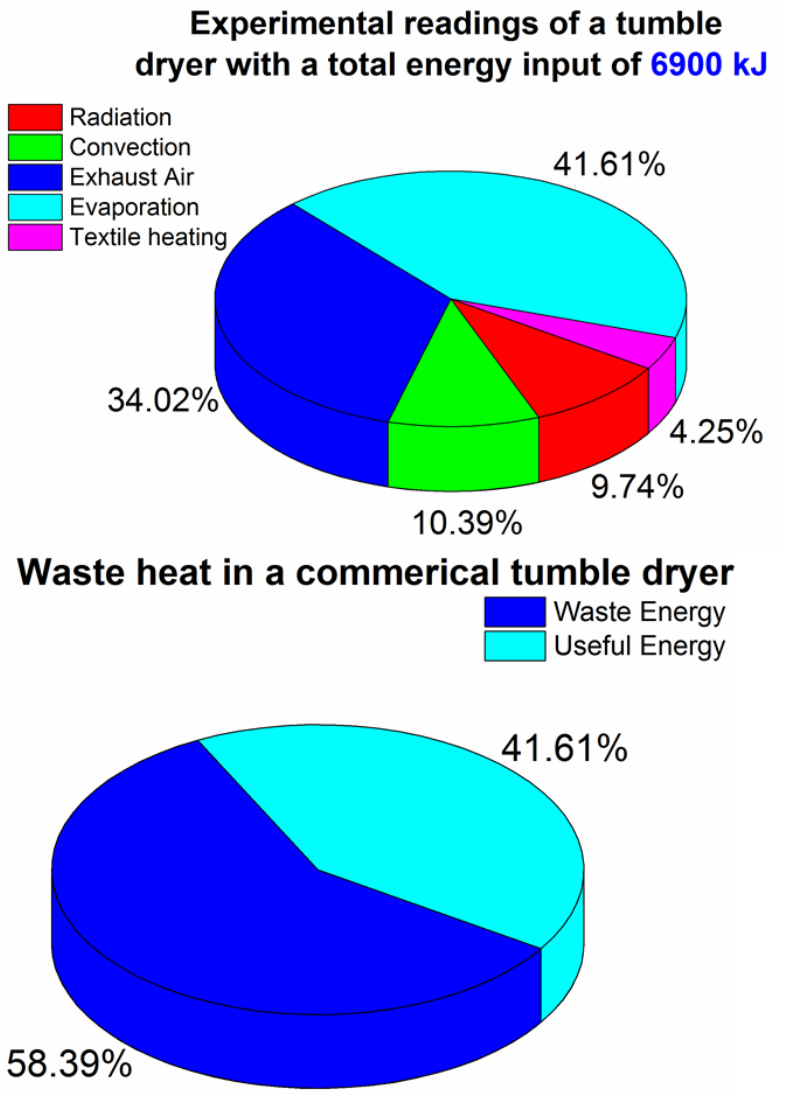

Figure 1.1: Energy flow in a typical air-vented textile dryer (Lambert et al., 1991)

it would result in ~$4 billion energy savings, and prevent ~16 million tons of CO_2 emissions annually. Research on improving the energy efficiency of tumble dryers includes exhaust gas recirculation, recuperation, and heat modulation. These enhancements showed the potential for up to 50% efficiency enhancement, but have found limited implementation due to a significant increase in system footprint, drying times, and costs. Dryers produce a significant amount of low-to-medium-temperature waste heat (Tuğrul Oğulata, 2004; Li et al., 2012) that can be recuperated to reduce drying time and enhance energy efficiency.

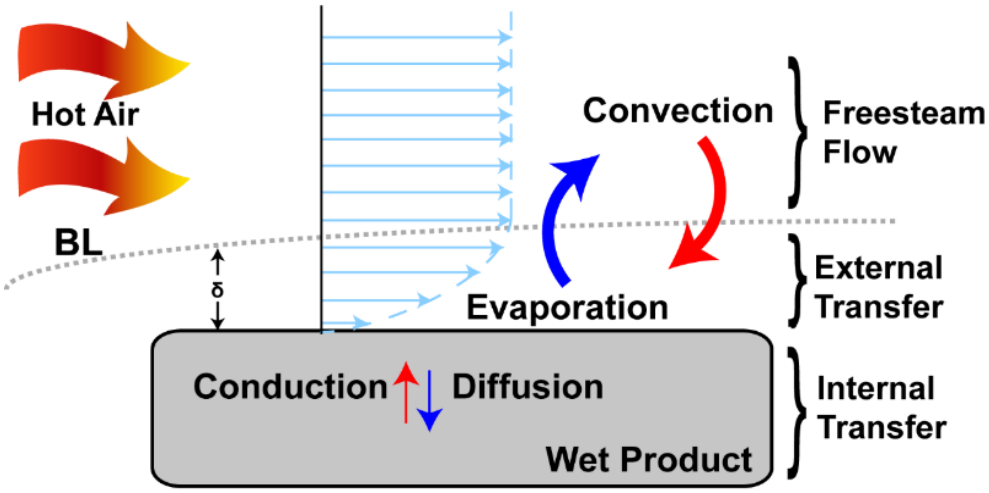

Figure 1.2: Transport phenomena occurring within the wet product and air in typical convective dryers

1.3 Drying Theory

1.3.1 Convective Drying

The essence of all drying processes is the removal of volatile substances (moisture) from a mixture to yield a solid product. In general, drying is accomplished by thermal techniques, and thus involves the application of heat, most commonly by convection from a hot air stream as shown in Figure 1.2. During convective drying of solids, two phenomena occur simultaneously: energy (heat) transfer from the surroundings, and mass (moisture) transfer from within the solid.

1.3.2 Drying Mechanics

Drying can be achieved through evaporation, or mechanically through the use of presses or centrifuges. Typical drying curves are shown in Figure 1.3a-b. The rate of change of moisture content with respect to time (Figure 1.3a) is known as the drying rate. In the first phase, the drying rate is low because most of the heat transferred to the wet

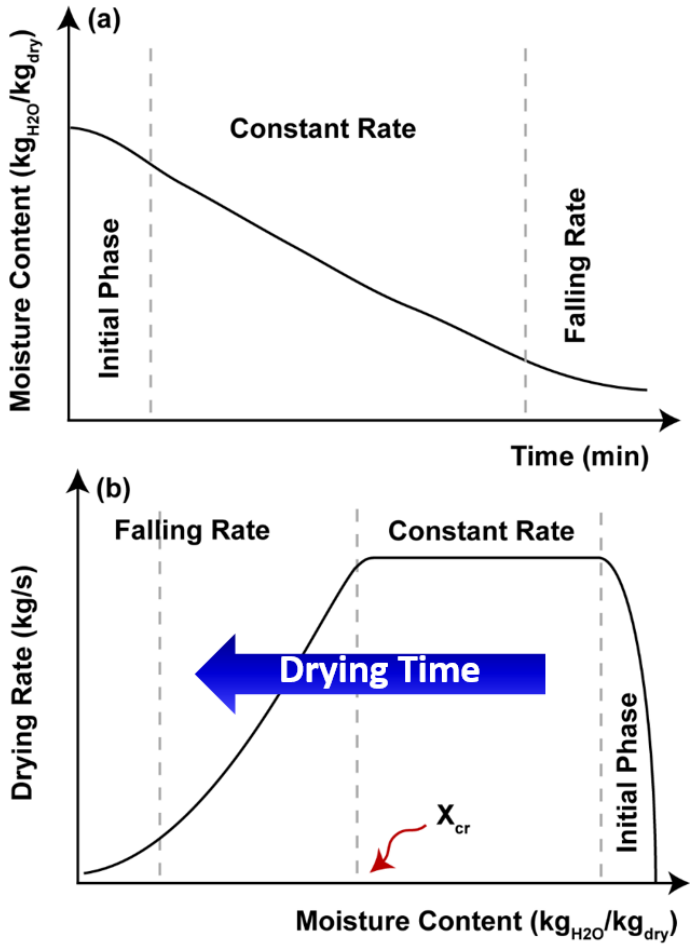

Figure 1.3: Drying Curves (a) moisture content as function of time (b) drying rate variation as function of moisture content

material is used to raise its temperature. As the material heats up, the drying rate increases to a peak and then reaches a plateau. In the second phase, in which the drying rate is relatively constant, a balance between heat and mass transfer occurs, and constant temperature and vapor partial pressure at the surface of the material are achieved. Moisture removal is highly dependent on conditions of the air stream, such as temperature, relative humidity, and flow rate, as well as conditions of the wet material, such as interface area and temperature. This phase continues until the moisture content of the material reaches a critical point known as the critical moisture content, when most of the unbound moisture has been removed. The third phase begins as the moisture film at the surface of the material

becomes unsaturated, i.e., the vapor pressure of the air layer at surface is less than that of the saturated case. Towards the end of the falling rate phase, the bound moisture diffuses from within the material to the surface. The falling period ends once the moisture is at the desired moisture content, as shown in Figure 1.3b. The proposed study focuses on thermal drying processes in which evaporating water is carried away by the drying medium, in this case, a hot dry air stream.

Thermal drying is energy intensive due to the unavoidable thermodynamic constraint of supplying sufficient energy to provide the latent heat of evaporation (> 2000 kJ kg^{-1}) for the water vapor removed (Kudra, 2004; Mujumdar, 2014). Industries and researchers have been working to reduce the overall energy consumption in drying. Most of the methods applied to convective drying are based on heat recovery from the exhaust air, because a significant amount of heat used in drying appears in the exhaust stream (Moraitis and Akritidis, 1997; Krokida and Bisharat, 2004; Kudra, 2004; Tuğrul Oğulata, 2004; Walmsley et al., 2015). Other energy saving techniques that are investigated in this study include thermal energy storage (TES) and heat pumping.

1.4 Adsorption-based TES and heat pumping

Energy storage can bridge the gap between the supply and demand of energy in different phases of drying, providing significant cost savings, and reducing the environmental impact of power generation during peak demand periods. Thermal energy storage (TES) can employ heating/cooling (sensible), melting/solidification (latent/phase change), or thermochemical processes (sorption, chemical reactions) (Demir et al., 2008; Cabeza et al., 2017). High energy density (~ 300 kWh m^{-3}) can be achieved using thermo-

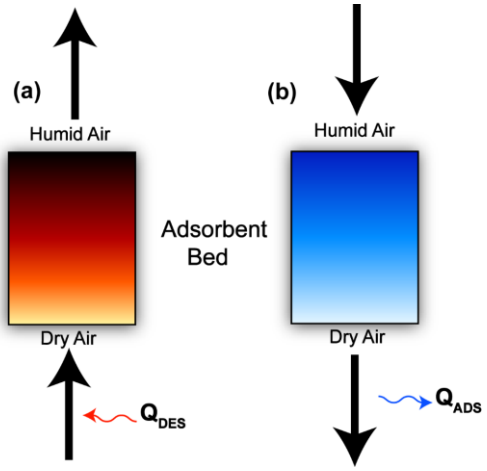

Figure 1.4: Open adsorption cycle (a) desorption (b) adsorption stage

chemical storage. Open adsorption systems store thermal energy and provide hot dry air during the discharge phase, making them very attractive for drying (Chi and Wasan, 1970; Hauer and Dallmayer, 1996; Hauer and Fischer, 2011; Krönauer et al., 2015).

Adsorption systems can be used for heat pumping and storage in various thermal processes. An open-adsorption TES is well suited for situations in which water or water vapor is the adsorbate, because it can communicate directly with the moisture in the ambient air. As shown in Figure 1.4, an air stream transports heat and moisture to and from the adsorbent bed. Such systems can reduce energy consumption due to relatively high coefficients of performance (COP) for heating/dehumidification (Núñez et al., 2007; Sultan et al., 2015), and high thermal energy densities in storage applications (Demir et al., 2008; Cabeza et al., 2017; Lefebvre and Tezel, 2017). Additionally, such systems are relatively inexpensive and suitable for retrofit applications. Thermal energy storage can be achieved by separating the desorption stage from the adsorption stage. Theoretically, after the desorption stage, the adsorbent can stay in the charged state without thermal losses until the adsorption stage is activated. Thus, implementing an open-adsorption system in a

convective thermal drying application such as a textile tumble dryer would help in reducing its energy consumption. A review of the state-of-the art energy saving techniques in textile drying is presented in Chapter 2.

1.5 Research needs and objectives

The above discussion shows that drying remains a complex process to simulate due to the coupled heat and mass transfer processes taking place simultaneously. A typical air-vented tumble dryer rejects almost 60% of its input energy. Very few studies have actually simulated the drying process as a way to optimize and investigate energy saving methods. Some studies have investigated techniques to reduce energy consumption without any consideration for the drying time. For instance, Wei et al. (2018a) investigated modulation of heat input, which reduced energy consumption, but increased the drying time significantly. Furthermore, there are some conflicting results in the literature regarding the effects of exhaust gas recirculation on energy consumption and drying time. Lambert et al. (1991) and Ma et al. (2018) reported that recirculating the exhaust gas is favorable; however, Williamson and Bansal (2004) found it to be detrimental. Additionally, there are no studies that have investigated implementing a thermal energy storage unit to enhance drying efficiency.

The primary objective of this work is to simulate, develop, and demonstrate energy-saving techniques for drying processes, using a gas-fired commercial tumble dryer as the representative system. To accomplish this objective, the following tasks are conducted:

- Develop and validate transient thermodynamic, heat transfer, and mass transfer models for the drying process in a commercial gas-fired tumble dryer.

- Investigate and demonstrate experimentally the effect of waste heat recovery techniques (exhaust gas recirculation and recuperation) on energy consumption and drying time.
- Design, model, demonstrate, and validate a single-bed open-adsorption thermal energy storage system.
- Investigate the use of an adsorption heat pump to further enhance the efficiency of convective drying.

1.6 Dissertation outline

The dissertation is organized as follows:

- **Chapter 2** focuses on the literature addressing drying theory and the underlying mass, species and heat transfer phenomena, identification of the most energy-consuming steps in the process, assessment of the potential for energy savings, and the energy saving techniques that have been considered in the literature.
- **Chapter 3** presents the development of transient thermodynamic, heat, and mass transfer models for a commercial gas-fired tumble dryer. The models are compared with data from experiments conducted in this study.
- **Chapter 4** describes the experimental facility used to demonstrate the energy saving with exhaust gas recirculation, recuperative heat exchange, and TES.
- **Chapter 5** describes the effect of waste heat recovery techniques (exhaust gas recirculation and recuperation) on the drying time, drying efficiency, and total energy consumption. Data from both experiments are compared with the results predicted by theoretical models.

- **Chapter 6** describes an adsorption-based thermal energy storage system integrated with a gas-fired dryer. Predictions of the heat and mass transfer model to capture the dynamics of the adsorbent bed are compared with experimental results from this study.
- **Chapter 7** describes the integration of an adsorption heat pump with a gas-fired tumble dryer. The effects of combining several energy saving techniques such as exhaust gas recirculation, recuperation, and thermal storage are also demonstrated experimentally.
- **Chapter 8** summarizes the important findings and conclusions from this work in addition to recommendations for future research.

CHAPTER 2. LITERATURE REVIEW

Drying is a ubiquitous process in a wide range of applications and industries, including residential and commercial textile drying, agriculture, chemical processing, and the pharmaceutical industry. Thermal drying is energy intensive due to the unavoidable thermodynamic constraint of supplying sufficient energy to provide the latent heat of evaporation (> 2000 kJ kg^{-1}) for the removal of water vapor. There is a critical need to reduce the overall energy consumption in drying, and several methods to do so have been explored. Most energy saving approaches for convective drying are based on heat recovery from the exhaust stream, because a significant amount of heat used in drying appears in the exhaust stream. Different techniques have been attempted to reduce energy consumption in different types of dryers (gas-fired, electrical, and heat pump dryers). This chapter focuses on the literature addressing drying theory and the underlying mass, species and heat transfer phenomena, identification of the most energy-consuming steps in the process, assessment of the potential for energy savings, and the energy saving techniques considered in the literature. Insights gained from this study are used to identify the optimal techniques to minimize energy consumption and drying time for a variety of drying scenarios.

2.1 Introduction

Drying – or removing volatile substances from a solid – is one of the most energy intensive processes. This process, which is applied to food products, textiles, paper, wood, ceramics, and pharmaceuticals, accounts for 10-25% (Kudra, 2004; Bhandari, 2015) of US energy consumption in industrial processes. Although drying is one of the oldest processes (Kerkhof and Coumans, 2002), current dryers, with typical lifetimes of a few decades, were

not designed to cope with the present world energy demand. Despite the development of more energy-efficient dryers, drying remains one of most energy-intensive processes due to thermodynamic constraints. Dryers produce a significant amount of low-to-medium-temperature waste heat (Tuğrul Oğulata, 2004; Li et al., 2012) that can be recuperated to reduce drying time and enhance energy efficiency.

Convective dryers, in which a hot air stream passes over the surface of the material to be dried, are the most common dryers used for textiles (Mujumdar, 2014). Mathematical modeling of the drying behavior of textile materials enables process design and minimization of energy costs (Kahveci and Cihan, 2007). A robust, reliable, and accurate model for drying also aids in selecting the most promising techniques for further testing. Drying models can be challenging and computationally intensive (Turner and Mujumdar, 1996). In most early studies, the approach was primarily empirical (Akyol et al., 2015; Mokhtari Yazdi et al., 2015; Fontana et al., 2016). Ng and Deng (2008) developed a semi-empirical model for clothes drying based on a termination control method. However, their model covers only the last constant-rate and falling-rate periods of the drying cycle. Deans and Tranxaun (1992) used modified convective transport equations to calculate mass transfer at the air-textile interface. Haghi (2001) employed a mathematical model developed by Nordon and David (1967) with the rate equation for mass transfer between the moisture in the fabric fibers and the moisture in the air within the fabric pores. These types of models provide some local insights but are too complex and computationally expensive to be used for optimization at the device and system level. Moreover, the model developed by Nordon and David (1967) requires an immense amount of input regarding thermophysical properties and heat and mass transfer coefficients. Earlier studies such as

the one by Lambert et al. (1991) developed an aggregated model composed of sub-models and suggested a method to quantify the moisture condition based on the water content and type of textile. In contrast, Wei et al. (2017) and Yi et al. (2016) developed semi-empirical models based on a physical understanding to describe the heat and mass transfer in the drum. El Fil and Garimella (2021) developed a lumped model to predict the performance of a gas-fired tumble dryer. The model uses some empirical parameters such as water content parameter obtained from the study by Lambert et al. (1991).

Rasti et al. (2020) presented a comprehensive review of different models that predict the performance (evaporation rate, drying time, and energy consumption) of different types of tumble dryers. Most of these models use empirical fitting models, the Chilton-Colburn analogy (Rasti et al., 2020) to predict the overall mass transfer coefficient, or computational fluid dynamics (CFD). An accurate model is crucial to determine the optimal operating conditions that minimize the energy consumption of the tumble dryer. Additionally, a high-fidelity model allows simulation of waste heat recovery scenarios to identify the most promising methods prior to experimentation. This chapter presents the literature on drying theory and the underlying mass, species, and heat transfer phenomena, identification of the underlying mechanisms and major energy consuming steps in the process, potential for energy savings, and the energy saving techniques that have been considered in the literature.

2.2 Drying Methods

There are many methods to extract moisture out of textiles, which can be broadly categorized into mechanical and thermal methods, as depicted in Figure 2.1.

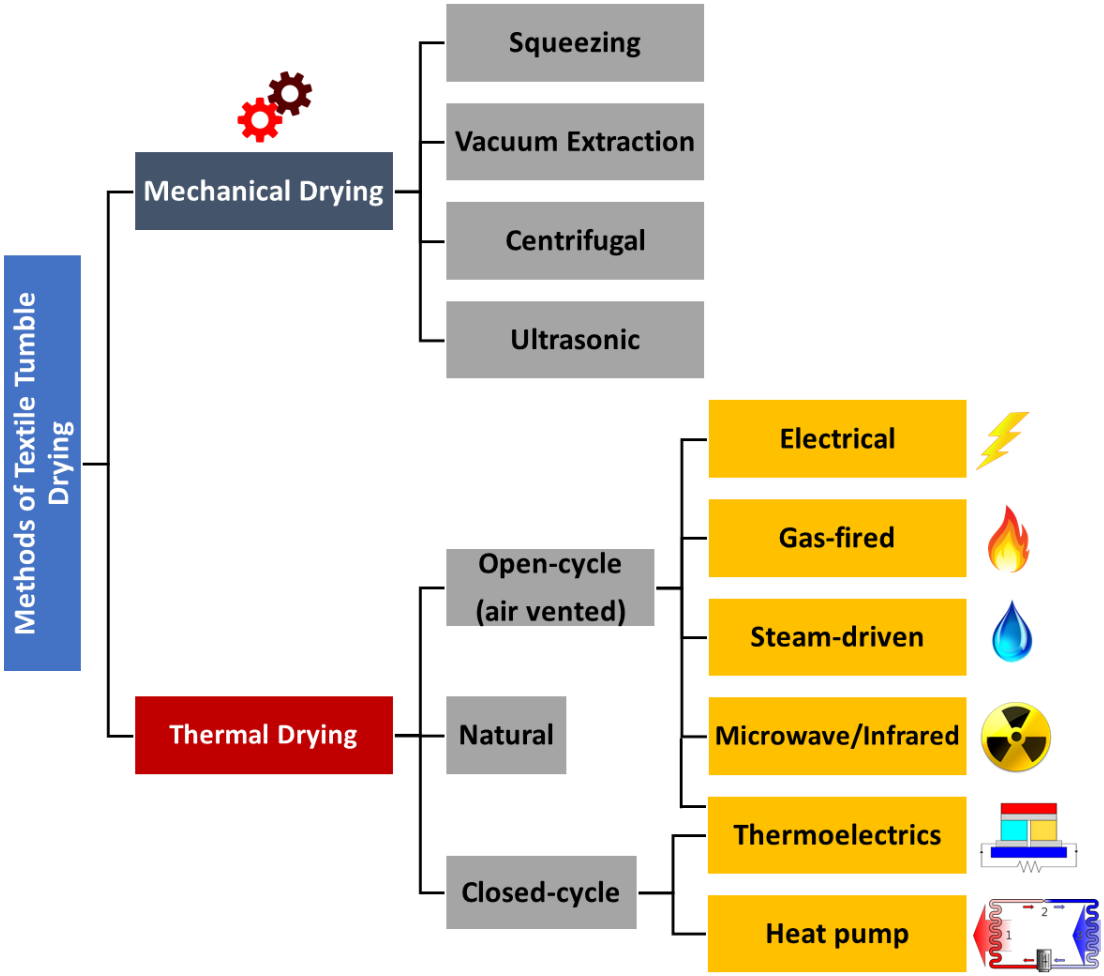

Figure 2.1: Taxonomy of textile tumble drying methods

Both mechanical and thermal drying techniques are discussed here with a focus on the latter. Additionally, the limitations of each of the thermal techniques are assessed based on two figures of merit. The drying efficiency of the thermal tumble dryer is defined to be the fraction of the total energy input used to evaporate water in the process, and can be expressed by Equation (2.1):

$$\eta_d = \frac{\int_{t=0}^{t=t_f} \dot{m}_e h_{fg} dt}{\int_{t=0}^{t=t_f} \dot{E}_{in} dt} \tag{2.1}$$

where $\dot{m}_e$ is the evaporation mass flow rate, $\dot{E}_{in}$ is the total power input, and t_f is the final time at which the moisture content in the textile is less than 0.04. The second figure of merit, the specific moisture extraction ratio (SMER), is given by Equation (2.2):

$$SMER = \frac{\int_{t=0}^{t=f} \dot{E}_{in} dt}{\int_{t=0}^{t=t_f} \dot{m}_e dt} \tag{2.2}$$

The SMER represents the energy required by the dryer to remove 1 kg of water. A lower SMER signifies a more efficient drying process. The minimum SMER (for thermal dryers) can be estimated from the enthalpy of vaporization of water at atmospheric pressure (Conde, 1997; Kudra, 2004; Gluesenkamp et al., 2020) and is expressed by Equation (2.3)

$$SMER_{\min} \simeq h_{fg} \tag{2.3}$$

The drying efficiency can be expressed as the ratio of minimum SMER to the actual SMER of the dryer (Equation 2.2). This is analogous to how the second law efficiency is defined for typical heat pumps application, where the second law efficiency is given by the ratio of the actual coefficient of performance (COP) to the Carnot COP of the system. Therefore, the drying efficiency can be written as Equation (2.4):

$$\eta_d = \frac{SMER_{\min}}{SMER_i} \tag{2.4}$$

2.2.1 Mechanical Drying

Mechanical drying is defined as a process in which water is extracted from a textile without any thermal energy. The most common techniques are squeezing, vacuum extraction, centrifuging/spin drying, and ultrasonic drying as depicted in Figure 2.2.

This technique is usually chosen based on the material of the textile, and these processes can either be batch-wise or continuous. Typically, the best mechanical drying process for delicate fabrics is vacuum extraction because less force is applied to the fabric than in centrifuging (Bhandari, 2015). In squeezing processes (Figure 2.2a), dewatering is achieved by passing the textiles between a pair of rollers and is by far the most inexpensive

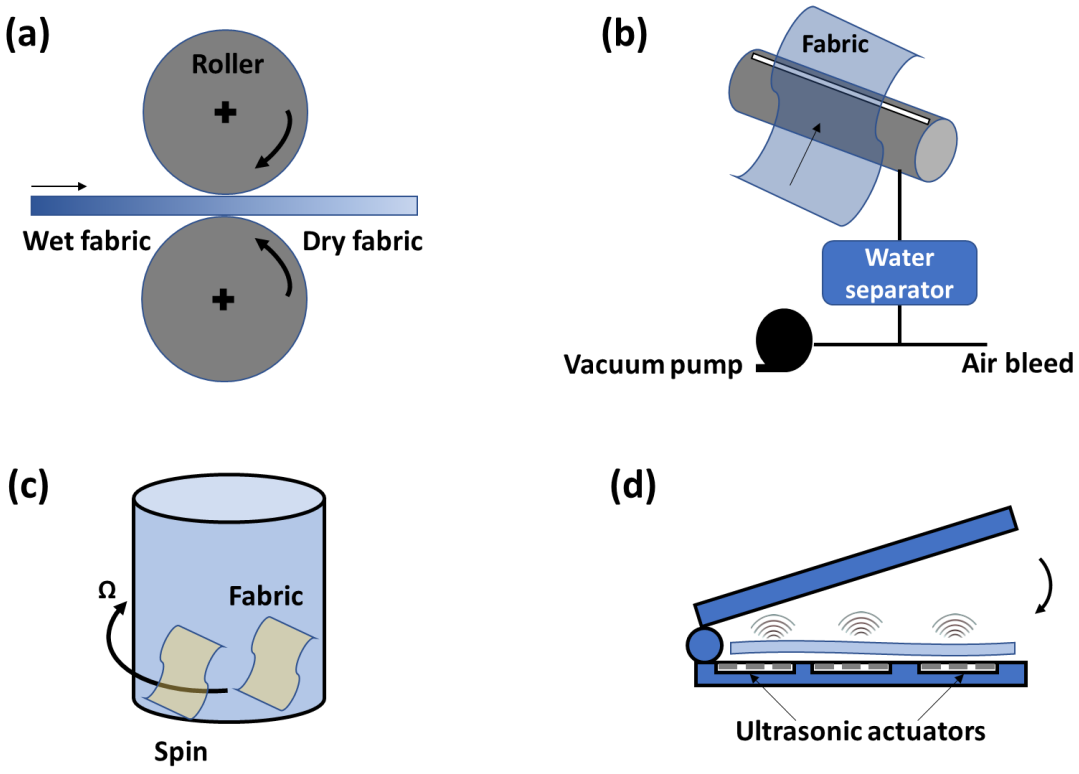

Figure 2.2: Mechanical textile drying techniques (a) squeezing, (b) vacuum extraction, (c) centrifuging, and (d) ultrasonic drying

method used to dehydrate the textile. Figure 2.3 shows the SMER for mechanical drying techniques. The energy required to remove the water by squeezing is ~ 0.02 kWh kg^{-1}; however, this technique can reduce the moisture content to only 60% depending on the properties of the fibers (Bhandari, 2015). In vacuum extraction (Figure 2.2b), the textile passes over an open slot in which vacuum is maintained. The energy required for vacuum extraction is almost 12 times that of squeezing, i.e., 0.19 kWh kg^{-1}. Vacuum extraction systems can reduce the moisture content by ~ 30-50% in carpet drying (Mujumdar, 2014). Centrifuging or "spin drying" (Figure 2.2c) uses high speed rotation to dewater the textile. In terms of energy requirement, centrifuging lies between squeezing and vacuum extraction. Centrifuging is able to reduce the remaining moisture content in the textile to ~ 50%. The energy required in centrifuging is about 0.1 kWh kg^{-1} (China Energy and Hasanbeigi, 2010).

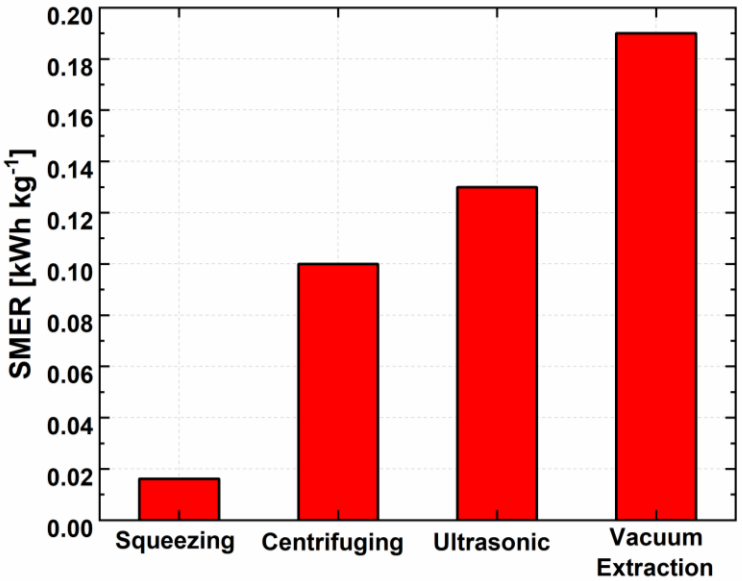

Figure 2.3: Energy required to evaporate one kilogram of water in different mechanical textile drying techniques.

Another mechanical textile drying technique, reported by Peng et al. (2017), is direct-contact ultrasonic drying (shown in Figure 2.2d), which requires no heat input in removing the water from the textile. The ultrasonic textile dryer uses high frequency mechanical vibrations generated by piezoelectric ceramics. In principle, the process may be similar to ultrasonic atomization; however, this process is still poorly understood, with two different theories, capillary wave theory and cavitation theory, offered to explain the process. Cavitation theory suggests that a hydraulic shock is generated by the implosion of cavitation bubbles at the liquid-gas interface that are generated by the decrease in pressure associated with the ultrasonic waves. In contrast, capillary wave theory postulates that upon exciting a liquid droplet, the ultrasonic waves are transmitted through the liquid generating capillary waves at the interface, resulting in the breakoff of microdroplets. James et al. (2003) and Avvaru et al. (2006) studied the kinematics of droplet atomization and were able to approximate the minimum oscillating force that would atomize the droplet and help overcome the surface tension force. Assuming the droplet forms a hemispherical cap on the surface of the transducer, the minimum oscillating force $\left(F_o\right)$ can be estimated by Equation (2.5):

$$F_o \sim m_{drop} A_w \omega^2 \sim \frac{\pi}{12} d^3 \rho A_w {\omega_f}^2 \tag{2.5}$$

where A_w is the amplitude of the applied wave, d is the droplet diameter, and ω_f is the angular frequency of the wave. The surface tension depends on the temperature and the diameter of the water droplet. The relative magnitude $\left(R\right)$ of the oscillating force to the surface tension can be expressed by Equation (2.6):

$$R = \frac{F_o}{F_s} \sim \frac{d^2 \rho A_w {\omega_f}^2}{12\sigma \cos\theta} \tag{2.6}$$

where σ is the liquid surface tension and θ is the contact angle formed at the liquid-solid interface. It is favorable to have $R > 1$ to initiate the drying process. Due to the fact that ultrasonic dryers use mechanical energy to dewater the textile, there is no need to supply the minimum thermal energy of ~ 0.646 kWh kg^{-1}. Peng et al. (2017) investigated ultrasonic drying on saturated textiles $4 \times 4\,mm^2$ in size and showed that the ultrasonic dryer used 10 times less energy than the conventional electrical tumble dryer. The challenge with the current ultrasonic dryers is mainly in the small volumes of textile that can be dried through the process. Conventional tumble dryers are known for the large batches of textiles that can be dried in a single drying cycle. Because the wave propagation through the textile is a function of its thickness, a bulky load could reduce the effectiveness of ultrasonic drying. Mechanical drying techniques require less energy to remove moisture from the textile compared to thermal drying; however, most of the mechanical drying methods cannot reduce the moisture content to below ~ 0.4 – 0.5. In addition, mechanical drying requires higher grade energy than the lower grade energy that is used in thermal dryers.

2.2.2 Thermal Drying

The fundamental drying mechanisms in thermal drying are discussed here. Convective dryers with air as the drying medium are the most common type of dryers used for drying textiles in both industrial and residential settings. Thermal tumble dryers are batch-wise dryers in which a constant mass of textile is dried per cycle. As depicted in

Figure 2.1, there are three main methods in which thermal drying can be achieved: natural drying, air-vented dryers, and closed-cycle dryers.

2.2.2.1 Natural Drying

Natural drying is the oldest method of drying textiles, and is accomplished without the active addition of any primary energy, and depends primarily on natural/forced convection with the ambient air surrounding the textile. The drying rate is a function of the ambient temperature, relative humidity, the moisture content in the textile, the volume of the drying textile, and the velocity of the ambient air. The drying efficiency in this case would approach infinity, i.e., $\eta_d \to \infty$ since the denominator in Equation 2.1 approaches 0. Natural drying, of course, is much slower than other convective drying techniques.

2.2.2.2 Electric Dryers

Electric dryers are used often in residential settings and are typically air-vented dryers. Dryers that use an electric heater require a large amount of electricity, ~2.5 – 5.4 kW. Most of the air-vented electric tumble dryers in the U.S. use a 5.4-kW electric heater (Bassily and Colver, 2003b; Yadav and Moon, 2008a; Huelsz et al., 2013). The SMER of a standard capacity (> 0.125 m^3) electrical dryer is estimated to be 1.65 kWh kg^{-1}.

Figure 2.4a shows the airflow in a standard electric resistance dryer (ERD). Ambient air is heated as it flows over a resistive heater. In the drum, the hot dry air causes moisture in the textile to evaporate and carries this moisture with it as it is ejected to the outside. Because the input air is drawn from the ambient, the drying rate depends on the ambient relative humidity and temperature. The relative humidity dictates the amount of

moisture that can be extracted. Therefore, as the relative humidity of the ambient air increases, the drying rate decreases. For instance, one can consider two cases in which the intake air enters at 0% and 100% relative humidity. In the case where the air is completely dry, i.e., RH = 0%, in addition to the sensible drying in the drum, due to the significant difference in the partial pressure of water vapor between the air and the textile, passive moisture removal ("free drying") occurs. However, this does not come at zero energy expense due to the fact that air should be blown over than textile by a fan or blower. Drying efficiency is proportional to the drying rate, i.e., $\eta_{d,RH=0\%} > \eta_{d,RH=100\%}$. Similarly, the energy required to remove moisture when the intake air RH = 0% would be less than that when the intake air RH = 100%, i.e., $SMER_{RH=0\%} < SMER_{RH=100\%}$.

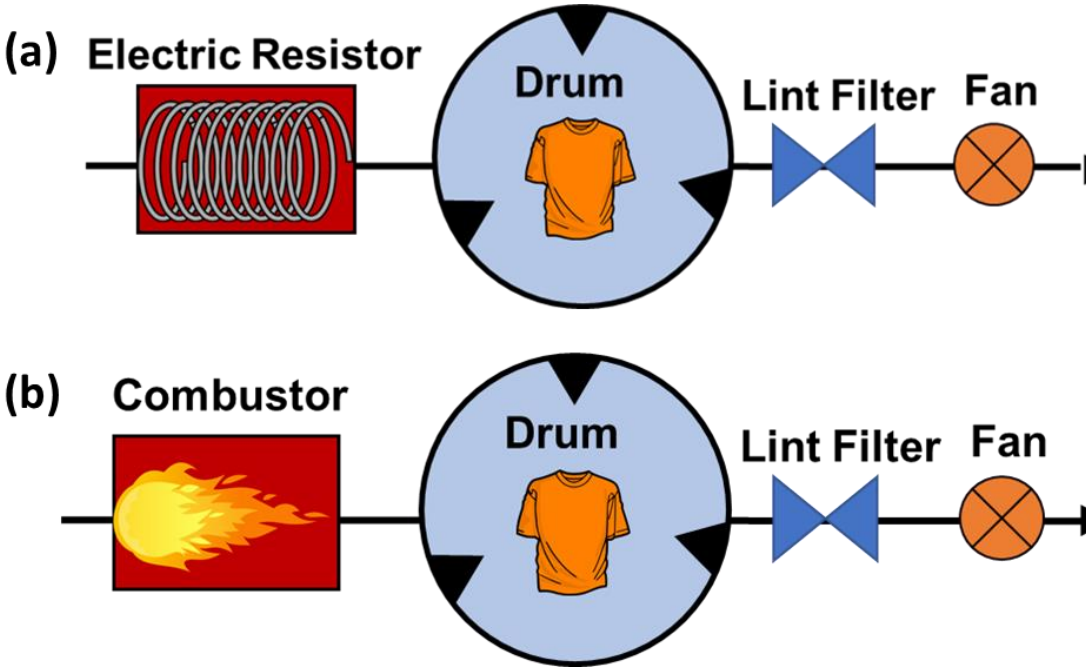

Figure 2.4: (a) Schematic of electric-resistor dryer (ERD) (b) Schematic of a gas-fired tumble dryer

ERDs have been extensively studied (Hekmat and Fisk, 1984b; Conde, 1997; Bansal et al., 2001; Bassily and Colver, 2003b; Krokida and Bisharat, 2004; Yadav and Moon, 2008a; Huelsz et al., 2013; Wei et al., 2017; Novak et al., 2019). Hekmat and Fisk (1984b) authored one of the earliest studies that investigated residential ERDs and proposed several ways to improve the efficiency of drying. Decreasing the air mass flow rate resulted in an 8% decrease in energy consumption due to the significantly higher temperature at the inlet of the drum, while increasing the temperature of the intake air decreased it by 15% because of a higher evaporation rate. Lambert et al. (1991) recirculated the exhaust gas of a 4-kW ERD and determined that a maximum efficiency improvement of 15% could be achieved at a recirculation ratio of 0.75. Additionally, Lambert et al. (1991) showed that more than half of the energy input to electrical dryers is typically lost to frame heating (~1.4%), textile heating (~4.4%), losses to the surroundings (~20.6%), and through the exhaust (~34%), and therefore, only ~ 40% of the total input energy contributes to the evaporation process. Conde (1997) extended the study by Lambert et al. (1991) to demonstrate that the use of heat-recovery heat exchangers (typically cross flow air-to-air heat exchangers used to preheat the airstream at the inlet of the drum) improves the energy efficiency of the drying process. Conde (1997) implemented a triangular, plain-fin, crossflow heat exchanger on a 6-kg ERD and observed an increase in drying efficiency as the mass of textile in the drum increases. This increase in drying efficiency is due to an increase in the evaporation rate as the amount of moisture available increases too. Bansal et al. (2001) observed that recuperative heat exchangers can improve the energy efficiency of ERDs by ~14%. Bassily and Colver (2003b) experimentally evaluated the effects of the operating parameters on the performance of a residential ERD. They varied the electrical

input power, load weight (m_{cl}), fan speed (Ω_d), and initial moisture content (X_{init}) of the clothes, and concluded that current tumble dryers can be further optimized by controlling the operating conditions to achieve extra energy savings. Ahn et al. (2019) conducted experiments to investigate the drying mechanisms of two ERDs of different capacities, 3.2 kg and 6.2 kg. They found that air entering the electrical heater was preheated by the heat leaking from the heater and the drum walls, which recovered 5.4 – 8.5% of energy input. Ma et al. (2018) investigated the possibility of simultaneous heat recuperation and exhaust recirculation on a residential electrical dryer with a 7-kg capacity and power rating of 800 W. The study showed that the SMER was reduced from 1.113 kWh kg^{-1} to 1.099 kWh kg^{-1} with a recirculation ratio of 0.6. Additionally, the drying efficiency was enhanced by ~ 50% when compared to a conventional ERD. The above discussion indicates that existing ERDs are far from the thermodynamic limit, despite years of study. From these studies, the average baseline drying efficiency of ERDs can be approximated to be ~ 40 – 50% (Lambert et al., 1991; Deans and Tranxaun, 1992; Deans, 2001). Figure 2.5 shows the energy required in convective dryers compared to the minimum thermal energy required to remove water, i.e., $SMER_{\min}$. Optimization of operating conditions, waste heat recovery techniques, and extra insulation can improve the performance of ERDs; however, the energy consumed by the enhanced dryer would still be at ~ 2.2 times the minimum SMER.

2.2.2.3 Gas-fired Dryers

Gas-fired tumble dryers (GFDs) are more widespread in commercial settings than in residential ones. There are over 35,000 commercial dryer facilities in the US, in hotels, hospitals, resorts, prisons, and stand-alone laundry services. These units consume ~ 53

billion kWh of primary energy (Pescatore and Carbone, 2005). Figure 2.4b shows a schematic of the airflow for a standard GFD. Ambient air enters the combustor, which directly heats the air stream using combustion of natural gas. The remainder of the process is identical to that for an ERD. Combustion processes add moisture due to the water in the flue gas. The humidity ratio of the air leaving the drum is therefore slightly higher than that in the intake air. However, due to elevated temperatures achieved during combustion, 160 – 230°C, evaporation is not significantly affected by the moisture added after the combustor. Typically, commercial gas-fired tumble dryers (~ 11.33 kg capacity) have an SMER of 1.52 kWh kg^{-1} (El Fil and Garimella, 2021). In a very similar fashion to ERDs, the drying efficiency of baseline commercial GFDs is < 50%, i. e., $\eta_d \leq 0.43$.

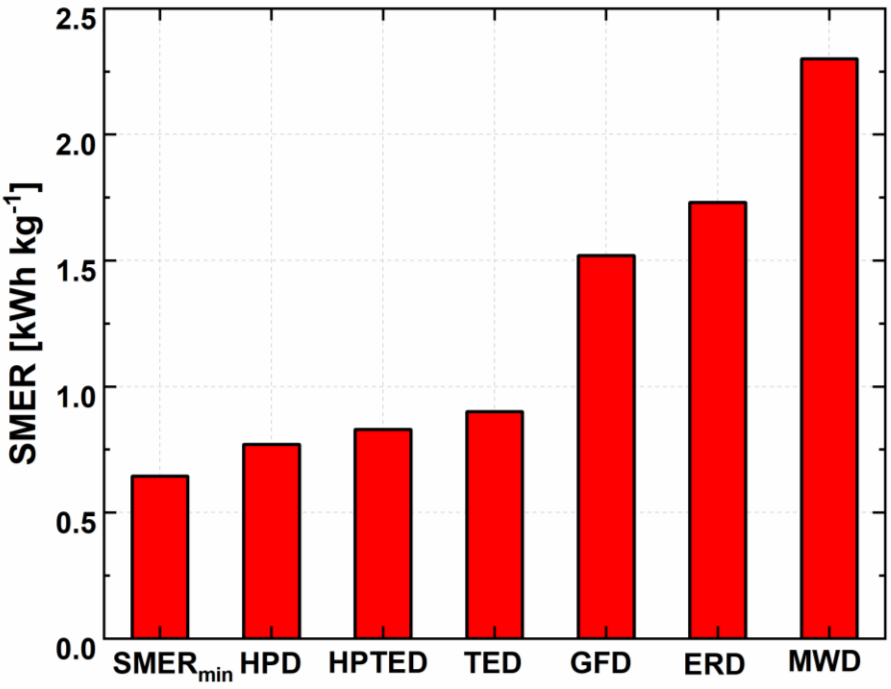

Figure 2.5: Energy required to evaporate one kilogram of water in different convective/thermal textile drying techniques.

Most of the studies in the literature have focused on investigating and improving the performance of small residential ERDs; therefore, very few studies have investigated GFDs. Williamson and Bansal (2004) investigated the performance of a large (dry load capacity ~ 210 kg) GFD with and without exhaust gas recirculation. Unlike electric dryers, Williamson and Bansal (2004) found that recirculating any fraction of the exhaust gas decreases the evaporation rate. This decrease in evaporation rate increased the drying time, resulting in a higher SMER. However, these findings contradict other studies that suggested exhaust gas recirculation would enhance the energy efficiency and the rate of moisture removal (Conde, 1997; Deans, 2001). These differences can be attributed to differences in operating conditions. For example, Williamson and Bansal (2004) investigated a GFD that is 10 times the capacity of dryers investigated in the other studies.

Huang et al. (2020) compared the performance of a GFD to that of an ERD and heat pump dryer (HPD) as function of textile load. Their experiments showed that when increasing the mass of textile from 1.5 kg to 6 kg, the SMER of gas-fired and electric dryers increase initially, followed by a decrease. Among the three dryers, the GFD and the HPD demonstrated the best performance in terms of energy consumption (SMER). The performances of both gas-fired dryer and electrical dryers were not that sensitive to change in ambient temperature; however, the performance of the heat pump dryer depended heavily on the ambient temperature. El Fil and Garimella (2021) studied the performance of a commercial GFD (~ 11.33 kg capacity). They demonstrated experimentally that when recirculating 51% of the exhaust gas, the SMER decreases by 9%. Additionally, when an air-to-air crossflow heat exchanger was used, the SMER of the gas-fired tumble dryer was reduced by 15%. In addition to energy savings, El Fil and Garimella (2021) showed that a

recuperative heat exchanger and gas recirculation reduced the drying time by 12.5% and 9.5%, respectively. Ahmadi et al. (2021) proposed a sorption-based technique to enhance the energy performance of a 3.83-kg capacity GFD. Their approach was to absorb water vapor from the humid air leaving the drum into a membrane-based lithium bromide (LiBr) dehumidification module. The heat of absorption released in this process could be used to preheat the inlet air. Desorption was driven by the combustor. The SMER of the GFD compared to the baseline dryer decreased by 12%.

As shown in Figure 2.5, the energy required by a baseline GFD is 2.3 times that of the minimum SMER. This can be attributed in part to the fact that open-cycle air vented tumble dryers have significant air leakage due to negative pressure inside the drum (Boudreaux et al., 2020). Additionally, the high elevated temperatures in the gas-fired tumble dryer increase the heat loss from the dryer to the surroundings. With the enhancement technologies discussed above, the energy required by the gas-fired tumble dryer is ~ 1.8 times that of the minimum thermodynamic limit, which is more promising than the improvements in electric tumble dryers (~18%).

2.2.2.4 Microwave/Infrared Dryers

Microwave drying is based on heating of the water volumetrically by electromagnetic radiation in the frequency range of 300 MHz–300 GHz with wavelengths ranging from 1 mm to 1 m (Kumar and Karim, 2019). Electromagnetic energy typically propagates through space through time-dependent magnetic and electric fields (Feng et al., 2012). As the microwave penetrates the drying material, the material heats up volumetrically, thereby allowing for a higher diffusion rate and pressure gradient to

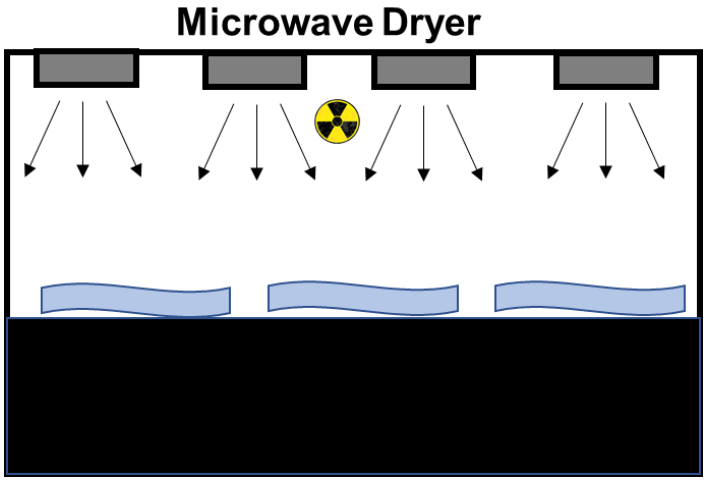

Figure 2.6: Schematic of microwave dryer (MWD)

transport the moisture through the material. Figure 2.6 shows a schematic of a typical microwave textile drying furnace.

In principle, there are two mechanisms of microwave heating: ionic conduction and dipolar reorientation. During ionic conduction, the ions are accelerated by the electric field and collide with other molecules, dissipating kinetic energy. In dipolar reorientation, electric dipoles rotate to align with the electric field. As the rotating dipoles interact with the surrounding material, intermolecular friction dissipates the energy in form of heat (Orfeuil, 1987; Bhandari, 2015). According to Lambert's law, the microwave energy absorbed can expressed as:

$$Q = k_{eff} \left|\vec{E}\right| = 2\pi f \varepsilon_0 \varepsilon_r^{'} \tan\delta \left|\vec{E}\right| \qquad (2.7)$$

Where Q is the microwave energy, k_{eff} is the effective electrical conductivity, f is the frequency, ε_0 is the permittivity of free space, which is taken as $8.8514\times10^{-12}\,\mathrm{F\,m^{-1}}$

(Rattanadecho and Makul, 2016), $\varepsilon_r^{'}$ is the relative dielectric constant, $\tan\delta$ is the loss coefficient, and $\vec{E}$ is the electric field intensity. The most common microwave dryers (MWDs) operate at a frequency of 2450 MHz (Kumar et al., 2016). Figure 2.4f shows a schematic of a microwave dryer where textile can be dried by panel heaters as they flow over a moving plate.

Microwave drying has been implemented for many drying applications such as for textiles (Vrba et al., 2005; Pourová et al., 2006; Büyükakıncı, 2012), food (Maskan, 2001; Kahveci and Cihan, 2007; Haghi and Amanifard, 2008; Feng et al., 2012; Chandrasekaran et al., 2013; Kumar et al., 2016; Kumar and Karim, 2019), wood (Du et al., 2005; Li et al., 2008; Vongpradubchai and Rattanadecho, 2011), and gypsum (Tuncer et al., 1993; Kim et al., 2008; Sadeghiamirshahidi and Vitton, 2019). For textiles, microwave drying might not be the best option mainly because of the thickness of the garments in a full load of wet textiles, which will result in uneven drying (Bhandari, 2015). Further studies are also needed to investigate the effect of microwave drying on the mechanical and thermophysical properties of textiles with time. The energy requirement is highly dependent on parameters such as the fiber type, thickness, and desired final moisture content. For instance, the SMER to dry 100% polyester packages is 0.53 kWh kg^{-1}; however, drying loose cashmere would require 4.91 kWh kg^{-1} (Vrba et al., 2005; Mujumdar, 2014). As shown in Figure 2.5, microwave drying is the most energy-intensive among the thermal drying processes, although it provides one of the faster methods of drying. When compared with the minimum thermal energy required, microwave drying consumes ~ 3.6 times the latent heat of vaporization. Several factors can contribute to this drying performance, including primarily the low efficiency of conversion from electricity to microwaves ($\eta_c = 0.6 - 0.8$),

in addition to the 0.8 – 0.9 efficiency of conversion from alternating current (AC) to direct current (DC) (Vrba et al., 2005; Rattanadecho and Makul, 2016). With all these conversion factors, the efficiency of microwave drying is estimated to range between 38 – 68% (Gluesenkamp et al., 2020), which is in the same range as baseline ERDs.

In a manner similar to microwave energy, infrared (IR) energy is produced electrically. There is only one reported study in the literature based on IR textile drying. Weaver (2017) investigated an IR heater operating in the 2.5–10 μm wavelength range and targeted the 3-μm absorption peak of water. Unlike electrical heating, in which heat is transferred through convection, the energy in IR is transferred through radiation. Because of the lack of sufficient literature on this technique, IR drying is not considered further in this work.

2.2.2.5 Heat Pump Dryers

Heat pump dryers have been introduced as a measure to improve drying energy efficiency. In closed-loop condensing tumble dryers, the moisture exiting from the drum is condensed to extract additional latent energy and provide a dry air stream to the inlet of the drum. There are several methods to achieve condensation in the exhaust air stream, the most common of which are by cooling the stream with a heat pump (Bengtsson et al., 2014; Gatarić et al., 2019; Lee et al., 2019) or by using liquid-coupled heat exchangers (Jian and Zhao, 2017). A heat pump dryer (HPD) can utilize any type of heat pump, although vapor compression heat pumps are the most common.

Figure 2.7 depicts a schematic of a typical vapor compression HPD. A fan is used to circulate the air inside the closed-loop dryer. The vapor compression heat pump consists

of four components (compressor, evaporator, condenser, and expansion valve). The humid air leaving the drum is dehumidified in the evaporator by cooling it below its dew point temperature. The heat rejected by the condenser of the heat pump is used to heat the cold, dry air before it enters the drum. Cochran et al. (2009) improved the energy utilization of an electric tumble dryer by using a surface tension element (STE) to replace the air-to-air plate heat exchanger condensing surface. The advantage of using an STE in place of the plate heat exchanger is that since there is no condensation build up on the STE surface, local condensation will be increased as compared to the case for the flat plate. The STE was able to enhance energy performance by 4%. TeGrotenhuis et al. (2017) simulated a hybrid heat pump textile dryer and reported energy savings of 50% compared with a typical residential ERD.

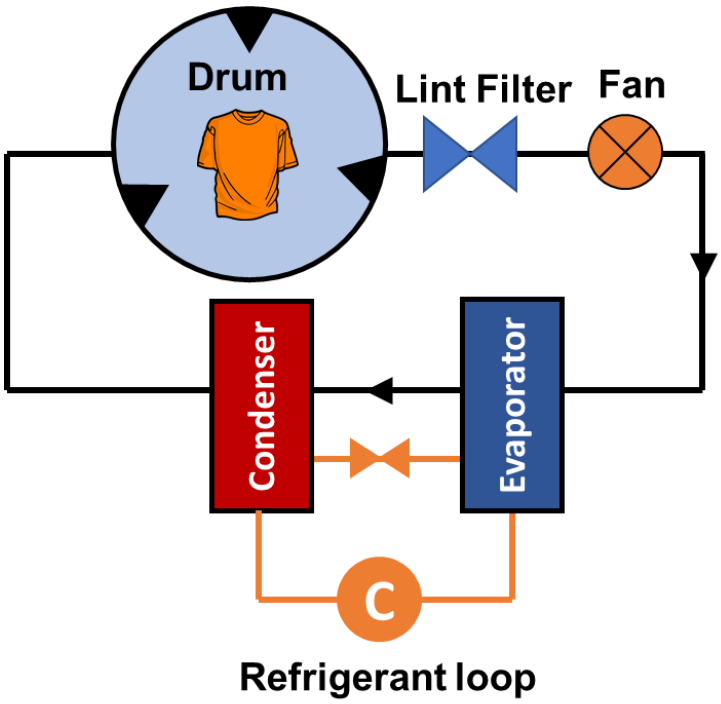

Figure 2.7: Schematic of closed-loop heat pump dryer (HPD)

HPDs have shown a significant reduction in energy consumption compared to air-vented tumble dryers; however, this comes at the expense of drying time. The drying time in an HPD is typically 2-4 times the drying time in an ERD or a GFD (TeGrotenhuis et al., 2017; Gatarić et al., 2019). To overcome these challenges, some researchers have investigated a multi-stage HPD to further recover any waste heat. Cao et al. (2014a) developed a two-stage heat pump tumble dryer prototype and compared its performance to that of an ERD and a hybrid dryer (recuperation + vapor compression HP). The two-stage heat pump dryer used three main technologies to enhance the performance over baseline dryers. The prototype used compact heat exchangers, high-efficiency brushless DC fan motors, and a two-stage vapor injection refrigeration cycle. The two-stage vapor compression heat pump dryer achieved an energy reduction of 59% and 25% compared to the baseline electric dryer and hybrid heat pump dryer, respectively. Do et al. (2013) experimentally investigated the performance of a closed-cycle condensing dryer (air-vented HPD) augmented with an air-to-air heat exchanger and showed that the energy consumption was complex function of electric resistance heater capacity and water condensation rate. The greater the heating power, the shorter the drying time, in turn resulting in a more efficient drying process. The cooling air flow rate and the drying air flow rate did not have a significant effect on the performance of the dryer. Bansal et al. (2010a) developed a novel household HPD based on a heat exchanger using hot water. A conventional electric dryer was retrofitted with a water-to-air finned-tube heat exchanger to replace the electric heating element. The new drying concept was able to shorten the drying time by ~ 15 minutes. Other studies of HPDs were conducted by Cranston et al.

(2019) and Ahmadi et al. (2021). The latter study used an absorption heat pump with LiBr as the working fluid to enhance the performance of a gas-fired tumble dryer by 12%.

Although heat pump dryers have shown promising energy performance, they use working fluids with high global warming potential (GWP) such as R114, R22, and R134a, and LiBr-H_2O. There are some efforts to design an efficient heat pump tumble dryer using a low-global warming potential working fluid such as CO_2. Sarkar et al. (2006) simulated a transcritical CO_2 heat pump tumble dryer. However, the study did not report whether there was any enhancement in SMER of the dryer compared to conventional ERDs. Mancini et al. (2011) compared the performance of a transcritical CO_2 cycle with that of a subcritical R134a cycle for an HPD. The results showed that the SMER when using CO_2 was approximately the same as when using R134a; however, the drying time was extended by 9%. Figure 2.5 shows an average representative SMER of a HPD (depicted in Figure 2.7). HPDs show the closest performance to the thermodynamic limit, consuming ~ 1.17 times the energy corresponding to $SMER_{\min}$. This is because in HPDs, a significant fraction of energy used to evaporate the moisture from the textile is retrieved during the condensation phase. The performance of HPDs is mainly dictated by the heating coefficient of performance (COP), i.e., the desired capacity divided by the electrical energy input. The COP of a heat pump dryer can be expressed by Equation (2.8):

$$COP = \frac{\dot{Q}_{sensible} + \dot{Q}_{latent}}{\dot{W}_{elect}} \tag{2.8}$$

The COP is a function of various operating conditions such as the evaporator temperature and the temperature at which the air enters to drum (post condenser). Further

information heat pump dryers can be found in (Colak and Hepbasli, 2009; Bengtsson et al., 2014; Cao et al., 2014a; Gatarić et al., 2019; Lee et al., 2019).

2.2.2.6 Thermoelectric Dryers

Thermoelectric dryers using thermoelectric modules integrated into tumble dryers have shown promising results (Liu et al., 2008; Junior et al., 2012; Goodman et al., 2017; Patel and Gluesenkamp, 2018; Patel et al., 2018; Somdalen and Köhler, 2018; Patel et al., 2021). As depicted in Figure 2.9a-b, thermoelectric dryers can be of two types: a closed loop thermoelectric dryer (TED) (Figure 2.8a) and an open-cycle thermoelectric heat pump dryer (TEHPD) (Figure 2.8b). Thermoelectric modules are solid-state devices consisting of two semiconductors sandwiched together in a thin layer. Applying voltage across the thermoelectric module results in a temperature difference. Therefore, a thermoelectric module can perform the same function as the heat pump in an HPD. The cold side of the thermoelectric element is used to condense the moisture carried by the air leaving the drum, while the hot side is used to preheat the air before it enters the drum. Thermoelectric dryers

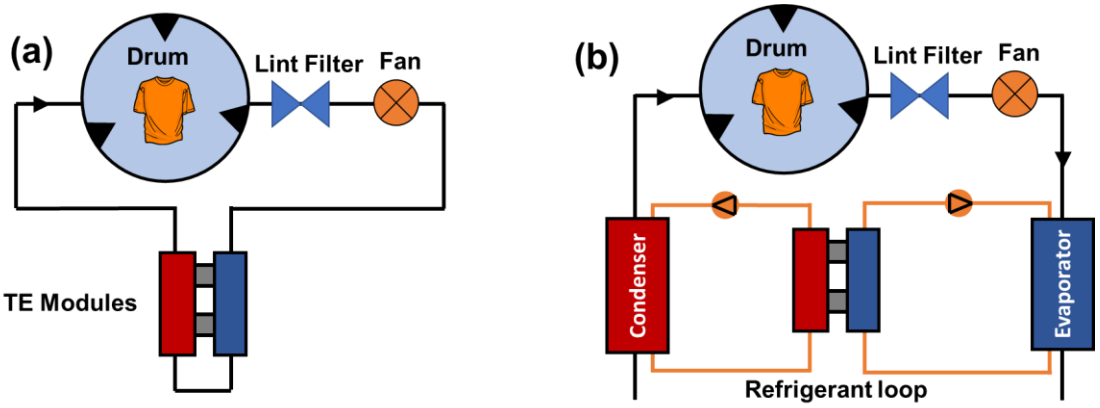

Figure 2.8: Schematic of (a) thermoelectric dryer (TED) and (b) thermoelectric heat pump thermoelectric dryer (TEHPD)

typically have fewer moving parts and have no refrigerants, which can be advantageous compared to HPDs.

Liu et al. (2008) were the first to numerically and experimentally investigate a closed-loop TED used to dry flax fibers. A one-dimensional mathematical model was developed to predict the temperature distribution in the module. The prototype contained 40 thermoelectric modules and a perforated-wall hexagonal drying cabinet. The experiments were conducted on wet fabric weighing 2.1-4.1 kg. The results showed that SMER and the drying rate are complex functions of several operating conditions such as initial mass of the wet textile, electric power input, and drying temperature. The drying time during the experiments was four hours. Goodman et al. (2017) developed a thermodynamic model and experimentally characterized the energy consumption and efficiency of a 3.83-kg closed-loop TED. The thermoelectric module can reduce the energy consumed by a conventional electric tumble dryer by 38%; however, the drying time was significantly increased. Patel et al. (2018) compared the performance of a TED with that of a 3.83-kg ERD. The thermoelectric unit used in the prototype consisted of four commercially available modules. The energy factor increased by 75% compared to baseline electric dryers, while the drying time was extended by a factor of five.

To avoid extending the drying time and improve the performance of the dryer, researchers have developed novel approaches in implementing thermoelectric modules. Patel et al. (2021) used pumped secondary loops with conventional finned-tube heat exchangers, which significantly reduced the drying time and made thermoelectric dryers competitive with the state-of-the-art HPDs. The new open-loop thermoelectric tumble dryer (depicted in Figure 2.9b) resulted in an SMER of 0.81 kWh kg^{-1} with a drying time

ranging between 64.6-84.3 minutes for a standard load size of 3.83 kg. This showed a 47% improvement in drying time compared to the closed-loop thermoelectric dryer. Figure 2.5 shows that energy required to remove water from the textile for an open-loop and a closed-loop thermoelectric dryer is only 1.25 times and 1.4 times, respectively, compared to the minimum thermodynamic energy required to evaporate a kilogram of water. Although the efficiency of thermoelectric heat pumps is typically lower than that of vapor compression HPDs, the studies in the literature show that thermoelectric heat pumps are promising in textile drying application. Further improvement, specifically the temperature lift across the module, should be considered. With the current technological advancements and material limitations, the thermoelectric module can only provide a temperature lift of 10-20 K. For instance, with an overall temperature lift of 20 K, exhaust air from the drum can be cooled to ~ 9°C to ensure condensation of the humid air, while the inlet air is heated up to 29°C. With such temperature ranges, TED cannot compete with GFDs, HPDs, and other hybrid dryer designs such as TEHPDs, in terms of drying time.

2.2.2.7 Drying Limits

As discussed in previous sections, most textile drying research conducted in the literature is mainly concerned with enhancing the energy efficiency of the dryer without assessing the maximum possible drying potential. Most textile tumble dryers achieve drying through evaporation. Theoretically, the drying efficiency, defined in Equation 2.1, is assumed to always have a maximum value approaching unity. There are many assumptions embedded in this approximation. The most important are that there are no heat losses within the dryer and that evaporation takes place instantaneously. However, this is not always true in textile drying. Often, the wet textile is at a lower temperature and requires

the addition of sensible heat to raise the temperature of the moisture inside it to initiate the evaporation process. Gluesenkamp et al. (2020) investigated the efficiency limits of evaporative textile drying in ERDs and HPDs. Their study suggested that for some applications, the drying efficiency can exceed 1 if "free drying" is considered. Free drying is defined as water evaporation taking place spontaneously without adding any energy input. Gluesenkamp et al. (2020) derived an equation to quantify the ideal drying efficiency for a generic dryer (mainly electric/heat pump dryers) expressed in Equation (2.9):

$$\eta_{d,ideal} = \frac{\Delta m_w h_{fg}}{\underbrace{\Delta m_w h_{fg}}_{\text{latent}} + \underbrace{\left(T_f - T_i\right)\left(\Delta m_w c_{p,w} + m_{cl} c_{p,cl}\right)}_{\text{sensible}}} \tag{2.9}$$

where the denominator is the total ideal energy input for evaporation in which all the energy input was actually used for evaporation, T_f is final temperature, T_i is the initial temperature, and Δm_w is the amount of water evaporated throughout the process. Equation (2.9) suggests that $\eta_{d,ideal} < 1$ because the sensible energy term is always positive. In a case of the closed-loop HPD, the moisture from the textile is removed only when it condenses in the evaporator. Therefore, the latent heat in the evaporator dominates the moisture extraction in heat pump tumble dryers; any sensible heat removed from the air will be re-added in the closed-loop cycle through condensation. The drying efficiency for a closed-loop heat pump dryer is given by Equation (2.10) (Gluesenkamp et al., 2020):

$$\eta_{d,ideal}^{HPD} = \varphi_{LH} \mathrm{COP} \tag{2.10}$$

where φ_{LH} is the latent heat fraction of the ideal energy input and COP is the coefficient of performance for the operating heat pump in the tumble dryer. The drying efficiency is

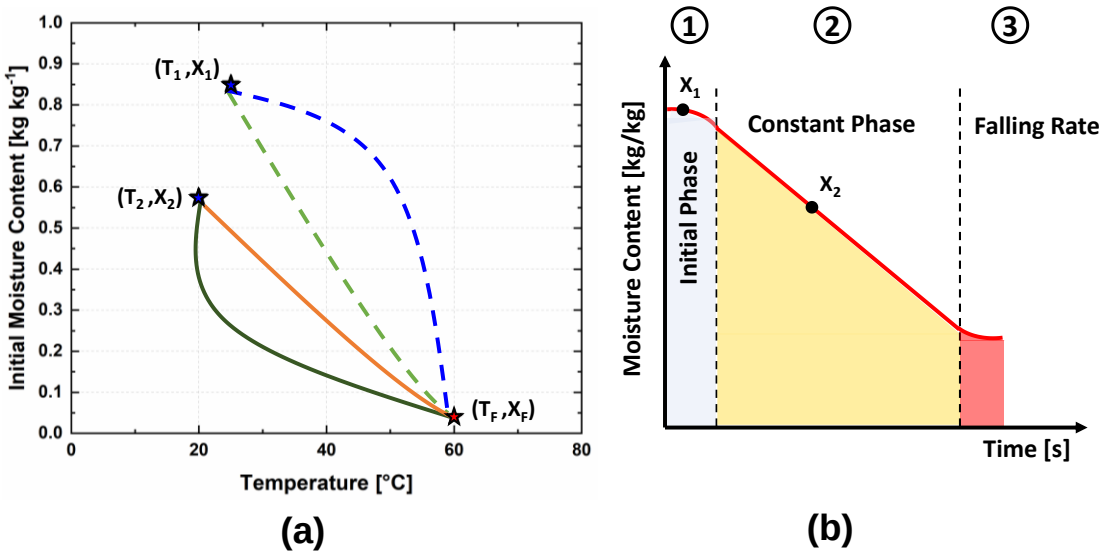

Figure 2.9: (a) Different thermodynamic paths during drying process (b) Moisture content as function of time for porous media showing the three drying phases

dependent on the COP of the heat pump, which means that it is a function of the temperature lift across which the heat pump operates. The Carnot COP can be expressed as:

$$\mathrm{COP}_{carnot} = \frac{T_C}{T_H - T_C} \tag{2.11}$$

Equation 2.11 implies two performance limits. The first limit is when $\Delta T_{lift} \to \infty$, i.e., the temperature difference between the hot and cold reservoir is infinite. The drying efficiency for such a case tends to 0, and the SMER of the dryer would approach infinity. However, as the temperature lift increases, it facilitates evaporation process in the drum, which is advantageous to the drying process, at the cost of the requirement of high-grade energy input. One the other hand, at the second limit where $\Delta T_{lift} \to 0$, i.e., the drying efficiency

approaches infinity. However, when the temperature lift is too small, the temperature of air entering the drum decreases, resembling forced convection natural drying, with the associated penalty of excessively long drying times typical of natural drying.

Textile drying is a complex process that involves coupled mass, heat, and momentum transport phenomena in porous media. The approach to evaluate the theoretical limit of drying in the literature has often treated drying as a path-independent thermodynamic process. As shown in the analysis described in the previous sections, only the initial and final values of temperatures and mass of moisture removed are considered rather than the path taken to achieve the final state. However, in practice, the actual drying efficiency is in fact path dependent. Figure 2.9a shows different thermodynamic paths that can be taken during evaporation. For instance, State 1 is representative of a typical initial point for a GFD while State 2 corresponds to that of a HPD. The starting point of a drying cycle dictates the time required to evaporate the available moisture. Figure 2.9b shows a typical drying curve for hygroscopic materials with the stat points for GFDs and HPDs overlaid. For instance, if the initial moisture content is 85% (State 1), the three drying phases will take place. During the initial phase (transient phase), water in the textile migrates to surface by capillary flow. This is also known as unbound (free) water transport. Then during the second stage, the heat and mass transfer balance is achieved as the drying rate is constant. During the third stage, the main mechanism of moisture transport changes to bound moisture diffusion from within the textile. However, if the drying cycle starts from an initial moisture content of 57.5% (State 2), then only two drying phases will take place. The different drying mechanisms occurring in the two cases would lead to different drying

rates. Therefore, calculating the drying efficiency using only the initial and final state points might not actually reflect the true efficiency of a given dryer.

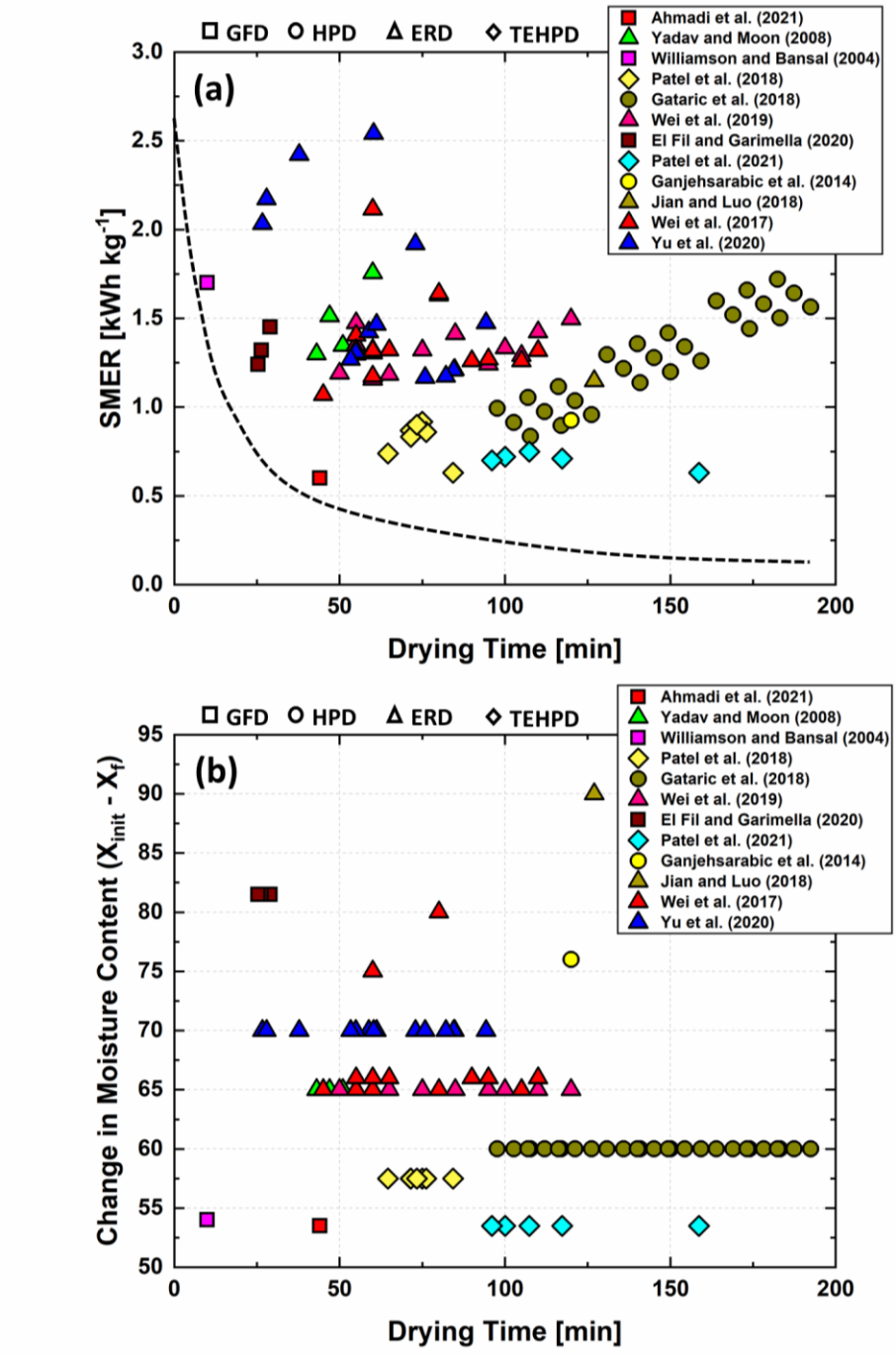

Figure 2.10: (a) State-of-the-art performance of tumble dryers (b) Change in moisture content as function of drying time

Figure 2.10a shows the performance of the state-of-the-art textile tumble dryers. Despite having different operating conditions, such as different bone-dry mass and initial moisture content, the most promising technologies are HPDs and TEHPDs. This is because the SMER was the closest to the minimum thermal energy required to evaporate the moisture from the textile. With additional energy savings and heat recovery techniques, the energy required to remove the water from the textile could be less than the minimum SMER. Figure 2.10b shows the different initial moisture content for some of the experimental studies in the literature. It is clear that there is no common initial moisture content for the experiments by different investigators, which makes it harder to compare the energy consumption and the drying time achieved in each cycle. However, Figure 2.10a shows that GFDs can achieve low SMER while maintaining a relatively short drying time. To compare the performance of different dryers with different initial moisture content, a normalized drying efficiency is defined as follows:

$$\eta_d^* = \eta_d (X_{init} - X_f) \tag{2.12}$$

The drying efficiency for each of the studies was calculated from the SMER using Equation (2.4). Figure 2.11 shows the normalized efficiency as function of drying time. The higher the normalized efficiency, the better the performance of the dryer. The performance of GFDs and ERDs is on par; however, GFDs have on average lower drying times than ERDs. Heat pump dryers show the best drying efficiencies as compared to the GFDs, ERDs, and TEDs; however, drying times can be significantly longer. The GFD investigated by Ahmadi et al. (2021) had the highest normalized efficiency of 0.576. This performance

shows the advantages of integrating a sorption-based GFD to recover the available waste heat, resulting in improved drying efficiency.

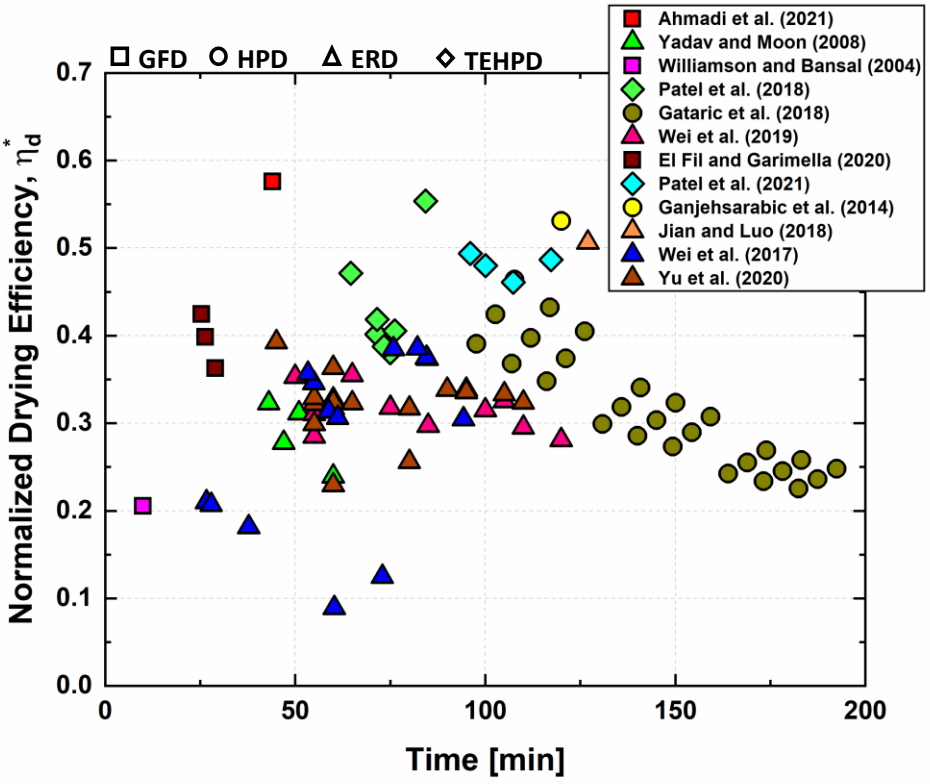

Figure 2.11: Normalized drying efficiency versus drying time

2.3 Conclusion

Textile tumble dryers on the market today suffer from low energy efficiency, non-uniform drying, long drying times, and significant degrading of textile quality. The commonly used technique to save energy in tumble dryers is by controlling the process through early termination. However, controlled termination techniques do not provide sufficient energy savings due to the fact that varying the operating conditions does not

influence the drying time nor drying efficiency significantly. This can lead to either under-drying or over-drying of the textile. Most of the energy-saving methods applied to convective drying are based on heat recovery from the exhaust air, because a significant amount of heat used in drying appears in the exhaust stream. Other energy saving methods include alterations to the main cycle operation to make a better use of the available energy. These methods include changing open-cycle, air-vented dryers to closed-cycle HPDs. Current tumble dryers, other than gas-fired tumble dryers, have not been able to use high temperatures to advantage effectively. To increase the temperature of the air entering the drum without excessive external energy input, researchers have implemented different types of heat pumps into the tumble dryer (Conde, 1997; Junior et al., 2012; Cao et al., 2014a; Weaver, 2017; Cranston et al., 2019). “Not-in-kind” dryers including thermoelectric-powered, sorption-driven, and ultrasonic dryers have shown promising enhancement in energy performance. The following key conclusions can be drawn from this assessment:

- Models that simulate the performance of tumble dryers are still empirical or semi empirical; a physics-based model that captures the physical phenomena in each drying phase should be developed to further optimize the drying process.
- Heat pump dryers show promise compared to the minimum SMER (1.17× times). However, the long drying times of these dryers must be reduced to facilitate widespread adoption.
- Air-vented ERDs and GFDs show significant enhancement in energy efficiency with waste heat recovery techniques such as exhaust gas recirculation (~ 10%) and recuperation (~ 15%).

- TEHPDs outperformed ERDs, GFDs, and TEDs by 2.08, 1.83, and 1.08 times, respectively.
- Research on tumble dryers should be guided by the maximum drying limit for each dryer, compact design, and the need for reduction in drying time.

CHAPTER 3. MATHEMATICAL MODEL

3.1 Introduction

Based on the gaps identified in the literature, a transient mathematical model to predict the performance of textile dryers is developed here. This computational model for the drying process is developed for a commercial gas-fired tumble dryer. Thermodynamic, heat transfer, and mass transfer analyses associated with the drying medium (air) and textile are conducted at every stage. Each stage is modeled independently and coupled sequentially to simulate a full baseline drying process.

Drying occurs in the drum, where the air and the textile tumbling together exchange heat and moisture. The kinetics of clothes drying inside the dryer involves continuous variation of temperature and moisture content with time. The mean integral values for these variables can be derived by solving the differential equations for moisture and heat transfer in a porous material. First, a lumped thermodynamic model of the gas-fired dryer is developed. Then, to understand the kinetics of moisture transfer, a transient 2-D axisymmetric model of the textile in the drum is developed.

3.2 Lumped Model Development

3.2.1 Air-vented Dryers

A mathematical model is developed to predict the temperature and humidity of the air and the moisture content of the wet textile. The theoretical model is used to compare the

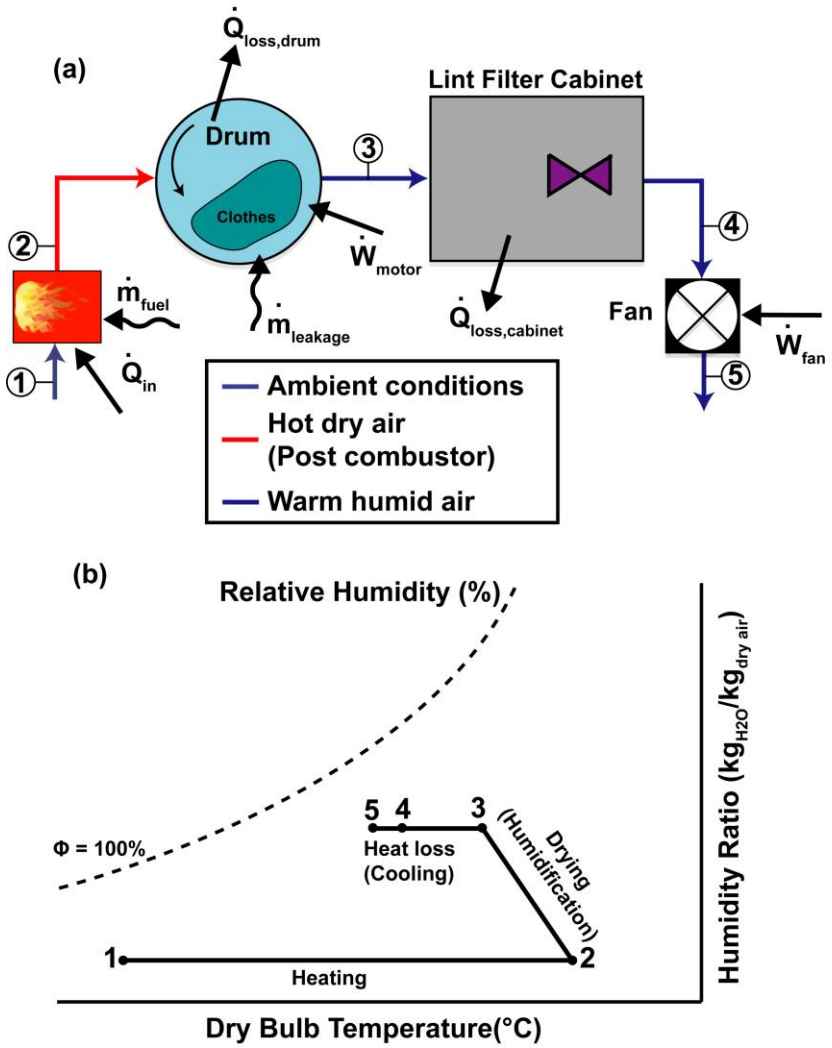

Figure 3.1: (a) Baseline schematic of a gas-fired air-vented tumble dryer (b) Psychrometric chart of the baseline drying cycle

energy consumption between the baseline and energy saving techniques investigated in this work. Figure 3.1a shows a schematic of a commercial gas-fired tumble dryer, while Figure 3.1b displays the baseline drying process on a psychrometric chart.

In this cycle, ambient air at State 1 enters the combustor, which heats the air stream to State 2. The hot air enters the drum where it flows through the load of wet textiles. Moisture from the wet load increases the humidity of the air and is removed from the drum as the humid air stream at State 3. After that, the air enters the lint filter cabinet, where it loses

some of its energy to the surroundings. The lint filter in the cabinet collects most of the lint released during drying. The humid air exits the lint filter at State 4 without any significant change in its enthalpy; however, there is a pressure drop induced by the lint filter. Finally, the air leaves through the fan at State 5. The fan drives the air flow through the dryer by inducing a negative gauge pressure in the cabinet of the dryer. The dryer is divided into four submodules: the combustor, the drum, lint filter cabinet, and exhaust fan.

3.2.2 Lumped Approach

3.2.2.1 Combustor

Gas-fired tumble dryers differ from steam, electrical, and thermoelectric dryers due to the fact that the inlet humidity ratio of inlet air increases because of the moisture added in the combustion reaction (El Fil and Garimella, 2021). In this study, the molar composition of natural gas is simplified to 90% methane (CH_4), 5% ethane (C_2H_6), and 5% Nitrogen (N_2).

$$\underbrace{0.9\mathrm{CH_4}+0.05\mathrm{C_2H_6}+0.05\mathrm{N_2}}_{Natural\ Gas}+\underbrace{\left(2.151+\gamma\right)\left(O_2+3.76\mathrm{N_2}\right)+\zeta\mathrm{H_2O}}_{Humid\ Air}\rightarrow \mathrm{CO_2}+\left(1.95+\zeta\right)\mathrm{H_2O}+\left(8.137+3.76\gamma\right)\mathrm{O_2} \tag{3.1}$$

where ζ is the number of moles of water in the incoming air calculated based on the ambient relative humidity, and γ is the number of moles of excess air. The stoichiometric air-to-fuel ratio for natural gas is 2.151 mol air/mol fuel combusted. To calculate the number of moles of water in the incoming air, the ratio of partial pressure of water vapor to the total pressure of air is used, as given by Equation (3.2).

$$\zeta=\frac{p_v}{p_{atm}}\left(n_{dry,air,R}+\zeta\right) \tag{3.2}$$

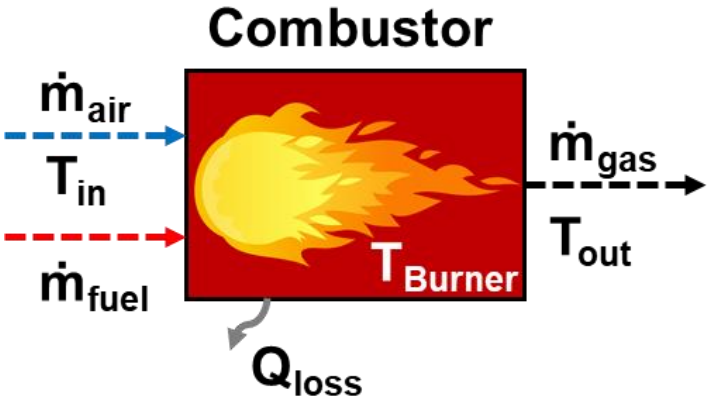

Figure 3.2: Control volume of the combustor/burner

The HHV and LHV for the natural gas resulting from the chemical balance above were 50.71 MJ kg_{fuel}^{-1} and 45.77 MJ kg_{fuel}^{-1}, respectively. After calculating the coefficients of the combustion reaction given in Equation (3.1), a thermodynamic analysis of the combustor is performed to quantify the heat released and the temperature of air entering the drum. To calculate the heat of combustion, an energy balance over the combustor (Figure 3.2) was performed, as given by Equation (3.3):

$$H_R + Q_{in} = H_p + \Delta W_{sf} + Q_{loss} \tag{3.3}$$

where ΔW_{sf} is the net shaft work, which is negligible in this study, Q_{in} is added heat at the beginning of the reaction, and Q_{loss} is the heat lost due to natural convection and radiation from the combustor. To capture the transient behavior of the combustor, a lumped capacitance approach is adopted (Ulloa et al., 2013). At the burner outlet, the combustion gases, $\dot{m}_{gas}$, are assumed to be exiting at T_{out}. The mass balance and energy balances on the combustor are given by Equations (3.4) – (3.6):

Table 3.1: Operating conditions of the combustor

Operating Parameter	**Value**
Burner Material	Stainless Steel (AISI 316)
Burner thermal capacitance $\left(mc_p\right)_{burner}$	5.09 kJ/K
Overall heat conductance $\left(UA_{comb}\right)$	8.02 W/K
Combustion efficiency $\left(\eta_{comb}\right)$	0.62
Air mass flowrate $\left(\dot{m}_{air}\right)$	0.10 kg/s
Flue volumetric flowrate $\left(\dot{V}_{fuel}\right)$	8.62×10^{-4} m^3/s
Gas burner rating	18.8 kW

$$\dot{m}_{air} + \dot{m}_{fuel} = \dot{m}_{gas} \tag{3.4}$$

$$\left(mc_p\right)_{burner} \frac{dT_{burner}}{dt} = \eta_{comb}\dot{m}_{fuel}LHV - \dot{m}_{fuel}c_{p,\,fuel}\left(T_{out} - T_{in}\right) - UA_{comb}\left(T_{burner} - T_{in}\right) \tag{3.5}$$

$$\frac{T_{out} - T_{in}}{T_{burner} - T_{in}} = \exp\left(-\frac{UA_{comb}}{\dot{m}_{gas}c_{p,gas}}\right) \tag{3.6}$$

The operating conditions of the combustor are summarized in Table 3.1.

3.2.2.2 Drum

Drying occurs in the drum, where the air transfers heat to the tumbling textile, with water vapor, in turn being transferred to the air. A lumped-parameter drying model was developed to analyze the effects of the energy enhancements studied in this work. The following assumptions are made:

- The air and textile within the drum are well-mixed
- The thermophysical properties and moisture content of the textile are uniform

- Textile and drying air are homogenous, with uniform initial moisture content $X = m_w / m_{cl,dry}$.

Mass, species, and energy equations were derived for the drum. The species balance given by Equation (3.7) shows that the increase in humidity ratio of the air is equal to the evaporation rate.

$$\dot{m}_e = \dot{m}_a \left(\omega_4 - \omega_3 \right) \tag{3.7}$$

Furthermore, the moisture transfer rate from the surface of the wet textile is equal to the rate of reduction of its corresponding moisture content, as shown by Equation (3.8).

$$\dot{m}_e = m_{cl,dry} \frac{dX}{dt} \tag{3.8}$$

In Equation (3.8), $m_{cl,dry}$ is the dry mass of the textile in the drum. Evaporation involves simultaneous heat and mass transfer between the heated air and the textile. The mass transfer at the surface of wet textile is given by Equation (3.9):

$$m_{cl,dry} \frac{dX}{dt} = h_m A_{cl} \left(\alpha_{cl} \omega_{cl}^{surf} - \omega_3 \right) \tag{3.9}$$

where α_{cl} is the water activity coefficient that depends on the moisture content and type of textile as defined by Lambert et al. (1991), and ω_{cl}^{surf} is the humidity ratio of the air at the surface of the textile. An energy balance on the drum gives:

$$\left(m_{cl,dry} c_{p,cl} + X m_{cl,dry} c_{p,w} + m_d c_{p,d} \right) \frac{dT_{cl}}{dt} = -\dot{Q}_{loss} + \dot{m}_2 h_2 + \dot{m}_l h_l - \dot{m}_3 h_3 \tag{3.10}$$

where $\dot{Q}_{loss}$ is the heat lost from the drum through natural convection and radiation, $\dot{m}_i$ is mass flow rate of dry air and h_i (kJ/kg-moist) is the psychrometric enthalpy for the i^{th} state. The loss term is expressed as $\dot{Q}_{loss} = h_{eff} A_{cl} \left(T_{cl} - T_{amb} \right)$, where h_{eff} is the effective heat transfer coefficient due to natural convection and radiation (Bergman et al., 2011; Ahn et al., 2019). The air leakage into the drum, $\dot{m}_l$, is quantified based on the work of Bansal et al. (2016) and Boudreaux et al. (2020). During the experiments, the air leakage was quantified by measuring the pressure within the cabinet of the dryer. The technique used to quantify the leakage in this study extrapolates from the data on an air-vented electric dryer (Boudreaux et al., 2020). The leakage locations considered in this study are at the grill to the combustor (heater) and lint filter in the cabinet to the blower/fan. Lint plays an essential role in controlling air leakage to the dryer and therefore can impact the overall performance of the drying cycle. As lint builds up in the lint filter, the fan motor experiences an additional resistance, which reduces the mass flow rate of the air. Furthermore, this changes the pressure difference in the dryer chamber and the ambient, which in turn changes the air leakage. The main source of air leakage is at the lint filter cabinet and the orifice in the drum door. Most of the lint is generated towards the end of the drying cycle, i.e., during the falling rate phase. As the surface of the textile becomes unsaturated, i.e., $X < X_{crit}$, the amount of lint generated increases compared to the initial and constant drying phases. As the amount of lint increases, an additional resistance to the blower is observed. This reduces the amount of air flowing to the drum for the same fan power, which decreases the evaporation rate. The lint filter was maintained and cleaned between every batch of drying load.

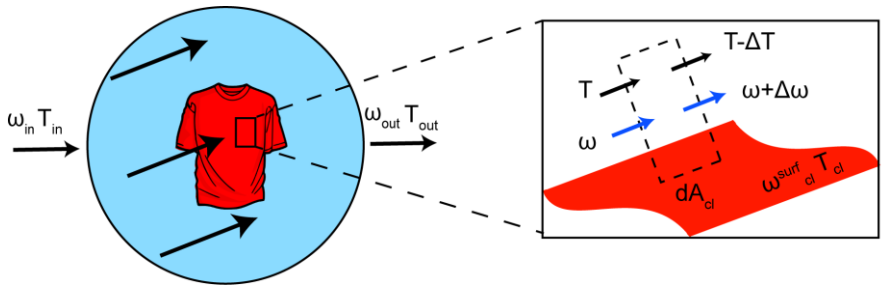

Figure 3.3: Control volume in the drying drum used to quantify area-heat and area-mass transfer coefficients

The air heats up the textile sensibly; however, due to evaporation, some latent energy is transferred from the textile to the air. The heat transfer between the air and the textile material interface is given by Equation (3.11):

$$\left(c_{p,cl} + Xc_{p,w}\right) m_{cl,dry} \frac{dT_{cl}}{dt} = h_h A_{cl} \left(T_3 - T_{cl}\right) - \dot{m}_e h_{fg} \left(T_{cl}\right) \tag{3.11}$$

The effective area-heat and area-mass transfer coefficients used in Equations (3.9) and (3.11) were calculated from measurements in the present study similar to the approach used by Gluesenkamp et al. (2019) and Ahn et al. (2019). The differential control volume used to quantify both area-heat $(h_h A_{cl})$ and area-mass $(h_m A_{cl})$ transfer coefficients is shown in Figure 3.3. Air enters the drum at T_{in} and ω_{in} and exits at T_{out} and ω_{out}. The surface temperature (T_{cl}) and humidity ratio (ω_{cl}^{surf}) are assumed to be spatially uniform for all the textiles in the drum. For the differential control volume, with a wet surface of differential area, Equations (3.12) and (3.13) describe the sensible and latent air energy change, respectively.

$$\frac{\Delta T}{T_{cl} - T} = \frac{h_h dA_{cl}}{\dot{m}_{air} c_p} \tag{3.12}$$

$$\frac{\Delta\omega}{\omega_{cl}^{surf} - \omega} = \frac{h_m dA_{cl}}{\dot{m}_{air}} \tag{3.13}$$

Integrating Equations (3.12) and (3.13) over the total textile surface area results in Equations (3.14) and (3.15), respectively:

$$\frac{T_{out} - T_{cl}}{T_{in} - T_{cl}} = \exp\left(- \frac{h_h A_{cl}}{\dot{m}_{air} c_p} \right) \tag{3.14}$$

$$\frac{\omega_{out} - \omega_{cl}^{surf}}{\omega_{in} - \omega_{cl}^{surf}} = \exp\left(- \frac{h_m A_{cl}}{\dot{m}_{air}} \right) \tag{3.15}$$

3.3 Spatial Model Development

3.3.1 Process Overview

Early theories to explain textile drying were largely based on temperature and on empirical drying curves (Prat, 2002). During the latter part of the twentieth century, more comprehensive heat and mass transfer models were developed and integrated with the previous drying models. Whitaker (1977) introduced a volume averaging theory and derived a general drying model to help integrate the complex heat, mass, and momentum transfer phenomena in porous media. The convective drying models in porous media may be classified in three ways: hygroscopicity of the porous media, internal mass transfer mechanisms, and motion of the evaporation front. Some of the models include simultaneous heat and mass transport in a single phase (solid, liquid, or gaseous) based on continuum physics. Whitaker (1980) developed a rigorous model that includes both continuous and discontinuous states for granular porous media. The term “granular” referred to porous media consisting of a rigid solid phase that contains no moisture. The

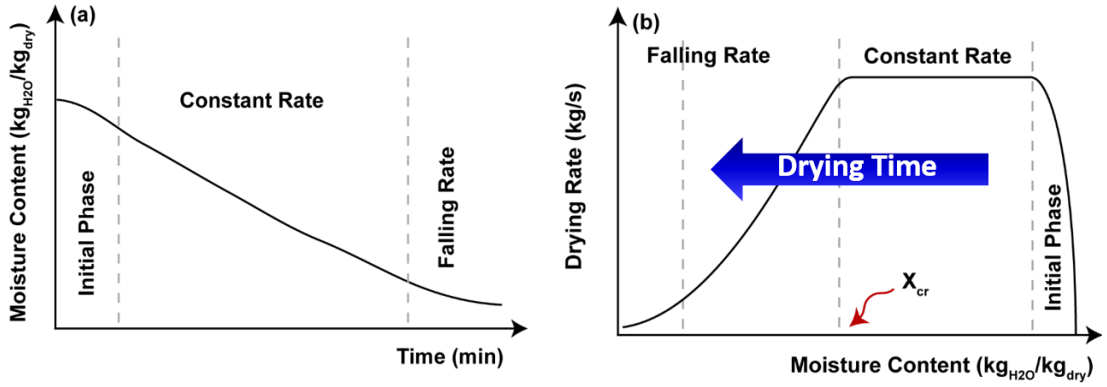

Figure 3.4: Drying Curves (a) moisture content as function of time (b) drying rate variation as function of moisture content

internal mass transfer mechanisms considered were bulk flow in both liquid and gaseous phases. The momentum equation to describe the moisture movement within the solid was based on Darcy's law with the moisture partial pressure gradient and gravity as the driving forces. Hadley (1982) combined diffusion and forced flow of humid air through the porous medium. The moving evaporation front approach was used to describe the humidity and temperature distribution.

According to a recent review of theoretical drying models and their corresponding numerical implementations, drying evaporation models have been used to understand the capillary, gravitational, and other forces in moisture and temperature gradients during drying (Vu and Tsotsas, 2018). Typically, the moving front divides the drying medium into two zones: a wet region and a dry region as depicted in Figure 3.5. Chen and Schmidt (1990) used a set of one-dimensional equations describing the coupled heat and mass transfer in the wet and dry region. Typical drying curves for hygroscopic materials are shown in Figure 3.4a and 5b. The rate of change of moisture content with respect to time (Figure 3.4a) is known as the drying rate. In the first phase, the drying rate is low because most of the heat transferred to the wet material is used to raise its temperature. As the

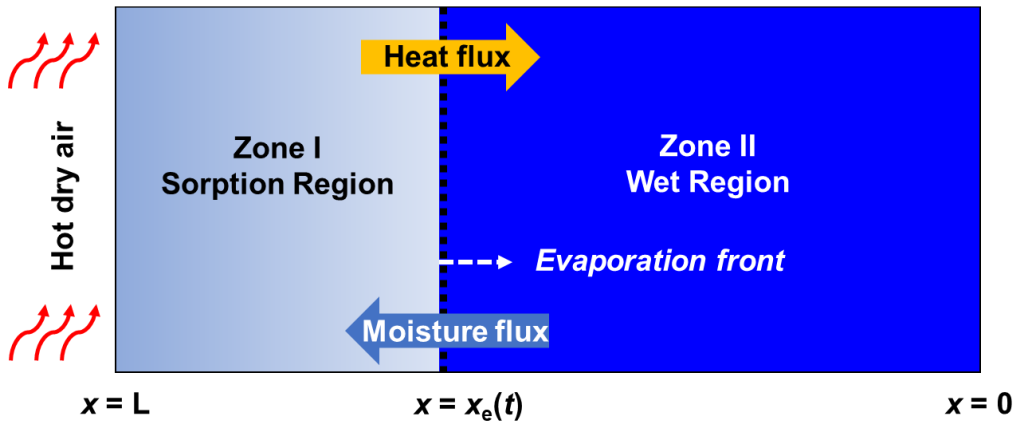

Figure 3.5: Computational domain of receding evaporation front model

material heats up, the drying rate increases until it reaches a plateau. In second phase, where the drying rate is relatively constant, a balance between heat and mass transfer occurs, and constant temperature and vapor partial pressure at the surface of the material are achieved. Moisture removal is highly dependent on conditions of the air stream such as temperature, relative humidity, and flow rate, as well as conditions of the wet material such as interface area and temperature. This phase continues until the moisture content of the material reaches a critical point known as the critical moisture content, where most of the unbound moisture has been removed. The third phase begins when the moisture film at the surface of the material becomes unsaturated, i.e., the vapor pressure of the air layer at surface is less than that of the saturated case. Towards the end of the falling rate phase, the bound moisture diffuses from within the material to the surface. The falling period ends once the moisture is at the desired moisture content, as shown in Figure 3.4b. The present study focuses on thermal drying processes where evaporating water is carried away by the drying medium – in this case a hot dry air stream.

3.3.2 Transient Spatial Model

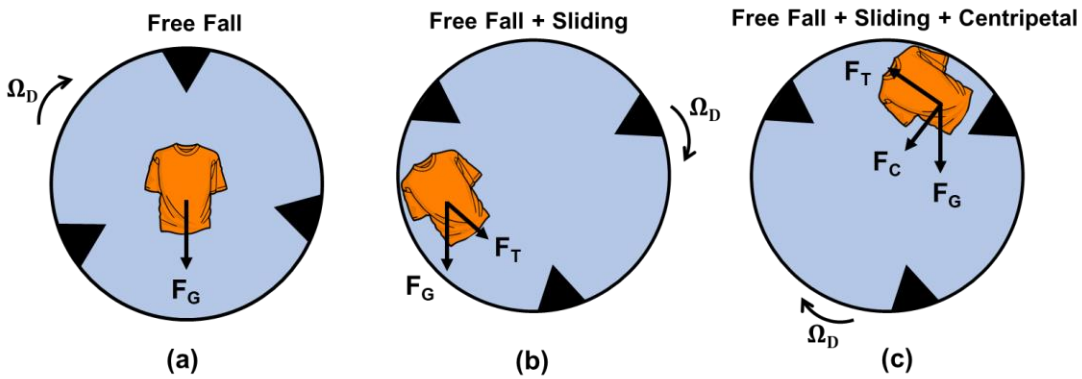

Figure 3.6: Forces acting on the textile (a) free falling, (b) free falling and sliding (c) free falling, sliding, and centripetal forces

3.3.2.1 Heat and Moisture Transfer in the Drum

General considerations for textile movement, and the corresponding modeling assumptions are presented here. In the drum, the textile gets tumbled around in three distinctive movements depicted in Figure 3.6a-c. The textile motion during the drying period directly influences the velocity field, which in turn changes the operating conditions (temperature, moisture, and momentum) at the interface between the hot drying air and textile.

Free fall represents the movement of the textile where only the gravitational force is acting, as seen in Figure 3.6a. Falling is the movement of the textile from successfully rotating within the drum up to the top; detaching from the walls of the drum, the textile is thrown into a free fall. The gravitational force is quantified based on the instantaneous mass of the drying textile inside the drum given by $F_g = m_{cl,i} g$. On the other hand, sliding on the walls of the rotating drum represents the motion of the textile moving on the wall of the drum up to a certain point where then it slides back down. The sliding component is

given by $m_{cl} g \sin\theta$, where θ is the inclination angle which increases as the fabric moves upward. While sliding, the frictional force, F_F, tends to keep the cloth from sliding down. Finally, the centripetal force, $F_C = m_{cl,i} R_d \Omega_d^2$, represents the movement of the textile while in contact with the walls of the rotating drum. Yu et al. (2020) and Park et al. (2013) studied the topology of the textile in the drum. The latter studies used ANOVA and post hoc test using the LSD method to investigate the influence of textile motion and material properties on the weight of the drying textile. For the purpose of this study, the topology and trajectory followed by the tumbling textile is concentrated mainly in the middle of drum for most of the drying period as depicted by Figure 3.7a (Park et al., 2013; Yu et al., 2020). Figure 3.7b-c shows a simplification of the topology of the textile during the drying process.

A heat and mass transfer model of drying is developed here using the simplified topology depicted in Figure 3.7b-c. The radius of the textile cylinder is estimated using Equation 9:

$$R_{cl} = \sqrt{\frac{m_{cl,dry}}{\pi L_d \rho_{cl}}} \tag{3.16}$$

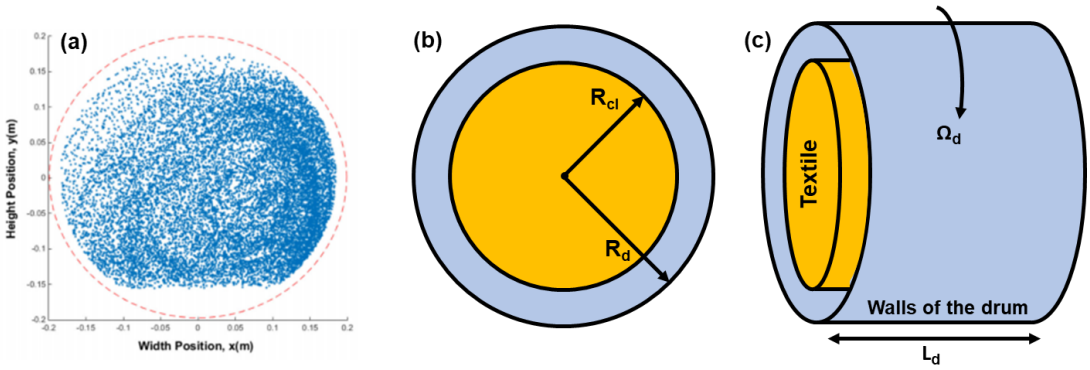

Figure 3.7: Fabric trajectory during a drying cycle (Park et al., 2013) (b) cross-sectional view of simplified geometry (c) longitudinal view of simplified computational domain.

where $m_{cl,dry}$ is the dry mass of the textile, L_d is the axial length of the drum, and ρ_{cl} is textile density. As drying air flows over the textile, a sorption region appears when all the unbounded water gets evaporated from the surface. At this stage, the evaporation front recedes from the surface, and textile gets divided into two zones as depicted in Figure 3.8. In the sorption region, the liquid water is no longer continuous; however, the main internal moisture transport mechanisms are bound water transport and vapor diffusion to the surface of the textile. At this stage, evaporation takes place throughout the sorption region and at the evaporation front. As drying continues, the wet region eventually disappears, leaving only the sorption region, which will be totally dried out. Due to the complex nature of drying, the following assumptions typical of drying of porous media are used:

- Mass, momentum, and energy transport within the textile are 1-D in radial direction
- The textile is macroscopically homogenous and no shrinking occurs
- Solid fibers of the textile are rigid and impermeable to air
- The change in thermophysical properties of the textile is negligible
- Moist air is assumed to be a binary mixture of inert air and water vapor; both treated as ideal gases
- Solid, liquid, and gaseous phases are in thermal equilibrium

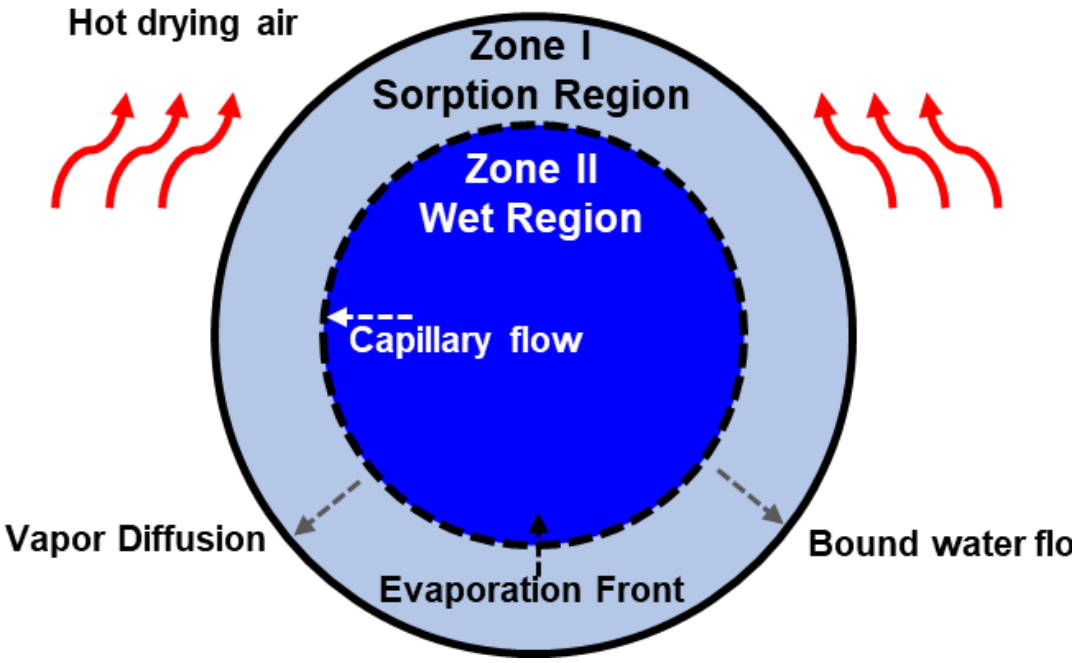

Figure 3.8: Schematic of the two-zone model for a drying process

3.3.2.2 Wet Region in the Textile

Using a differential radial control volume depicted in Figure 3.9, mass conservation for the liquid phase $(i=\ell)$ and the gaseous phase $(i=g)$ is expressed as Equations (3.17) and (3.18), respectively:

$$\frac{\partial}{\partial t}\left(\varepsilon_{cl}\rho_{\ell}S_{\ell}\right)=-\frac{\partial}{\partial r}\left(v_{\ell}\rho_{\ell}\right)-\dot{m}''' \tag{3.17}$$

$$\frac{\partial}{\partial t}\left(\varepsilon_{cl}\rho_{g}S_{g}\right)=-\frac{\partial}{\partial r}\left(v_{g}\rho_{g}\right)+\dot{m}''' \tag{3.18}$$

where ε_{cl} is the porosity of the textile, v is the velocity of the species, and S is the liquid volumetric saturation defined as the ratio of the liquid volume in the textile to the void volume in the textile, as shown in Equation (3.19):

$$S_\ell = \frac{V_\ell}{V_{void}} = \frac{\varepsilon_\ell}{\varepsilon_{cl}} \tag{3.19}$$

Using Darcy's law, the velocities of liquid and gaseous phases due to capillary flow are expressed by Equation (3.20):

$$v_i = -\frac{\kappa_i}{\mu_i}\frac{\partial P_i}{\partial r} \tag{3.20}$$

where κ is the permeability and μ is the dynamic viscosity of either the liquid or the gaseous phase. Since the gaseous phase is a binary mixture of water vapor and air, according to Fick's law, the mass flux is defined as:

$$j_i = -\rho_g D_{eff}\frac{\partial}{\partial r}\left(\frac{\rho_i}{\rho_g}\right) \tag{3.21}$$

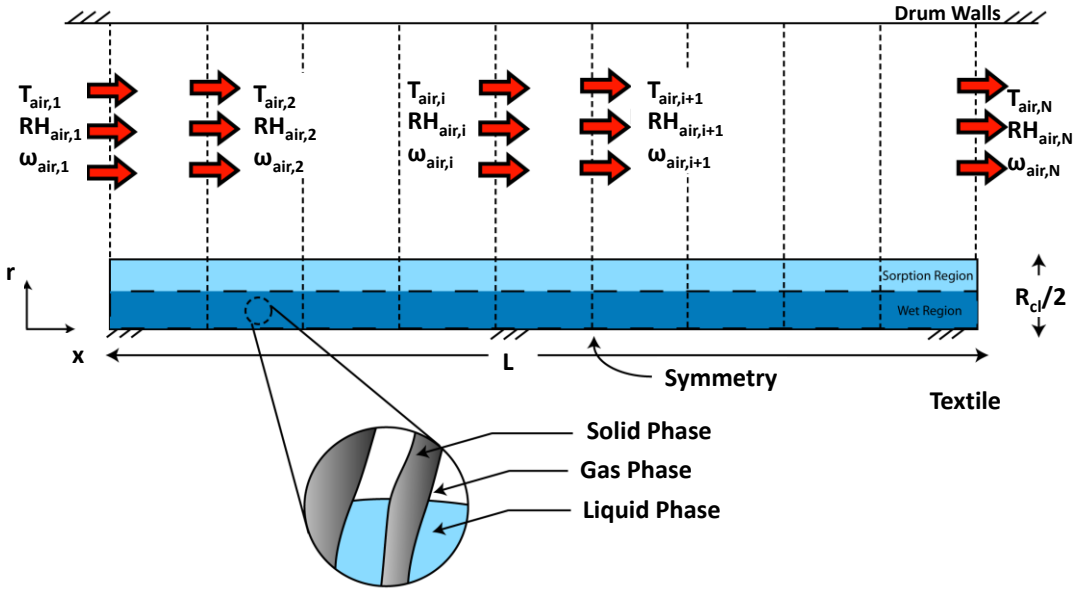

Figure 3.9: Schematic of cylindrical control volumes used to describe the drying process

where ρ_i is the density of either water vapor or air and D_{eff} is the effective binary diffusion coefficient. After quantifying the mass and velocities of each of the phases in the wet region, the general principle of energy conservation is used on the prescribed control volume. The energy balance in the textile is given by Equation (3.22):

$$\left[\varepsilon_{cl}\left(S_\ell \rho_\ell c_{p,\ell} + S_g \rho_g c_{p,g}\right) + \left(1-\varepsilon_{cl}\right)\rho_{cl} c_{p,cl}\right]\frac{\partial T}{\partial t} + \left(\rho_\ell v_\ell c_{p,\ell} + \rho_g v_g c_{p,g}\right)\frac{\partial T}{\partial r} = \frac{\partial}{\partial r}\left(k_{eff}\frac{\partial T}{\partial r}\right) - \dot{m}'''h_{fg} \tag{3.22}$$

3.3.2.3 Sorption Region in the Textile

As discussed in Section 3.3.1, bound water flow appears in the sorption region. The equations derived above still hold; however, the liquid velocity $\left(v_\ell\right)$ changes to the bound water velocity $\left(v_b\right)$, which results in the following continuity equation for the liquid phase:

$$\frac{\partial}{\partial t}\left(\varepsilon_{cl} S_\ell \rho_\ell\right) + \frac{\partial}{\partial r}\left(\rho_\ell v_b\right) = -\dot{m}''' \tag{3.23}$$

Therefore, the overall continuity equation becomes:

$$\frac{\partial}{\partial t}\left(\varepsilon_{cl} S_\ell \rho_\ell + \varepsilon_{cl} S_g \rho_g\right) + \frac{\partial}{\partial r}\left(\rho_\ell v_b + \rho_g v_g\right) = 0 \tag{3.24}$$

The velocity of the gaseous phase can be calculated using Equations (3.20); however, the velocity of the bound moisture cannot be derived from Darcy's law due to the fact that liquid is discontinuous. Therefore, the bound moisture is expressed as a function of the volumetric saturation gradient on the bound water (Ghali et al., 1994; Chen et al., 2001; Lee et al., 2002):

$$v_b = -\varepsilon_{cl} D_b \frac{\partial S_\ell}{\partial r} \tag{3.25}$$

where D_b is the bound water diffusion coefficient. The energy equation in the sorption region is given by Equation (3.26):

$$\begin{aligned} &\left[\varepsilon_{cl} S_\ell \rho_\ell c_{p,\ell} + \varepsilon_{cl} S_g \rho_g c_{p,g} + (1-\varepsilon_{cl}) \rho_{cl} c_{p,cl}\right] \frac{\partial T}{\partial t} - \frac{\partial}{\partial t}\left(\varepsilon_{cl} \rho_\ell \int_0^{S_\ell} \frac{\partial \Delta h_s}{\partial r} dS_\ell\right) \\ &+ \left(\rho_\ell v_b c_{p,\ell} + \rho_g v_g c_{p,g}\right) \frac{\partial T}{\partial r} - \rho_\ell v_b \frac{\partial \Delta h_s}{\partial r} = \frac{\partial}{\partial r}\left(k_{eff} \frac{\partial T}{\partial r}\right) - \dot{m}'''\left(h_{fg} - \Delta h_s\right) \end{aligned} \tag{3.26}$$

where Δh_s is the differential heat of sorption.

3.3.2.4 Airflow

For conservation of moisture and energy in the airflow, the conservation of dry air is trivial; however, the conservation of moisture in the air flow is given by Equation (3.27):

$$\rho_a \frac{\partial \omega}{\partial t} + j_a \frac{\partial \omega}{\partial x} = \dot{m}''' \tag{3.27}$$

where ω is the humidity ratio in the air flow. Due to the short length of the drum, the pressure drop is negligible. The energy balance in the air flow is given by Equation (3.28)

$$\left(c_{p,a} + \omega c_{p,v}\right)\left(\rho_a \frac{\partial T_a}{\partial t} + j_a \frac{\partial T_a}{\partial x}\right) = \frac{1}{\Delta x}\left[h_c\left(T_s - T_a\right) + h_m h_{fg}\left(\rho_{v,s} - \rho_{v,a}\right)\right] \tag{3.28}$$

where h_c is the convective heat transfer coefficient, h_m is the mass transfer coefficient, $\rho_{v,s}$ is the density of the vapor at the surface of the textile, and $\rho_{v,a}$ is the density of vapor in the air flow. The thermophysical and transport variables are discussed in Section 3.3.2.6.

3.3.2.5 Initial and Boundary Conditions

The system of five non-linear differential equations developed above to describe the heat and mass transfer occurring in the drum can be used to obtain T, S_ℓ, P_g, T_a, and ω. The initial conditions for liquid phase volumetric saturation, gas pressure, and temperature of the porous textile are given by:

$$S_\ell\left(r,x,t=0\right)=S_{\ell 0} \tag{3.29}$$

$$P_g\left(r,x,t=0\right)=p_{atm} \tag{3.30}$$

$$T\left(r,x,t=0\right)=T_{cl,0} \tag{3.31}$$

Additionally, the initial conditions for the humidity ratio and temperature of the air are as follows:

$$\omega\left(r,x,t=0\right)=\omega_{amb} \tag{3.32}$$

$$T_a\left(r,x,t=0\right)=T_{amb} \tag{3.33}$$

Due to symmetry in the topology of the textile, the gradients of the volumetric saturation of the liquid phase, total gaseous pressure, and the temperature of textile at the center $\left(r=0\right)$ are all zero as given by Equation (3.34) – (3.36):

$$\left.\frac{\partial S_\ell}{\partial r}\right|_{r=0}=0 \tag{3.34}$$

$$\left.\frac{\partial P_g}{\partial r}\right|_{r=0} = 0 \tag{3.35}$$

$$\left.\frac{\partial T}{\partial r}\right|_{r=0} = 0 \tag{3.36}$$

The other set of boundary conditions would be at the surface of the drying textile, i.e., at $r = R_{cl}$. The pressure at the surface is assumed to be constant and equal to the atmospheric pressure as shown by Equation (3.37):

$$P_g\left(r = R_{cl}\right) = p_{atm} \tag{3.37}$$

The mass and energy balance across the control surface are used as the boundary conditions to close the set of variables for the textile. The mass balance at the drying surface in the wet region is given by Equation (3.38):

$$j_{conv}\left(r = R_{cl}\right) = j_{\ell}\left(r = R_{cl}\right) + j_v\left(r = R_{cl}\right) \tag{3.38}$$

The energy balance at the drying surface in the wet region is given by Equation (3.39):

$$\begin{aligned} &h_c\left(T\left(r = R_{cl}, x, t\right) - T_a\left(x, t\right)\right) + h_m h_{fg}\left[\rho_v\left(r = R_{cl}, x, t\right) - \rho_{v,a}\left(x, t\right)\right] - \left(j_{\ell} h_{\ell}\big|_{r=R_{cl}} + j_g h_g\big|_{r=R_{cl}}\right) \\ &= -k_{eff}\left.\frac{\partial T}{\partial r}\right|_{r=R_{cl}} \end{aligned} \tag{3.39}$$

As mentioned previously, the evaporation front recedes into the porous textile, dividing it into a wet zone and sorption zone. In many studies that simulate drying, empirical desorption isotherms are used to obtain the maximum or critical moisture

content. However, in this study, the moving boundary conditions are obtained from continuity conditions at the evaporation front, i.e., at $r = r_e(t)$.

The initial and boundary conditions for dependent variables (ω and T_a) in the air flow are required to close the set of conservation equations. The initial conditions for humidity ratio and temperature of the drying air are given by Equations (3.40) and (3.41):

$$\omega(x, t=0) = \omega_{amb} \tag{3.40}$$

$$T_a(x, t=0) = T_{amb} \tag{3.41}$$

Finally, at the inlet of the drum or exit of the combustor, the humidity ratio and temperature of the air are given by:

$$\omega(x=0, t) = \omega_{post-comb} \tag{3.42}$$

$$T(x=0, t) = T_{post-comb} \tag{3.43}$$

3.3.2.6 Model Parameters

The governing equations, initial conditions, and boundary conditions contain physical properties, transport properties, and other parameters that could be expressed in terms of the dependent variables. Liquid volumetric saturation defined in Equation (3.19) can be expressed in terms of the moisture content in the textile. The more common moisture content term, X, is defined as the mass of liquid to mass of dry textile as given by Equation (3.44):

$$X = \frac{m_\ell}{m_{cl,dry}} = \left(\frac{\rho_\ell}{\rho_{cl}}\right)\left(\frac{\varepsilon_{cl}}{1-\varepsilon_{cl}}\right) S_\ell \tag{3.44}$$

Permeability, κ_i, is a transport property that indicates the permeability of the textile to a particular fluid. In this study, the textile is assumed to be an isotropic porous medium. Van Den Brekel and De Jong (1989) experimentally obtained the specific permeability, which is defined as the product of the intrinsic and relative permeability, of several textiles, including terry towels, which are the focus of this study. The specific permeability of liquid water in terry towels was measured to be $1.16\times10^{-11}\,\mathrm{m}^{-2}$. Similarly the vapor and gas permeabilities were taken from Durur and Öner (2013).

Effective diffusivity, D_{eff}, describes the resistance to diffusion in porous solid media, and is typically (Gibson and Charmchi, 1997) expressed as:

$$D_{eff} = \frac{D_a}{\tau} \tag{3.45}$$

where τ is the tortuosity or correction factor, and D_a is the molecular diffusion coefficient for water vapor in air (Gibson and Charmchi, 1997):

$$D_a = 2.23\times10^{-5}\left(\frac{T}{273.15}\right)^{1.75} \tag{3.46}$$

The movement of bound water is also known as sorption liquid diffusion near the dryness phase in the sorption zone. Several studies indicated that for capillary hygroscopic porous materials such as textiles, the bound water moves along fine capillaries. The velocity of bound water (Equation (3.25)) is expressed in terms of the bound moisture

diffusivity, which is in turn a function of the liquid saturation as given by Equation (3.47) :

$$D_b = D_{b0}\left(\frac{S_\ell - S_{eq}}{S_{ms} - S_{eq}}\right)^3 \exp\left(-\frac{E_A}{RT}\right) \tag{3.47}$$

where E_A is the activation energy of bound water movement, D_{b0} is 0.062 for the textile, and E_A/R is taken as 4830 K^{-1} (Peishi and Pei, 1989).

The heat and mass transfer coefficients are functions of the velocity field in the drum, the moisture content in the textile and the drying air, type of textile, and other operating conditions of the air in the vicinity of the textile. The convective heat and mass transfer coefficients decrease during the falling rate period. During the falling rate period, the moisture content of the textile decreases to below the critical moisture content $\left(X_{crit}\right)$ of the textile. Most of the moisture (in liquid phase) is now water vapor diffusing at the interface between bulk air and the surface of textile. Since the ratio of thermal conductivity of liquid water to that of water vapor is ~ 24, the heat transfer coefficient during the falling period decreases compared to the initial and constant drying phases. Additionally, the difference between the water vapor partial pressure in the vicinity of the textile and that of the bulk air decreases, thereby decreasing the mass transfer rate. Nissan et al. (1959) verified that the heat transfer coefficient decreases through drying experiments on textiles during the fall rate phase. The following expressions given by Equations (3.48) and (3.49) are used to describe the heat and mass transfer coefficients, respectively:

$$h_c = \begin{cases} h_{c0}\left[\dfrac{\dfrac{\dot{m}_e'' c_{p,a}}{h_{c0}}}{\exp\left(\dfrac{\dot{m}_e'' c_{p,a}}{h_{c0}}\right)-1}\right] & t_i < t < t_{fp} \\ h_{c0}\left[\lambda + (1-\lambda)\dfrac{X\left(r = R_{cl}\right) - X_{ms}}{X_{crit} - X_{ms}}\right] & t_{fp} \le t < t_{end} \end{cases} \tag{3.48}$$

$$h_m = \begin{cases} h_{m0}\left[\dfrac{\dfrac{\dot{m}_e''}{\rho_a h_{m0}}}{\exp\left(\dfrac{\dot{m}_e''}{\rho_a h_{m0}}\right)-1}\right] & t_i < t < t_{fp} \\ h_{m0}\left[\lambda + (1-\lambda)\dfrac{X\left(r = R_{cl}\right) - X_{ms}}{X_{crit} - X_{ms}}\right] & t_{fp} \le t < t_{end} \end{cases} \tag{3.49}$$

where λ is a constant for a given material, h_{c0} is the heat transfer coefficient based on parallel flow along a short cylinder (Wiberg and Lior, 2005), and h_{m0} is the mass transfer coefficient determined by Equation (3.50):

$$h_{m0} = \frac{h_{c0}}{\rho_a c_{p,a} Le^{\frac{2}{3}}} \tag{3.50}$$

where ρ_a is the air density, $c_{p,a}$ is the specific heat of the air, and Le is the dimensionless Lewis number. The heat and mass transfer coefficients were modified by an Ackermann

Table 3.2: Parameters used in the Spatial Model

Operating Parameter	Value
Atmospheric Pressure (p_{atm})	101.3 kPa
Ambient Temperature (T_{amb})	25°C
Ambient Humidity Ratio (ω_{amb})	0.008 kg kg^{-1}
Intra porosity of textile (ε_{cl})	0.70
Specific heat of textile ($c_{p,cl}$)	1.34 kJ kg^{-1} K^{-1}
Density of textile (ρ_{cl})	1.55 kg m^{-3}
Mass of dry textile ($m_{cl,dry}$)	7.66 kg
Correction factor (τ)	16.7
Permeability of liquid in textile (K_{ℓ})	1.16×10^{-11} m^{-2}
Ratio of E_A/R	4830 K^{-1}
Bound water diffusion coefficient (D_{b0})	0.062 m^2/s
Textile correction factor (λ)	0.5
Initial moisture content $X(t=0)$	0.85
Maximum moisture content (X_{ms})	1.0
Critical moisture content (X_{crit})	0.3

correction factor (Ackermann, 1937; Bird et al., 2006) to take into account the transpiration at the surface of the textile during the first and second drying phase. When the average moisture content in the textile approaches the critical moisture content, the fall period of the drying processes begins. At this time, the heat and mass transfer coefficients are modified using a correction factor. The correction factor is strictly a function of the material of textile and the instantaneous moisture content at the surface of the textile. The multiplier to modify the heat and mass transfer coefficients during the falling period has also been used by Peishi and Pei (1989). A summary of model parameters is shown in Table 3.2.

3.3.3 Numerical Analysis

The governing equations are discretized using a finite volume scheme. First-order upwind differencing is used for the advection terms. Humid air is used as the drying fluid and 100% cotton terry towels are used as the textile. The textile was sliced into 16 radial and 9 axial slices, which were enough to ensure grid-independence in both the axial and radial directions. To ensure numerical stability, a time step (Δt) of 10^{-5} s was chosen. The simulations are carried out in MATLAB using the built-in ODE15s (Shampine and Reichelt, 1997).

3.4 Figures of Merit

To assess the enhancement in energy efficiency and reduction in drying time, two figures of merit are considered. The expression for the specific moisture extraction ratio (SMER) is given by Equation (3.51):

$$SMER = \frac{\int_{t=0}^{t=\Delta t} \dot{E}_{in} dt}{m_{w,r}} \tag{3.51}$$

where $\dot{E}_{in}$ is the total power input (including electrical motors) to the dryer, and $m_{w,r}$ is the total mass of water evaporated:

$$\dot{E}_{in} = \dot{Q}_{combustor} + PEF \quad \dot{W}_{fan} + \dot{W}_{drum} \tag{3.52}$$

$$m_{w,r} = \int_{t=0}^{t=\Delta t_d} \dot{m}_e dt \tag{3.53}$$

To account for the different energy sources, a primary energy factor of 2.66 based on the data from the December 2019 Monthly Energy Report (Dunn, 2020) is used to convert an electrical energy input into a primary energy input.

SMER represents the total energy input to evaporate 1 kg of water. A lower SMER signifies a higher performance dryer. Another figure of merit is the drying efficiency, which represents the fraction of the total input energy that is used for evaporation. The drying efficiency is expressed by Equation (3.54):

$$\eta_d = \frac{\int_{t=0}^{t=\Delta t_d} \dot{m}_e h_{fg}\left(T_{cl}\right) dt}{\int_{t=0}^{t=\Delta t_d} \dot{E}_{in} dt} \tag{3.54}$$

Finally, the drying time $\left(\Delta t_d\right)$ is the time taken to achieve the desired final moisture content $\left(X_f\right)$ and is expressed by Equation (3.55):

$$X\left(t = \Delta t_d\right) = X_f \tag{3.55}$$

3.5 Results and Discussion

3.5.1 Lumped Model Results

The predictions of the mathematical model described in Section 3.2 are compared with experimental data here based on the drum outlet temperature and humidity ratio, evaporation rate, and instantaneous moisture content in the textile. Figure 3.10 shows the variation of the air exit temperature and humidity ratio at the exit of the drum. The drying process can be divided into three phases as shown in Figure 3.10a-b. The first phase is the

initial transient phase, where the air temperature and humidity ratio are increasing. In this phase, the air is heating up the textile and drying starts, this indicated by the rise in the exit humidity ratio.

At t = 300 s, the second phase of drying starts. During the second phase, the air temperature remains at a nearly constant temperature. The air temperature during the

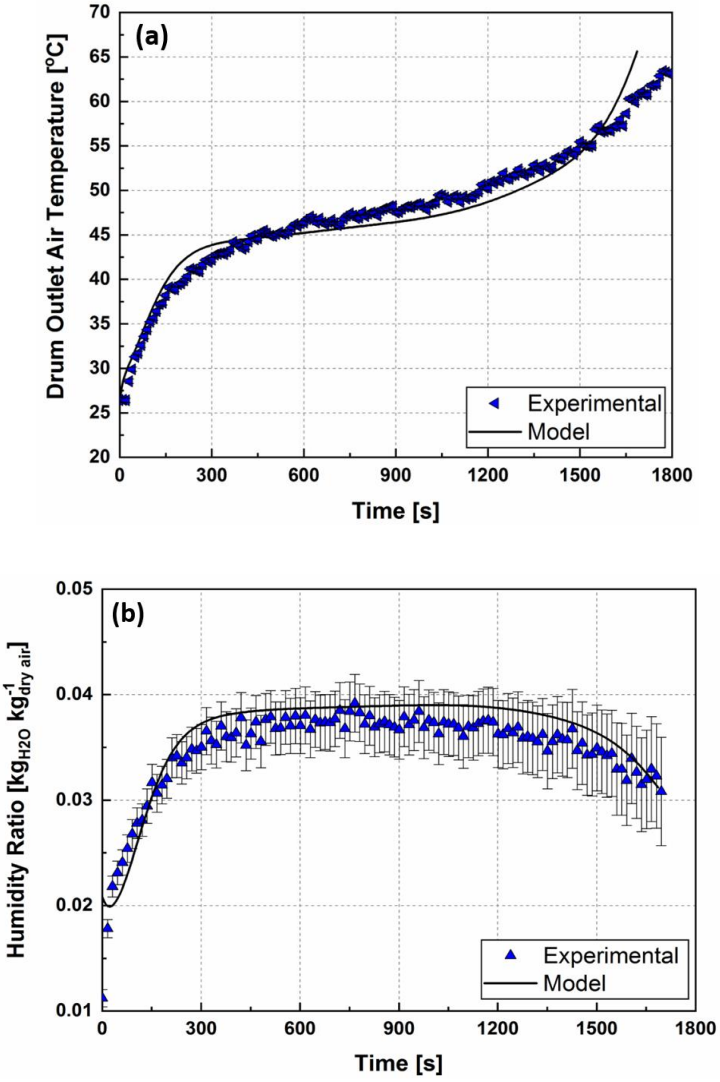

Figure 3.10: Baseline validation at the exit of the drum (a) air temperature (b) humidity ratio

second phase ranges from 45°C to 50°C. Also, during the second stage, the surface of the textile is always saturated with water. Therefore, the rate of evaporation remains constant, since it is mainly driven by the difference in partial pressure of the water vapor at the surface of the textile and the air at the bulk of the drum. At t = 1350 s, the rate at which the air temperature is changing increases. At this drying stage, air at the vicinity at the surface of the textile is not saturated with water, i.e., it has a relative humidity < 100%; this is accounted for using the water activity factor (Lambert et al., 1991) (shown in Equation (3.9)). The internal moisture in the terrycloth towel starts to migrate to the surface slowly by capillary flow and vapor diffusion. Therefore, the rate of evaporation decreases, as reflected by the sudden drop in the exit air humidity ratio. The model developed here predicts these distinct physical phenomena during the three drying phases. The average absolute deviation (AAD) is used to compare the measured and predicted values, as defined in Equation (3.56).

$$\text{AAD} = \frac{1}{n}\sum_{i=1}^{n}\left|\frac{predicted - measured}{measured}\right| \tag{3.56}$$

The model shows good agreement in predicting the drum exit air temperature and humidity ratio with AADs of 6.6% and 7.2%, respectively. Figure 3.11 shows the variation of the instantaneous textile moisture content and evaporation rate. The instantaneous moisture content is calculated using Equation (3.57):

$$X(t) = \frac{1}{m_{cl,dry}}\left(X_i m_{cl,dry} - \int_0^t \dot{m}_e dt\right) \tag{3.57}$$

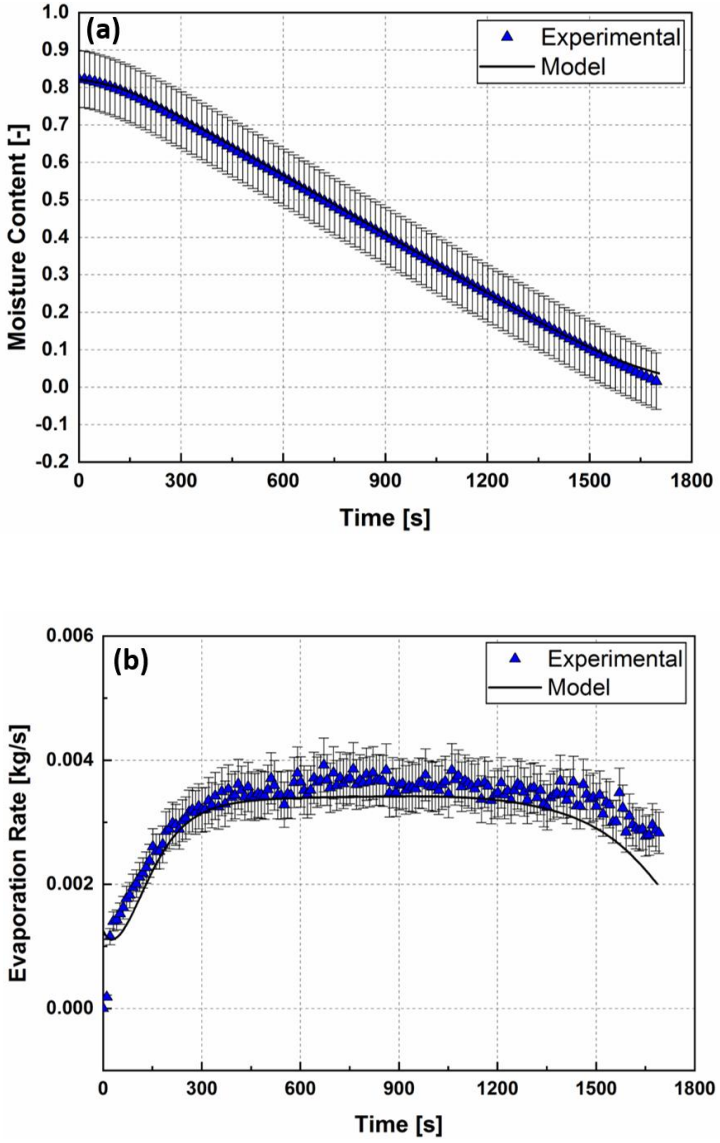

Figure 3.11: Baseline validation of (a) instantaneous moisture content (b) evaporation rate

The evaporation rate is defined as the mass flow rate of the evaporated water vapor. Figure 3.11a shows the variation in moisture content as a function of time. When the evaporation rate, depicted in Figure 3.11b, is constant during the second phase, the moisture content decreases almost linearly. The slope of the moisture content $\left(dX/dt\right)$ with time is proportional to the rate of evaporation. The evaporation rate remains nearly constant from

t = 300 s to t = 1350 s while the moisture content drops from 70% to 14%. The model shows good agreement in predicting the moisture content and evaporation rate, with AADs of 1.2% and 3.2%, respectively. The drying time, defined by the criterion in Equation (3.55) with a final moisture content of 3.5%, was achieved at 1725 s. The baseline drying efficiency (Equation (3.54)) is 41%. This shows that more than 58% of the energy input to the dryer is not used for evaporation. About 4% of the total energy is used to heat the textile up to the temperature at which evaporation starts. The rest of energy is carried away by the exhaust gas or lost to the ambient.

3.5.2 Spatial Model Results

The predictions of the mathematical model derived in Section 3.3 are discussed and compared with data collected from the combustor and the drum. Figure 3.12a shows temperature variation at the exit of the combustor, i.e., the inlet of the drum as a function of drying time. As shown in Figure 3.12a, the combustion process can be divided into two stages: an initial transient stage and a constant steady stage.

The transient effects on temperature are captured well by the model. The transient stage extends from $t_d = 0\,\text{s}$ until $t_d = \sim 300\,\text{s}$, after which the temperature tends to stabilizes at the constant steady state value. The built-in combustor in the dryer has a firing rate of 18.8 kW. The fuel flow rate is kept constant throughout the experiment. The air enters the combustor at ambient conditions (T = 24°C and $\omega = 0.0072\,\text{kg}_\text{w}\text{kg}^{-1}_{\text{dry air}}$) and exits at a temperature of 198.8°C. Figure 3.12b shows the variation of inlet and exit humidity ratios at the combustor. Combustion adds humidity to the products per the chemical

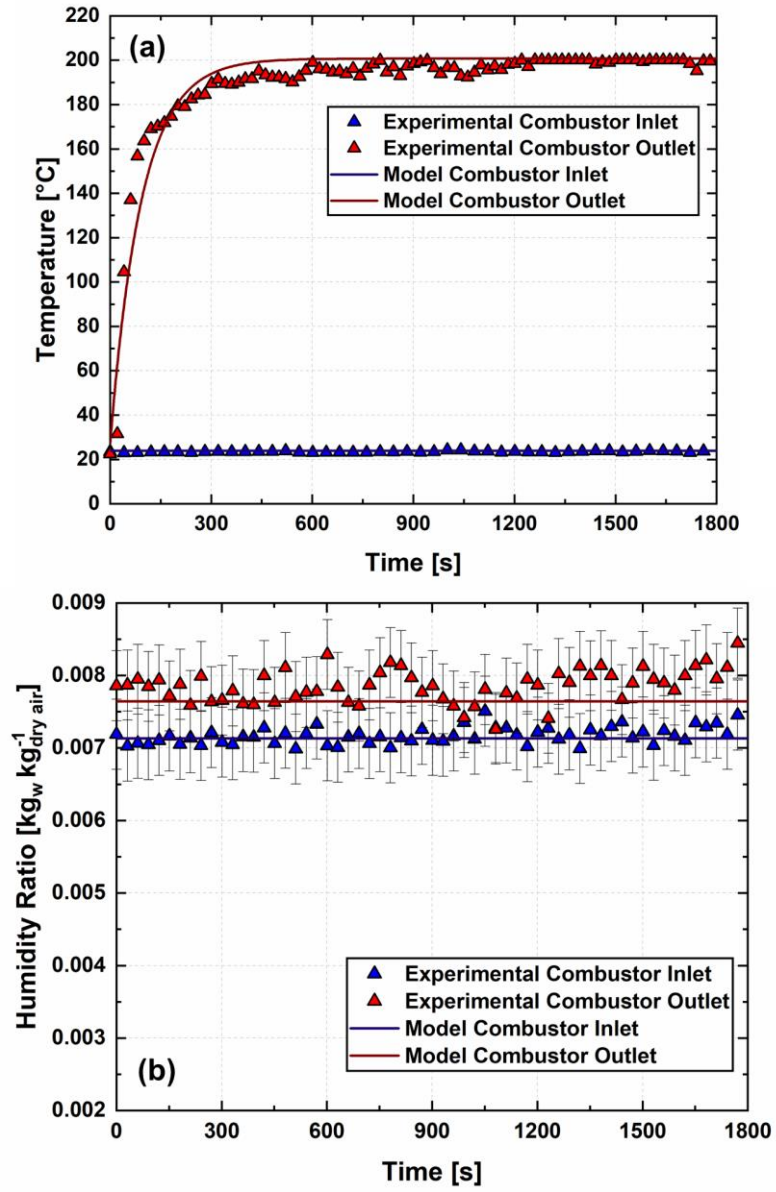

Figure 3.12: Comparison of experimental and predicted data: combustor (a) exit temperature and (b) exit humidity ratio

reaction shown in Equation (3.1). The average humidity ratio increases from $0.0072\,\mathrm{kg_w\,kg^{-1}_{dry\,air}}$ at the inlet of the combustor to $0.0078\,\mathrm{kg_w\,kg^{-1}_{dry\,air}}$. The resulting 8.33% in humidity ratio due to nature of the combustion is not ideal for drying; however, the increase in temperature by a $\Delta T \sim 175°\mathrm{C}$ makes the resulting air ideal for the evaporation

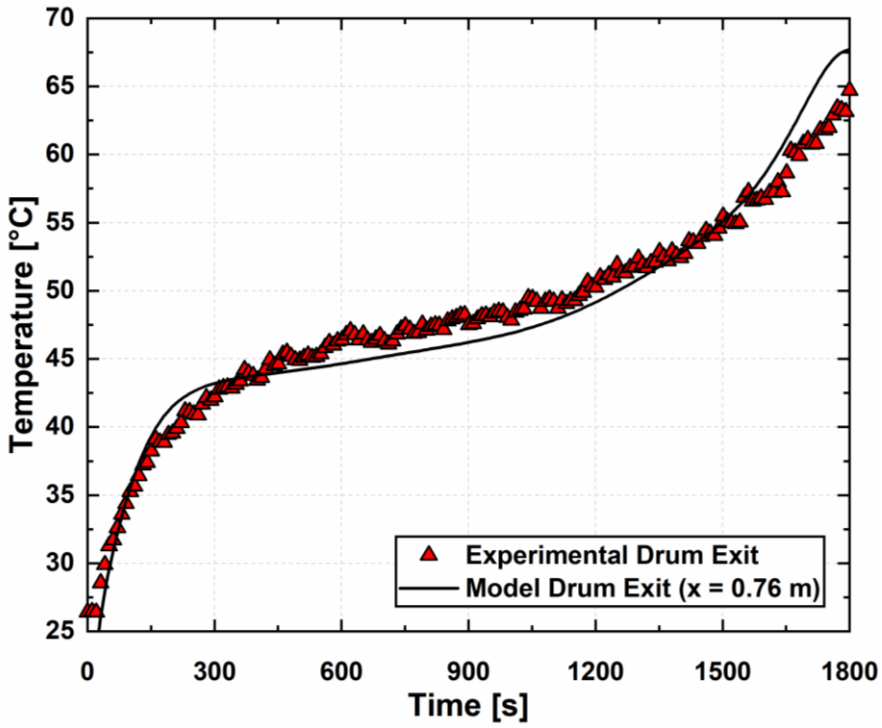

Figure 3.13: Comparison of experimental and predicted air temperature at the exit of the drum

in the drum. The model predicts two stages in the combustor. The model shows good agreement in predicting the combustor exit air temperature and humidity ratio with AADs of 4.2% and 5.6%, respectively.

While the model predicts the combustor performance well, it is essential to compare it to the experimental data from the drum. Figure 3.13 shows the variation in the air exit temperature from the drum as function of drying time. As discussed in Section 3.3.1, the drying cycle can be divided into three stages: initial drying stage $\left(0 \le t_d < 300\,\text{s}\right)$, constant drying stage $\left(300 \le t_d < 1400\,\text{s}\right)$, and the falling stage $\left(1400 \le t_d < 1800\,\text{s}\right)$. During the constant drying stage, the temperature remains nearly constant as can be seen in Figure 3.13; the air temperature during this phase rose by less than 8.5°C. This is mainly due to

the fact that during that stage of drying, the surface of the textile is still saturated with water. When the moisture level at the surface of the textile drops below the saturation point, a sudden increase in air and surface temperature can be observed. The effect on the surface temperature is discussed later in the paper.

Figure 3.14 shows the humidity ratio at the exit of the drum. The air exit humidity ratio is nearly constant at $0.035\,kg_w kg^{-1}_{dry\ air}$ during the second phase of drying, which given that the humidity ratio at the exit of the combustor is constant, indicates the evaporation rate is constant. The data collected at the exit of the drum were in good agreement with the simulated temperature and humidity ratio at rear of the drum. The corresponding AADs between the predicted and the experimental air temperature and humidity ratio were 6.8% and 7.7%, respectively.

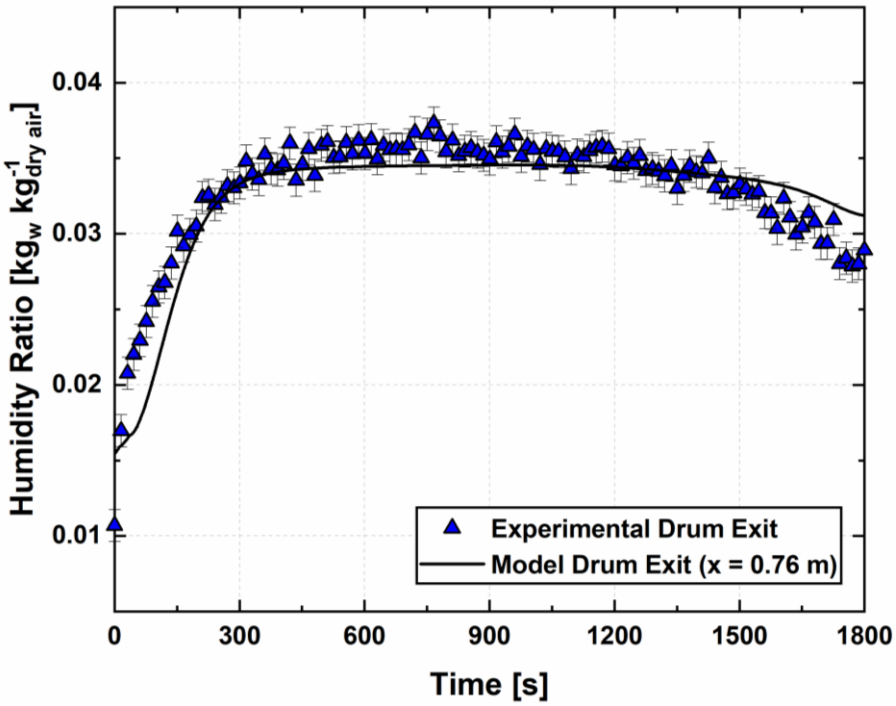

Figure 3.14: Comparison of experimental and predicted air humidity ratio at the exit of the drum

Figure 3.15a shows a contour surface plot of the instantaneous moisture content at the surface of the textile. The instantaneous moisture content is calculated using Equation (3.57). Surface moisture content helps in determining which drying stage is taking place. The initial drying stage is characterized by a lower change in moisture content. This is reflected as a change of less than 5.8% during the initial stage. Additionally, as the drying continues, the evaporation front is at the surface of the textile until the end of the second stage. The moisture content decreases in a linear fashion, implying that the rate at which water is lost from the surface of the textile is constant at a value of 3.52×10^{-3} kg s^{-1}. The moisture content of the textile falls from 77% to 16% during the second stage. At $t_d = 1400$ s, the falling stage starts indicating that the evaporation front starts receding. The slope of the moisture content curve becomes non-linear at during the third stage. As per Equations (3.48) and (3.49), the heat and mass transfer coefficients are functions of the moisture content. The moisture content at the surface $X\left(r = R_{cl}\right)$ of the textile decreases

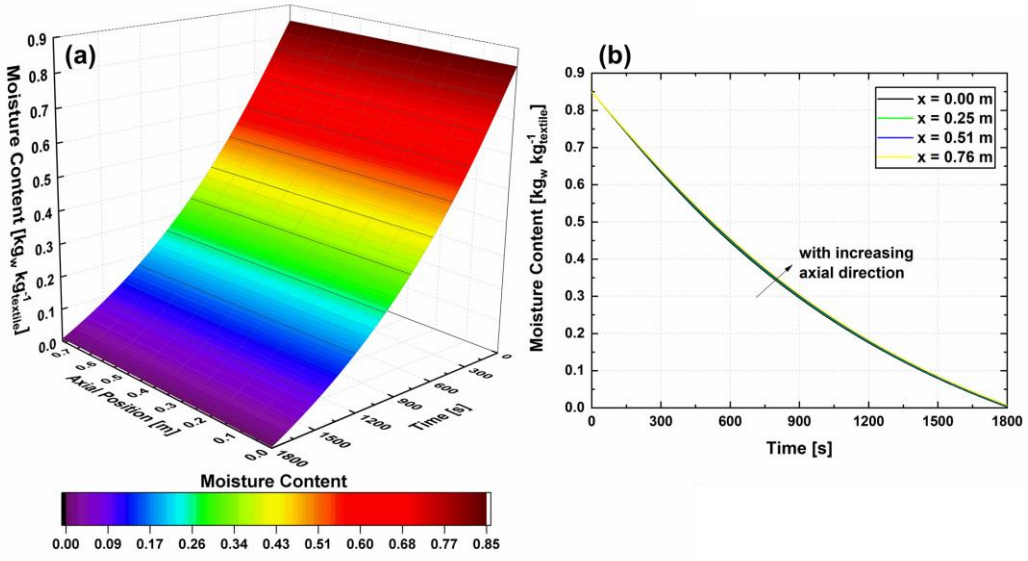

Figure 3.15: (a) Surface plot of the instantaneous moisture content at the surface of the textile (b) 2-D projection of the moisture content at various axial location in the drum.

with decreasing moisture in the textile, which in turn decreases heat and mass transfer coefficients as discussed in Section 3.3.2.6. The evaporation rate during the third stage decreases by an average of 32%, i.e., 2.36×10^{-3} kg s^{-1}. Figure 3.15b shows a 2-D projection of the moisture content at different axial locations in the drum. It is important to note that there are no significant variations in the moisture content or evaporation rate axially. For instance, at $t_d = 1000$ s , the moisture content at the surface of the textile is 0.252, 0.256, 0.258, and 0.260 at $x = 0$, 0.25, 0.51, and 0.76 m, respectively. The variation of moisture content across the axial length of the drum is less than 3.2%. This behavior is as expected due to the vigorous mixing and tumbling in the drum.

Figure 3.16 shows a contour surface plot of the surface temperature of the textile. As depicted in the latter figure, the temperature of the textile increases from 24°C to almost

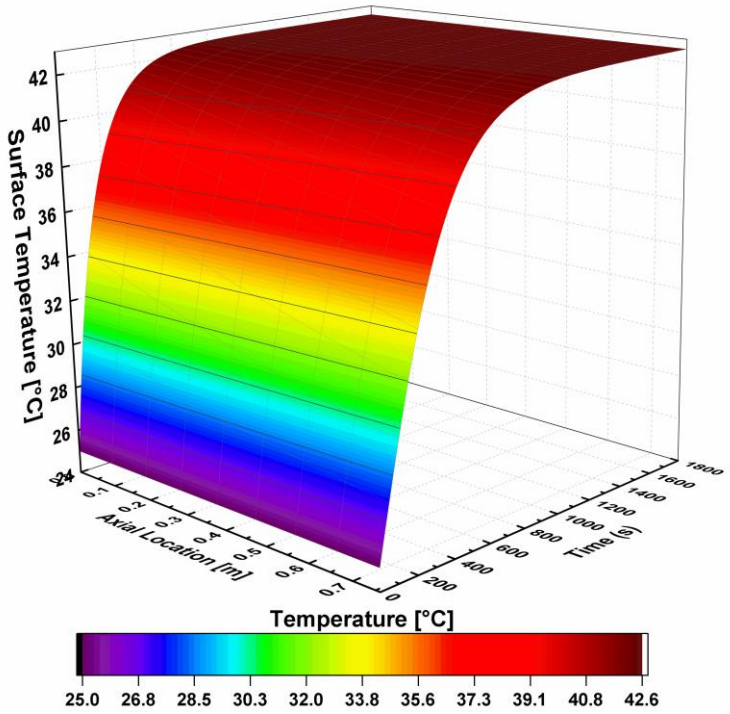

Figure 3.16: Surface plot of the instantaneous surface temperature of the textile

38°C by the end of the first stage of drying. During the second stage, the textile surface temperature continues to rise until it levels off at T = 40.5°C. During the third stage of drying, due to the fact that the surface of the textile is not fully saturated, the surface temperature rises slightly by 2.2°C. As moisture continues to be transported from the inside of the textile to the surface, the surface temperature rises at a relatively low rate. To validate the predicted textile surface temperatures, the wireless temperature and humidity transducers were placed inside the drum securely wrapped by wet textile. Figure 3.17 compares the measured textile surface temperature with the predicted temperature at an axial drum location of x = 0.38 m. This axial location was selected as representative of the middle of the drum. Additionally, Figure 3.17 shows a temperature change of less than 1.9°C across the axial distance of the drum. The model predicts the surface temperature of the textile with an AAD of 5.1%.

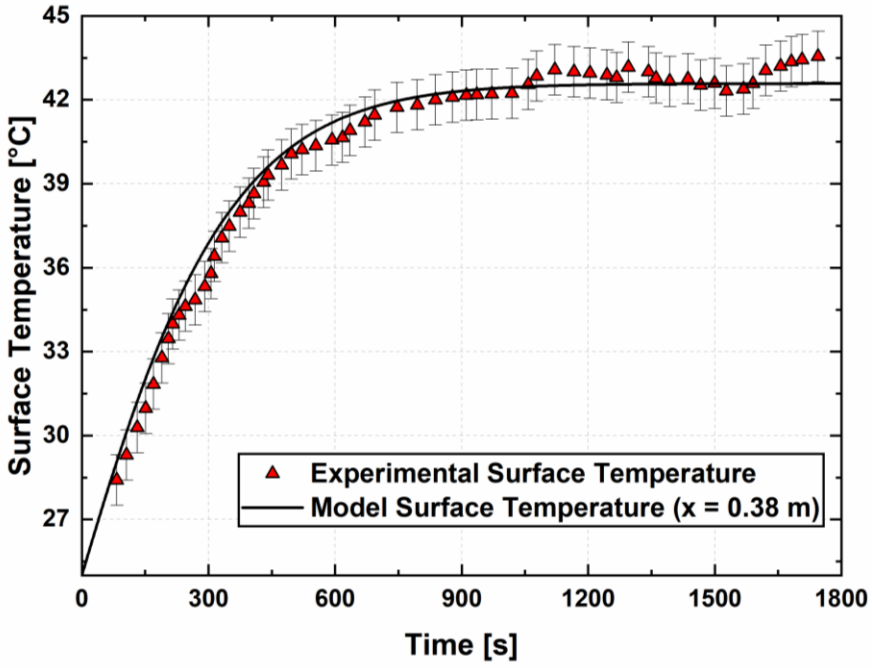

Figure 3.17: Comparison of the measured and predicted surface temperature at x = 0.38 m (middle of the drum)

3.5.3 Comparison of Lumped and Spatial Model

After validating the model with data, the performance of the gas-fired tumble dryer is assessed here. Table 4 summarizes and compares the three figures of merit between the experiments, the two-dimensional model developed in this work, and the lumped model developed by El Fil and Garimella (2021). The measured drying time to reach a moisture content of 3.5% was 1725 s. Both numerical models showed good agreement in predicting the drying time, drying efficiency, and the SMER. Specifically, the drying times predicted by the lumped and spatially resolved models were 1744 s and 1735 s, respectively. While both models had similar performance, the distributed parameter model has the advantage of not using any empirical data to predict the performance of the dryer. The drying efficiency was predicted by both models with a maximum AAD of 2.2%. The drying efficiencies predicted by the lumped model and the 2-D model were 40.3% and 40.8%, respectively, as compared with the measured average drying efficiency of the dryer, which was 41.2%. Both models slightly under predict the drying efficiency, which is mainly due to the fact that in the actual gas-fired dryer, there are some heat gains from the ducting between combustor and the drum that were not considered in the models. These heat gains are mainly through conduction through the wall and natural convection, which helps in increasing the temperature in the drum, and enhances the evaporation rate. The measured SMER of the current gas-fired tumble dryer is 1.45 kWh kg^{-1} of water removed. Since both models predicted a lower drying efficiency of the dryer, the SMER predicted by the lumped and spatially discretized model were 1.51 and 1.49 kWh kg^{-1}, respectively. The heat of vaporization of water is ~0.664 kWh kg^{-1}. This shows that current performance of the tumble dryer is far from the thermodynamic limit, indicating the possibility for

Table 3.3: Performance summary, predicted and measured values

	Drying time (s)	Drying efficiency (%)	SMER (kWh kg^{-1})
Experimental	1725	41.2	1.45
Lumped Model	1744	40.3	1.51
Spatial Model	1735	40.8	1.49

improvements through a variety of measures. The model developed here provides insights into the physics of moisture transport in the textile and airflow. These insights can be used to guide the development of techniques to improve the energy efficiency of such dryers.

3.6 Conclusion

This chapter presents a lumped and 2-D transient models for a commercial gas-fired tumble dryer using a moving evaporation front approach. The 2-D transient model accounted for the heat and mass transfer processes in the drum without input from the experimental procedure. Models were compared with experimental data, and with a lumped model previously developed in Section 3.2. The simulations predicted the performance of the combustor and the drying process in the drum with an AAD of 4.9% and 7.3%, respectively. The spatially discretized model showed good agreement with the lumped model, due to the vigorous mixing in the drum. Compared to the theoretical thermodynamic limit, the performance of the tumble dryer is only 45.8% of the ideal potential. The model developed here can therefore be useful in developing techniques to reduce the drying time and SMER of the dryer.

CHAPTER 4. EXPERIMENTAL APPROACH

There have been several experimental studies in the literature where the energy consumption and drying efficiency of textile dryers are investigated. However, the experiments were mostly conducted on electric resistive dryers or heat pump dryers. Very few studies actually investigated gas-fired tumble dryers. The energy input in a gas-fired tumble dryer being through combustion needs special attention. In this chapter, a description of the experimental set up and approach is presented. Additionally, this chapter focuses on experimentally optimizing the performance of a commercial gas-fired tumble dryer. A 11.33 kg capacity gas-fired tumble dryer is used for testing. The effects of varying airflow, fuel flow rate, mass of the bone-dry textile, initial moisture content, and drum rotational speed are explored. Based on these data, reduced-order models for predicting the specific moisture extraction ratio, drying efficiency, and drying time are developed.

4.1 Introduction

Lambert et al. (1991) developed a mathematical model for an electric-resistance dryer (ERD). The model was then empirically fitted by deploying heat and mass transfer coefficients for the constant drying period phase and sorption isotherm (α- factor) for the falling rate phase. This factor was used by many studies that followed to simulate textile drying (especially 100% cotton) (Deans and Tranxaun, 1992; Conde, 1997; Deans, 2001; Yadav and Moon, 2008b; El Fil and Garimella, 2021). Conde (1997) used sorption isotherms to study the performance of a textile tumble dryer while varying the dry load from 1.5 kg to 6 kg. The drying rate for 3 kg load was almost twice that for 6 kg case. Additionally, Conde (1997) installed a plate-fin heat exchanger in the dryer and showed

that the energy recovery potential from the exhaust stream is as high as 20%. Deans (2001) investigated the effects of mass of textile, ambient conditions (temperature and relative humidity), electrical power input, and air flowrate to show that the mass of the textile and power input are the major parameters that influence drying. The sensitivity analysis by Deans (2001) showed the specific energy consumption and drying time of the load can be reduced by either increasing the airflow rate or increasing power input.

Bassily and Colver (2003b) conducted experiments on a residential ERD to analyze the effects of fan power, drum rotational speed, initial dry weight of the textile, initial moisture content, and electric power, and used insights from these experiments to develop a correlation for area-mass transfer coefficient inside the drum of the dryer (Bassily and Colver, 2003a). The correlation depended on the Sherwood number, Reynolds number, Schmidt number, Gukhman number, drum rotational speed, and the initial dry weight of the textile. Bassily and Colver (2003a) concluded that the mass transfer coefficient is a function of airflow rate, drum exit conditions (temperature and relative humidity), and type of textile. On the other hand, the effective mass transfer area is a function of the rotational speed of the drum and the initial dry mass of the textile. Stawreberg and Nilsson (2010) developed a statistical model based on experiments on a condensing tumble dryer. The maximum specific moisture extraction ratio (SMER) was achieved by increasing power supply and increasing the internal airflow, while decreasing the external airflow. Stawreberg and Nilsson (2013) also studied two control strategies for a venting tumble dryer to increase the drying efficiency of small load capacity dryers. They found that reducing airflow and the heater supply resulted in a 6% increase in drying efficiency. This conflicts with the findings of previous studies (Lambert et al., 1991; Bassily and Colver,

2003a; Bassily and Colver, 2003b) who found that increasing the airflow rate was advantageous.

Several researchers have attempted to minimize the use of empirical parameters in models for residential ERD; however, there are no physics-based models that capture the underlying heat and mass transfer phenomena in the drum. Wei et al. (2017) developed a model to describe momentum, heat, and mass transfer in an air-vented tumble dryer. The heat and mass transfer coefficients were empirically determined and corrected using the multiplier used by Peishi and Pei (1989). Wei et al. (2017) conducted 16 experiments where the moisture content, initial dry load, heat input, air velocity, and rotational motor speed were varied. The latter study concluded that the drying rate is highly influenced by the air velocity, heater power, and motor rotational speed. The optimal conditions to maximize the drying rate were a heater power of 4.5 kW, air velocity of 8.5 m s^{-1}, and motor rotational speed of 1200 rpm. Wei et al. (2018a) conducted 12 experiments where several important parameters (drum rotation speed, heater power, and airflow velocity) were monitored and controlled to reduce the energy consumption of a 4-kW ERD. The energy consumption of the dryer was reduced by 21.5% and fabric smoothness improved by 0.9 grade, when the heater power input is controlled throughout the drying process. Wei et al. (2019) also conducted experiments with different textile types and sizes, initial dry mass, and drum rotational speed. They were able to study the effect of fabric movement by measuring the trajectory of a single fabric within the drum using a high-speed camera. A drum rotational speed of 45 – 50 rpm was found to be optimal to minimize energy consumption and drying time due to the fabric movement patterns. Novak et al. (2019) investigated the effects of inlet air temperature, relative humidity, and airflow on an air-vented ERD and developed

a correlation to predict drying time and the area-mass transfer coefficient during the constant drying rate period. Novak et al. (2020) investigated the influence of the initial state of the dry load and the drum speed on heat pump dryer (HPD) performance and predicted the mass flow rate of the extracted moisture collected and weighed as condensate. Shen et al. (2016) adopted a different approach than previous studies by introducing the concept of drum effectiveness. They developed a quasi-steady state model to simulate the performance of an HPD. Heat and mass transfer effectivenesses were modeled to investigate the effects of key variables such as compressor discharge temperature, energy consumption, and drying time. Gluesenkamp et al. (2019) used empirical data from seven different textile dryers including a gas-fired dryer (GFD), a thermoelectric dryer (TED), and five ERDs of different capacities to estimate the effectivenesses using dimensional analysis to obtain the terms relevant to heat and mass transfer effectiveness.

4.2 Experimental Approach

4.2.1 Test Equipment

A Speed Queen 025 series commercial gas-fired tumble dryer (~11.33 kg maximum capacity) is used to experimentally validate the transient models developed for the performance of the dryer and the energy savings techniques investigated in this work. Figure 4.1a shows the experimental setup, while Figure 4.1b depicts a block diagram of the facility including the sensors, actuators, loggers, and real time data acquisition.

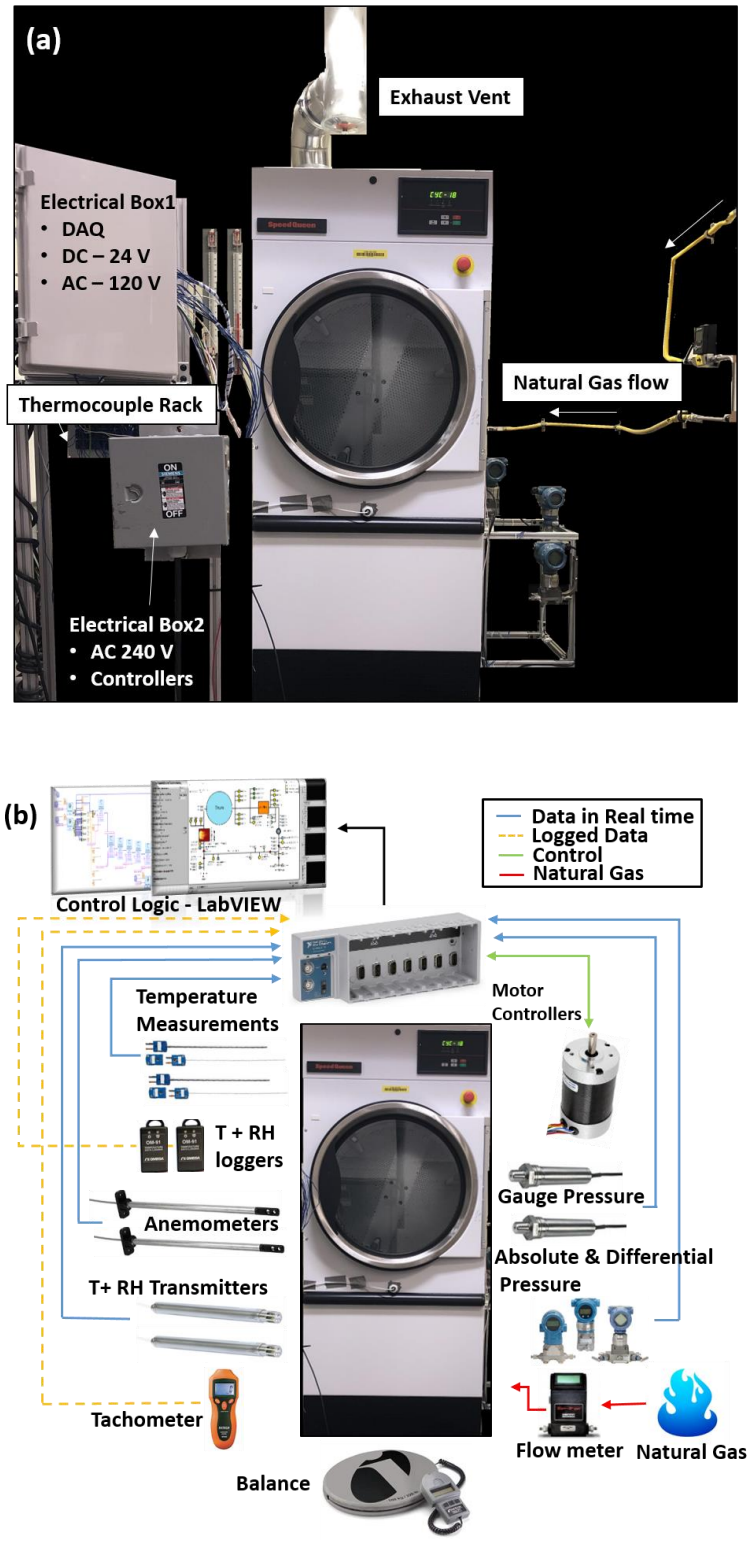

Figure 4.1: Experimental test facility (a) actual lab set up (b) block diagram with all instrumentation

Table 4.1: Instrumentation specifications and uncertainties

Variable Measured	Instrument/Sensor	Range	Uncertainty
Air Temperature in the ducts and combustor	OMEGA®: TMQSS-125G-6 KMQSS-125G-6	 0 to 315°C 0 to 1070°C	 ±0.25 K
Air Temperature and Humidity	OMEGA®: HX94C	2 to 95% 0 to 100°C	±2% ±0.6 K
High Temperature and Humidity	OMEGA®: HX94C	3 to 95% -40 to 180°C	±2% ±0.5 K
Air Temperature and Humidity inside the drum	OM-92-NIST	0 to 100% -30 to 80°C	±3% ±0.4 K
Air velocity	OMEGA®: FMA900A	0 to 25.4 m s^{-1}	±0.51 m s^{-1}
Absolute and differential pressure measurements	Rosemount® 3051CG 3051CA3F22A1AK5 3051CD2A22A1AB4	-6 to 6 kPa 0 to 200 kPa	±0.012 kPa ±0.060 kPa
Tachometer	FLIR Extech 461920	2 to 99,999 rpm	±0.05% of reading
Fuel mass flowrate	Sierra® Toptrak 820	0 to 500 slpm	±0.75 slpm

To monitor the drying process accurately, the combustor duty, air flow, drum rotation speed, temperature, and humidity are measured at different locations. T-type and 4 K-type calibrated thermocouples with an accuracy of ±0.25°C, temperature and humidity transmitters HX-94 (accuracy of ±2% on relative humidity, ±0.6°C), pressure transducers (Rosemount® 3051CG ±60 Pa), wireless temperature and humidity data loggers (OMEGA OM-92 accuracy of ±2.5% on relative humidity, ±0.3°C), air velocity anemometer FMA900A (±0.508 m/s), balance (±3% of the reading), and a tachometer (±2 RPM) were installed on the test facility. Table 4.1 summarizes the instrumentation and the corresponding uncertainties. The number and location of the anemometers and thermocouples were chosen based on ANSI/ASHRAE standards (Hall et al., 2018). The real time data acquisition system was programmed in LabVIEW (NI, 2019).

4.2.2 Baseline Experiments

The baseline operating conditions are outlined in Table 4.2. To ensure repeatability of the experiments, the terrycloth towels used as the standard textile load should always start at the same conditions. A commercial washer is used to initialize the load to a constant repeatable moisture content of 85%. The drying procedure is a "time dry" of a total of 32 minutes, of which the heater is ON at high heat for 30 minutes and then the heater is turned OFF while the fan remains ON for the remaining time. This cooling at the end of drying lowers the temperature of the textile for handling purposes.

A dry mass of 7.66 kg of terrycloth towels is used for experiments. After wetting the towels in the washer, the load is then placed in the drum of the dryer drum along with four OM-92 sensors. Two of these data loggers are fixed to the arm of the drum to measure

Table 4.2: Operating conditions for testing

Operating Parameter	**Value**
Ambient temperature	24 ± 2.5ºC
Ambient relative humidity	50 ± 5%
Drum motor	0.2 kW
Drum RPM	48 RPM
Fan motor	0.4 kW
Fan RPM	3400 RPM
Gas burner rating	18.8 kW
Initial dry mass	7.66 ± 0.23 kg
Initial wet mass	14.17 ± 0.42 kg
Textile Material	Terrycloth towels (100% woven cotton)

the air temperature and humidity. The other two data loggers are fixed to terrycloth towels to measure the temperature and humidity of the air at the surface of the textile.

A terrycloth towel load with a moisture content of < 3.5% is considered to be dry. A flow meter measures the fuel flow rate to the combustor during the drying experiment, allowing the combustor load to be determined. The experimental mass flow rate of the water evaporated in the drum is quantified from the measured humidity ratios at the inlet and outlet of the drum. To ensure repeatability, each experiment was repeated three times. In all experiments, mass and energy balances were performed to ensure that all mass and energy flows were accounted for in the data analysis. After recording the temperature, relative humidity, air velocity, and pressure at various locations, the data was analyzed on the Engineering Equation Solver EES Software (Klein, 2020b) platform. A detailed sample calculation of baseline drying performance and propagation of error is presented in Appendix A.

4.2.3 Optimization Experiments

The prototype used in this study is a Speed Queen 025 commercial GFD (~ 11.33 kg maximum capacity). Figure 4.2 shows the test facility used to run the experiments. The experimental facility was instrumented to monitor the combustor temperatures, air stream velocity, drum rotational speed, fuel mass flow rate, pressure, temperature, and humidity at different locations.

The temperatures were measured using 36 T-type and 4 K-type calibrated thermocouples with an uncertainty of $\pm$ 0.25 K. The fuel mass flow rate is measured using a SIERRA TopTrak® 820 with an accuracy of $\pm$ 1.5% of the full scale. A tachometer with

an uncertainty of ± 0.05% of the reading was used to measure to rotational speed of the drum. The number and location of all the thermocouples and anemometers were selected based on ANSI/ASHRAE standards. According to the ASHRAE standard 111, to accurately measure the air velocity in air flowing in circular ducts, three holes 60° from each other are drilled to cover all locations recommended using the log-linear method. The velocity is then averaged and multiplied by the duct area to get the flow. To measure the dry bulb temperature of the air passing through circular ducts within an uncertainty of ± 0.25 K, the thermocouples were calibrated. A total of 4 T-type thermocouples were installed at 90° angles. The real time data acquisition system was programmed in NI LabVIEW (Instruments, 2019).

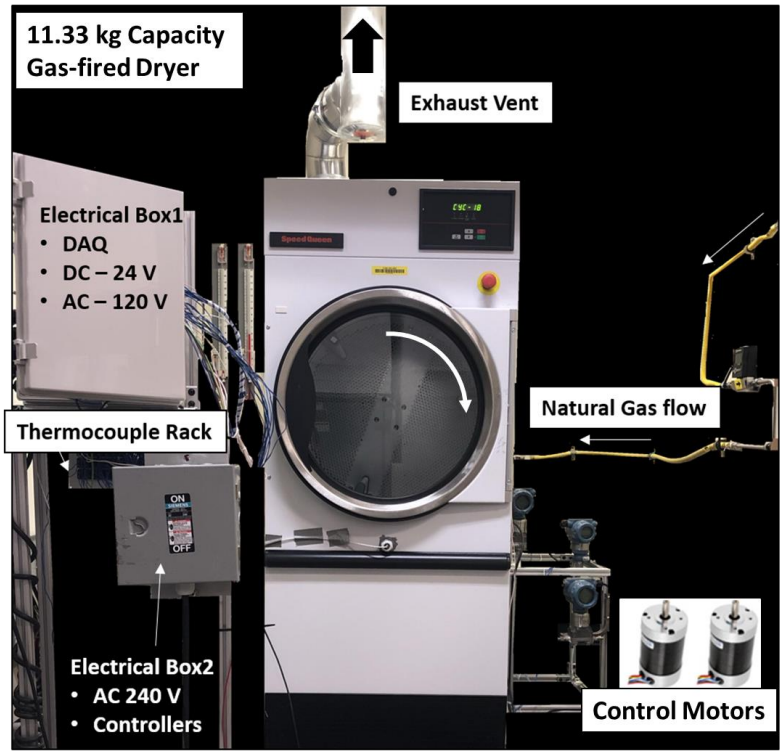

Figure 4.2: Experimental prototype for optimization experiments

Experiments were conducted on this dryer to investigate the effects of fuel mass flow rate, air flow rate, initial moisture content, bone-dry mass, and rotational drum speed on the energy consumption and drying time. The fuel flow rate was controlled and measured using a mass flow meter (Table 4.1) installed downstream of the natural gas supply. The initial moisture content and the bone-dry mass of the textile were controlled by measuring the weight before and after the drying cycle. To control the airflow rate and rotational drum speed of the dryer, two additional AC motors were connected to the control loop of the GFD. Figure 4.3 shows a block diagram of the additional loop.

The two additional motors were installed and connected to a 120V power supply and to the default control settings of the dryer. The fan motor runs at 3000 to 3800 rpm, which provides an air volumetric flow rate ranging from 0.165 – 0.283 $m^3 s^{-1}$. The rotational speed of the drum motor was varied from 1250 to 2200 rpm, which in turn varies the drum rotational speed from 39 to 64 rpm. The two fixed motors on the dryer were re-wired and

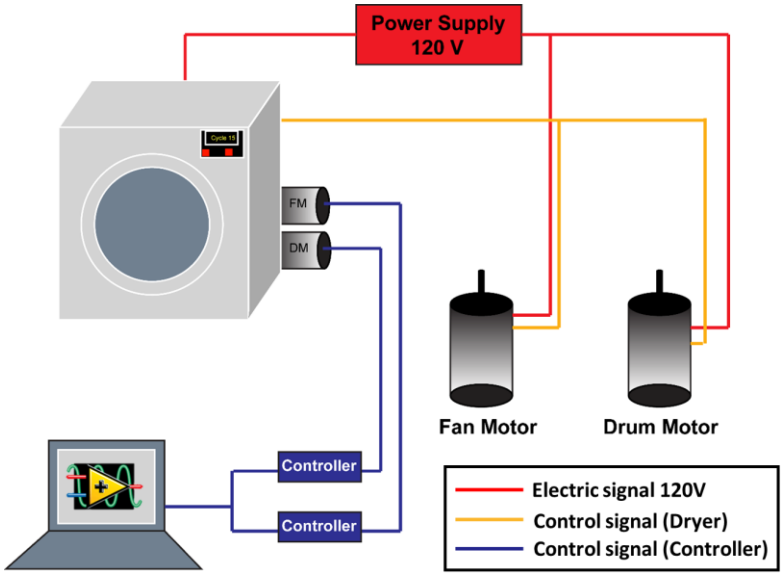

Figure 4.3: A block diagram showing the secondary loop connected to the dryer to control the drum rotational speed and the airflow rate

connected to a LabVIEW controller where the signal to the fan or drum motor is altered by the user. The parametric experiments were conducted after installing the secondary motor loop on the dryer. Figure 4.3 summarizes the operating conditions for the experiments conducted on the gas-fired tumble dryer. As shown in Figure 4.3, the first run is considered the baseline as it is the default setting for a high heat condition the dryer, i.e., without any external control. The 26 experiments are categorized into 5 subgroups, varying the bone-dry mass (Type A), varying the initial moisture content (Type B), varying the drum rotational speed (Type C), varying the ratio of the fuel mass flow rate (Type D, e.g., 50% indicates that fuel supplied is half of the baseline mass flowrate), and varying the air flow rate (Type E).

4.2.4 Data Reduction

The air temperature, relative humidity, and velocity at different locations in the GFD are recorded in NI LabVIEW (Instruments, 2019) at a sampling rate of one datapoint every second. The fuel flow rate and pressures are also recorded. The measured data are analyzed on the Engineering Equation Solver (EES) (Klein, 2020b) platform. The humidity ratio is calculated based on the measured air temperature, relative humidity and pressure as shown in Equation (4.1):

$$\omega = 0.62198 \frac{\varphi P_{w,sat}\big|_{T=T_{air}}}{P - \varphi P_{w,sat}\big|_{T=T_{air}}} \tag{4.1}$$

Table 4.3: Test matrix

	Type	Textile bone dry mass (kg)	Initial MC (%)	Ratio of $\dot{m}_{fuel}$ (%)	Airflow rate ($m^3\ s^{-1}$)	Drum Speed (RPM)
1	Baseline	7.66	85	100	0.236	48
2	Type A	1.92	85	100	0.236	48
3		3.83	85	100	0.236	48
4		5.75	85	100	0.236	48
5		9.57	85	100	0.236	48
6		11.33	85	100	0.236	48
7	Type B	7.66	50	100	0.236	48
8		7.66	75	100	0.236	48
9		7.66	100	100	0.236	48
10		7.66	125	100	0.236	48
11		7.66	150	100	0.236	48
12	Type C	7.66	85	100	0.236	39
13		7.66	85	100	0.236	42
14		7.66	85	100	0.236	45
15		7.66	85	100	0.236	51
16		7.66	85	100	0.236	54
17		7.66	85	100	0.236	64
18	Type D	7.66	85	33	0.236	48
19		7.66	85	50	0.236	48
20		7.66	85	66	0.236	48
21		7.66	85	75	0.236	48
22	Type E	7.66	85	100	0.165	48
23		7.66	85	100	0.189	48
24		7.66	85	100	0.212	48
25		7.66	85	100	0.259	48
26		7.66	85	100	0.283	48

where φ is the measure relative humidity, $P_{w,sat}$ is the saturation partial pressure of water vapor in the air, and P is the measured ambient pressure in the dryer cabinet. The air density is a function of the temperature, relative humidity, and pressure, i.e., $\rho = f\left(T_a, RH_a, P\right)$. The air mass flow rate is estimated using Equation (4.2):

$$\dot{m}_a = \rho A_{duct} V_{air} \tag{4.2}$$

where ρ is the air density, A_{duct} is the cross-sectional area of the duct, and V_{air} is the measured air velocity. The evaporation rate is estimated using Equation (4.3):

$$\dot{m}_e = \dot{m}_a \left(\omega_{out}^{drum} - \omega_{in}^{drum} \right) \tag{4.3}$$

where ω_{out}^{drum} is the drum exit humidity ratio and ω_{in}^{drum} is the drum inlet humidity ratio. The instantaneous moisture content of the textile is estimated using Equation(4.4):

$$X(t) = \frac{1}{m_{cl,dry}} \left(X_{init} m_{cl,dry} - \int_{t=0}^{t=\tau} \dot{m}_e \mathrm{dt} \right) \tag{4.4}$$

where X_{init} is the initial moisture content and $m_{cl,dry}$ is the bone-dry mass of the textile. To evaluate the performance of the dryer under different conditions, three figures of merit are selected. Figures of merit used to evaluate the performance are described in Chapter 3.

4.3 Results and Discussion

4.3.1 Effect of bone-dry mass

To study the effect of the bone-dry mass, all the other operating conditions in Table 4.2 are held constant. Figure 4.4 shows the effect of changing the bone-dry mass on the drum exit temperature. As the weight of the textile increases in the drum, the resistance to airflow through the combustor also increases. The additional pressure drop induced by the increased mass of textile reduces the airflow rate passing through the dryer despite having the fan motor running at constant rotational speed. This increases the temperature of the air entering the drum. In all of the runs, the textiles were initialized by the washer extractor to have a moisture content of 85%. For dry textile weight varying from 1.92 to 11.33 kg,

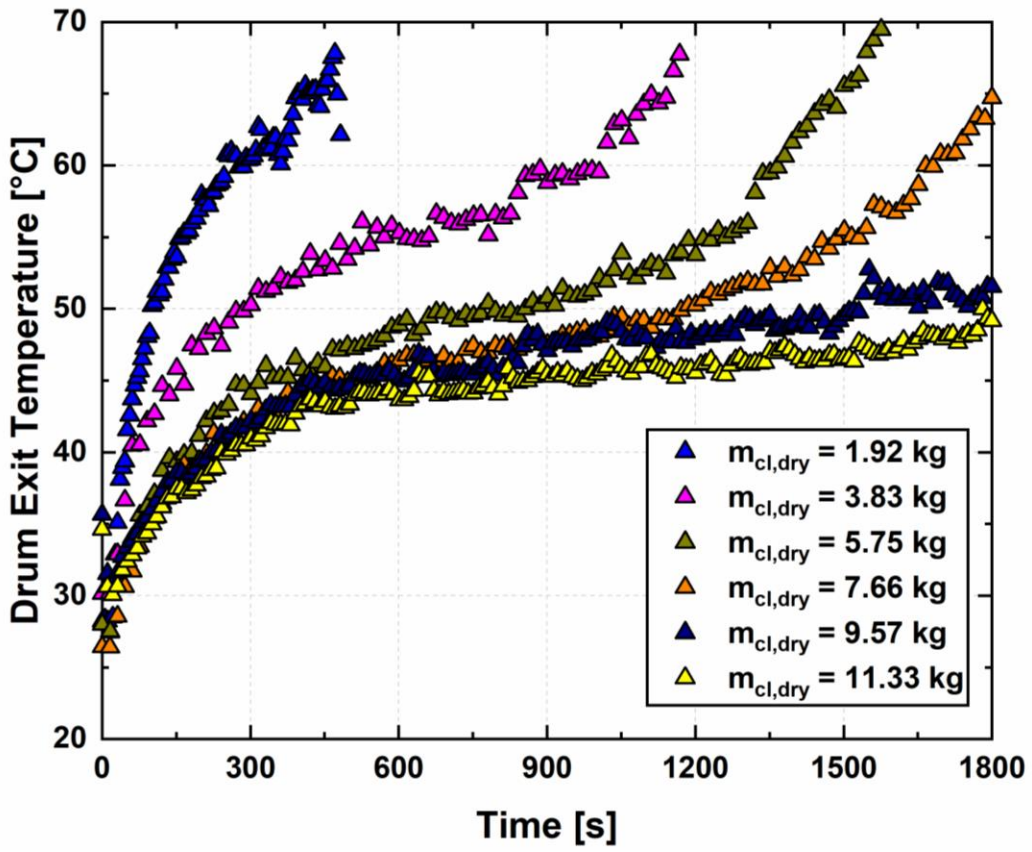

Figure 4.4: Drum exit temperature as function of time for different bone-dry mass (Type A)

the amount of water to be evaporated to achieve a final moisture content of less than 0.035 varies from 1.56 to 9.23 kg, respectively. The increased amount of available water extends the drying time since the energy input to the dryer is fixed. As shown in Figure 4.4, for a bone-dry mass of 1.92 kg, a final moisture content of 0.035 was achieved after 483 s is compared to baseline case ($m_{cl,dry}$ = 7.66 kg) of 1725 s. Additionally, the drum exit temperature decreases as the mass of textile increases. This is due to the different drying mechanics in each drying cycle. For instance, at low masses, i.e., $m_{cl,dry}$ = 1.92 kg, the temperature increases sharply during the initial and falling drying phase. However, the

constant drying phase is negligible at lower masses. For $m_{cl,dry}$ = 7.66 kg, all three drying phases are prominent. At t = 600 s, the temperature of the air exiting from the drum is 55.3°C, 49.7°C, 46.2°C, 44.5°C, and 42.9°C for masses of 3.83 kg, 5.75 kg, 7.66 kg, 9.57 kg, and 11.33 kg, respectively. However, at t = 1500 s the temperature of air exiting the drum is 65.4°C, 53.7°C, 48.9°C, and 43.4°C for masses ranging from 5.75 kg, 7.66 kg, 9.57 kg, and 11.33 kg, respectively. There is a significant change in the temperature of air exiting the drum due to the different drying mechanisms. Comparing $m_{cl,dry}$ = 5.75 kg and 11.33 kg at t = 1500 s, the temperature of air leaving the drum differs by 22°C. For $m_{cl,dry}$ = 11.33 kg, the falling rate drying phase is never achieved during the 1800 s cycle; therefore, evaporation is still taking place, as compared to the case for $m_{cl,dry}$ = 5.75 kg, in which the falling rate drying phase is achieved after t = 1200 s. During the falling rate phase, the moisture content of the textile decreases significantly, which reduces the evaporation rate, and therefore, increases the temperature of the air exiting the drum.

Figure 4.5 shows the variation of the relative humidity at the exit of the drum. As the mass of the bone-dry textile increases, the air flowrate decreases; however, the effective mass transfer area increases, which increases the evaporation rate. High evaporation rates increase the relative humidity of air at the exit of the drum. As mentioned previously, the additional mass of textile with additional water weight extends the drying time. At t = 1200 s, the relative humidity of the air exiting the drum is 11%, 30%, 44%, 56%, and 58%, for masses of 3.83 kg, 5.75 kg, 7.66 kg, 9.57 kg, and 11.33 kg, respectively. Because the falling rate period is never reached at high masses ($m_{cl,dry} \geq 9.57$ kg), the relative humidity is higher than that for lower masses ($m_{cl,dry} \geq 5.75$ kg). Finally, as the bone-dry mass

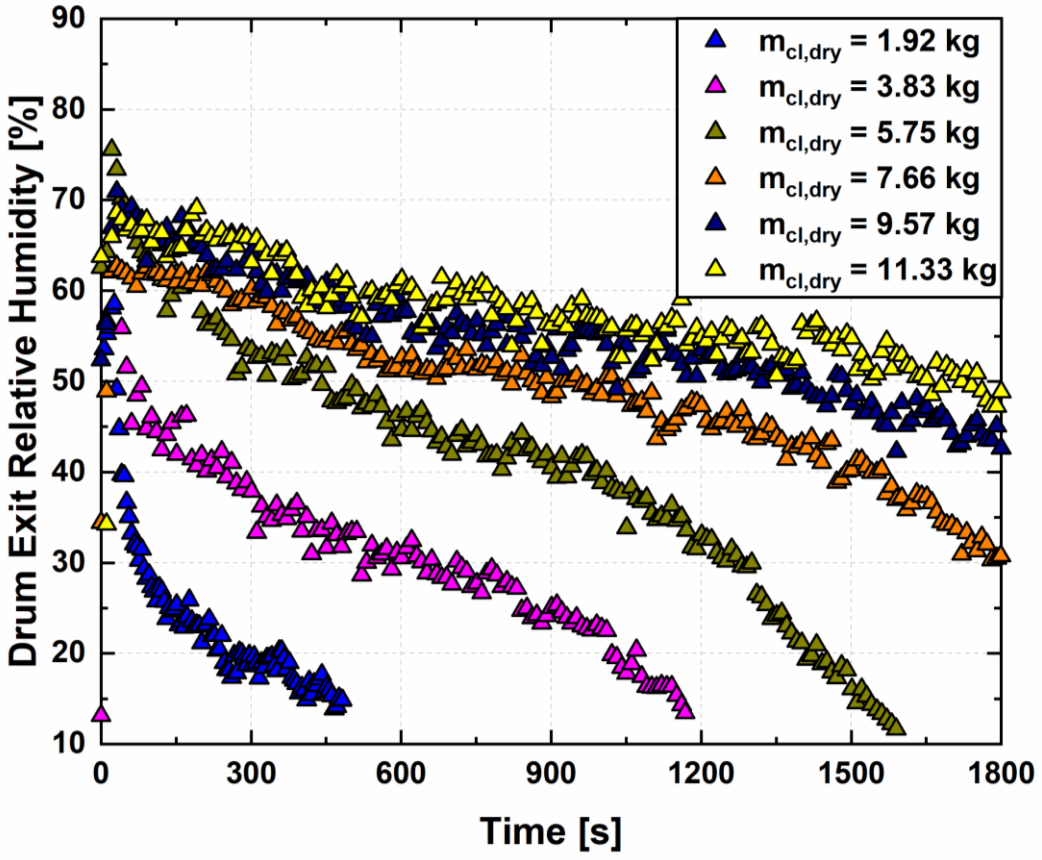

Figure 4.5: Relative humidity as function of time for different bone-dry mass load (Type A)

increases, the evaporation rate increases, and therefore, the temperature of the air exiting the drum decreases while the relative humidity increases.

4.3.2 Effect of initial moisture content

Figure 4.6 shows the variation of moisture content as function of drying time for different drying cycles with initial moisture content varying from 50% to 150% of the baseline case. The moisture content was varied while maintaining a constant bone-dry mass of 7.66 kg. Increasing the moisture content increases the amount of water initially available for evaporation. As the initial moisture content increases, the constant drying phase increases

too, which elongates the total drying time. As shown in Figure 4.6, the baseline case of starting with an initial moisture content of 85% shows that the desired moisture content in achieved in 1725 s, as compared to 904 s and 1322 s for initial moisture content of 50% and 75%, respectively. At high moisture content, i.e., MC = 150% of the baseline case, the second drying phase (constant drying phase) spans 90% of the drying cycle. This would mean that to get to a moisture content of 3.5%, at least two 30-minute drying cycles are required. The curves of the moisture content are in similar shape in terms of slopes, which translates to evaporation rate. Because the initial bone-dry mass is held constant, the effective mass transfer area does not change; however, the amount of water available is increasing as the initial moisture content increases, which increases the drying time. It should be noted that both energy consumption and drying time in the dryer can be reduced

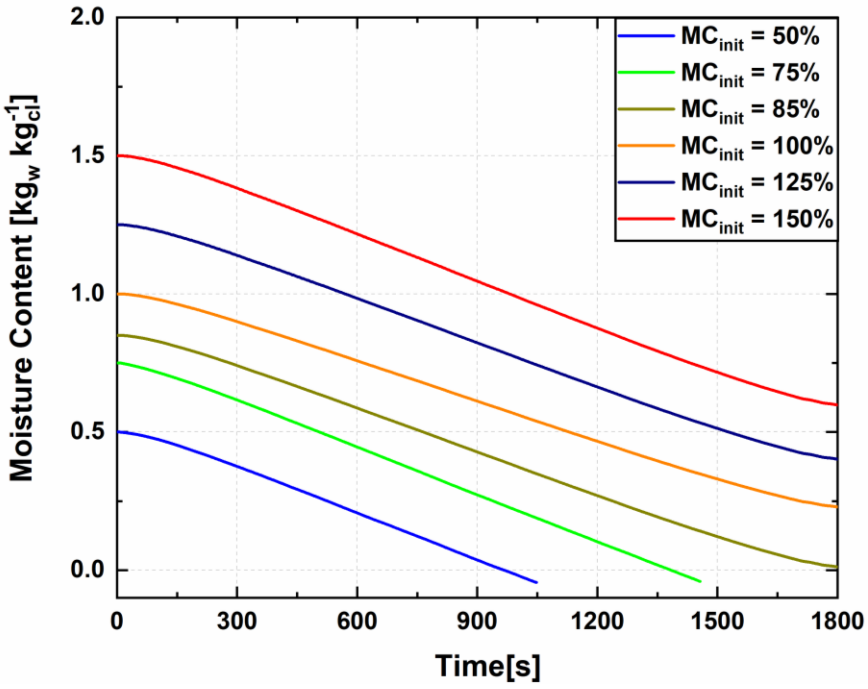

Figure 4.6: Change in moisture content as function of drying time for different initial moisture content loads. (Type B)

by decreasing the initial moisture content by elongating the dry spin period of the washer extractor.

4.3.3 Effect of drum rotational speed

The effect of varying rotational speed from 39 rpm to 64 rpm on drying was investigated next. Figure 4.7 shows the variation of the air temperature at the exit of the drum as function of time. As the drum rotational speed increases, the air temperature leaving the drum decreases due to the higher evaporation rates. However, at high rotational speeds, i.e., Ω_d = 64 rpm, the temperature of the air leaving the drum exceeds all other

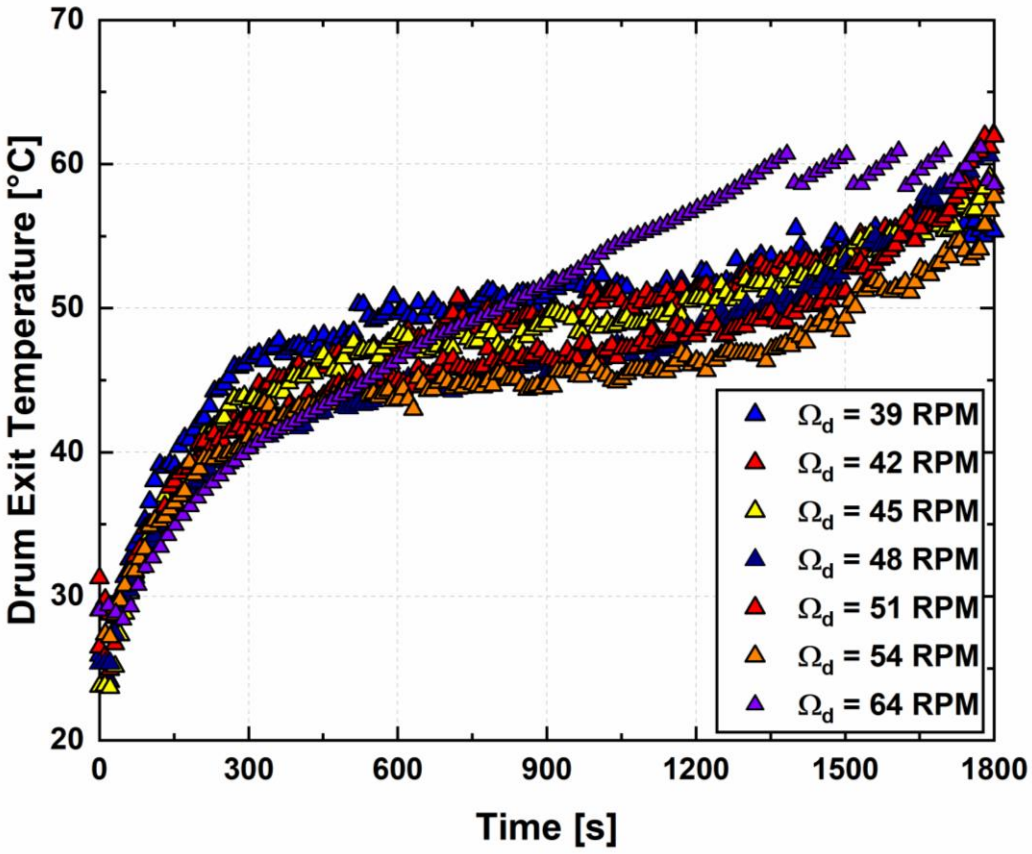

Figure 4.7: Drum exit temperature as function of drying time at different drum rotational speeds (Type C)

temperatures after t = 900 s. This change in trend suggests that there is an optimal rotational speed that would increase the drying rates, and therefore, shorten the drying time. To further understand the change in the air exit temperature, the textile topology provides further insights. Figure 4.8a-c shows the textile topology at three representative rotational speeds. At low rotational speed, i.e., Ω_d = 39 rpm, the tangential force is not sufficient to lift and tumble the textile. Therefore, as depicted in Figure 4.8a, the textile accumulates on the lower left side of the drum. The empty spaces are indicated by a yellow dotted contour. At these low rotational speeds, the hot dry air entering the drum from the combustor bypasses most of the textile, and the effective mass transfer area is reduced, which decreases the evaporation rate. At high rotational speeds, i.e., Ω_d = 64 rpm, the tangential force is strong enough that it drags the textile along the walls of the drum without experiencing any "tumbling" effects.

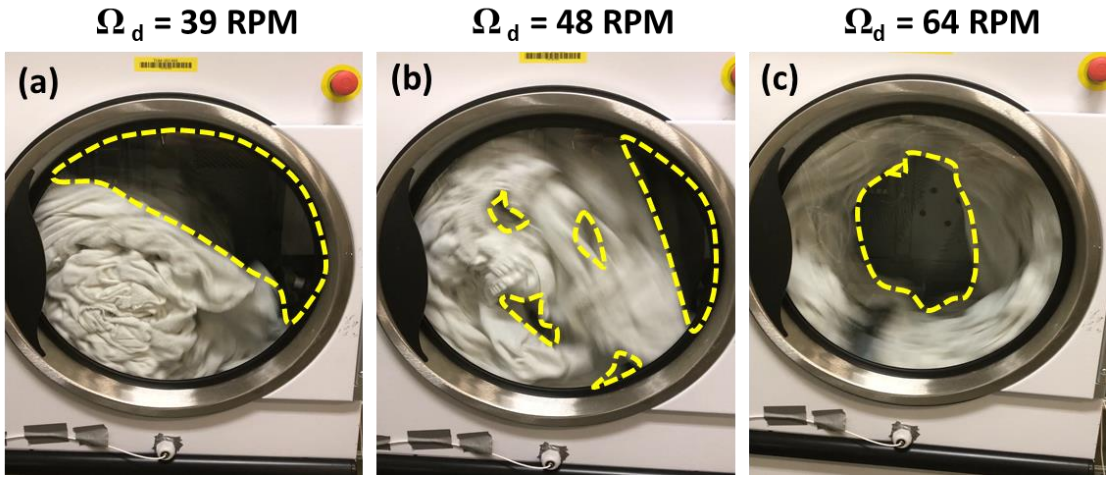

Figure 4.8: Textile topology for different rotational speeds (a) 39 RPM, (b) 48 RPM, and (c) 64 RPM.

Figure 4.8c shows that as the textiles are concentrated only on the walls of the drum, the air bypasses the textile from the center. The annular shape formed by the textile reduces the effective mass transfer area. As shown in Figure 4.7, the temperature of the air reaches 54.5°C after 900 s, which indicates that when the moisture content of the inner annulus of the textile drops significantly (i.e., $X \leq 3.5\%$), the air from the combustor bypasses the rest of the textile and exits at high temperatures. On the other hand, Figure 4.8b shows the topology of the textile at the baseline rotational speed, i.e., Ω_d = 48 rpm, which illustrates the "tumbling" effect. The tumbling effect reduces the empty spaces (as shown in Figure 4.8b), thereby increasing the effective mass transfer area. At a rotational speed of 48 rpm, the air gaps are minimized and the hot dry air from the combustor has to interact with the textile as it leaves the drum.

Figure 4.9 shows the variation of the instantaneous moisture content as function of time for different rotational speeds. (The slopes of the curves are proportional to the drying rate.) As the rotational speed increases, the slopes of the moisture content curves become steeper, indicating a higher drying rate. However, due to the air bypassing the textile at Ω_d = 64 rpm, the drying rate is reduced by 8.1% and 11.2% when compared to that at Ω_d = 48 rpm and Ω_d = 51 rpm, respectively. At extreme low and high rotational speeds, the textile does not undergo sliding, falling, and rotation. Therefore, there is an optimal rotational speed that maximizes the drying rate, in turn reducing the energy consumption and shortening the drying time. Insights from the experimental results show that running the gas-fired tumble dryer at a rotational speed of 51 rpm would maximize the drying rate compared to

the baseline case. Energy consumption and drying time reduction are discussed further in Section 4.3.6.

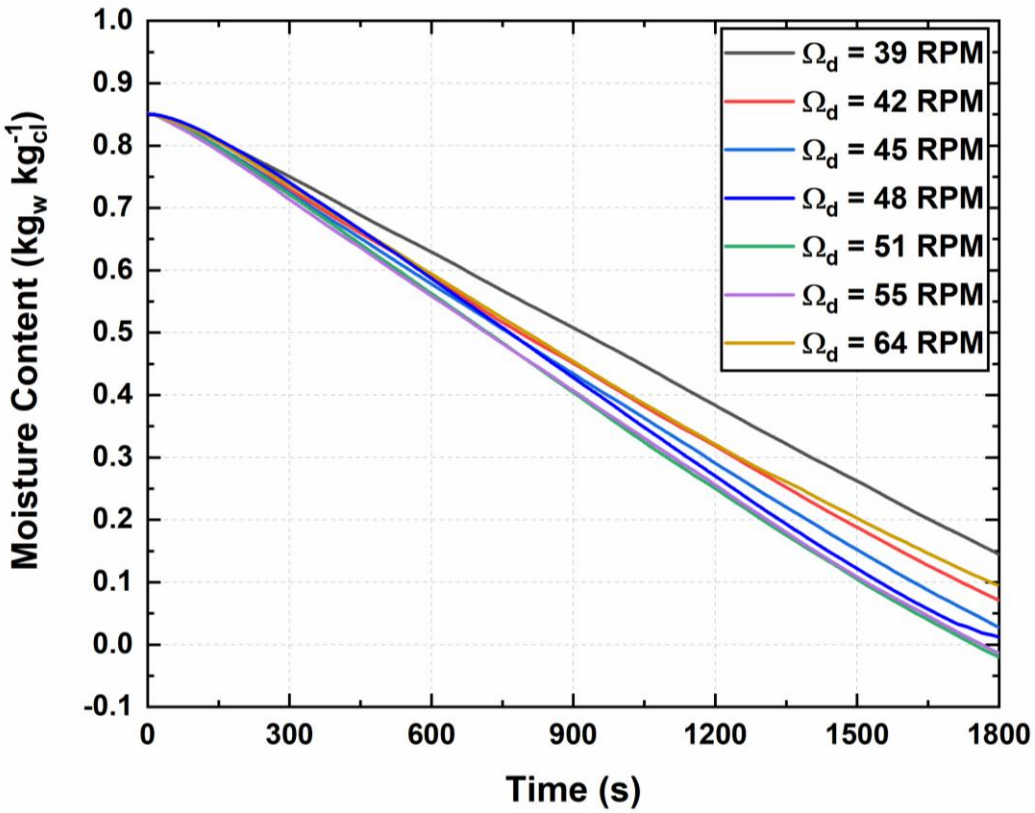

Figure 4.9: Variation of instantaneous moisture content as function of drying time for different rotational drum speeds (Type C)

It is important to note that for all the tested rotational drum speeds, the capillary flow taking place in the textile is stable. The capillary number represents the relative effect of viscous drag forces versus surface tension forces acting across an interface between a liquid and a gas. Typically, in porous media such as textile, a stable Capillary number ranges between 10^{-8} and 10^{-3} (Ding and Kantzas, 2007). For the highest drum rotational speed of 64 RPM, the maximum capillary number was 7.04×10^{-4}.

Insights from these experiments suggest that it is possible to modulate the rotational speed of the drum to further improve the energy savings. The rotational speed can be varied during a single drying cycle depending on the instantaneous moisture content in the textile. At the beginning of the drying cycle, the textile has a high moisture content. If the rotational speed of the drum is maximized (~64 RPM), this would help remove the free water (unbounded water) on the surface through convective (evaporation) and mechanical (centrifuging) mechanisms. As the drying cycle continues, the moisture content in the textile decreases. To maintain the same overall conductance, the effective heat and mass transfer areas are increased by decreasing the drum rotational speed (~48 – 51 RPM). This can be further optimized based on the drying efficiency.

4.3.4 Effect of fuel flow rate

The fuel flow rate was reduced from 100% at the base case to 33% of the baseline, with all other operating conditions held constant. Figure 4.10 shows the variation of the air temperature at the drum inlet for different fuel ratios. As expected, the lower the fuel supply to the dryer, the lower the temperature at the inlet of the drum. For a fuel ratio of 100%, i.e., the baseline case, the inlet steady state temperature is ~ 180°C. This temperature decreases to about 140°C, 120°C, 90°C, and 60°C for fuel ratios of 75%, 66%, 50%, and 33% of the baseline, respectively. As the temperature at the inlet decreases, the evaporation rate decreases due to the lower driving temperature difference between the surface of the textile and air in the bulk of the drum. Additionally, due to the low driving force $(\Delta T = T_{air}^{bulk} - T_{cl}^{surf})$, the rate at which the textile heats up to reach the temperature at which evaporation is initiated decreases, thereby increasing the drying time. This reduction in fuel

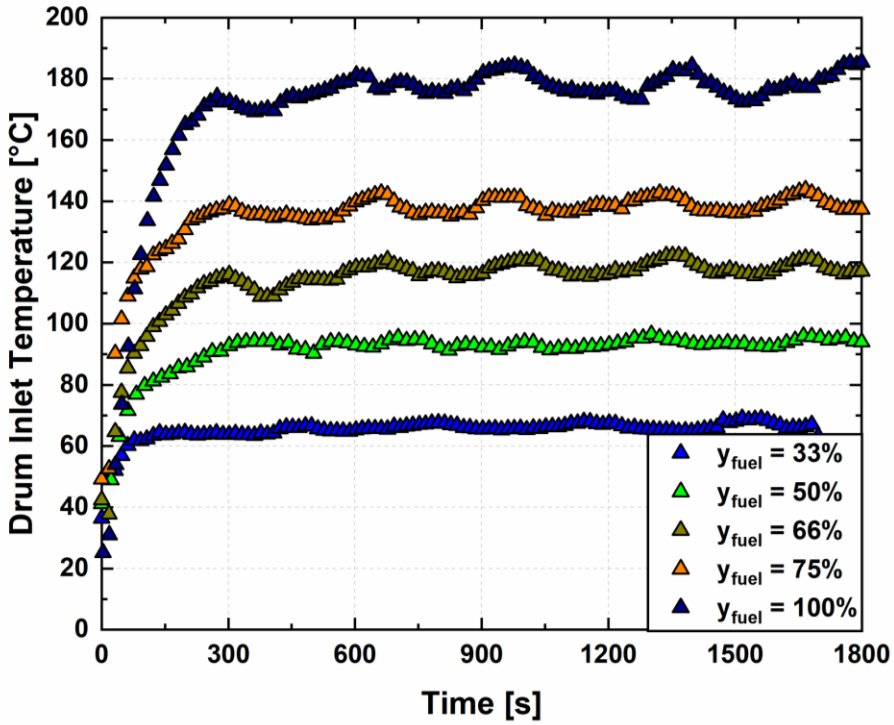

Figure 4.10: Drum inlet temperature as function of drying time at different fuel ratios (Type D)

flow rate, i.e., as heat modulation, in which the total energy input to the dryer is significantly reduced, elongates the drying time by 3 – 4 times. Therefore, to keep the drying time at less than 1800 s, a 100% fuel ratio is required.

4.3.5 Effect of air flow rate

The fan motor speed is controlled to vary the volumetric flow rate of air from 0.165 to 0.283 $m^3 s^{-1}$, keeping other operating conditions constant. As the fan speed increases, the air flow rate through the combustor increases, while decreasing the inlet air temperature to the drum as depicted in Figure 4.11. At low air flowrates, the temperature of the air entering the drum increases to about 200 – 215°C, while at high flowrates, the temperature entering the drum decreases to about 160°C. Figure 4.12 shows the evaporation rate for three

representative air flowrates. Despite having an inlet temperature of ~208°C at a volumetric flow rate of 0.189 $m^3 s^{-1}$, the evaporation rate decreased as compared to the baseline. For a volumetric flowrate of 0.283 $m^3 s^{-1}$, the evaporation rate is 0.0045 kg s^{-1}, which is 21% more than the evaporation rate for the baseline case. There are two factors that influence the drying rate, the first is an increase in the drum inlet temperature, while the second is the air flow rate. The experiments show that the effect of air flow rate dominates the drying rate as compared that of the inlet temperature. This due to the fact that increasing the air flow rate increases the mass flow rate of air inside the drum, which directly increases the evaporation rate as shown by Equation (4.3). Increasing the air flowrate increases both the heat transfer and mass transfer coefficients inside the drum. The heat transfer coefficient is

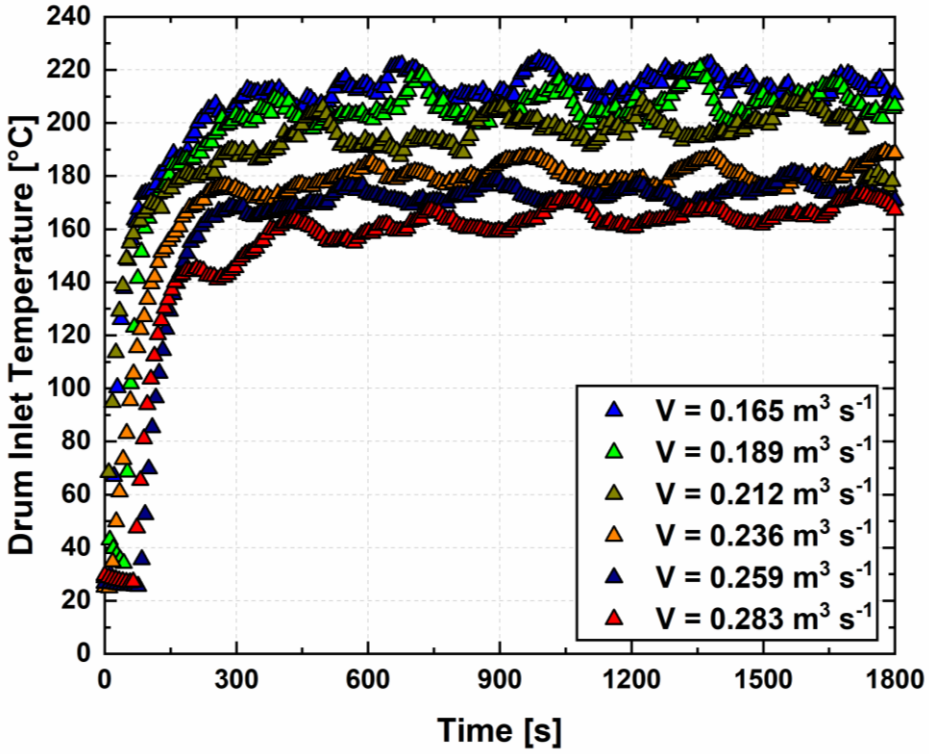

Figure 4.11: Drum inlet temperature as function of drying time at different airflow rates (Type E)

increased due to higher velocities and vigorous mixing at the interface between the textile and bulk air. The mass transfer coefficient increases due to high velocities that keep the moisture boundary layer at the surface of textile relatively thin. The increase in evaporation rate $\left(\dot{m}_e\right)$ is directly related to the increase in the slope of the moisture content.:

$$\dot{m}_e = m_{cl,dry} \frac{dX}{dt} \tag{4.5}$$

Figure 4.13 shows the variation of the moisture content as a function of time for different air volumetric flowrates. As discussed previously, for low air flowrates the drying rate decreases significantly as compared to the base case. For instance, at a volumetric

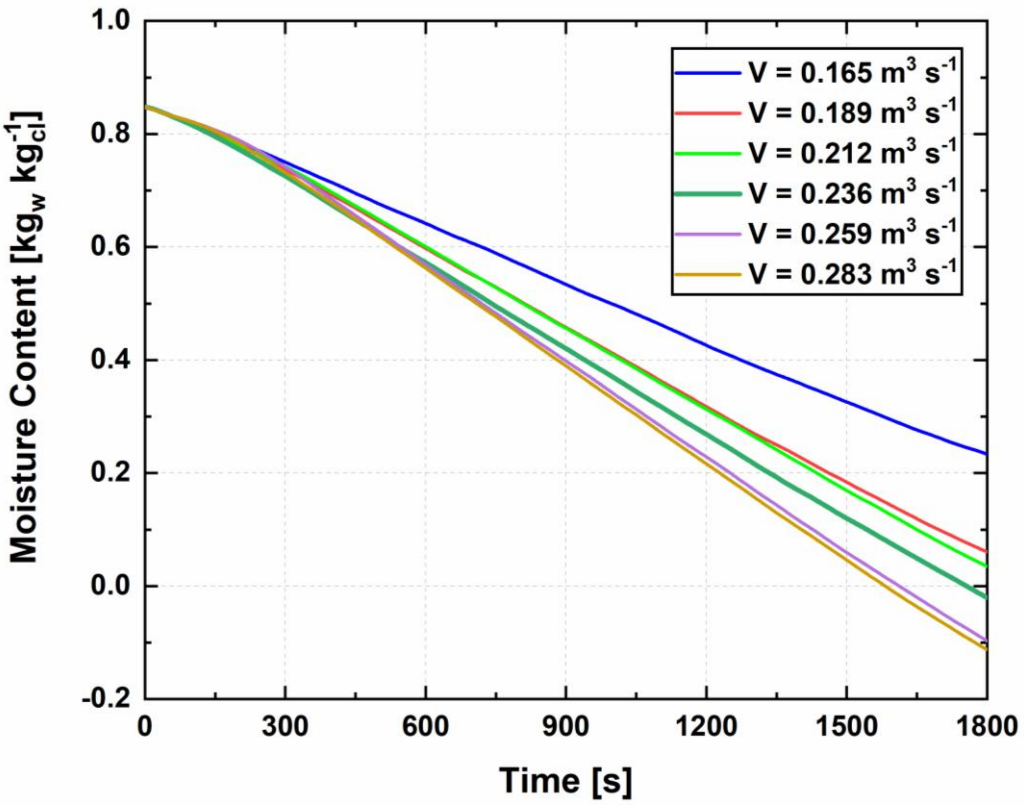

Figure 4.13: Variation of moisture content as function of drying time at different airflow rates (Type E)

flowrate of 0.165 $m^3 s^{-1}$, the drying rate decreased by 51.7% compared to the baseline case. At high volumetric flow rates (0.283 $m^3 s^{-1}$), the drying rate increases by 24.2% compared to the baseline case. This results in decreasing the drying time by 150 s. Additionally, when the fan speed varies, the negative pressure inside the drum also changes, which influences the mass flow rate of the air and air leakage. A higher fan speed leads to more air leakage due to the larger negative pressure induced inside the chamber of the dryer, and the increasing air leakage into the drum results in a higher drying rate and correspondingly lower drying time.

4.3.6 Dryer overall performance

The effects of five different input parameters on the drying process were discussed above. In this section, the drying performance is discussed using the three figures of merit – energy consumption (SMER), drying time, and drying efficiency. Table 4.4 summarizes the drying performance observed in the overall set of experiments in this study. When the bone-dry mass is increased with a constant initial moisture content, the energy consumption increases due to the longer drying time required to evaporate the added water. Having the dryer at its maximum bone-dry capacity of 11.33 kg, the SMER is 1.84 kWh kg^{-1}, which is 27% more than the baseline case. The drying time was elongated to 2184 s compared to 1725 s for a bone-dry load of 7.66 kg. In the next set of experiments (Type B), as the initial moisture content increases, the SMER, drying efficiency, and drying time increase due to the additional water content that must be evaporated. As shown in Table 4.4, at a low initial moisture content of 50%, the SMER, drying efficiency, and drying time are 0.76 kWh kg^{-1}, 39.2%, and 904 s, respectively. When the initial moisture content increases to 150% of the dry load, the SMER and drying efficiency increase by 39% and 6%, respectively. It

Table 4.4: Summary of the overall performance

Experiment Number	SMER (kWh kg^{-1})	Drying Efficiency (%)	Drying time (s)
1	1.45	41.2	1725
2	0.41	38.7	483
3	0.98	39.6	1160
4	1.26	40.7	1504
5	1.67	42.8	1986
6	1.84	43.2	2184
7	0.76	39.2	904
8	1.11	40.3	1323
9	1.68	41.9	1999
10	1.83	42.6	2187
11	2.01	43.3	2396
12	1.77	38.1	2101
13	1.60	39.8	1907
14	1.52	40.4	1806
15	1.41	44.0	1688
16	1.43	43.8	1702
17	1.65	35.6	1968
18	0.56	49.3	2655
19	0.99	48.1	2356
20	1.22	45.5	2187
21	1.26	43.1	1983
22	1.82	36.9	2169
23	1.61	39.5	1910
24	1.55	40.7	1849
25	1.33	43.4	1574
26	1.31	46.7	1563

was also found that the optimal drum rotation speed is 51 rpm, at which the drying time and SMER decrease by 2.1% and 2.4%, respectively. Additionally, the drying efficiency increased to 44% due to an increase in the effective mass transfer area. When decreasing the fuel flowrate to the dryer, the total input energy to the dryer decreases; however, the drying efficiency increases due to lower heat losses to the surroundings as the air entering the drum is at a lower temperature. Varying the air flowrate had the highest influence on the SMER, drying efficiency, and drying time. This is due to the fact that increasing the air

flowrate in the drum increases the heat and mass transfer coefficients as discussed in Section 4.3.5. At the highest air flowrate i.e., 0.283 m^3 s^{-1}, the SMER is reduced to 1.31 kWh kg^{-1}, while the drying efficiency increased to 46.7%. Despite the larger electrical energy input to the fan motor, total energy input to the dryer is decreased, because the drying cycle duration is reduced.

As shown in Table 4.4, the SMER, drying efficiency, and drying time are correlated to the five input factors in a simple, straightforward manner that facilitates their use as reduced-order models for design and optimization studies, as well as for the implementation of computationally inexpensive control algorithms. The drying time as a function of all the input parameters is given by Equation (4.6):

$$t_d = a_0 + a_1 m_{cl,dry} + a_2 MC + a_3 \dot{m}_{fuel} + a_4 \dot{V}_a + a_5 \Omega_d \quad (4.6)$$

Table 4.5: Correlation coefficients for drying time

Coefficient	Value
a_0	1927.637
a_1	172.985
a_2	13.537
a_3	$- 3.506 \times 10^5$
a_4	$- 5.218 \times 10^3$
a_5	- 2.337

The coefficients for this correlation based on the experiments shown in Table 4.3 are provided in Table 4.5. Figure 4.14 shows the measured drying times compared with those predicted by the reduced-order model and also by the first-principles model. The measured and reduced-order model (Equation (4.6)) predicted drying times are in good agreement, with a coefficient of determination (R^2) of 0.89. The theoretical model also showed good agreement in predicting the experimental results for the different types of experiments,

while maintaining a maximum uncertainty of 9.7% of the measured value. However, for the experiments in which the initial moisture content was varied resulted in slightly higher errors at lower moisture contents. This is due to the fact that at low moisture contents, i.e., 50% and 75%, the initial water content is lower, which results in an under predicted heat and mass transfer coefficient, which in turn leads to low evaporation rates that overpredict the drying time.

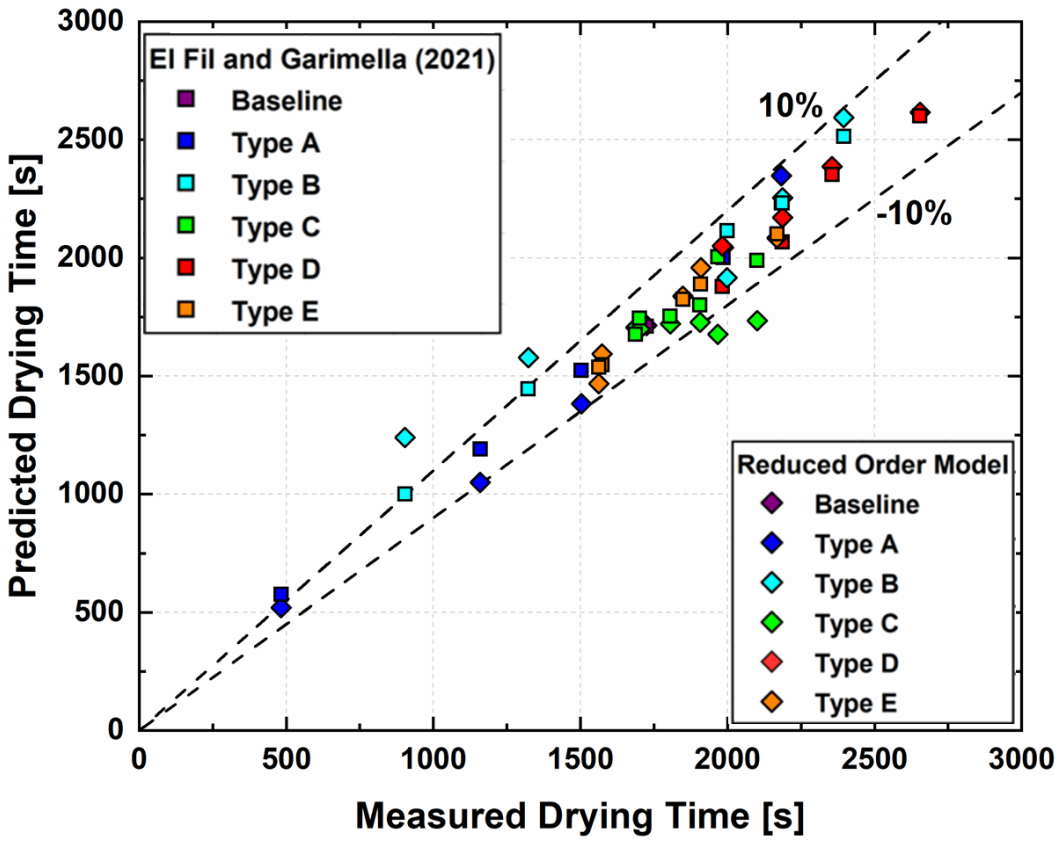

Figure 4.14: Predicted versus measured drying time

The correlation for drying efficiency is given by Equation (4.7):

$$\eta_d = b_0 + b_1 m_{cl,dry} + b_2 MC + b_3 \dot{m}_{fuel} + b_4 \dot{V}_a + b_5 \Omega_d \tag{4.7}$$

Table 4.6: Correlation coefficients for drying efficiency

Coefficient	Value
b_0	33.910
b_1	0.468
b_2	3.793×10^{-2}
b_3	$- 3.195 \times 10^{3}$
b_4	67.068
b_5	-0.063

with the coefficients provided in Table 4.6. Figure 4.15 a comparison between the measured and predicted (reduced-order and theoretical models) drying efficiencies. The measured and reduced-order model (Equation (4.7)) predictions of drying efficiency are in

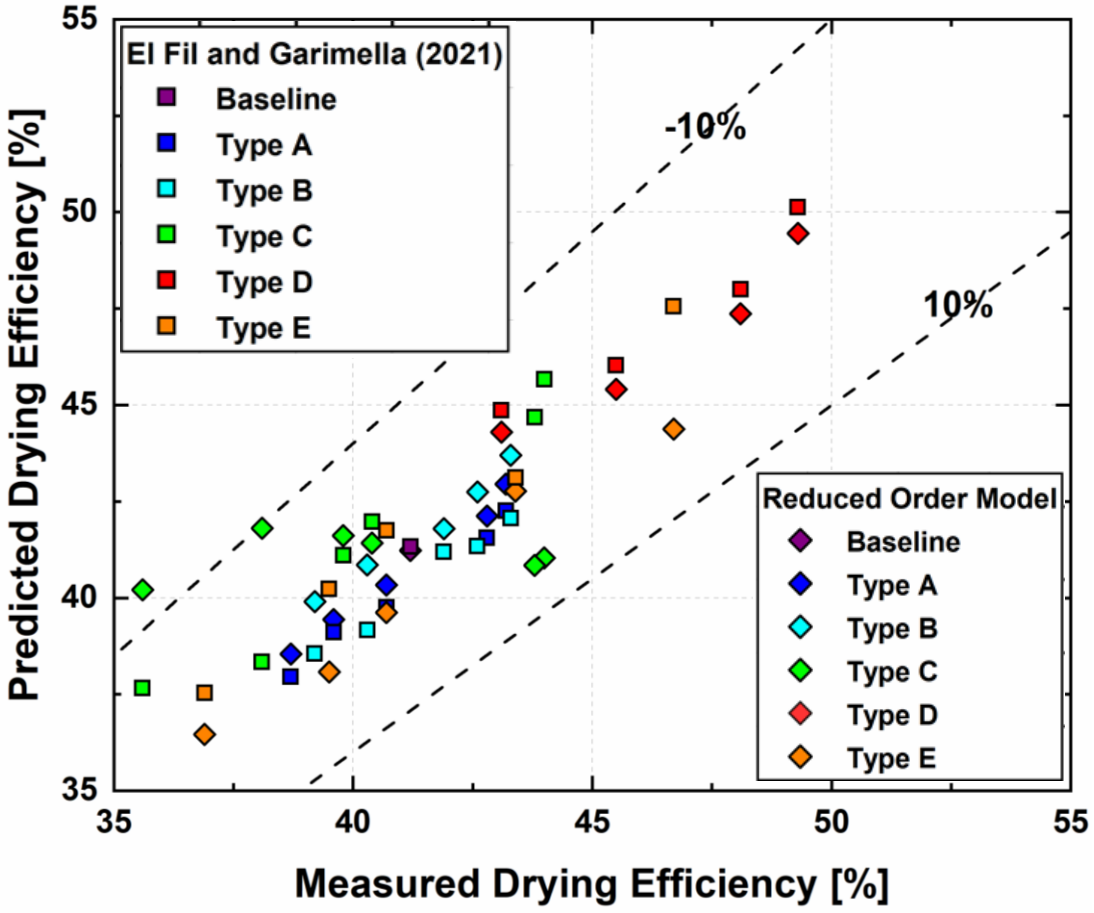

Figure 4.15: Predicted versus measured drying efficiency

good agreement, with a coefficient of determination (R^2) of 0.91. The theoretical model predicts the measured drying efficiency within a maximum uncertainty of ±8.1% of the measured value, while the reduced-order model prediction is within a maximum uncertainty of 11.5% of the measured quantity.

The energy consumption of the gas-fired dryer is correlated using the expression for SMER given by Equation (4.8):

$$SMER = c_0 + c_1 m_{cl,dry} + c_2 MC + c_3 \dot{m}_{fuel} + c_4 \dot{V}_a + c_5 \Omega_d \tag{4.8}$$

Table 4.7: Correlation coefficients for SMER

Coefficient	Value
c_0	-0.571
c_1	0.146
c_2	1.122×10^{-2}
c_3	281.888
c_4	-4.320
c_5	2.390×10^{-3}

with the coefficients provided in Table 4.7. The effect of the rotational speed on the SMER is minimal compared to other parameters. Figure 4.16 shows a plot comparing the measured, reduced-order model predicted, and the theoretical model SMER values for all experiments conducted in this study. The measured and predicted SMER by reduced-order model are in good agreement with a coefficient of determination of 0.88. The theoretical model exhibited good agreement with the measured data with a maximum uncertainty of 7.1% of the measured value. The outliers shown in Figure 4.16 corresponded to the experiments where the moisture content was varied. This slight discrepancy can be attributed to an overpredicted mass transfer coefficient due to the moisture transfer

mechanism inside the textile. For instance, at high moisture content, the moisture transport is due to two main mechanisms: capillary flow and unbound moisture diffusion. One the other hand, at low moisture content, the transfer mechanism is mainly unbounded moisture diffusion. The correlation used to predict the area-mass transfer was developed for initial moisture content exceeding 60%.

It should be noted that the theoretical spatial model developed in Chapter 3 provides deeper insights into the underlying heat and mass transfer phenomena. However, the reduced-order models developed here can provide quick and accurate evaluation of drying

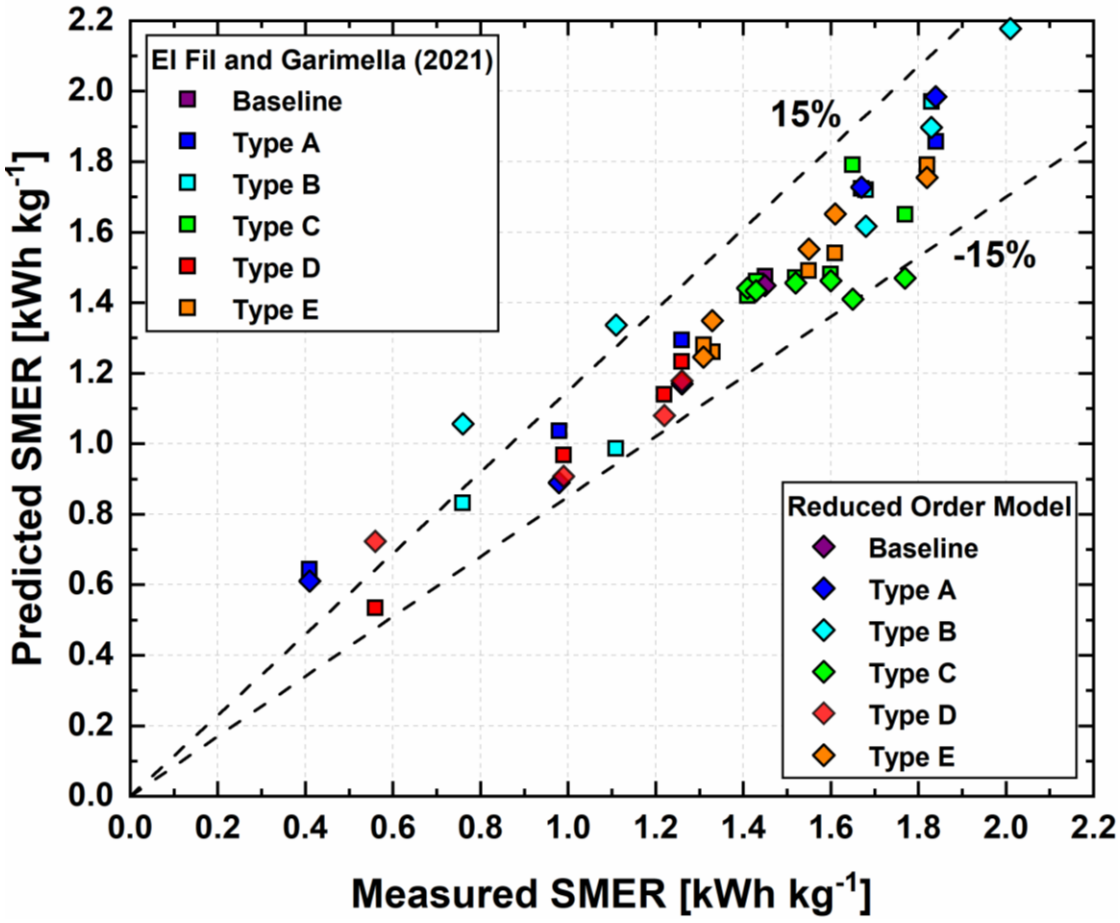

Figure 4.16: Predicted versus measured SMER

performance. The theoretical model took 492 s to simulate the performance of gas-fired drying cycle of 1800 s when using an Intel® Core i7-4600U CPU at 2.10 GHz with an installed memory (RAM) of 8 GB. On the other hand, it takes less than 6 s to predict the drying performance using the reduced-order model, while maintaining an uncertainty of less than ±10% of the measured value. Therefore, the reduced-order models can be used by laundry manufacturers as an accurate and quick method to design and optimize commercial dryers.

4.4 Conclusion

An experimental study of textile drying in an air vented gas-fired tumble dryer was performed to analyze the influence of inlet conditions on the energy consumption, drying efficiency, and drying time. For the baseline case, the model shows good agreement in predicting the drum exit air temperature, humidity ratio, the moisture content, and evaporation rate, with AADs of 6.6%, 7.2%, 1.2% and 3.2%, respectively.

The results from the optimization experiments showed that the drying time can be reduced by 162 s from the baseline value of 1725 s while also decreasing the SMER to 1.31 kWh kg^{-1}, i.e., a 9.65% reduction compared to the baseline case. Insights from the experiments show that varying the air flowrate had the strongest influence on the performance of the dryer. A correlation for predicting the drying time was developed, and showed that the influence of different inlet operating conditions on the drying time. The higher the air flowrate, the lower the drying time. Reduced-order models to predict the drying efficiency and SMER were also developed. The results showed that the SMER is influenced by all the inlet parameters; however, there is a low dependence on the rotational speed of the

drum. The reduced-order models show good agreement with the theoretical and measured figures of merit. These correlations can be used as tools to optimize dryer performance and implement control algorithms in commercial gas-fired tumble dryers to reduce energy consumption and drying time.

CHAPTER 5. WASTE HEAT RECOVERY

In this chapter, two waste heat recovery methods are presented. To reduce the wasted energy, exhaust gas recirculation and recuperative heat exchange are investigated numerically and experimentally. The improvement is assessed based on three figures of merit: drying efficiency (η_d), specific moisture extraction ratio (SMER), and drying time (Δt_d).

5.1 Introduction

Researchers have proposed various methods to reduce total energy consumption by optimizing operating parameters, recirculating exhaust air, waste heat recovery through heat exchangers, or a hybrid of these approaches. Hekmat and Fisk (1984a) proposed decreasing the mass flow rate and increasing the temperature of the intake air, which decreased energy consumption by 8% and 15%, respectively. Lambert et al. (1991) recirculated exhaust gas at different recirculation ratios and enhanced drying efficiency by 15%. Conde (1997) demonstrated that the use of heat-recovery heat exchangers improves the energy efficiency of drying. Bansal et al. (2001) found that recuperative heat exchangers can improve the performance of conventional tumble dryers significantly. Bassily and Colver (2003b) evaluated the effects of operating parameters of an electrically driven dryer, including the electrical input power, fan speed, load weight, and initial moisture content of the clothes experimentally, and concluded that the performance of tumble dryers can be further optimized. Recently, Wei et al. (2018b) and Novak et al. (2019) optimized drying inlet conditions and performance to yield smooth and undamaged textiles at the desired moisture content for electric tumble dryers. This energy saving

technique has been investigated thoroughly in the literature. To modulate the heat in a single drying cycle, the primary heater is turned off and on to reduce the total energy consumption. However, this reduces the air temperature in the drum, which increases the drying time. Heat modulation was demonstrated to reduce energy consumption by ~50% while extending the drying time by three times. The energy saving techniques investigated in this study aimed to reduce the drying time and energy consumption simultaneously. Despite many studies to optimize tumble dryers, there are few studies that address these issues for gas-fired tumble dryers. Although the optimization of tumble dryers has been undertaken for several years, non-optimal dryers can still be found in the US market.

Ahn et al. (2019) investigated the thermal characteristics and drying mechanisms of such a dryer experimentally and found that air entering the electrical heater was preheated by the heat leaking from the heater and other parts in the dryer which recovered about 5-8% of heat. This resulted in a slight enhancement in energy efficiency despite an increase in drying time. Another device considered in the literature to reduce energy consumption in drying is the nozzle dryer, which does not require heat addition (Shelton and Christiansen, 1999). Nevertheless, the difficulties in lint removal and the need for vacuum generation makes this option unattractive. On the other hand, Shaik et al. (2018) used a finned-tube heat exchanger to recover 0.11 kWh (per 1 kg of water removed) from the exhaust air stream. Ma et al. (2018) developed a hybrid residential electrical dryer by recycling heat via heat exchange and a recirculation control system. The latter system reduced power consumed by the dryer by 16% while maintaining the same drying time. As mentioned previously, there have been various efforts to improve the efficiency of small electric residential dryers, but the energy efficiency of larger commercial gas-fired tumble

dryers has not received commensurate attention, despite their being more energy intensive. The only study in the literature on this topic is by Williamson and Bansal (2004), in which they investigated large (dry load capacity ~ 210 kg) commercial gas-fired tumble dryers. Recirculation was found to decrease the energy efficiency and moisture removal rate from dryers, which was attributed to a significant decrease in the evaporation rate. The dryer with recirculation did not show any falling-rate period, and the exit humidity always stays high, leading to high concentrations of water vapor in the drum. Thus, the recirculation of the exhaust stream retards the evaporation rate. Williamson and Bansal (2004) found that recirculation is ineffective and should possibly only be used in situations where the drying profile is allowed to reach the falling-rate region.

5.2 Model Development

5.2.1 Exhaust Gas Recirculation

Exhaust gas recirculation (EGR) is a simple method to recycle and reclaim some of the energy that is otherwise lost to the ambient. As depicted in Figure 5.1a, a fraction of the exhaust stream is circulated back, thus preheating the air before it enters the combustor.

The recirculated stream is mixed directly with the incoming stream. The mass (moisture) and energy conservation balances to determine State 8 are given by Equations (5.1) and (5.2), respectively.

$$\dot{m}_1\omega_1 + \dot{m}_7\omega_7 = \dot{m}_8\omega_8 \tag{5.1}$$

$$\dot{m}_1 h_1 + \dot{m}_7 h_7 = \dot{m}_8 h_8 \tag{5.2}$$

The fraction of the recirculated air is defined in terms of volumetric flow rates rather than mass flowrates for convenience and controllability while running the experiments; however, in the analysis, mass conservation is satisfied. The total volumetric flow rate of air entering the combustor (State 8) is conserved and remains unchanged to avoid changing the air-to-fuel ratio. The expression for the recirculation ratio is:

$$y_{RR} = \frac{\dot{V}_7}{\dot{V}_8} = \frac{\dot{V}_7}{\dot{V}_7 + \dot{V}_1} \tag{5.3}$$

Recirculating the exhaust stream in a gas-fired tumble dryer implies that the chemical balance of the combustion reaction is also altered due to the recirculation of combustion products. To account for this phenomenon, the reactants of the chemical balance in Equation (3.1) are modified. The model assumes that the dominant combustion product is carbon dioxide (CO_2) (Turns, 2000; McAllister et al., 2011). Typically, combustion products of natural gas include CO_2, CO, C, SO_2, and NO_2; however, in this study, the effects of combustion gases are simulated as only water vapor and CO_2 while neglecting the rest of the products. This assumption limits the performance of the model, specifically at high recirculation ratios, where combustion gases are significant. The modified chemical balance is given by Equation (5.4):

$$\begin{aligned} \mathrm{NG} + (2.151+\gamma)(\mathrm{O_2} + 3.76\mathrm{N_2}) + ((1-y_{RR})\zeta + y_{RR}\sigma)\mathrm{H_2O} + \lambda\mathrm{CO_2} \\ \rightarrow (1+\lambda)\mathrm{CO_2} + (1.95+\zeta+\sigma)\mathrm{H_2O} + (8.137+3.76\gamma)\mathrm{N_2} + (0.176+\gamma)\mathrm{O_2} \end{aligned} \tag{5.4}$$

where $\lambda = f(y_{RR})$ is number of moles of carbon dioxide recirculated back and σ is the number of moles of the additional moisture recirculated back.

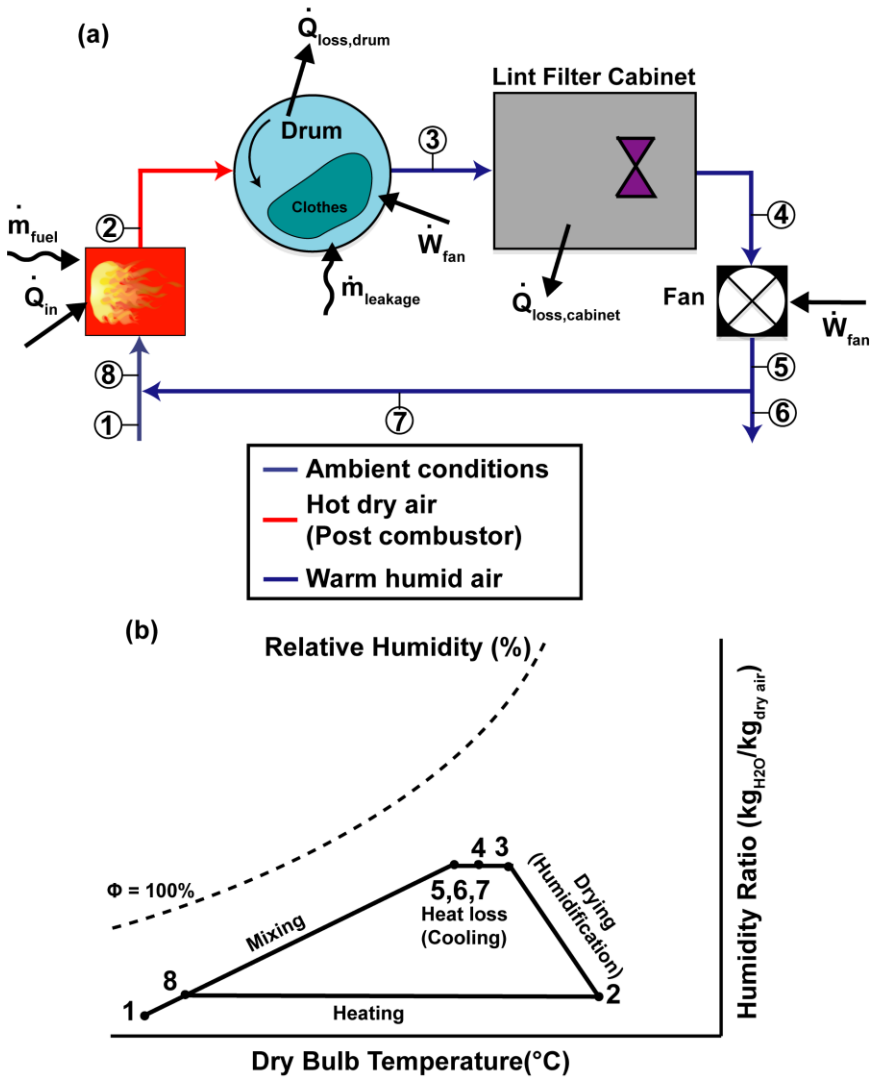

Figure 5.1: (a) Cycle schematic with exhaust gas recirculation (b) Psychrometric chart of the EGR drying cycle

5.2.2 Waste Heat Recovery via Recuperation

An alternative approach to recover the energy rejected with the exhaust is to install a recuperative compact heat exchanger (CHX). There are several studies on waste heat recovery using compact heat exchangers for commercial textile drying (Pulat et al., 2009; Fiaschi et al., 2017; Rakib et al., 2017; Fiaschi and Talluri, 2019), food drying (Law et al., 2013; Masud et al., 2020), and in the steel industry (Rakib et al., 2017). A schematic of the

recuperative process is shown in Figure 5.2a. Unlike EGR, the exhaust does not mix with the incoming air; thus, it is sensibly preheated without increasing the humidity. A thermodynamic analysis of the CHX is conducted to assess the performance and energy savings resulting from the installation of the compact heat exchanger in a gas-fired tumble dryer. The mass, species, and energy equations developed for the recuperative heat exchange are based on a quasi-steady state approximation, i.e., the energy storage term is neglected (Tuğrul Oğulata, 2004; Kandilli and Koclu, 2011; Zhou et al., 2018) because of the comparatively low thermal mass of the compact heat exchanger. The compact plate-fin heat exchanger was designed for high power density and to avoid condensation at State 6.

Therefore, the heat transfer rate is given by Equation (5.5):

$$\dot{Q}_{CHX} = \dot{m}_6 \left(h_5 - h_6 \right) \tag{5.5}$$

Similarly, the energy balance on the intake side is expressed by Equation (5.6):

$$\dot{Q}_{CHX} = \dot{m}_1 \left(h_7 - h_1 \right) \tag{5.6}$$

Since the geometry of the crossflow heat exchanger is known (along with all the surface areas and cross sectional flow areas), the energy balance can be also expressed as:

$$\dot{Q}_{CHX} = UA \cdot F \cdot LMTD \tag{5.7}$$

where F is the correction factor due to the cross flow configuration and LMTD is the log mean temperature difference calculated based on a counterflow orientation and can be expressed as:

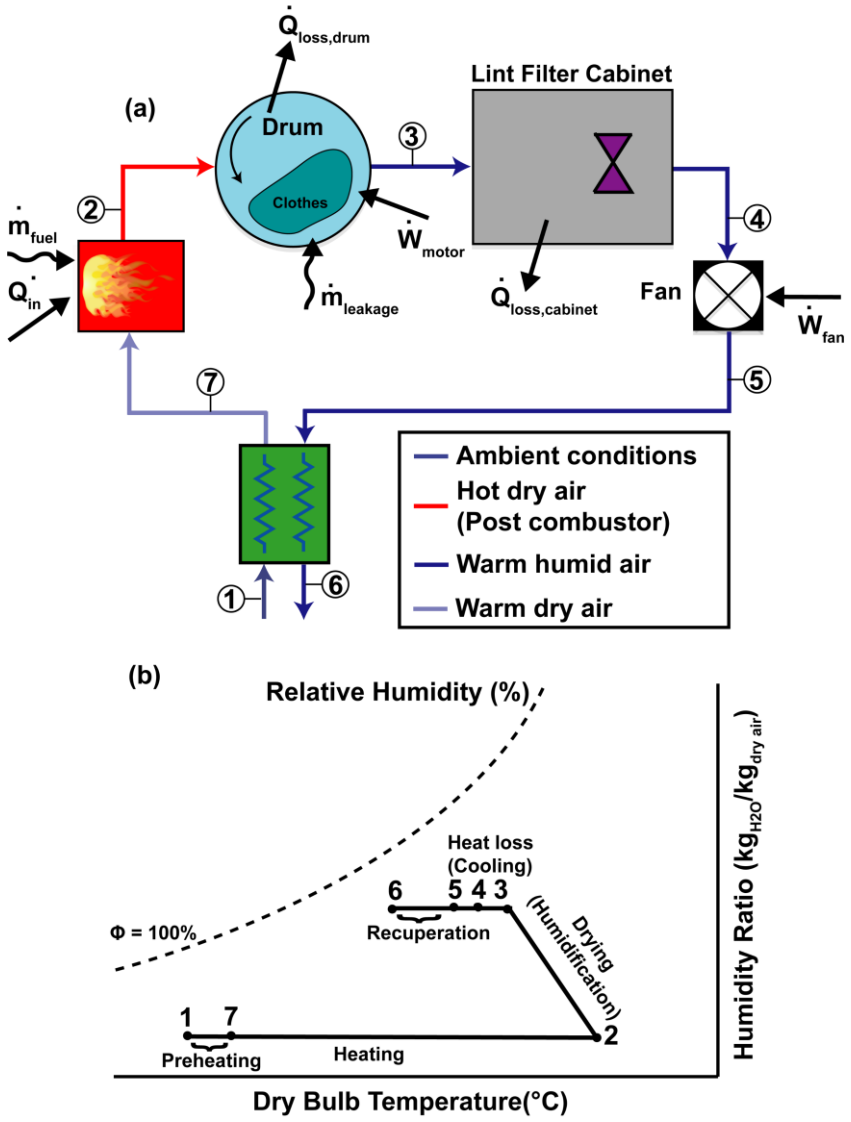

Figure 5.2: (a) Cycle schematic with waste heat recovery using an air-to-air cross flow heat exchanger (b) Psychrometric chart of recuperation drying cycle

$$LMTD = \frac{T_5 - T_7 \;-\; T_6 - T_1}{\ln\left[\dfrac{T_5 - T_7}{T_6 - T_1}\right]} \tag{5.8}$$

Equations (5.5), (5.6), and (5.7) are then used to fix State 7 and quantify the increase in the temperature of the air entering the combustor.

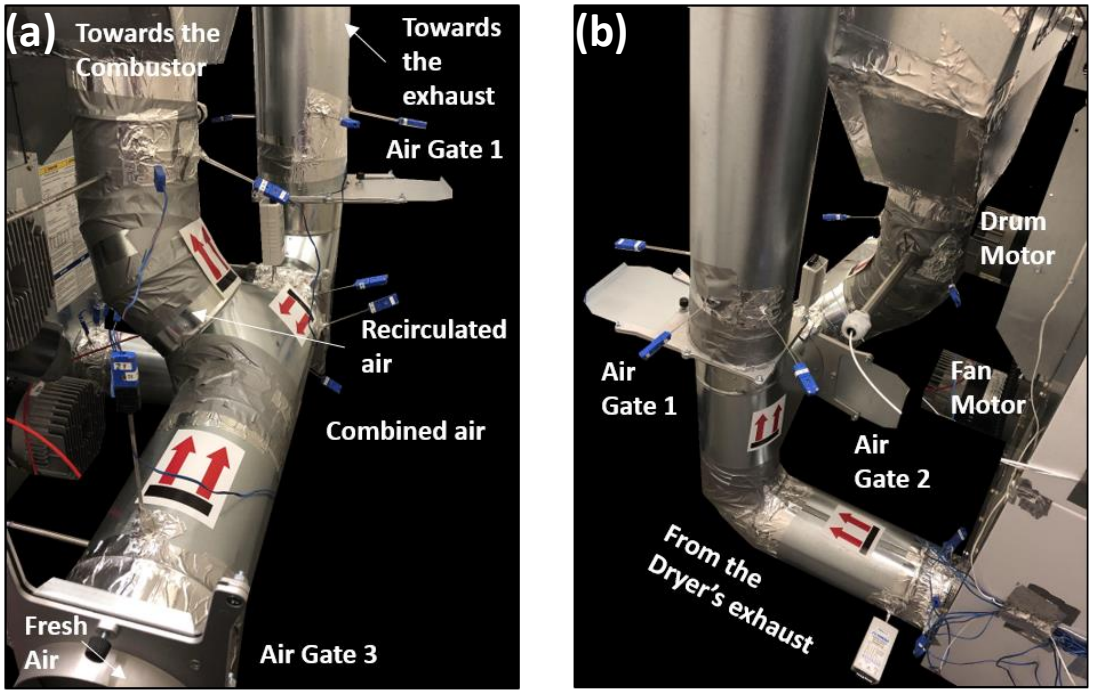

Figure 5.3: Experimental design for EGR (a) Inlet side (b) exhaust side of the EGR test set up

5.3 Experimental Approach

5.3.1 Recirculation Experiments

To test the effect of recirculation ratio, additional ducting was installed on the dryer's exhaust. The galvanized steel ducting has an outer diameter of 0.149 m. Figure 5.3a-b shows the modifications to the test facility to enable EGR.

To establish control on the volume of air recirculated, three air gates were installed at three different locations. Air Gate 1 was installed near the dryer exit duct to regulate back pressure. Air Gate 2 and an air damper were installed to regulate the volume of the air recirculated back. Finally, Air Gate 3 is installed on the intake duct to regulate the amount

of fresh air entering the combustor to maintain the same total volume of air as the baseline at the pre-combustor section. As shown in Figure 5.2b, the recirculated exhaust air from the dryer passes through Air Gate 2 and the damper where it mixes with the fraction of ambient air entering from Air Gate 3. The recirculated volumetric flow rate (State 7 on Figure 5.2a) is quantified by measuring the air velocity downstream of Air Gate 2:

$$\dot{V}_r = \frac{\pi D_d^2 V_r}{4} \tag{5.9}$$

A mass balance on the three branches (exhaust, recirculated, and exit) showed that air mass flow rate was conserved well within 4%. A detailed calculation of the recirculation ratio is presented in Appendix B. The recirculation ratios tested experimentally are shown in Table 5.1.

Table 5.1: Recirculation experiments test matrix

Experiment number	1	2	3	4
Recirculation ratio (%)	15 ± 3	30 ± 4	55 ± 5	75 ± 6

5.3.2 Recuperation Experiments

An air-to-air cross flow heat exchanger was installed on the gas-fired tumble dryer. Unlike the recirculation of exhaust air, this method is an open-loop circuit where there is no humid air being recirculated back to the drum. Figure 5.4 shows the CHX used in these experiments. The aluminum cross-flow heat exchanger weighs 6.3 kg and has additional headers on each of its four sides to facilitate airflow from the ducts to the heat exchanger. Additional details of the CHX are tabulated in Table 5.2.

Table 5.2: Recuperative heat exchanger characteristics

Parameter	Value
Material	Aluminum
Length	610 mm
Width	203 mm
Plate Spacing	8 mm
Mass	6.3 kg

The CHX was designed to maximize heat transfer while not exceeding the pressure drop that can be provided by the built-in fan. As shown in Figure 5.2a, air flows from the exhaust (State 5) through the heat exchanger to preheat the air sensibly, increasing its temperature without any increase in the humidity ratio. The humidity ratios at States 1 and 7 are equal. During the experiments, the flow rate of the fuel is held constant to maintain the same heat input at the combustor. Figure 5.5 shows the test facility used to assess the enhancement to the drying process that results from adding the recuperative heat exchanger. Figure 5.5a

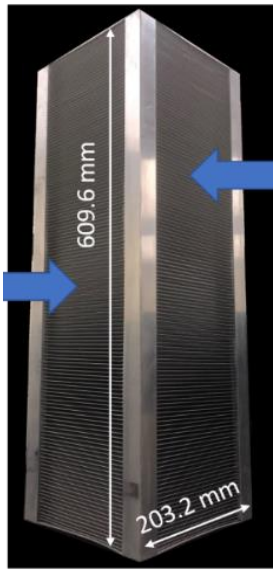

Figure 5.4: Plate-fin crossflow recuperative heat exchanger.

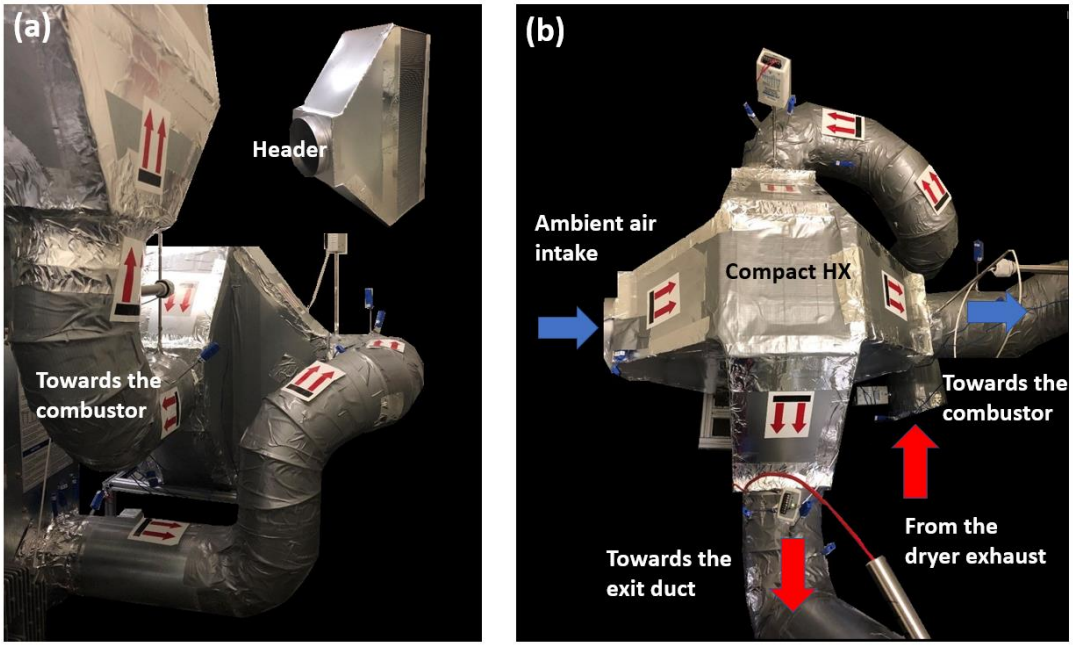

Figure 5.5: Experimental test set up for recuperation (a) side view (b) top view

shows path of the air flow from the exhaust to the heat exchanger. A close-up image of the headers used to transition the flow is shown in Figure 5.5a, while Figure 5.5b shows a top view of the compact heat exchanger. To quantify the heat duty of the heat exchanger, four T-type thermocouples, an air anemometer, and temperature and humidity transmitters were mounted on each inlet and outlet. To ensure repeatability of the experiments, each run was repeated three times. The procedure for data reduction and energy balance calculations on the recuperative heat exchanger is presented in Appendix C.

5.4 Results and Discussion

5.4.1 Exhaust gas recirculation

Figure 5.6 shows the air temperatures at the inlet of drum for the recirculation ratios tested. A steady state temperature is typically reached by t = 300 s. For the baseline run, the

average inlet air temperature to the drum was 185°C. As shown in Figure 5.6, as the recirculation ratio increases, the inlet temperature of the air to the drum increases slightly. The air inlet temperature for recirculation ratios 30% and 55% is higher than the baseline by minimum of 6°C and maximum of 12°C. However, at high recirculation ratio, for instance at $y_{RR} = 0.75$, the inlet temperature to drum decreases to 163°C.

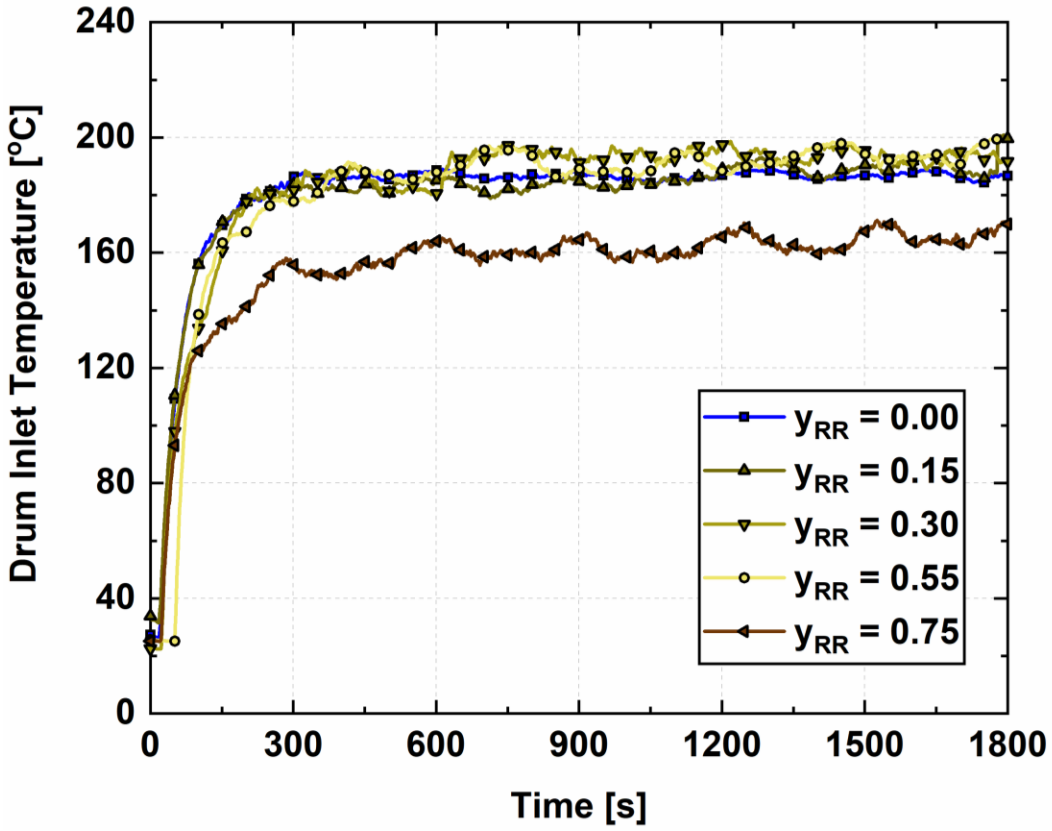

Figure 5.6: Drum inlet air temperature for different recirculation ratios (u_T = ± 0.25°C)

This is attributed mainly to the increase in the moisture content of the reactants of combustion, and lower amount of oxygen seen at the inlet of the combustor. The specific heat capacity of water vapor is ~ 88% higher than that of dry air, which leads to a decrease

in the temperature of the combustion gases. Typically, the exhaust gas is at high temperature and high humidity. As the recirculation ratio increases, the amount of water vapor in the combustion products also increases, which reduces the temperature of flue gases (products of combustion). Higher humidity increases the heat capacity of the reactants, which results in lower combustion temperatures. At low recirculation ratios, the air-to-fuel ratio in the combustor does not get affected significantly; therefore, due to having the reactants at higher temperatures than the baseline case, the temperature of the products also increased. For instance, at recirculation ratios of 30% and 55%, the average air inlet drum temperature was maintained at a temperature of 196°C. This increase in temperature at the inlet of the drum is favorable for evaporation. However, the higher the recirculation ratio, the higher the moisture fraction recirculated back into the dryer. High humidity ratio air being recirculated is unfavorable for evaporation because it minimizes the driving potential inside the drying drum, which is the difference in partial pressure of water vapor between the textile and the air in the bulk of the dryer. Gas-fired tumble dryers are sensitive to the recirculated moisture (humidity ratio), as it influences the drying performance at two locations, i.e., at the combustor, and at the drum. Figure 5.7 shows the influence of different recirculation ratios on drum exit air temperature. At recirculation ratios < 0.55, the average exit temperature increased slightly (by 3.8°C) due to fact that air inlet temperature also increased. The recirculated humidity is not high enough to significantly influence the temperature entering the drum as depicted in Figure 5.6. However, at high recirculation ratio (y_{RR} ~ 0.75), the exit air temperature drops on average by 4.6°C as compared to the baseline case. This is primarily due to the fact that at the inlet of the drum, the air is at a significantly lower temperature, by about 20°C, than the base

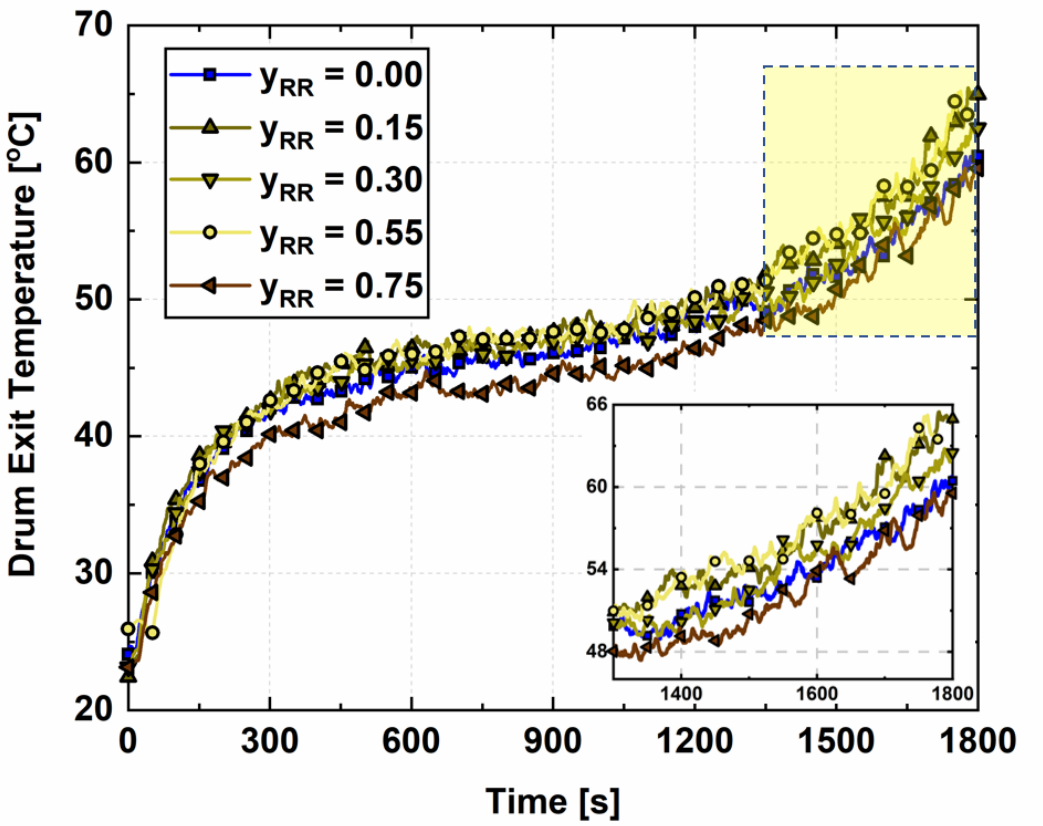

Figure 5.7: Drum exit air temperature for different recirculation ratios (u_T = ± 0.25°C)

case. It is important to note that this model is validated experimentally for recirculation ratios ranging from 0% to 75%. Therefore, the simulated results for higher recirculation ratios, i.e., $0.8 < y_{RR} \leq 1$, would require further validation due to the limitations of the model at high recirculation ratios.

Figure 5.8a shows the measured textile moisture content for each of the recirculation ratios tested. For low recirculation ratios, the slope of the moisture content with time is steeper than that of the moisture content for the base case. The increase in the air inlet temperature increased the overall evaporation rate, and the increased humidity was not high enough to hinder evaporation appreciably. For instance, at a recirculation ratio of

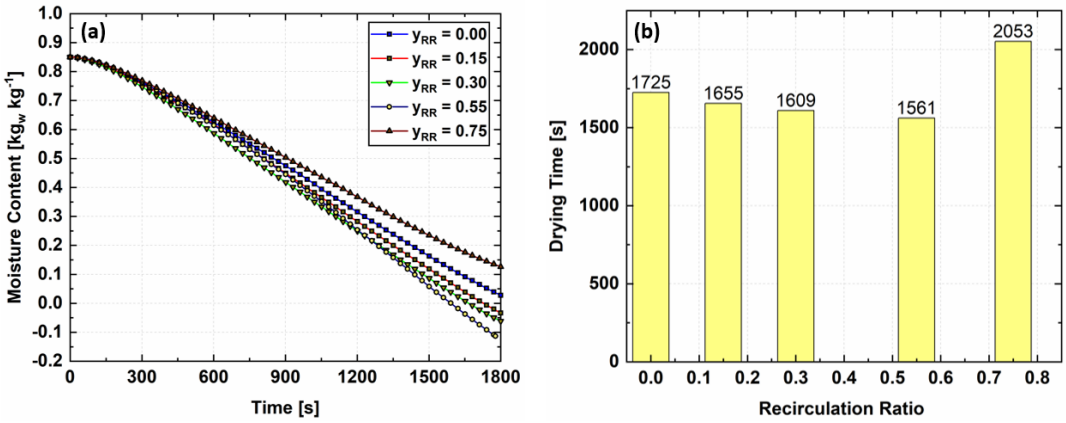

Figure 5.8: Experimental comparison of (a) instantaneous moisture content (b) drying time

30%, an increase in the inlet temperature by 10.1°C resulted in an increase in the evaporation rate by 9.8%. By the end of the drying experiment at t = 1800 s, the moisture content achieved for recirculation ratios of 0%, 30%, and 75% was 2.8%, -2.1%, and 12.6%, respectively. A negative moisture content signifies that the final mass of terrycloth towels is less than the initial dry mass. This occurs when the actual bone-dry mass of the terrycloth towels is less than the initial dry of mass because it is typically in equilibrium with the partial pressure of water vapor in the ambient air. The change in sign as the recirculation ratio increases from 30% to 75% indicates that the evaporation rate decreases significantly, resulting in a wet load $\left(X_f = 12.6\%\right)$. Figure 5.8b shows the drying time for each of the recirculation ratios. The drying time shows a minimum at a recirculation ratio of 0.55. Because the cycle ends after 1800 s, the drying time was extrapolated for a recirculation ratio of 75%.

Figure 5.9 shows a comparison between predicted and measure drying efficiencies. The model predicts that the optimal drying efficiency $\left(\eta_d = 46.2\%\right)$ will be achieved at a

recirculation ratio of 51%, which is in good agreement with the experiments. At recirculation ratios exceeding 70%, the overall efficiency is always lower than that of the baseline due to high amount of humidity and combustible gases being recirculated. The model slightly over predicts the measured drying efficiency due to the assumption that the recirculated gas is composed of only water vapor and carbon dioxide, ignoring other minor combustion products that might affect dryer performance. Nonetheless, the model shows good agreement with the experimental data, with an AAD of 3.7%.

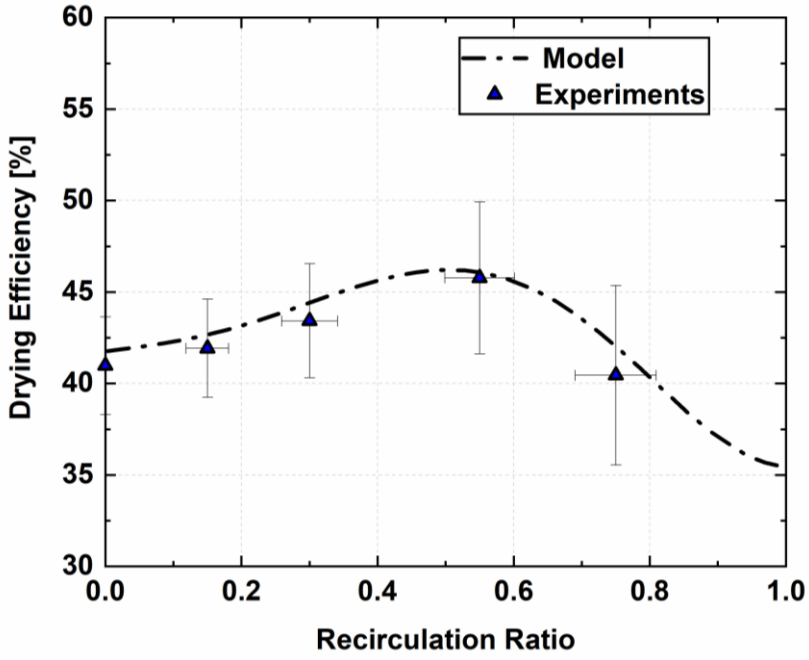

Figure 5.9: Comparison of predicted and measured drying efficiency for different recirculation ratios

5.4.2 Recuperation

Figure 5.10 shows the variation of the inlet and outlet temperatures of the recuperative CHX. The cold-side inlet of the CHX is the ambient air entering the cycle. The air outlet

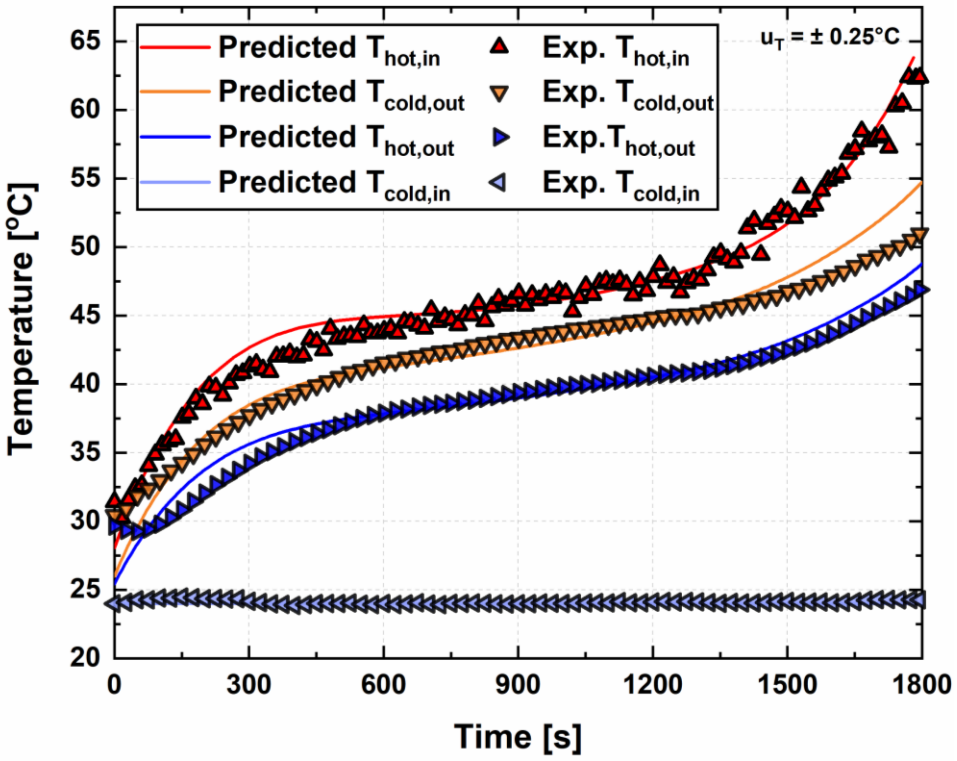

Figure 5.10: Comparison of predicted and measure temperatures at the inlets and outlets of the crossflow heat exchanger

temperature of the cold-side was increased to a minimum of 29°C during the first phase of drying and reached 50°C by the end of the cycle. Preheating the inlet air led to increases in the air temperature at the inlet of the drum. The inlet temperature of the drum was increased from 197°C to 212°C. This resulted in a 14.7% higher evaporation rate in the drum compared to the baseline. The four temperatures at the inlet and outlet of the CHX were compared with the predicted values. The model neglects the thermal storage in CHX walls, which is appreciable when the exhaust temperature is changing rapidly, as occurs in the first and third phases of drying. Overall, the model showed good agreement with the data, with an AAD of 6.9%.

Table 5.3: Performance summary for energy recovery methods

	Drying time (s)	Drying efficiency (%)	SMER (kWh kg^{-1})	Energy Saved (%)
Baseline	1725	41.2	1.45	-
Recirculation $(y_{RR} = 0.55)$	1561	45.1	1.32	9.4
Recuperation	1509	48.3	1.24	14.6

5.4.3 Energy Savings Comparison

Figure 5.11 shows the instantaneous moisture content of the optimal recirculation, recuperation, and baseline cases. In the recuperation experiments, the air enters the drum at high temperatures with no additional moisture; therefore, the moisture content decreases faster than for both baseline and the recirculation experiments. The average rates of decrease of moisture content for the recuperation, recirculation, and baseline cases are 5.6 $\times 10^{-4}$ s^{-1}, 5.2 $\times 10^{-4}$ s^{-1}, and 4.6 $\times 10^{-4}$ s^{-1}, respectively.

The drying time is directly influenced by the evaporation rate $(\sim dX/dt)$; therefore, at higher evaporation rates, the drying time is shorter. Table 5.3 summarizes the effect of the different energy saving methods considered here on drying efficiency, SMER, and drying time. A reduction in drying time was achieved in both scenarios. The drying time for the recuperation and recirculation cases showed a reduction of 12.5% and 9.5%, respectively as compared to the baseline case. The change in the drying efficiency is directly proportional to the change in the evaporation rate as given by Equation 15. Therefore, the evaporation rate increased by 8.9% when 55% of the exhaust gas was recirculated, while the evaporation rate increased by 16.1% when the dryer was connected

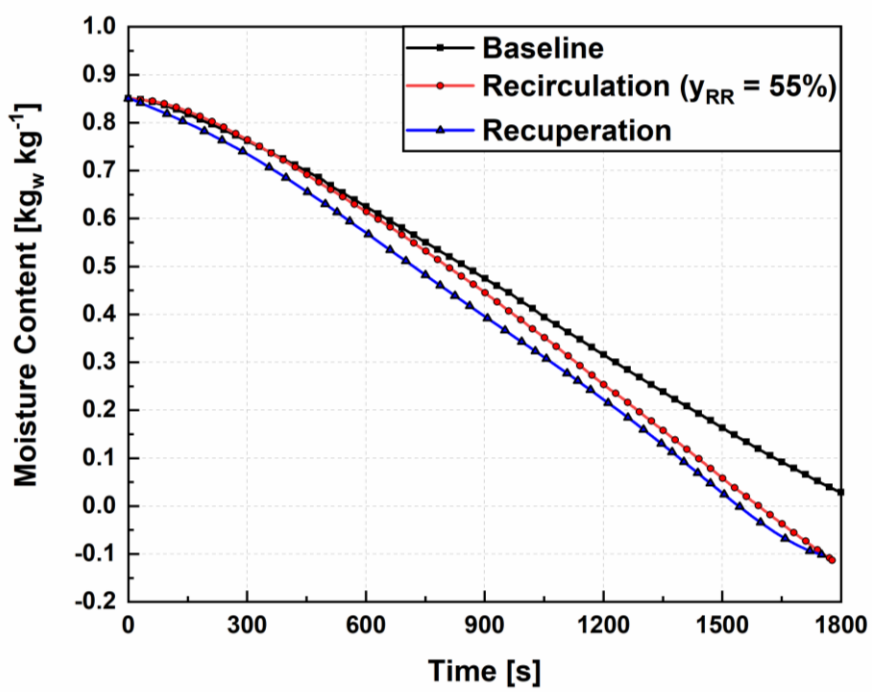

Figure 5.11: Comparison of demonstrated moisture content for energy recovery experiments.

to the CHX. The energy savings tabulated in Table 5.3 are based on the SMER. The percentage energy saving for each of the methods, is expressed by Equation (5.10):

$$\%ES = \frac{SMER_{enhanced} - SMER_{base}}{SMER_{base}} \times 100 \tag{5.10}$$

Recuperation was able to save significantly higher energy due to the absence of recirculated moisture that hinders evaporation and delays drying.

5.5 Conclusion

Recovery of waste heat from a commercial gas-fired tumble dryer through exhaust gas recirculation and recuperative heat exchange was investigated numerically and experimentally. Models accounting for the underlying heat and mass transfer processes

were validated through the experiments, and agreed well with the experiments for the baseline and waste heat recovery cases. For the baseline case, the model shows good agreement in predicting the drum exit air temperature, humidity ratio, the moisture content, and evaporation rate, with AADs of 6.6%, 7.2%, 1.2% and 3.2%, respectively.

In both methods, the combustor duty was fixed, while the drying time was varied to achieve the desired textile moisture content. The energy savings based on the SMER for recirculating 55% of the exhaust gas is 9.4%, while the demonstrated energy savings with recuperation is 14.6%. In such commercial tumble dryers, energy consumption and drying time are significant parameters. The drying time was reduced by 164 s and 216 s over the baseline when using exhaust recirculation and recuperation, respectively. It is important for the consumer to achieve the desired dryness of the textile load in the shortest time possible. In addition, it is financially beneficial for laundromats and other businesses to minimize drying time. The significant challenge of reducing energy consumption while also reducing drying time was accomplished and experimentally demonstrated through the techniques used in this study.

CHAPTER 6. ADSORPTION-BASED THERMAL ENERGY STORAGE

A novel adsorption-based thermal energy storage system is integrated into a gas-fired dryer here. An adsorbent bed is used to capture waste heat from the exhaust stream, store, and reuse it in the current and subsequent drying cycles. A heat and mass transfer model is developed to capture the dynamics of the thermal storage system, and validated experimentally on a 11.33-kg capacity gas-fired tumble dryer.

6.1 Introduction

Heat pump dryers can integrate vapor compression (Yadav and Moon, 2008a; Bansal et al., 2010b) or absorption (Ameen and Bari, 2004; Do et al., 2013; Walmsley et al., 2017; T'Jollyn et al., 2019) cycles. Cao et al. (2014b) proposed a two-stage vapor compression-based heat pump dryer and achieved 59% energy savings when compared to a conventional air-vented electrical dryer. TeGrotenhuis et al. (2017) investigated a hybrid heat pump dryer that demonstrated a 50% reduction in energy consumption. However, the drying time increased by 60%. Previous studies have shown that absorption-based heat pump dryers can reduce energy consumption by ~ 20% (Goh et al., 2011; T'Jollyn et al., 2019). Solid-state thermoelectric dryers offer a promising alternative to heat pump dryers, and also eliminate the use of working fluids with high global warming potential; however, despite significant energy savings (~50-60%) potential, the significant increase (Patel et al., 2018) in drying time is a major drawback. Ahmadi et al. (2021) proposed a membrane-based lithium bromide (LiBr) gas clothes dryer in which the waste latent heat in the exhaust stream is reclaimed, and showed an improvement in the combined energy factor (CEF), a

figure of merit they defined as the ratio of the dry mass load to the total energy input of the dryer, by 112% compared to an air-vented gas-fired dryer.

Another approach to save energy in appliances is through the use of adsorbent beds. Integrating compact adsorption beds systems into wet appliances is still in the early stages of development (Vasta et al., 2018). Hauer and Fischer (2011) developed an open-adsorption system for a dishwasher in which thermal energy from hot water is reversibly stored in a zeolite cartridge, which is regenerated during the washing stages, yielding a 25% energy savings. Another study investigated integrating a sorption bed with a dryer. Cranston et al. (2019) used a silica-supported ionic liquid composite material located between the evaporator and condenser of a heat pump dryer. The integration of the sorption bed to the heat pump dryer reduced the overall energy consumption by 6.9%. An additional resistance heater was used to regenerate the 3-kg sorption bed.

Adsorption systems can be used for heat pumping and storage in various thermal processes. Energy storage can bridge the gap between the supply and demand of energy at different phases of the drying process, providing significant cost savings, and reducing the environmental impact. An open-adsorption thermal energy storage (TES) system is well suited when water is the adsorbate, because it can communicate directly with the moisture in the ambient air. This work proposes a novel adsorption-based thermal energy storage system integrated within a commercial gas-fired tumble dryer to reduce energy consumption and drying time simultaneously. In the novel system, no additional energy input is needed to regenerate the adsorbent bed. The thermal energy in the exhaust stream, which is usually rejected to the ambient, is stored in the adsorbent bed to be used in subsequent drying cycles.

6.2 System Overview

Figure 6.1 shows a representative temperature profile of the air exiting the dryer. The shape of the temperature profile offers opportunities to further save and store the energy at the end of the drying cycle. Initially, the wet load must be heated up to a temperature at which evaporation starts (Stage I). As the drying cycle continues, most of the moisture evaporates from the textile (Stage II) in a relatively constant temperature phase. Towards the end of the drying cycle, the input energy is used to raise the air temperature further to evaporate the water trapped in internal pores of the textile (Stage III). Finally, the heater/combustor is turned OFF to prevent excessive temperatures for safe handling (Stage IV). The energy input at the end of the drying cycle is used to evaporate less 5% of the moisture content, and this heat can be stored using an adsorbent bed and reused in subsequent drying cycles to reduce energy consumption.

The adsorption-based thermal energy storage system investigated here employs an innovative approach of capturing the waste heat from the exhaust of a gas-fired tumble

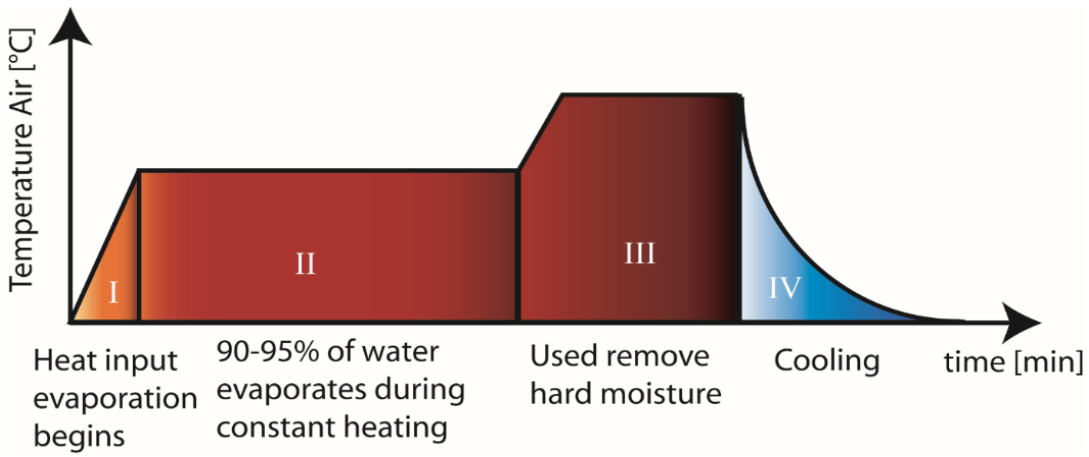

Figure 6.1: Schematic of typical temperature profile of air leaving the dryer

dryer and storing it for use in subsequent drying cycles. Unlike previous systems, no additional energy sources are required to regenerate the adsorbent bed; it is regenerated by the same exhaust stream that charges it. Furthermore, continuous operation is achieved with a single adsorbent bed. Figure 6.2 shows a schematic of the proposed system during the adsorption (Figure 6.2a) and desorption (Figure 6.2b) phases. During the initial stages of drying, warm humid air exiting the exhaust of the dryer (State 6) enters the adsorbent bed to initiate adsorption. The water vapor within the humid air is adsorbed onto the surface of the adsorbent material, which is accompanied by the release of the heat of adsorption. This results in hot dry air at the outlet of the adsorbent bed (State 7), which is ideal for the drying process. This return air is then mixed with the intake air at the inlet of the dryer. Towards the end of the drying process, air exiting the dryer (State 4) increases significantly in temperature while its humidity decreases. This decrease in water vapor partial pressure marks the transition from the adsorption phase to the desorption phase. During desorption, the adsorbent bed is regenerated by the hot dry air leaving the dryer in the last stages of the drying cycle. The hot dry air passes over the adsorbent, causing desorption of water vapor from the surface, which regenerates the bed for the next cycle. Integrating an adsorbent bed with the dryer increases the temperature of the air entering drum while decreasing its moisture content. After the first drying cycle, the thermal energy is stored in the form of thermochemical potential rather than being rejected to the ambient. The thermal energy is stored and reused in the next drying cycle to preheat the inlet air. This TES system uses water as the adsorbate and silica gel as the adsorbent.

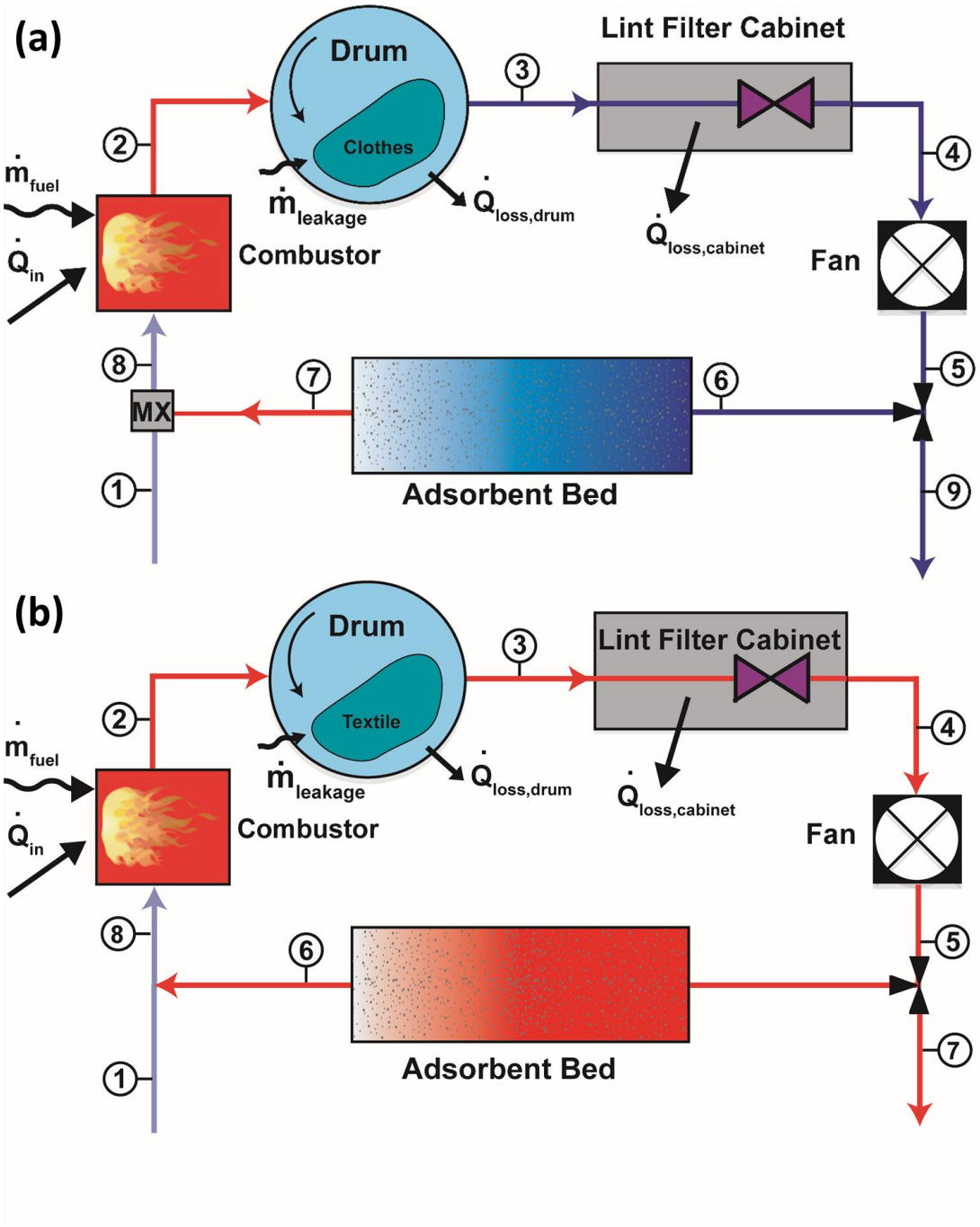

Figure 6.2: Schematic of the system showing (a) adsorption (b) desorption processes

6.3 Mathematical Model

The present study focuses on a transient thermodynamic model of a gas-fired tumble dryer with an integral adsorption-based TES system. The thermodynamic model is

implemented on the Engineering Equation Solver (Klein, 2020a) platform. A summary of the model is presented here. A submodule for the adsorption bed is developed and coupled to the dryer module to predict the overall performance metrics such as specific moisture extraction ratio (SMER), drying efficiency, and drying time. Figure 6.3 shows a block diagram of the drying and adsorption modules.

6.3.1 Dryer Module

Drying occurs in the drum where the hot dry air exiting the combustor transfers heat to the tumbling textile. The evaporation process involves simultaneous heat and mass transfer between the hot dry air and the wet textile. The mass transfer rate at the surface of the wet textile is given by Equation (6.1):

$$m_{cl,dry}\frac{dX}{dt} = h_m A_{cl}\left(\alpha_{cl}\omega_{cl}^{surf} - \omega_4\right) \tag{6.1}$$

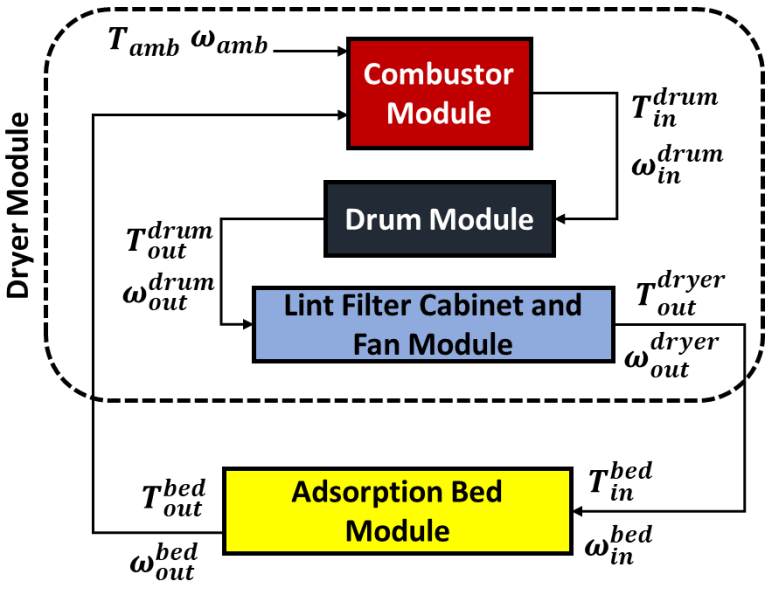

Figure 6.3: Flow diagram showing two interactive modules to predict system performance

where α_{cl} is the water activity coefficient that is a function of the moisture content and type of textile as defined by Lambert et al. (1991), and ω_{cl}^{surf} is the saturated humidity ratio of the air at the surface of the textile. An energy balance on the drum is given by Equation (6.2):

$$\left(m_{cl,dry}c_{p,cl} + Xm_{cl,dry}c_{p,w} + m_d c_{p,d}\right)\frac{dT_{cl}}{dt} = -\dot{Q}_{loss} + \dot{m}_3 h_3 + \dot{m}_l h_l - \dot{m}_4 h_4 \qquad (6.2)$$

where $\dot{Q}_{loss}$ is the heat lost from the drum through natural convection and radiation . The air leakage into the drum, $\dot{m}_l$, is quantified based on the work of Boudreaux et al. (2020). The heat transfer between the air and the wet textile is given by Equation (6.3):

$$\left(c_{p,cl} + Xc_{p,w}\right)m_{cl,dry}\frac{dT_{cl}}{dt} = h_h A_{cl}\left(T_3 - T_{cl}\right) - \dot{m}_e h_{fg}\left(T_{cl}\right) \qquad (6.3)$$

The effective area-heat $\left(h_h A_{cl}\right)$ and area-mass $\left(h_m A_{cl}\right)$ transfer coefficients used in Equations (6.1) and (6.3) were quantified from measurements in the present study similar to the work of Gluesenkamp et al. (2019) and described in Chapter 3. After determining the exit conditions of the drum, energy and mass balances are applied to lint filter and the fan to calculate the exit conditions of the dryer. The dryer exit conditions are then used as the inlet of the adsorbent bed module.

6.3.2 Adsorbent Bed Module

The mathematical modeling of the fluid flow through the adsorbent bed is presented here. The performance of the gas-fired tumble dryer with an adsorption TES system depends primarily on the adsorbent bed geometry. The adsorbent bed should be designed

to enable high heat transfer rates. Also, the bed should be sized in accordance with the allowable pressure drop of the blower that drives air flow through the dryer. Three types of bed are commonly investigated in the literature, packed bed, coated channels, and annular coated tubes (Chi and Wasan, 1970; Demir et al., 2008; Raymond and Garimella, 2011; Krönauer et al., 2015; Calabrese et al., 2018). Packed adsorbent beds are filled with loose adsorbent particles. They have good permeability and mass transfer characteristics, but often can suffer from poor contact of particles as well as low effective thermal conductivities, which result in high effective conduction resistances within the packing if the bed is poorly designed. A detailed model is developed to design the adsorbent bed with a packed bed geometry. Due to the fact that the working fluid and heat transfer fluid are the same in this case, the packed bed geometry is the preferred choice since the humid air is in direct contact with the adsorbent without any extra resistance such as in the annular fin adsorbent beds. Design parameters include length of the bed, mass of the adsorbent, and residence time of the bed before switching from adsorption to desorption stages.

Figure 6.4 shows the computational domain and the differential control volume (dV) of the adsorbent bed module. The energy and species conservation equations are applied to a differential control volume of an adsorbent packed bed filled with spherical silica gel particles. The following assumptions were made:

- The adsorbent has no affinity for species other than water.
- The air velocity in the packed bed is uniform along the radial direction, and the air flow is only in the axial direction i.e., $\vec{v} = U(x)\hat{i}$.
- The bed porosity is uniform.

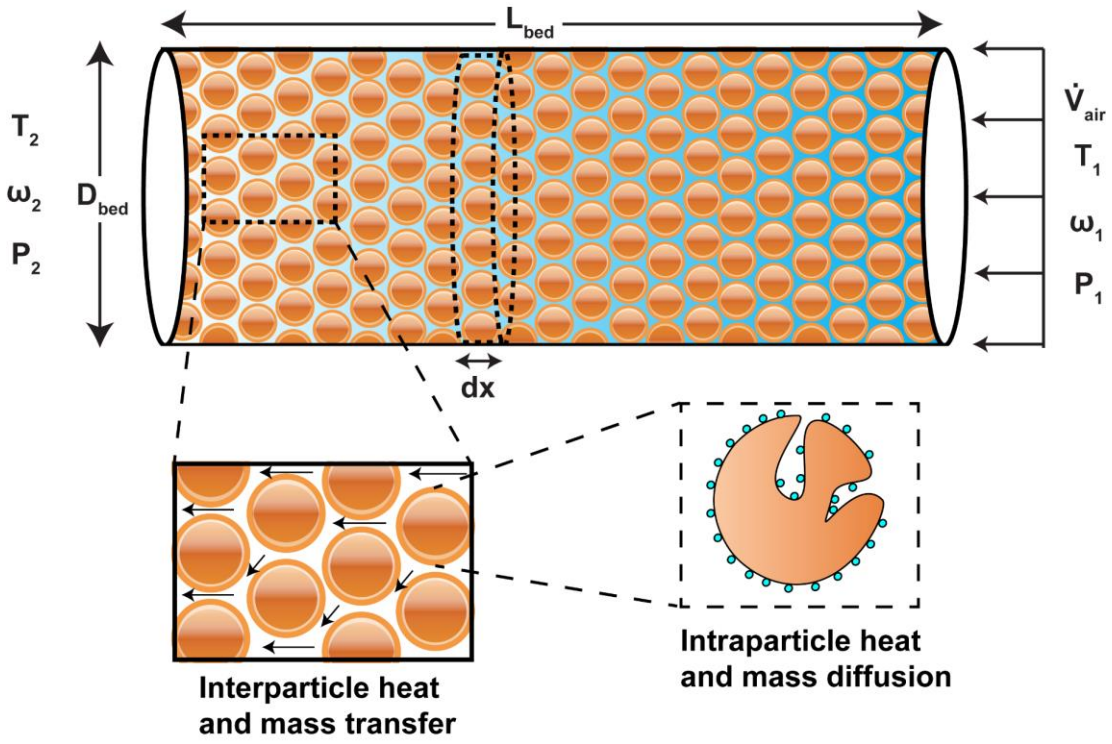

Figure 6.4: Computational domain for the adsorbent bed module showing inter- and intraparticle heat and mass transfer

- The pressure drop along the length of the bed has no significant effect on the properties of the air.
- The heat loss from the adsorption bed is negligible.
- Axial heat conduction in the walls of the bed is negligible.

The moisture balance in the gas stream is given by Equation (6.4):

$$\varepsilon\rho_a \frac{\partial\omega_a}{\partial t} + \rho_a U \frac{\partial\omega_a}{\partial x} + \rho_s \left(1-\varepsilon\right)\frac{dq}{dt} = 0 \qquad (6.4)$$

where ε is the porosity of the adsorbent bed, ρ_a is the density of the air, and ρ_s is the density of the adsorbent. Applying a moisture balance on the surface of the solid adsorbent results in:

$$\frac{dq}{dt} = \frac{\tilde{h}_m A_s}{\rho_s (1-\varepsilon)} (\omega_a - \omega_s) \tag{6.5}$$

where A_s is the specific surface area of the adsorbent bed and $\tilde{h}_m$ is the convective mass transfer coefficient. Applying energy conservation to the gas phase in the adsorbent bed results in the following:

$$\frac{\partial T_a}{\partial t} + \frac{U}{\varepsilon}\frac{\partial T_a}{\partial x} + \frac{\tilde{h}_h A_s}{\rho_a \varepsilon c_{p,a}}(T_a - T_s) - \frac{1-\varepsilon}{\varepsilon}\frac{\rho_s}{\rho_a}\frac{dq}{dt}(T_a - T_s) = 0 \tag{6.6}$$

where $\tilde{h}_h$ is the convective heat transfer coefficient in the adsorbent bed. An energy balance on the solid phase in the differential control volume of the silica gel packed bed results in Equation (6.7):

$$(1-\varepsilon)\rho_s c_{p,s}\frac{\partial T_s}{\partial t} = k_{eff}\frac{\partial^2 T_s}{\partial x^2} + \Delta H_{ads}\tilde{h}_m A_s(\omega_a - \omega_s) - \tilde{h}_h A_s(T_s - T_a) \tag{6.7}$$

where k_{eff} is the effective thermal conductivity, which is expressed as the geometric mean of the thermal conductivities of air (k_a) and silica gel (k_{ads}) (Bjurström et al., 1984):

$$k_{eff} = k_a^{\varepsilon} k_{ads}^{1-\varepsilon} \tag{6.8}$$

The thermal conductivity of silica gel is a function of the water content adsorbed by the solid pellet and can be expressed by Equation (6.9) (Kafui, 1994):

$$k_s\left(q,T_s\right)=0.37+0.97q+0.0014T_s \tag{6.9}$$

The average silica gel pellet is 3 mm in diameter; additional properties of the adsorbent bed are summarized in Table 6.1. Figure 6.5a shows the variation of thermal conductivity as a function of water uptake. The effective thermal conductivity of the silica gel bed over the range of water uptake under consideration is ~ 0.23 W m^{-1} K^{-1}.

The isosteric heat of adsorption released by silica gel during the adsorption phase was reported by Pesaran and Mills (1987a) and is given by Equation (6.10):

$$\Delta H_{ads}\left(q\right)=\begin{cases}3500-12400q & \text{if } q\le 0.05\\ 2950-1400q & \text{if } q>0.05\end{cases} \tag{6.10}$$

A curve fit to experimental data was developed by Pesaran and Mills (1987b) and resulted in a fourth order polynomial for the isotherm of silica gel type RD. The isotherm was identified by collecting humid air in equilibrium with silica gel at water content in the range of 0.08 – 0.38 $kg_w kg^{-1}_{\text{dry silica gel}}$. The equilibrium relative humidity is expressed as $RH_s=\sum_{i=0}^{4}a_i q^i$ (Figure 6.5b), where the polynomial regression constants are given by Table 6.2. The silica gel used in the adsorbent bed connected to the dryer has a porous structure

Table 6.1: Regression constants of the saturated relative humidity

Constants	Value
a_1	0.0078
a_2	-0.05759
a_3	24.16554
a_4	-124.478
a_5	204.226

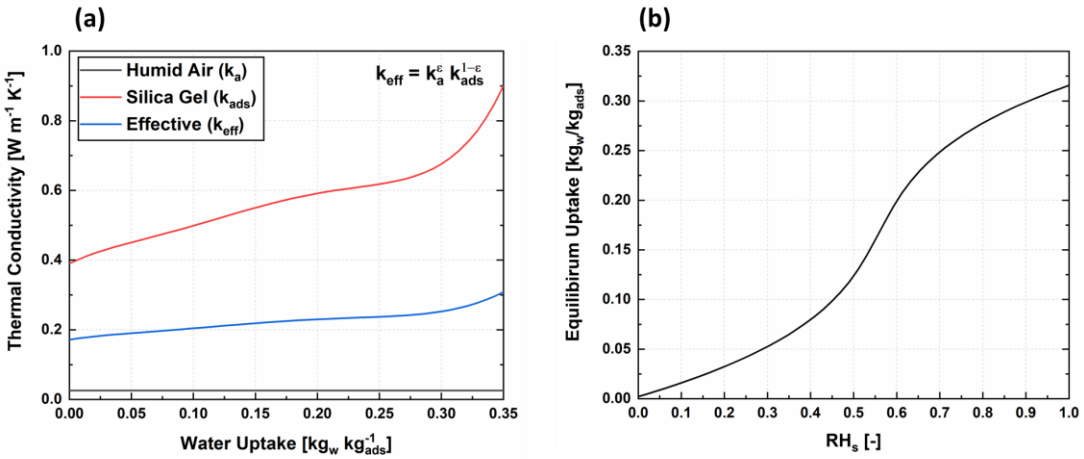

Figure 6.5: (a) Effective thermal conductivity and (b) isotherm of silica gel type RD

with affinity to water vapor. Silica gel Type RD has a type II isotherm. An advantage of a type II isotherm is that desorption does not require an air temperature higher than that of the solid silica gel pellets. Thus, an adsorbent bed filled with spherical silica gel type RD can reduce the energy required to regenerate the bed (Lee et al., 2020). The criteria used to select a suitable adsorbent during the screening study were a low regeneration temperature (~ 55 – 65°C), water vapor affinity, and cost. Having a Type II isotherm was definitely advantageous due to high water vapor uptake at the operating conditions, but the selection was not based on type of the isotherm, rather on the water vapor uptake capacity. Additionally, to keep the cost low, commercially available silica gel Type RD was used. The equilibrium relative humidity and the silica gel temperature are used to quantify the equilibrium moisture content of the air in the vicinity of the silica gel pellets, which can be expressed using Equation (6.11):

$$\omega_s = 0.622 \frac{RH_s \, P_{sat}(T_s)}{P - 0.378 RH_s \, P_{sat}(T_s)} \tag{6.11}$$

Table 6.2: Properties of the silica gel packed beds

Property	Value	Unit
Density (ρ_s)	1128	kg m^{-3}
Average pellet diameter (d_p)	3.0	mm
Bed porosity (ε)	0.32	-
Thermal conductivity (k_s)	$0.37 + 0.97q + 0.0014T_s$	W m^{-1} k^{-1}
Specific heat capacity ($c_{p,s}$)	$4186q + 921$	J kg^{-1} K^{-1}

The convective heat and mass transfer coefficients for a cylindrical packed bed of spherical particles are quantified using Equations (6.12) and (6.13) based on the correlations developed by Hougen and Marshall (1947), respectively:

$$\frac{\tilde{h}_h}{\rho_a U c_{p,a}} = 0.683\,\mathrm{Re}^{-0.51} \tag{6.12}$$

$$\frac{\tilde{h}_m}{\rho_a U} = 0.704\,\mathrm{Re}^{-0.51} \tag{6.13}$$

where Re is the Reynolds number based on the adsorbent pellet diameter, $\mathrm{Re} = \rho_a U d_p / \mu_a$. The set of differential equations (Equations (6.4) – (6.7)) has four unknown parameters T_a, T_s, ω_a, and q. To close the set of couple differential equations, the initial and boundary conditions are given by Equations (6.14) – (6.19):

$$T_a\left(x, t=0\right) = T_{amb} \tag{6.14}$$

$$T_s\left(x, t=0\right) = T_{amb} \tag{6.15}$$

$$\omega_a\left(x, t=0\right) = \omega_{amb} \tag{6.16}$$

$$q\left(x, t=0\right) = q_{amb} \tag{6.17}$$

$$T_a\left(x=0, t\right) = T_{out}^{dryer} \tag{6.18}$$

$$\omega_a\left(x=0, t\right) = \omega_{out}^{dryer} \tag{6.19}$$

The pressure drop in the packed bed filled with spherical silica gel particles is quantified using Ergun's equation (Nemec and Levec, 2005; Koekemoer and Luckos, 2015):

$$-\frac{dP}{dx} = \frac{150\mu}{d_p^2}\frac{\left(1-\varepsilon\right)^2}{\varepsilon^3}U + \frac{1.75}{d_p}\frac{\left(1-\varepsilon\right)}{\varepsilon^3}U^2 \tag{6.20}$$

This set of coupled, non-linear partial differential equations are solved using an explicit forward difference scheme using Engineering Equation Solver (EES) (Klein, 2020a) software. A time step of 10^{-2} s and an axial step of 0.1 mm is used to ensure numerical stability and grid independence.

6.4 Experimental Protocol

A Speed Queen series commercial gas-fired tumble dryer (~11.33 kg dry capacity) is used to experimentally validate the transient thermodynamic and heat and mass transfer models developed for integrating the drying process with the adsorption-based TES system. This test facility is also used to evaluate the effect of the adsorbent mass on the energy savings achieved by integrating an adsorbent bed. To monitor the drying process accurately, thermocouples, pressure transducers, relative humidity sensors, air velocity anemometers, and wireless temperature and humidity data loggers were installed on the facility. Details of these sensors, actuators, and loggers installed in the dryer are provided

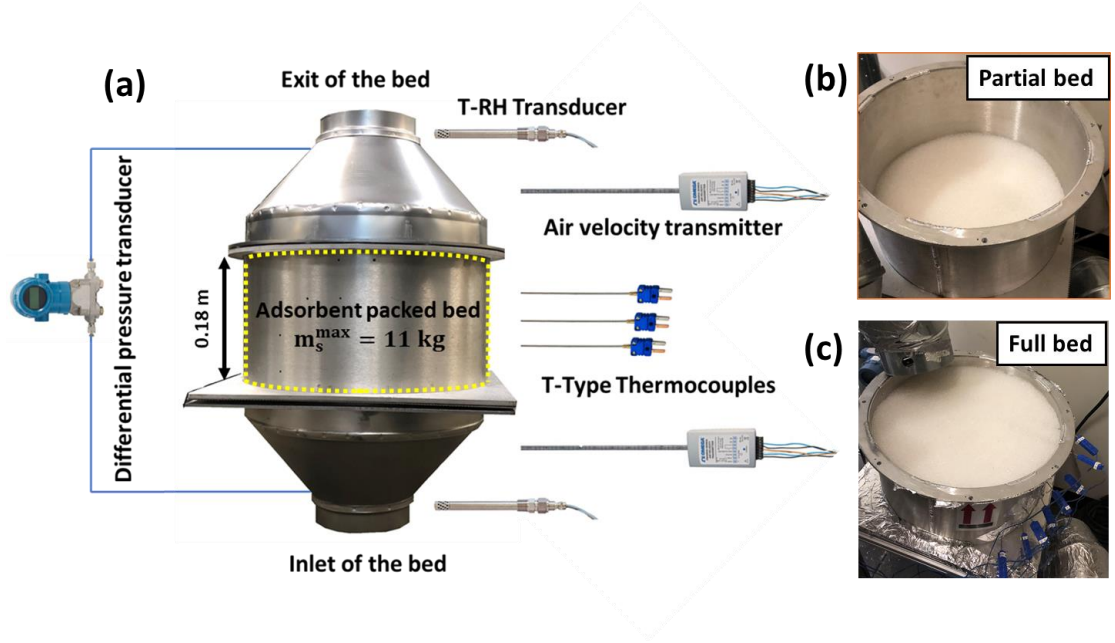

Figure 6.6: Adsorbent bed with sensors, actuators, and loggers; (b) partially filled adsorbent bed mads = 5 kg; (c) full bed filled with adsorbent mads = 11 kg

in Chapter 4. Figure 6.6a depicts a block diagram of the fabricated adsorbent bed including the sensors and actuators. The adsorbent bed is manufactured from 3.175-mm thick walls. This wall thickness minimized the thermal mass for transitioning between adsorption and desorption phases while still offering adequate structural strength. The adsorbent bed was designed with a variable length to assess the effect of mass of adsorbent on drying performance. Figure 6.6b and 6c show the bed filled with 5 kg $\left(L_{bed} = 0.07 \text{ m}\right)$ and 11 kg $\left(L_{bed} = 0.18 \text{ m}\right)$ of silica gel, respectively. The bed was coupled to the dryer by connecting the inlet header to the exit of the dryer. Appendix D presents details on incorporation of the adsorbent bed into the dryer.

Figure 6.7 shows the experimental facility. Prior to connecting the adsorbent bed to the dryer, the packed bed was filled with the desired mass of adsorbent and sealed using

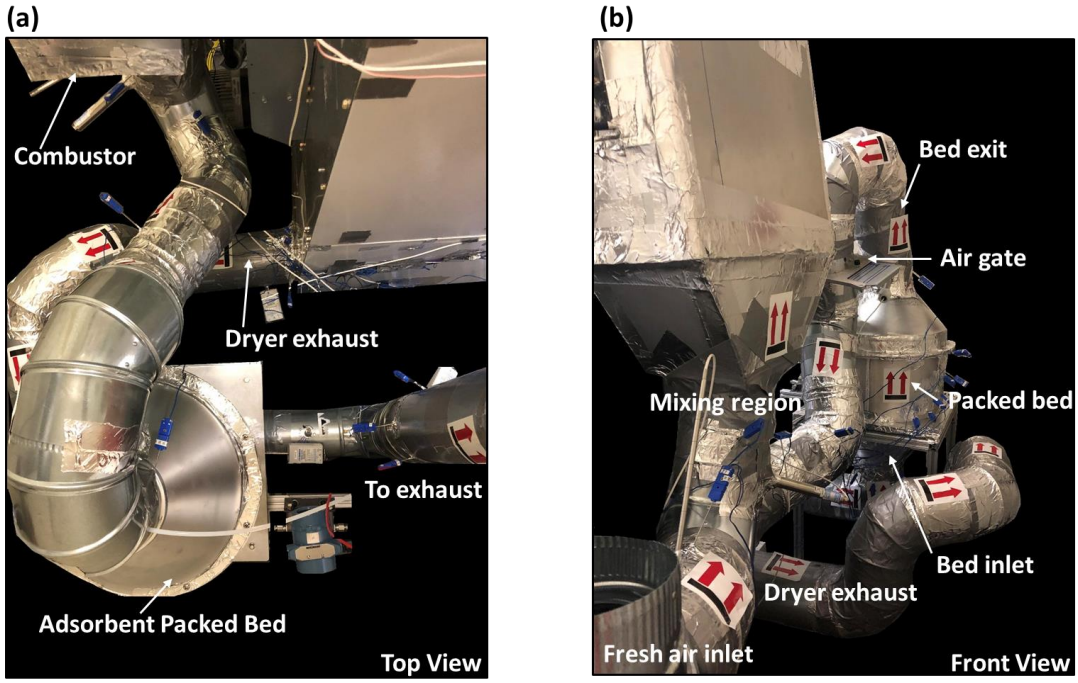

Figure 6.7: Experimental facility (a) top view; (b) front view

bolts on the inlet and outlet headers. The baseline operating conditions are outlined in Table 6.3. To ensure repeatability of the experiments, a standard textile load of 7.66 kg of terrycloth towels was used. A commercial washer extractor initializes the load to a repeatable moisture content of 85 ± 2%. Before adding the wet textile to the dryer, the bed is initialized by purging ambient air through the system. The drying procedure is a "time dry" which is a total of 32 minutes, out of which the combustor operates for 30 minutes, and is then turned off to cool the textile for safe handling. The textile load is considered dry if the final moisture content is less than 3.5%.

To investigate the effect of adsorbent mass and recirculation ratios, the adsorbent bed was connected to the dryer as shown in Figure 6.7a. The outlet of the adsorbent bed was connected to the inlet of the combustor as shown in Figure 6.7b. Two air gates and an air

Table 6.3: Operating conditions for experimental tests

Operating parameter	Value
Ambient temperature	24 ± 2°C
Ambient relative humidity	50 ± 5%
Drum RPM	48 ± 1 rpm
Fan motor RPM	3400 ± 5 rpm
Combustor firing rate	18.8 kW
Initial dry mass	7.66 ± 0.23 kg
Initial moisture content	85 ± 2%
Mass of adsorbent	5 kg, 8.5 kg, and 11 kg
Adsorbent material	Silica Gel Type RD
Bed diameter	0.38 m
Maximum length	0.18 m

damper were installed to control airflow. The volumetric flow rate of air entering the combustor is held constant to avoid changing the air-to-fuel ratio The recirculation ratio is given by Equation (6.21):

$$y_{RR} = \frac{\dot{V}_7}{\dot{V}_8} = \frac{\dot{V}_7}{\dot{V}_7 + \dot{V}_1} \tag{6.21}$$

Recirculating the conditioned exhaust stream in a gas-fired tumble dryer is different than it would be in electrical tumble dryers. This is due to the fact that the chemical balance of the combustion reaction is also altered. The details of the procedure to account for the effect of exhaust recirculation on the chemical process are described in Chapter 5. The test matrix is shown in Table 6.4.

Table 6.4: Experimental test matrix

		Recirculation Ratio				
		30 ± 4%	**50 ± 5%**	**60 ± 5%**	**70 ± 6%**	**80 ± 6%**
Mass of adsorbent	**5 kg**	×	×	×	×	×
	8.5 kg	×	×	×	×	×
	11 kg	×	×	×		

The experiments with maximum adsorbent capacity and high recirculation ratios could not be conducted because under those operating conditions, the maximum safe operating temperature of the combustor was exceeded.

6.5 Results and Discussion

The results of the heat and transfer model described in Section 6.3.2 to predict the drying performance parameters are compared with the experimental results and validate the model. The effects of adsorbent mass and recirculation ratio on drying performance are investigated.

Figure 6.8 shows the temperature of the air measured at the inlet and outlet of an 8.5-kg adsorbent bed for a recirculation ratio of 0.6 for four consecutive drying cycles. The adsorbent bed is purged with ambient air prior to the first drying cycle. During the first cycle, the temperature of the air leaving the adsorbent bed exceeds 66°C; however, in subsequent drying cycles, the peak temperature of the air leaving the bed decreases. This is due to the decrease in the water vapor uptake capacity of the silica gel. In fact, during the first drying cycle, no desorption occurred. The switch from adsorption to desorption can be seen in subsequent cycles as the point at which the inlet air temperature exceeds the outlet air temperature. The switching time decreases as the drying cycles continue, and the air temperature leaving the bed reaches a cyclic steady state at the third drying cycle. The temperature of the air leaving the bed when cyclic steady state is reached does not exceed 60°C. With an adsorbent bed mass of 5 kg and 11 kg, the cyclic steady state is achieved after second and fourth drying cycles, respectively. The results discussed below are presented for cyclic steady state.

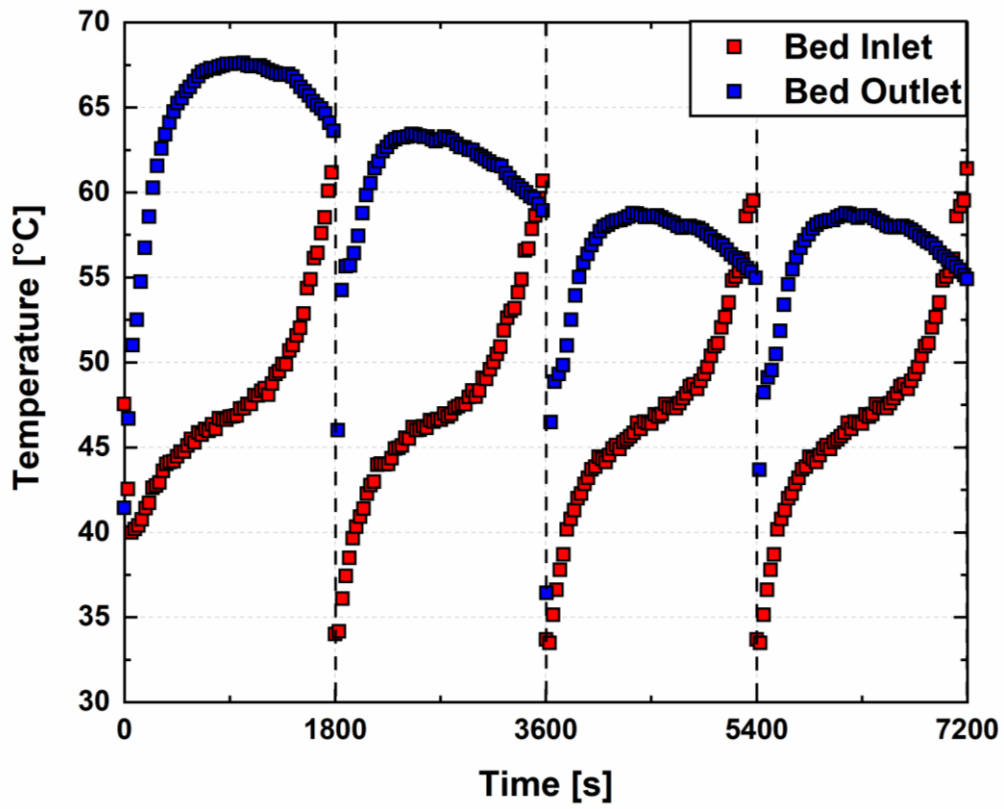

Figure 6.8: Cyclic temperatures at the inlet and outlet of the adsorbent bed with mads = 8.5 kg and recirculation ratio y_{RR} = 0.6.

6.5.1 Effect of adsorbent mass

To investigate the effect of the adsorbent mass on the drum inlet temperature, the recirculation ratio was fixed at 0.5. The temperature of the air entering the drum after achieving cyclic steady state for each case is shown in Figure 6.9. As the mass of adsorbent increases, the temperature of the air entering the drum increases. With no adsorbent bed, the steady state temperature is 167°C. The inlet temperature increases to 173°C, 185°C, and 197°C for mass of adsorbent bed of 5 kg, 8.5 kg, and 11 kg, respectively. As the mass of adsorbent increases, the total heat of adsorption (Q_{ads}) increases too because $Q_{ads} = m_{ads}\Delta H_{ads}\Delta q$ is a direct function of the mass of adsorbent available in the packed

bed. Since the overall bed dimensions are fixed, adding more adsorbent increases the overall surface area on which the adsorption process take place. By increasing the surface area, the adsorption rate increases, releasing a higher amount of heat of adsorption. Therefore, increasing the mass of adsorbent increased the temperature of the air leaving the adsorbent bed, which preheated the air at the inlet of the combustor due to direct mixing. The total heat of adsorption is also a function of the change in water vapor uptake. As drying proceeds, the humidity is adsorbed onto the surface of the silica gel, which increases the water vapor uptake. This increase in the water vapor uptake increases the amount of heat released and therefore heats up the air leaving the adsorbent bed. The average absolute deviation (AAD) is used to compare measured and predicted values, as defined by Equation (6.22):

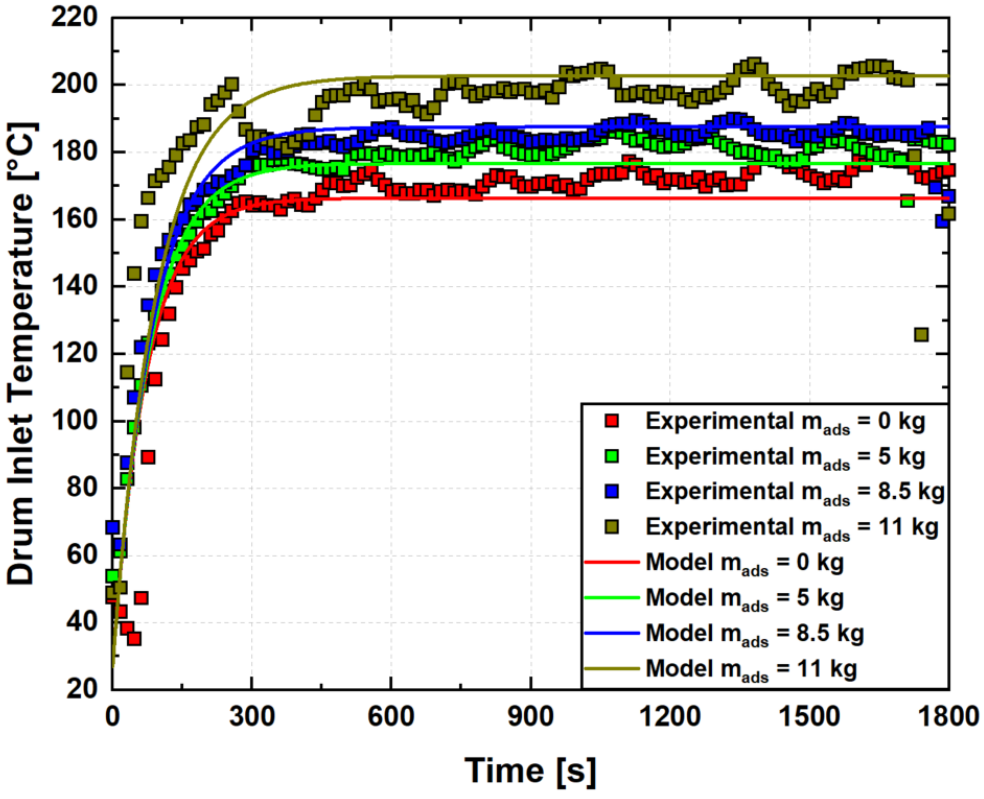

Figure 6.9: Variation of drum inlet temperature as function of time for different adsorbent masses at recirculation ratio y_{RR} = 0.5

$$AAD = \frac{1}{N}\sum_{i=1}^{N}\left|\frac{y_{predicted} - y_{measured}}{y_{measured}}\right| \tag{6.22}$$

The model shows a good agreement in predicting the drum inlet temperature with AAD of 7.1%. Figure 6.10 shows the air temperature at the exit of drum for different adsorbent bed masses. Due to the elevated temperature of air entering the drum as the mass of adsorbent increases, the temperature of the air exiting the drum increases. At t = 900 s, the air exits the drum at a temperature of 46.3°C, 47.5°C, 51.2°C, and 55.1°C, for adsorbent masses of 0 kg, 5 kg, 8.5 kg, and 11 kg, respectively. The model predicted the drum exit temperature for different adsorbent bed masses with an AAD of 8.4%. The model tends to underpredict

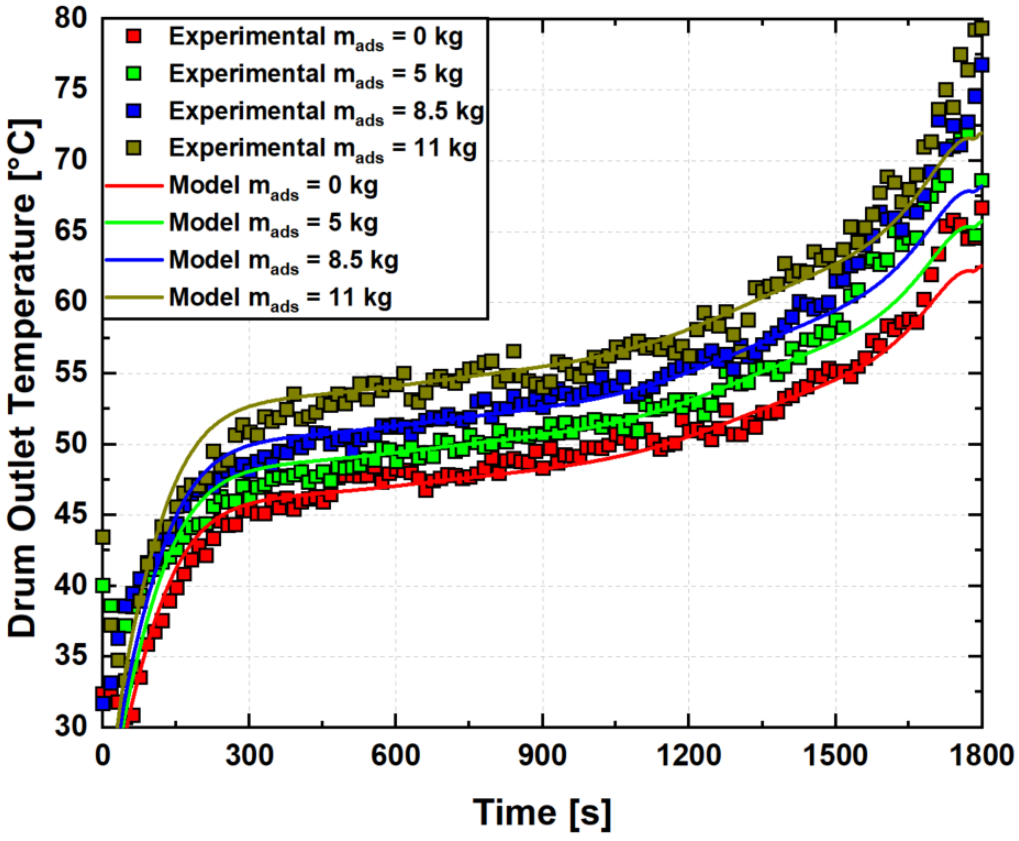

Figure 6.10: Variation of the drum outlet temperature as function of time for different adsorbent masses at a recirculation ratio y_{RR} = 0.5.

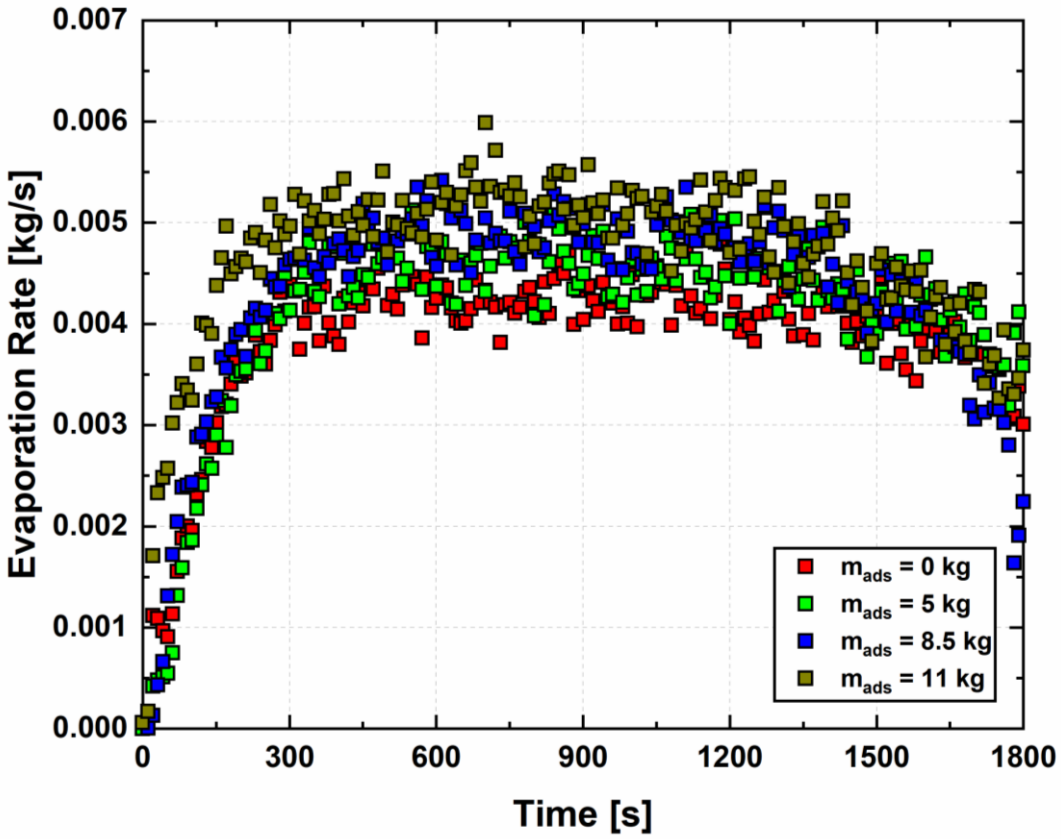

Figure 6.11: Variation of evaporation as a function of time for different adsorbent masses at recirculation ratio y_{RR} = 0.5

the temperature of the air leaving the drum due to a slight overprediction of the heat loss from the drum.

As the temperature of air entering and leaving the drum increases, as shown in Figures 6.8 and 6.9, the evaporation rate increases. As shown in Figure 6.11, the evaporation rate increased by 30.7% when an 11-kg adsorbent bed is added to the baseline system without an adsorbent bed. The air leaving the adsorbent bed during the adsorption phase is at an elevated temperature and low humidity ratio. When this premixes with the ambient air, the temperature of air entering the drum is higher than that of the base case.

Similarly, the humidity ratio of the air entering the drum with an adsorbent bed connected is lower than that of the base case. These two conditions increase the drying rate due to an increase in both heat and mass transfer driving forces. For $m_{ads} = 8.5\ \text{kg}$, the evaporation rate increased by ~23% compared to the base case. As shown in Table 6.4, at an adsorbent mass of 11 kg, there are two experiments at high recirculation ratios, i.e., $y_{RR} = 0.7$ and 0.8 that could not be conducted. This is because at a high adsorbent mass and high recirculation ratio, the temperature of the air entering the drum increases beyond 220°C, which causes the combustor to turn off for safety reasons.

6.5.2 Effect of exhaust gas recirculation ratio

To investigate the effect of recirculation ratio, the adsorbent bed mass was held constant. Figure 6.12 shows the air temperature measured at the inlet and outlet of the adsorbent bed for $m_{ads} = 8.5\ \text{kg}$. The breakthrough curves (temperature profiles) at $x = 0.125\ \text{m}$ are depicted in Figure 6.12 for three representative recirculation ratios. As the recirculation ratio increases, the air velocity in the bed increases. An increase in the air velocity translates to an increase in both the heat and mass transfer coefficients (Equations (6.12) and (6.13)).

At $y_{RR} = 0.3$, the average air temperature at the outlet of the adsorbent bed is 50.3°C. As the recirculation ratio increases, the temperature leaving the bed increases by 4.8°C and 8.6°C for a $y_{RR} = 0.5$ and 0.6, respectively. Due to an increase in the bed exit temperature, the inlet and exit temperatures of the drum also increase, thus increasing the evaporation rate. Figure 6.12 shows good agreement between measured and predicted

temperatures at the inlet and exit of the bed with an AAD of 4.6%. The model slightly under predicts the temperature of the air leaving the bed at the lowest recirculation ratio $(y_{RR} = 0.3)$. This is mainly due to underprediction of the convective heat and mass transfer in the adsorbent, which results in the lower adsorption rate, and therefore a lower air temperature at the exit of the bed.

Figure 6.13 shows the humidity ratio of the air at the inlet and outlet of the adsorbent bed for a mass of 8.5 kg. As can be seen here, the higher the recirculation ratio, the higher the difference between the exit and the inlet humidity ratios. At high recirculation ratios, the drying rate is high, and therefore, the humidity ratio of the air

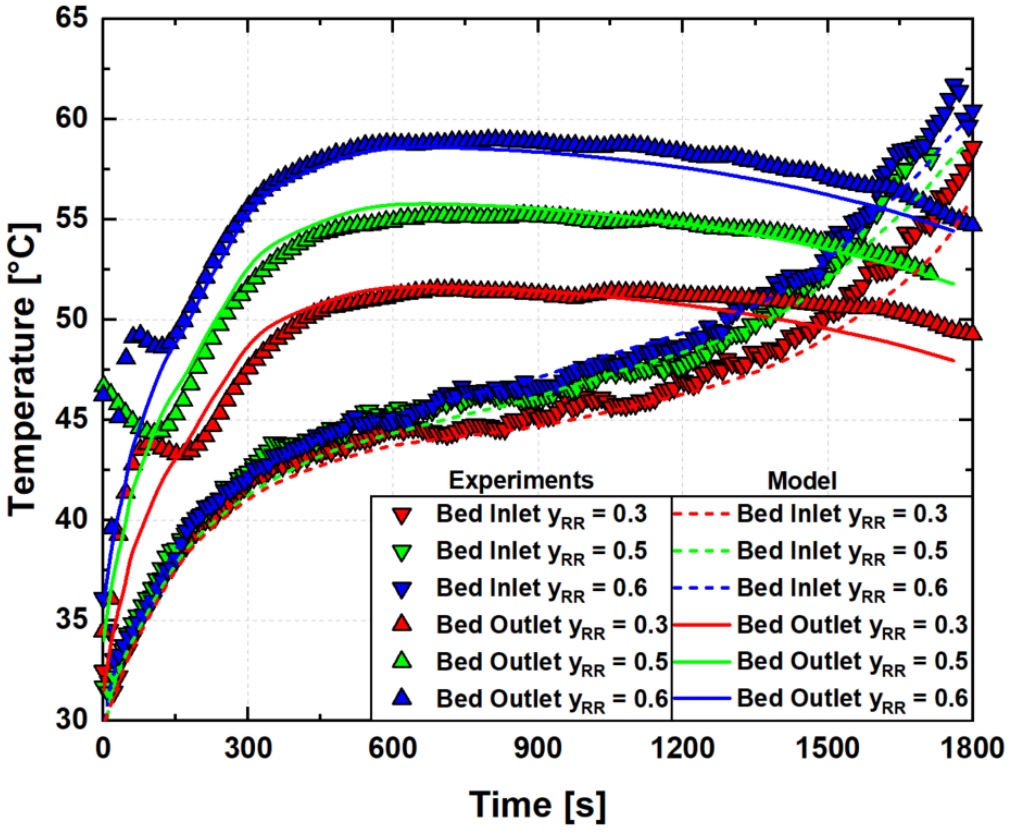

Figure 6.12: Predicted and measured inlet and outlet temperatures of the adsorbent bed at different recirculation ratios for m_{ads} = 8.5 kg

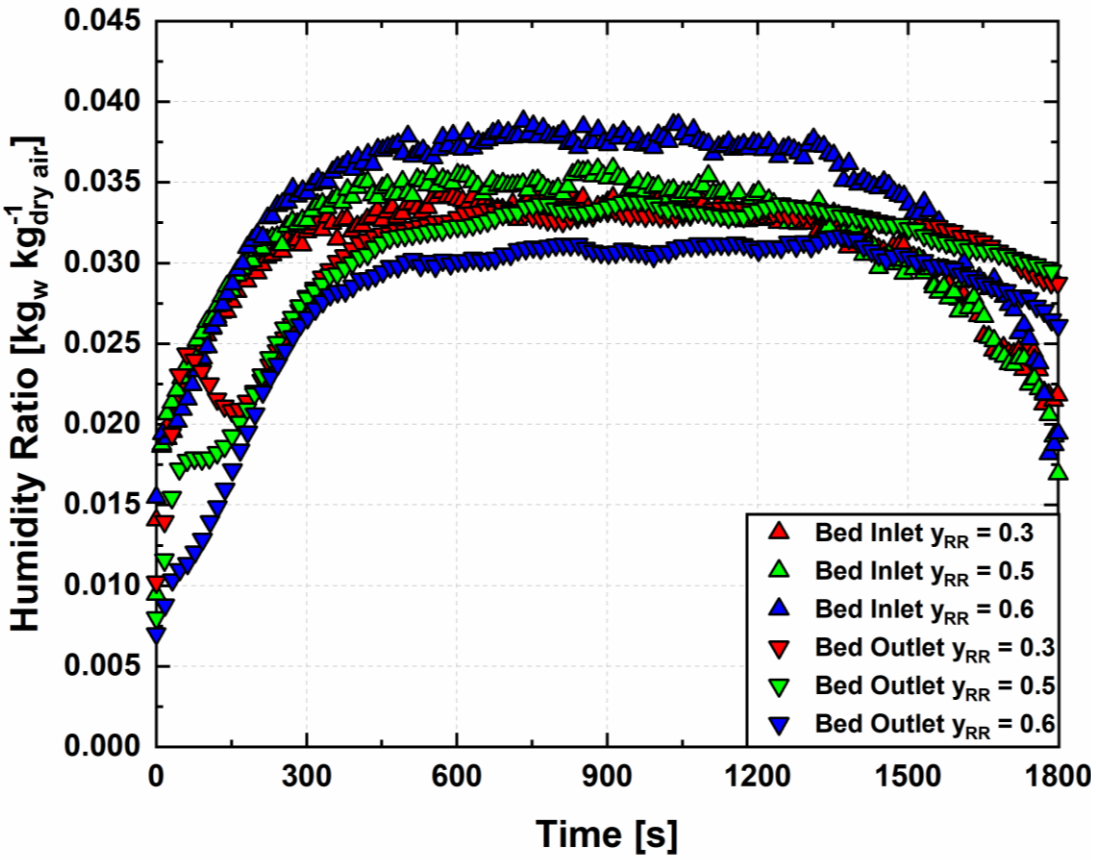

Figure 6.13: Variation of inlet and outlet humidity ratio of the adsorbent bed different recirculation ratios for m_{ads} = 8.5 kg

stream from the exhaust of the dryer increases as compared to the humidity ratio at low recirculation ratios ($y_{RR} \leq 0.5$). At $y_{RR} = 0.6$, the humidity ratio of the air leaving the adsorbent bed is the lowest as compared to $y_{RR} = 0.3$ and 0.5, due to an increase in the adsorption rate. This is mainly due to the increase in the mass transfer coefficient at higher flow rates, which enhances the adsorption process and results in low humidity ratio air at the exit. This is observed for all three recirculation ratios, where the difference in humidity ratios $\left(\Delta\omega = \omega_{in}^{bed} - \omega_{out}^{bed}\right)$ between the inlet and exit of the bed for $y_{RR} = 0.3,\ 0.5$, and 0.6 is $8 \times 10^{-3}\,\mathrm{kg_w kg^{-1}_{dry\ air}}$, $4 \times 10^{-3}\,\mathrm{kg_w kg^{-1}_{dry\ air}}$, and $0.9 \times 10^{-3}\,\mathrm{kg_w kg^{-1}_{dry\ air}}$, respectively.

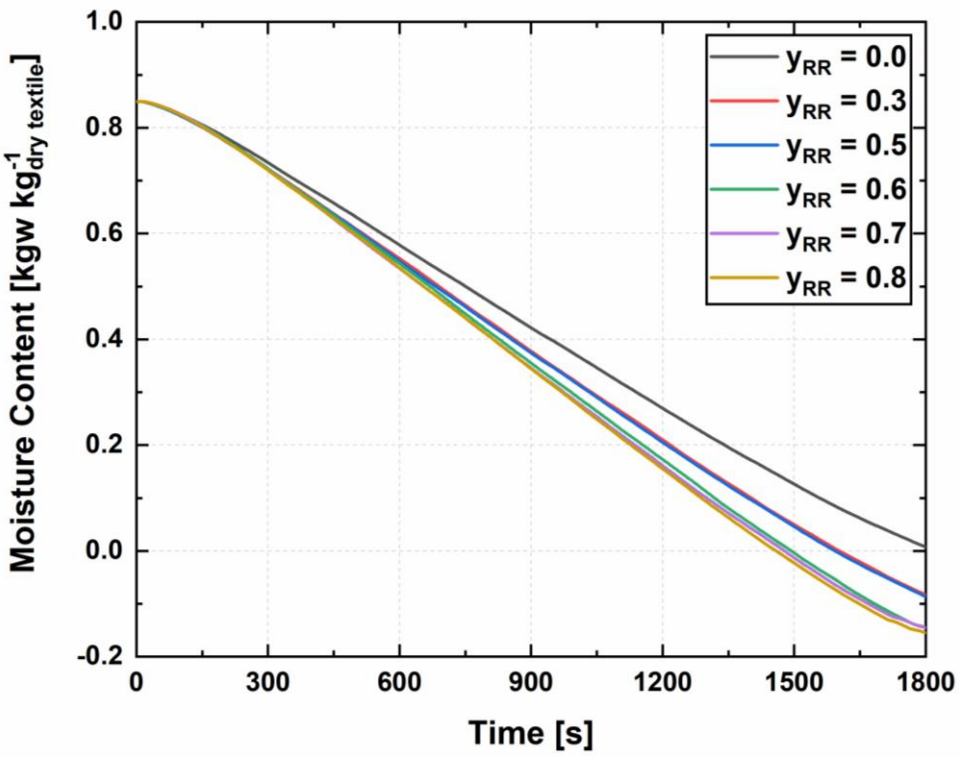

Figure 6.14: Variation of moisture content as function of time for different recirculation ratios with mads = 8.5 kg

Furthermore, the switching time between the adsorption and desorption phase increases slightly as the recirculation ratio increases. At $y_{RR} = 0.3, 0.5$, and 0.6, switching occurred at 1506 s, 1622 s, and 1676 s, respectively. This same trend extends to higher recirculation ratio of y_{RR} = 0.7 and 0.8. The adsorption phase was elongated at high recirculation ratio due to the lower initial equilibrium water uptake in the bed based on the isotherm depicted in Figure 6.5b. A lower equilibrium water vapor uptake at the beginning of the process indicates a higher bed capacity to adsorb water before the bed must be regenerated.

Figure 6.14 shows the moisture content variation of the clothes in the dryer as function of time for $m_{ads} = 8.5$ kg at different recirculation ratios. The measured moisture content is quantified by Equation (6.23):

$$X = \frac{1}{m_{cl.dry}} \left(X_{init} m_{cl.dry} - \int_{t=0}^{t=\Delta t} \dot{m}_e \mathrm{dt} \right) \tag{6.23}$$

For base case, i.e., with no adsorbent bed, the drying time was 1725 s compared to 1398 s with a recirculation ratio is 0.8. The drying time decreases by ~ 19% due to higher drying rates. As the recirculation ratio increases for the same adsorbent mass, the drying rate increases and therefore reduces the total energy consumption and the drying time.

6.5.3 Dryer performance

Figure 6.15 shows the measured drying time as a function of recirculation ratio for different masses of adsorbent. For $m_{ads} = 5$ kg, the drying time to achieve a moisture

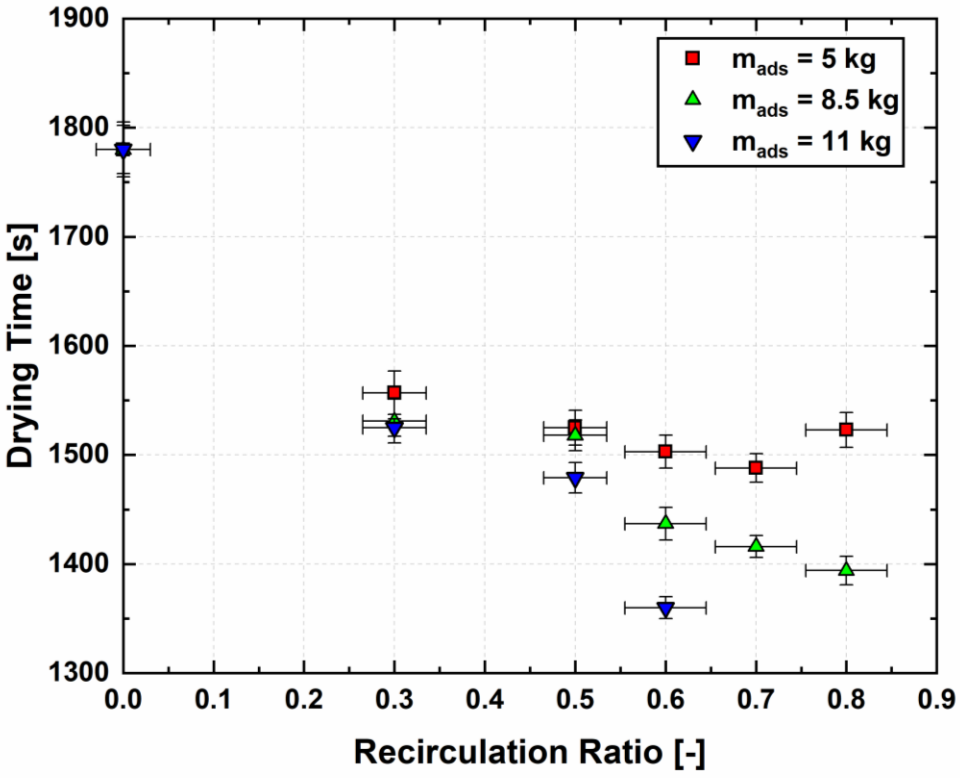

Figure 6.15: Drying time as function of recirculation ratio for different adsorbent masses

content less than 3.5% decreases as the recirculation ratio increases. However, at high recirculation ratios, i.e., $y_{RR} \geq 0.6$, the drying time increases as can be seen by the inflection point shown in Figure 6.15. At $m_{ads} = 5$ kg and $y_{RR} = 0.8$, the drying time is 1523 s compared to 1488 s for a recirculation ratio of 0.7. This is mainly due to recirculation back of some of the moisture. Due to the low mass of adsorbent, the increase in the air temperature at the inlet of the drum does not offset the humidity that is recirculated back, and therefore the drying time increases slightly, by 35 s. At higher adsorbent masses, as the recirculation ratio increases, the drying time decreases. This is because the temperature at the inlet of the drum exceeds 175°C, which is enough to offset the effects of any additional moisture being recirculated.

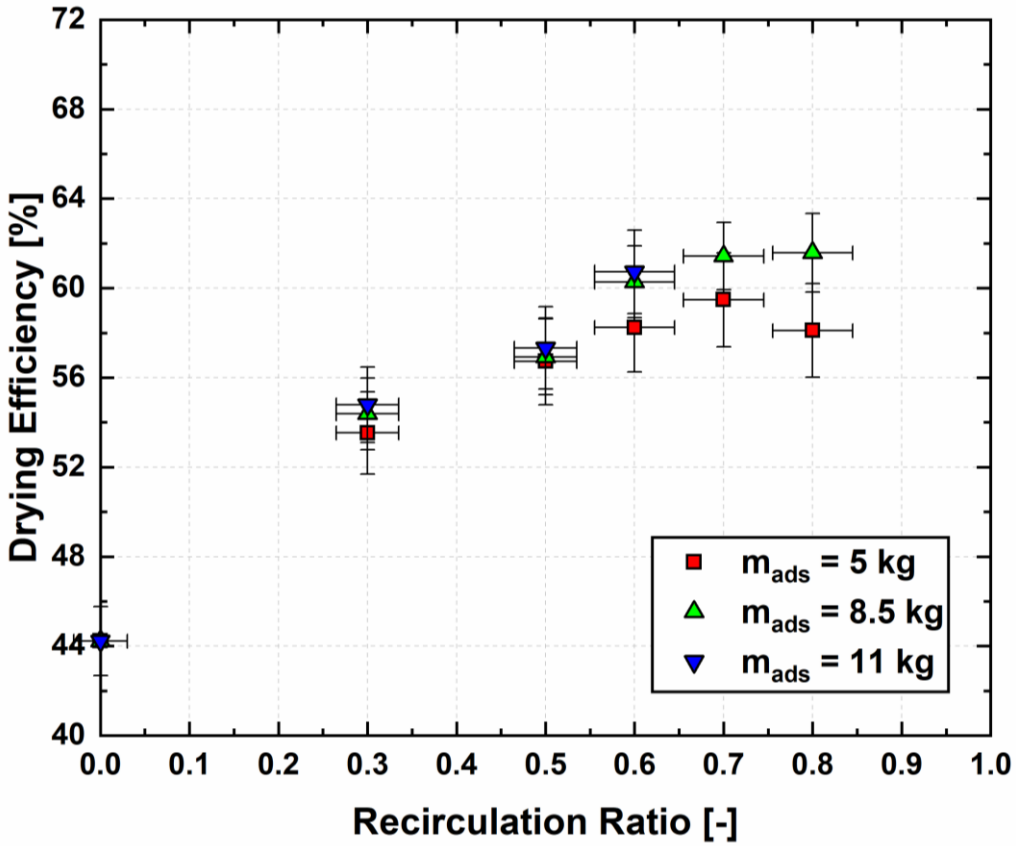

Figure 6.16 shows the variation of the measured drying efficiency as function of the recirculation ratio. For low adsorbent masses, i.e., $m_{ads} \leq 5$ kg, the drying efficiency increases from 44.2% for the base case $(y_{RR} = 0)$ to a maximum drying efficiency of 58.5% at a recirculation ratio of 0.7. Recirculating back additional exhaust gas reduces the drying efficiency slightly due to a reduction in the evaporation rate as discussed previously. However, at high mass of adsorbent, i.e., $m_{ads} > 5$ kg, the drying efficiency reaches a plateau of ~ 61.6% at a recirculation ratio of 0.7 at $m_{ads} = 8.5$ kg. For $m_{ads} = 11$ kg, the maximum drying efficiency of ~ 60.7% was achieved at $y_{RR} = 0.6$.

Figure 6.17 shows the measured SMER as a function of the recirculation ratio for all the experiments conducted in this study. The baseline energy consumption of the current

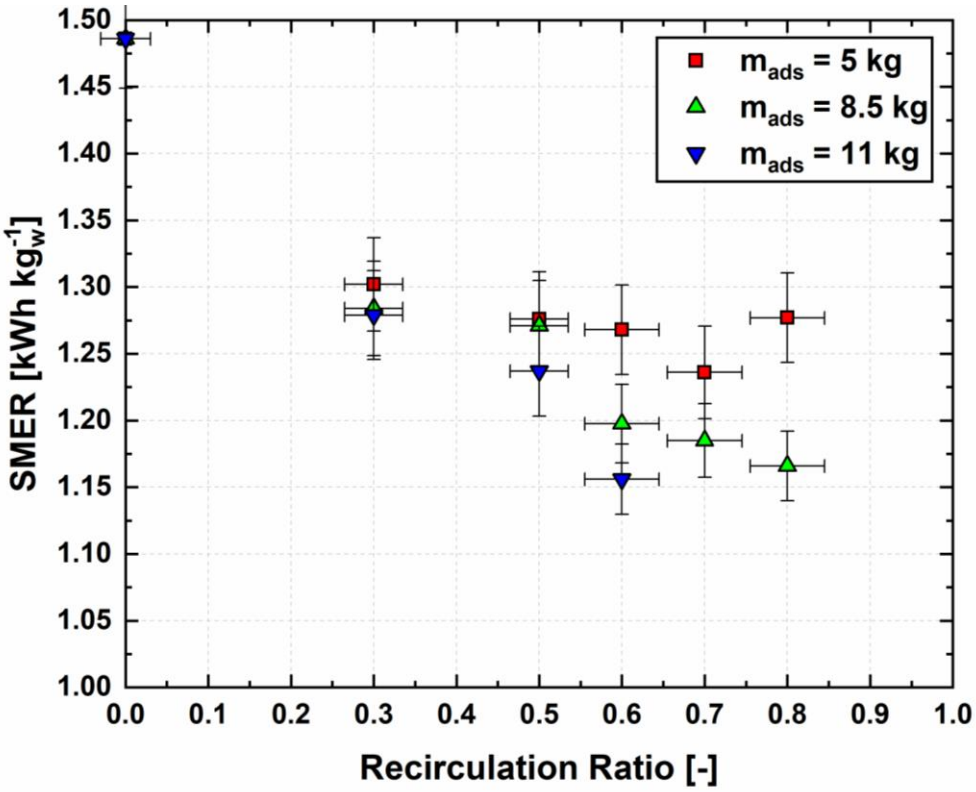

Figure 6.17: Specific moisture extraction ration (SMER) as a function of recirculation ratio for different adsorbent masses

Table 6.5: Overall energy consumption (SMER) in kWh kg^{-1}

		Mass of adsorbent			
		0 kg	**5 kg**	**8.5 kg**	**11 kg**
Recirculation Ratio	**0.0**	1.454	1.486	1.486	1.486
	0.3	-	1.302	1.284	1.279
	0.5	-	1.276	1.272	1.237
	0.6	-	1.268	1.198	1.156
	0.7	-	1.236	1.185	-
	0.8	-	1.277	1.166	-

gas-fired tumble dryer is 1.454 kWh kg_w^{-1}. For $m_{ads} = 5$ kg the minimum measured SMER was 1.234 kWh kg_w^{-1} at a recirculation ratio of 0.7. The adsorbent bed was able to store 0.22 kWh kg_w^{-1}. At a recirculation ratio of 0.8, the energy consumed does not decrease as much as for the lower recirculation ratio due to the slightly lower drying rates. The SMER achieved at $y_{RR} = 0.8$ and $m_{ads} = 5$ kg was 1.278 kWh kg_w^{-1}. When $m_{ads} = 8.5$ kg, the SMER decreases as the recirculation ratio increases. The minimum measured SMER was 1.166 kWh kg_w^{-1} at $y_{RR} = 0.8$. In the latter case, the total energy stored in the sorption bed increased to 0.29 kWh kg_w^{-1}. Finally, when the sorption bed was running at full capacity i.e., $m_{ads} = 11$ kg, the minimum measured SMER was 1.156 kWh kg_w^{-1}, at a recirculation ratio of 0.6. With a 0.18-m long sorption bed and a pressure drop of 0.175 kPa (compared to a baseline pressure drop of 0.06 kPa), integrating an 11-kg sorption bed with the gas-fired tumble dryer reduces energy consumption by 22.2%. Table 6.5 summarizes the

energy reduction achieved for different mass of adsorbents for the full range of recirculation ratios considered in this study.

6.6 Conclusion

A novel adsorption-based TES system was integrated with a commercial gas-fired tumble dryer. A silica gel sorption bed was added in the air stream of the dryer. The warm and humid exhaust stream from the dryer passes through the sorption bed. During the adsorption phase, the humidity from the exhaust stream is adsorbed onto the surface of the silica gel, releasing the heat of adsorption. Without the addition of any auxiliary energy source, the sorption bed is regenerated from the same exhaust stream while taking advantage of the water vapor partial pressure swing that occurs as drying proceeds. The theoretically model for this system predicts the air temperatures at the inlet and outlet of the drum with AADs of 7.1% and 8.4%, respectively. Integrating the gas-fired tumble dryer with the sorption bed reduces the overall energy consumption by 22%, while increase the drying efficiency to 60.7%. Additionally, the drying time is reduced by 385 s from a baseline value of 1725 s. These promising results suggest significant energy savings in textile drying with widespread market adoption. The process can be further optimized to increase the energy efficiency of the dryer while reducing the foot-print of the system.

CHAPTER 7. HEAT PUMPING AND COMBINED EFFECT OF ENERGY SAVING TECHNIQUES

In this chapter, an assessment of several energy saving techniques is conducted, including exhaust gas recirculation, recuperative waste heat recovery, adsorption-based thermal energy storage, and heat pumping, to achieve reduction in energy consumption and drying time. A single-stage two-bed adsorption heat pump is also considered to investigate the potential for additional performance improvements. Three figures of merit, specific moisture extraction ratio (SMER), drying efficiency $\left(\eta_d\right)$, and drying time $\left(\Delta t_d\right)$ were used to assess the drying performance of these energy saving techniques.

7.1 Introduction

Thermal energy storage can bridge the gap between the supply and demand of energy at different phases of the drying process, providing significant cost savings, and reduction of energy consumption and drying time. Thermal energy storage (TES) can employ heating/cooling (sensible), melting/solidification (latent/phase change), or thermochemical processes (sorption, chemical reactions) (Demir et al., 2008; Cabeza et al., 2017). Open adsorption systems store thermal energy and provide hot dry air during the discharge phase, making them very attractive for drying (Chi and Wasan, 1970; Hauer and Dallmayer, 1996; Hauer and Fischer, 2011; Krönauer et al., 2015). Some applications have already ben commercialized in niche markets. ZeoTech® developed a self-cooling portable beer barrel (Paksoy, 2007) consisting of zeolite embedded inside the external shell of the barrel. When the barrel needs cooling, the connection between the anhydrous zeolite and the evaporator is opened, and the heat of evaporation is rejected from the beer. When the

barrel is empty, the zeolite is regenerated using an auxiliary heat source. In collaboration with ZAE Bayern, Bosch developed a TES system for a dishwasher (Hauer and Fischer, 2011; Santori et al., 2013) . Thermal energy from hot water is reversibly stored in a zeolite cartridge, which is regenerated during the washing stages, yielding a 25% energy savings. Heat recovery, storage, and transportation on a large-scale industrial system (Krönauer et al., 2015) using flowing air through a zeolite 13X bed has also been demonstrated. Once the adsorbent material is regenerated, the dry reactor is transported to the site where it is discharged by flowing humid air through the adsorbent bed, releasing heat to drive industrial processes.

The above discussion indicates that thermal energy storage and heat pumping have the potential to enhance the energy efficiency of textile drying. In this chapter, five energy saving techniques for a commercial gas-fired tumble dryer, including exhaust gas-recirculation, recuperation, adsorption-based TES, and heat pumping, are investigated. A combination of some of these techniques is also considered. To understand the heat and mass transfer phenomena in each of these techniques, transient thermodynamic models were developed and validated experimentally on an 11.33-kg commercial gas-fired tumble dryer.

7.2 Energy saving techniques

7.2.1 Waste heat recovery: recirculation and recuperation

Exhaust gas recirculation (EGR) and recuperation (RHX) are simple methods to reclaim some of the energy being dissipated through the exhaust. Exhaust gas recirculation and recuperation were investigated in Chapter 5. A brief discussion of the methodology

used for EGR and RHX is provided here. A fraction of the exhaust air stream is recirculated and preheats the ambient air before it enters the combustor. The recirculation ratio (y_{RR}) is based on the volumetric flow rate:

$$y_{RR} = \frac{\dot{V}_7}{\dot{V}_8} = \frac{\dot{V}_7}{\dot{V}_7 + \dot{V}_1} \tag{7.1}$$

Recirculation also necessarily recirculates a fraction of the moisture. The recirculated exhaust stream is typically at higher temperature and higher humidity ratio than the ambient air. Therefore, a high recirculation ratio tends to increase the overall moisture content in the dryer, which in turn decreases the evaporation rate, increases energy consumption, and extends the drying time. There is an optimal recirculation ratio at which the higher temperature of the recirculated air compensates for the increased moisture content.

An alternative approach to recover thermal energy is to install a recuperative heat exchanger (RHX), which, unlike EGR, does not recirculate any moisture back into the dryer. The exhaust does not mix with the incoming ambient air as in EGR; therefore, the ambient air is sensibly preheated without increasing its moisture content. The performance of the dryer with an integrated RHX depends on its geometry, which is described in detail in Chapter 5. The compact plate-fin heat exchanger was designed for a high energy density while avoiding condensation of moisture. Mass and energy conservation equations were developed for this heat exchanger based on a quasi-steady state approach.

7.2.2 Adsorption-based thermal energy storage

An adsorption-based thermal energy storage system integrated with an air-vented gas-fired tumble dryer was investigated in Chapter 6. An adsorbent bed is added in the exhaust stream to reclaim and store the thermal energy in form of thermochemical potential to be reused in subsequent drying cycles. During the initial stages of drying, the exhaust stream (warm and humid) enters the sorption bed where its water content is adsorbed onto the surface of the adsorbent. This exothermic process results in hot and dry air at the exit of the sorption bed, which is ideal for the drying cycle. Towards the end of the drying cycle, the moisture content in the textile decreases significantly. Therefore, the exhaust stream is at an elevated temperature and low humidity ratio, which is favorable to initiate regeneration. Typically, this stream is just rejected to the ambient. However, with the adsorbent bed connected to the dryer, the thermal energy of the exhaust air stream is stored as thermochemical potential to be used in current and future drying cycles. A 1-D transient model that accounted for the inter- and intra-particle heat and mass transfer in the adsorbent bed was developed to optimize and predict the drying performance.

7.2.3 Adsorption heat pumping

Adsorption heat pumps (AHPs) use low- or zero- global warming potential refrigerants such as water and ammonia, and comprise four main components: solid sorption bed, an expansion valve, a condenser, and an evaporator, as shown in Figure 7.1a. The ideal

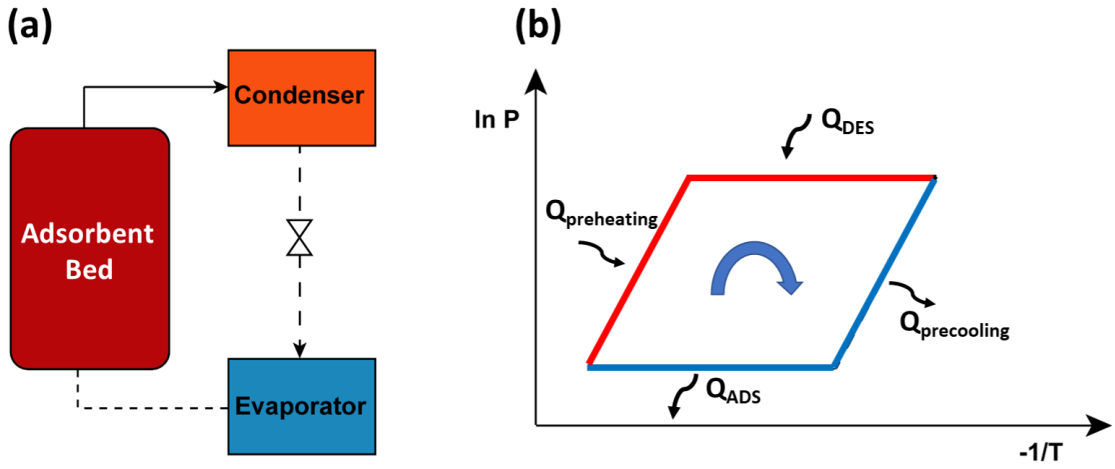

Figure 7.1: (a) A single-bed adsorption heat pump cycle schematic (b) Clausius-Clapeyron diagram of a single stage adsorption heat pump

thermodynamic cycle is presented in Figure 7.1b. An AHP typically has four phases operating between at least three different temperatures as follows:

- Isobaric adsorption: the valve between sorption bed and the evaporator is open, while the valve at the condenser is closed. The adsorbate is adsorbed onto the surface of the adsorbent, releasing the heat of adsorption.
- Isosteric heating: the valve between the evaporator and sorption bed is closed. Both bed valves are closed, the adsorbate remains constant through this phase, while pressure builds up until it reaches the condenser pressure.
- Isobaric desorption: the valve between the condenser and sorption bed is open. The adsorbate is desorbed and flows towards the condenser where it releases the heat of condensation that will be used later in the drying process.

- Isosteric cooling: the valves between the sorption bed, condenser, and evaporator are closed. The temperature of the sorption bed is cooled, the uptake remains constant as the pressure decreases until it reaches the evaporator pressure.

Three temperatures (ambient temperature (T_{amb}), post combustor temperature (T_{comb}), and the exhaust gas stream $(T_{exhaust})$) govern the incorporation of an AHP into an air-vented gas-fired tumble dryer. Figure 7.2 shows a cycle schematic of a gas-fired tumble dryer assisted by an adsorption heat pump. Integrating an AHP with a gas-fired tumble dryer can preheat the exhaust stream prior to mixing it with inlet ambient air. An air stream

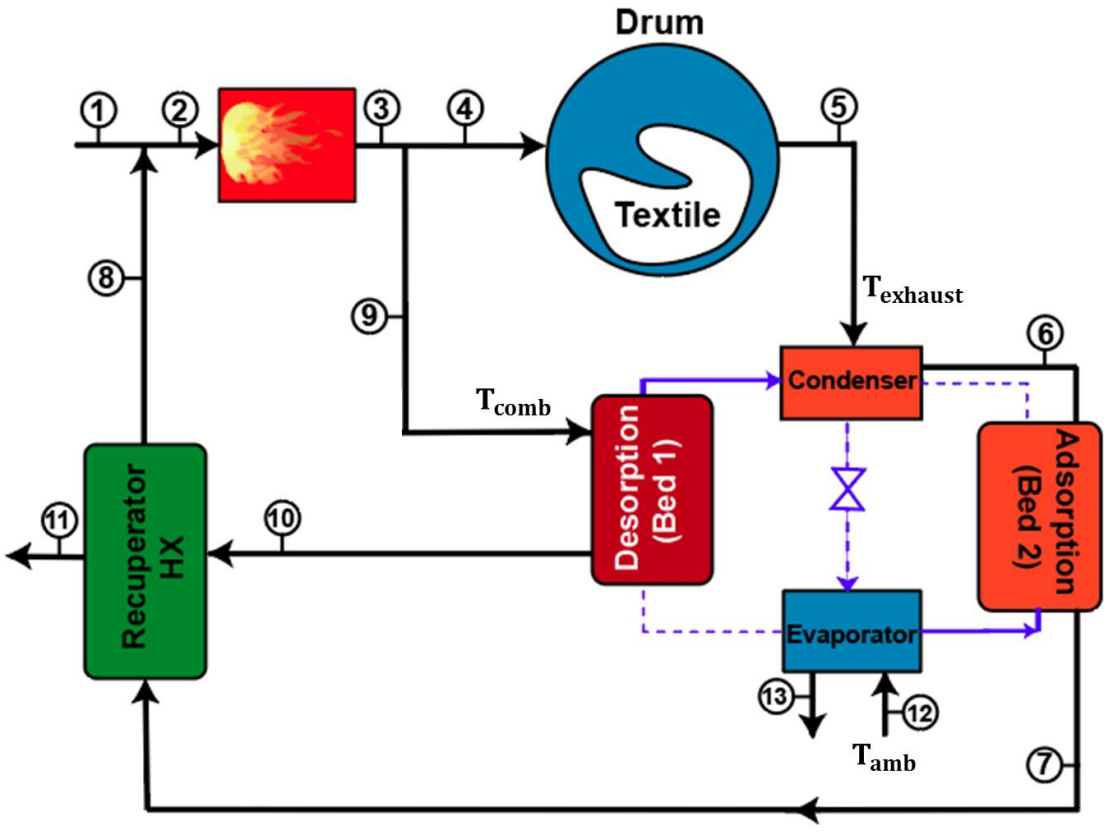

Figure 7.2: Gas-fired tumble dryer with an adsorption heat pump

is bled at the post combustion State 3 from the drying cycle to drive the heat pump. The air stream from the combustor, typically at an elevated temperature $\left(T_{comb} \geq 175°C\right)$, enters the sorption bed where it drives the cycle. The air stream heats up the desorption bed where the pressure builds up, and the water vapor flows to the condenser where it rejects the useful heat to the exhaust stream. The temperature of the exhaust stream increases as it exits the condenser (State 6). During the isobaric adsorption phase, the rejected heat from the sorption bed is used to further heat the exhaust stream (State 7). The air exiting the desorption bed at State 10 can potentially have significant energy that can harnessed and used to increase the temperature of the exhaust gas stream through an air-to-air recuperative heat exchanger.

To assess the performance of integrating a gas-fired tumble dryer with an adsorption heat pump, a detailed transient heat and mass transfer model was developed for a single-stage two-bed silica gel-water adsorption heat pump. The adsorbent beds used in this study are annular finned-tube heat exchangers. The dimensions and specifications of the bed geometry are given in detail in Raymond and Garimella (2021).

To simplify the mathematical model, the following set of assumptions was made:

- The temperature and pressure within the adsorbent beds are uniform.
- The sorption beds are filled with silica gel pellets that are treated as a porous continuous medium composed of uniform pellets, i.e., the bed porosity is constant.
- The physical properties of the metal tube and fins are constant.

- Heat losses from the sorption beds are negligible.

The linear driving force (LDF) approximation is used to model the intra-particle mass transfer. The adsorption rate is assumed to be proportional to the difference between the equilibrium and the instantaneous water vapor uptake as given by Equation (7.2):

$$\frac{dq}{dt} = K_{LDF}\left(q^{*} - q\right) \tag{7.2}$$

where the LDF mass transfer coefficient $\left(K_{LDF}\right)$ is expressed as:

$$K_{LDF} = \frac{F_0 D_{s0}}{R_p^2} \exp\left(-\frac{E_a}{RT}\right) \tag{7.3}$$

The parameters and constants used in the simulation are listed in Table 7.1. The cycle time-averaged heating power is given by Equation (7.4):

Table 7.1: Constants used to model the mass transfer in the adsorption cycle

Property	Value	Unit
Density $\left(\rho_s\right)$	2027	kg m^{-3}
Average pellet radius $\left(R_p\right)$	0.71	mm
Effective thermal conductivity $\left(k_{eff}\right)$	0.198	W m^{-1} k^{-1}
Specific heat capacity $\left(c_{p,ads}\right)$	924	J kg^{-1} K^{-1}
Shape parameter $\left(F_0\right)$	15	-
Heat of adsorption $\left(\Delta H_{ads}\right)$	2693	kJ kg^{-1}
Pre-exponent constant $\left(D_{s0}\right)$	2.54×10^{-4}	m^2 s^{-1}
Activation energy $\left(E_a\right)$	4.2×10^{4}	kJ mol^{-1}
Cycle time $\left(t_{cycle}\right)$	485	s

$$Q_{heating} = \dot{m}_5 c_{p,air} \int_0^{t_{cycle}} \left[\left(T_6 - T_5 \right) + \left(T_7 - T_6 \right) \right] dt \tag{7.4}$$

The time-averaged heating COP is given by Equation (7.5):

$$COP_{heating} = \frac{Q_{heating}}{\dot{m}_9 c_{p,air} \int_0^{t_{cycle}} \left(T_9 - T_{10} \right) dt} \tag{7.5}$$

7.2.4 Combination of waste heat recovery and thermal energy storage

The effects of incorporating a combination of EGR, RHX, and adsorption-based TES on the drying performance of a commercial gas-fired tumble dryer are investigated here. Figure 7.3 shows a cycle schematic of a system with these three energy-saving enhancements. A fraction $\left(y_{RR} \right)$ of the exhaust stream is recirculated to the dryer after passing through a sorption bed. Near the beginning of the drying cycle, the exhaust gas is typically warm and humid. The humid air enters the sorption bed where adsorption is

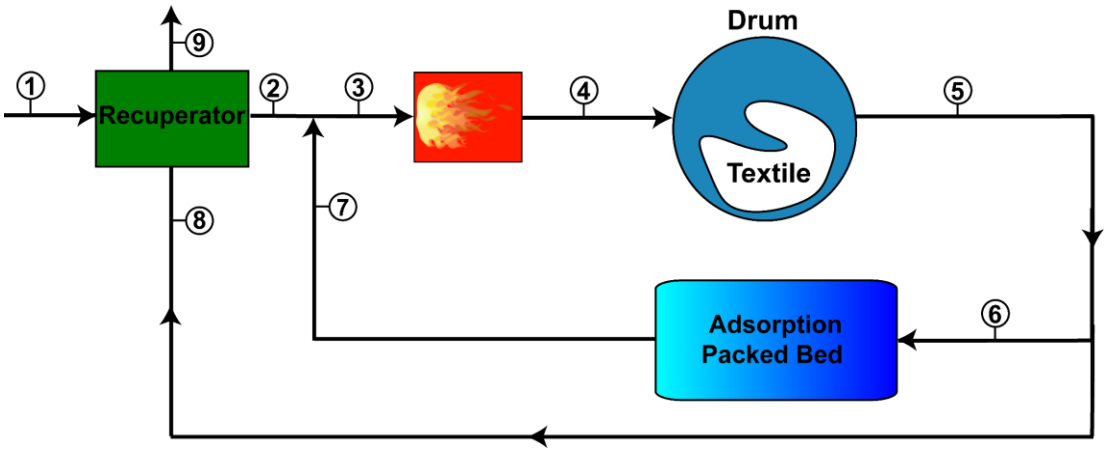

Figure 7.3: Exhaust gas recirculation, recuperation, and adsorption-based thermal energy storage with for a gas-fired tumble dryer

initiated. The air exits the bed as hot and dry. The remaining exhaust air fraction $(1-y_{RR})$ is passed through an RHX where the ambient air (State 1) is sensibly preheated to State 2. This technique takes advantage of the recirculation, but without recirculating any of the moisture. Additionally, this method heats the inlet air at two locations: sensibly through the RHX, and by direct mixing at the inlet of the combustor. Such a system was investigated experimentally on a commercial gas-fired tumble dryer.

Figure 7.4 shows a commercial gas-fired tumble dryer (~ 11.33 kg capacity) with both an adsorbent packed bed and a recuperative heat exchanger. Figure 7.4a shows the top view of the RHX, where a fraction of the exhaust stream of the dryer is used to preheat the fresh air at the intake of the heat exchanger. The preheated air is then mixed with the air leaving the adsorbent packed bed as depicted in Figure 7.4b.

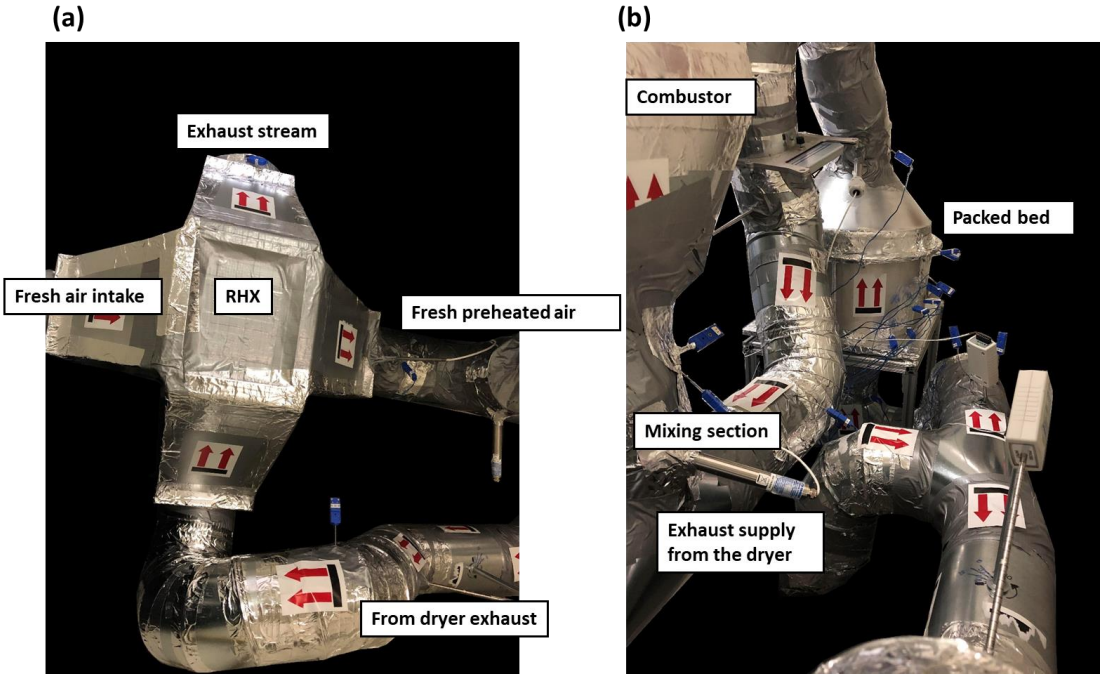

Figure 7.4: Experimental facility (a) top view of the air-to-air recuperative heat exchanger (b) front view showing the packed bed

7.3 Experimental Protocol

A Speed Queen series (Model No. SFNNYASP115TW01) commercial gas-fired tumble dryer is used to experimentally validate the mathematical models developed for incorporating EGR, RHX, and adsorption-based TES into the dryer, individually as well as together. To monitor and measure the drying process accurately, thermocouples, pressure transducers, relative humidity sensors, air velocity anemometers, and wireless temperature and humidity data loggers were installed onto the facility. The thermocouples and air velocity anemometers were installed based on ANSI/ASHRAE standards. The real time data acquisition system was programed in NI LabVIEW.

To ensure repeatability, all experiments were conducted on a standard terrycloth towels load, with each experiment repeated at least three times. The mass of dry terrycloth towels used in the experiments was 7.66 ± 0.23 kg. The experimental protocol is described below:

- A commercial washer is used to initialize the terrycloth towel load to the desired moisture content of 85 ± 2%.
- The adsorbent packed bed is purged with ambient air to ensure equilibrium and initialize the sorption bed.
- After the wet load is ready, four wireless temperature and humidity data loggers (OMEGA® OM-92-NIST) are installed onto the drum of dryer.
- The drying procedure used is a “time dry” that spans 32 minutes, of which 30 minutes are at high heat and 2 minutes with the heater turned OFF for handling purposes.

- The textile is considered dry when the desired moisture content of < 3.5% is reached.

The experimental moisture content is quantified using Equation (7.6):

$$X\left(t\right)=\frac{1}{m_{cl,dry}}\left(X_{init}m_{cl,dry}-\int_{0}^{\Delta t_d}\dot{m}_e dt\right) \tag{7.6}$$

The drying performance of the energy saving techniques is assessed based on three figures of merit. The specific moisture extraction ratio (SMER) is given by:

$$SMER=\frac{1}{m_{w,r}}\int_{t=0}^{t=\Delta t}\dot{E}_{in}dt \tag{7.7}$$

where $\dot{E}_{in}$ is the total power input, which includes the electric motors, and $m_{w,r}$ is total mass of water evaporated. SMER represents the amount of energy required to evaporate 1 kg of water. Therefore, a low SMER represents a more energy efficient dryer. The second figure of merit is the drying efficiency, which is the ratio of the actual amount of energy used to evaporate water to the total energy input of the dryer:

$$\eta_d=\frac{\int_{t=0}^{t=\Delta t}\dot{Q}_{evap}dt}{\int_{t=0}^{t=\Delta t}\dot{E}_{in}dt} \tag{7.8}$$

Finally, the third figure of merit is the drying time, which is the time taken for the wet textile to reach the desired final moisture content $\left(X_f \le 3.5\%\right)$:

$$X\left(t=\Delta t\right)=X_f \tag{7.9}$$

7.4 Results and discussion

7.4.1 Adsorption heat pump

A simulation of a two-bed adsorption heat pump integrated with the gas-fired tumble dryer was performed. Each sorption bed was assumed to have 10 kg of silica gel type RD sandwiched between the fins of the bed. The ratio of the air bleed coming out of the combustor to drive the adsorption heat pump is 0.2. The average temperature of the post combustor stream is ~ 170°C. If the fraction of air bleed from the combustor to drive desorption exceeds 0.2, the mass flow rate of the air entering the drum decreases

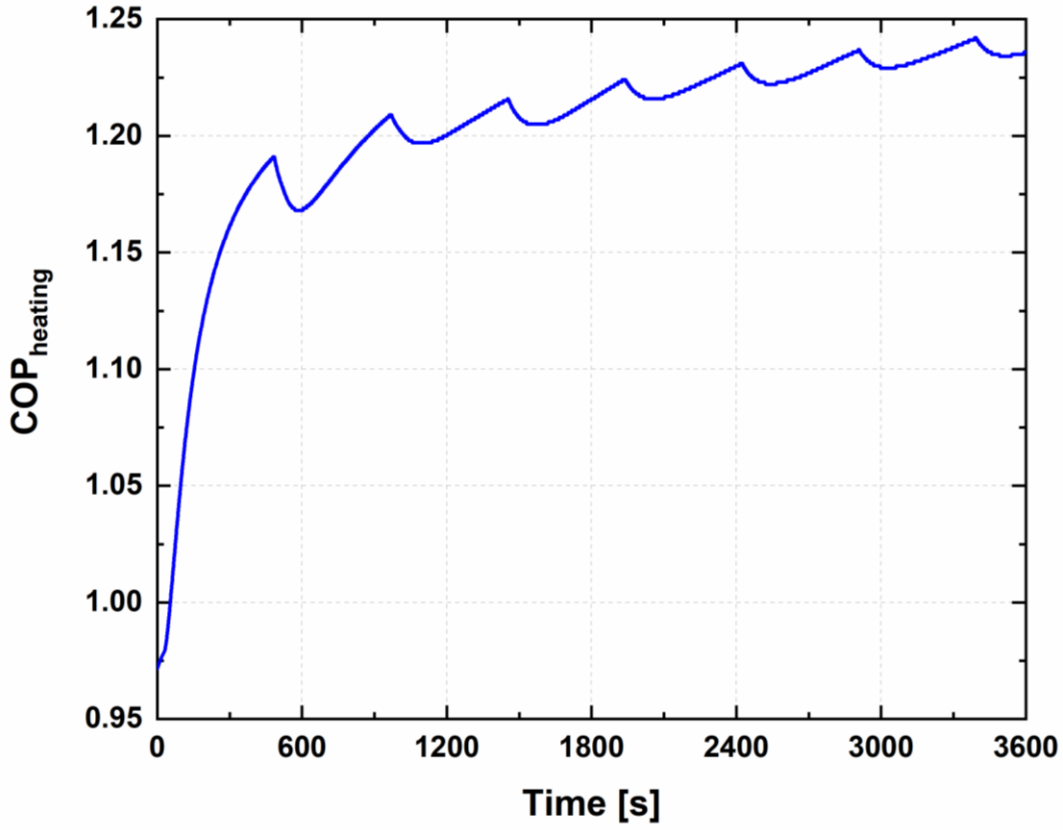

Figure 7.5: Instantaneous heating COP for two-bed adsorption heat pumps for two consecutive drying cycles

appreciably, which is detrimental to the drying process. However, a minimum bleed of 0.2 is needed to deliver the required desorption energy to the adsorbent bed to drive the heat pump. If the fraction of the air bleed from the combustor exceeds 0.5, the post combustor temperature would exceed 220°C, which is not safe for handling and could scorching the textile. Therefore, an air bleed of 0.2 is assumed in this work. Figure 7.5 shows the instantaneous heating COP achieved by the adsorption heat pump during two drying cycles. The instantaneous COP initially starts from a value less than unity due to transient effects. During the second half-cycle, the heating COP immediately decreases since there is a reduction in the heating output at the condenser and the adsorber. In the second half of the drying cycle, the temperature of the exhaust increases significantly, which makes provides a lower driving temperature difference for heat rejection from the condenser to the exhaust stream. Due to the batch-wise nature of the adsorption heat pump, the COP fluctuates as the sorption beds switch operations between adsorption and desorption. At cyclical steady state, the silica gel-water heat pump has a COP of 1.22. Typically, silica gel-water heat pumps have high efficiency because of the favorable metal/adsorbent mass ratio which arises out of the higher silica gel density.

Figure 7.6 compares the evaporation rate for integrating an AHP with a gas-fired tumble dryer to the baseline case without an AHP. The average evaporation rate of the base case over the entire cycle is ~ 0.0034 kg s^{-1}, while with the AHP, it actually decreases to ~ 0.0031 kg s^{-1}. This 8.82% reduction in the drying rate is mainly due to the reduction in the total air flow rate that enters the drum (State 4) due to the aforementioned bleed. Figure 7.6 also shows that the evaporation rate of the baseline case starts to fall at $t = 1460\ \text{s}$, while that of the dryer with an AHP starts to fall at $t = 1515\ \text{s}$. In the base case, with the

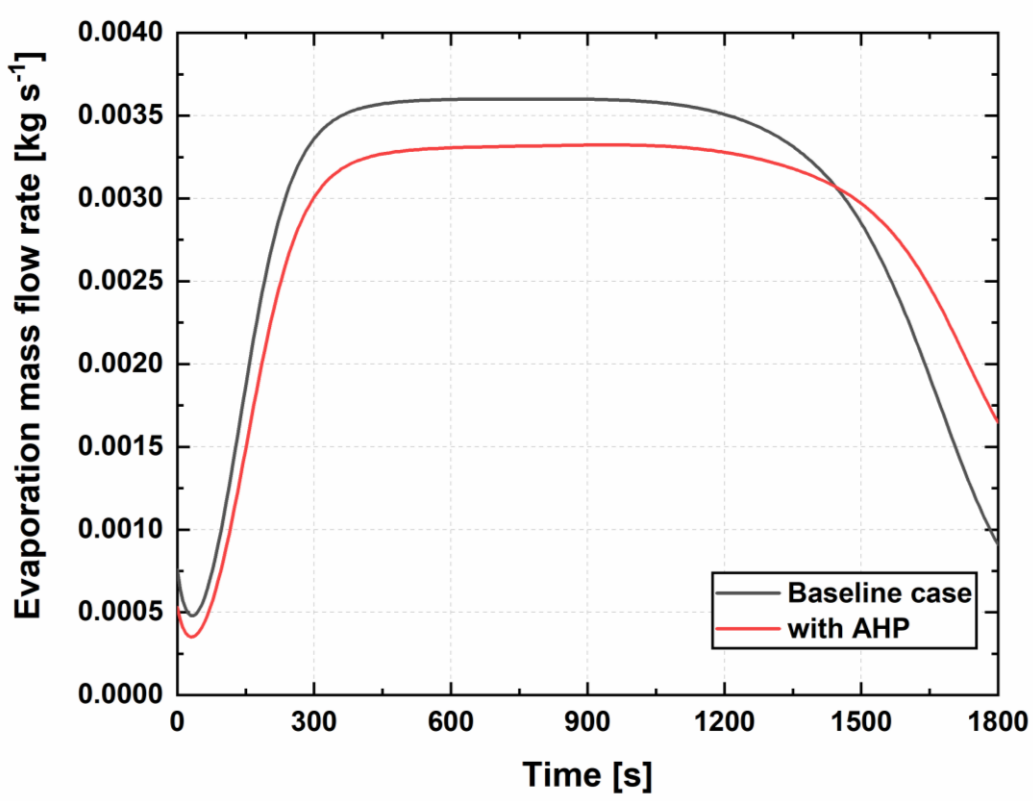

Figure 7.6: Effect of incorporating an adsorption heat pump into a single gas-fired tumble dryer

higher evaporation rate, the major portion of the moisture that must be evaporated is accomplished at this high rate earlier, and therefore, the remaining moisture content of the textile in the drum drops at a faster rate. Therefore, the time taken to dry the textile for the case with an adsorption heat pump is longer, by ~ 5.6%, than for the baseline case. The average temperature of the air entering drum with an AHP is ~ 170°C, which is 8°C higher than for the baseline case. Despite the increase in temperature entering the drum, the evaporation rate of dryer with an AHP was lower than the baseline case. The evaporation rate is directly proportional to the air flow rate and the difference between the humidity ratio of the air coming in and out of the drum. The evaporation rate is expressed as:

$$\dot{m}_{evap} = \dot{m}_a \left(\omega_5 - \omega_4 \right) \tag{7.10}$$

Two competing effects influence evaporation: the air mass flow rate, and the temperature of the air at the inlet of the drum. An increase in the temperature at the inlet of the drum tends to increase the heat transfer rate in the drum, which leads to faster evaporation. This results in a higher humidity ratio at the exit of the drum. However, the heat and mass transfer coefficients are highly influenced by the velocity at the interface between the textile and bulk air in the drum. Due to a lower mass flow rate of air entering the drum, the velocity at the interface decreases, and therefore decreases the evaporation rate despite the slight increase (~ 4%) in the temperature of the air entering the drum. In fact, to overcome the decrease in the air mass flow rate, the temperature of the air entering the drum should increase significantly, i.e., $\Delta T \geq$ 40°C. Integrating the adsorption heat pump with a bank of high-temperature dryers in a commercial facility that share common exhaust and intake air stream could increase the evaporation rate and render the AHP favorable.

7.4.2 Combination of waste heat recovery and thermal energy storage

The effects of implementing EGR, RHX, and adsorption-based TES in a gas-fired tumble dryer have been individually investigated in Chapters 5 and 6, respectively. Here, appropriate combination of all of these energy saving technologies is discussed. The combined experiments were conducted with a 5-kg sorption bed filled with commercially available silica gel type RD. The experiments were conducted with recirculation ratio $y_{RR} = 0.6 \pm 0.05$, where $y_{RR} = \dot{V}_7 / \left(\dot{V}_2 + \dot{V}_7 \right)$.

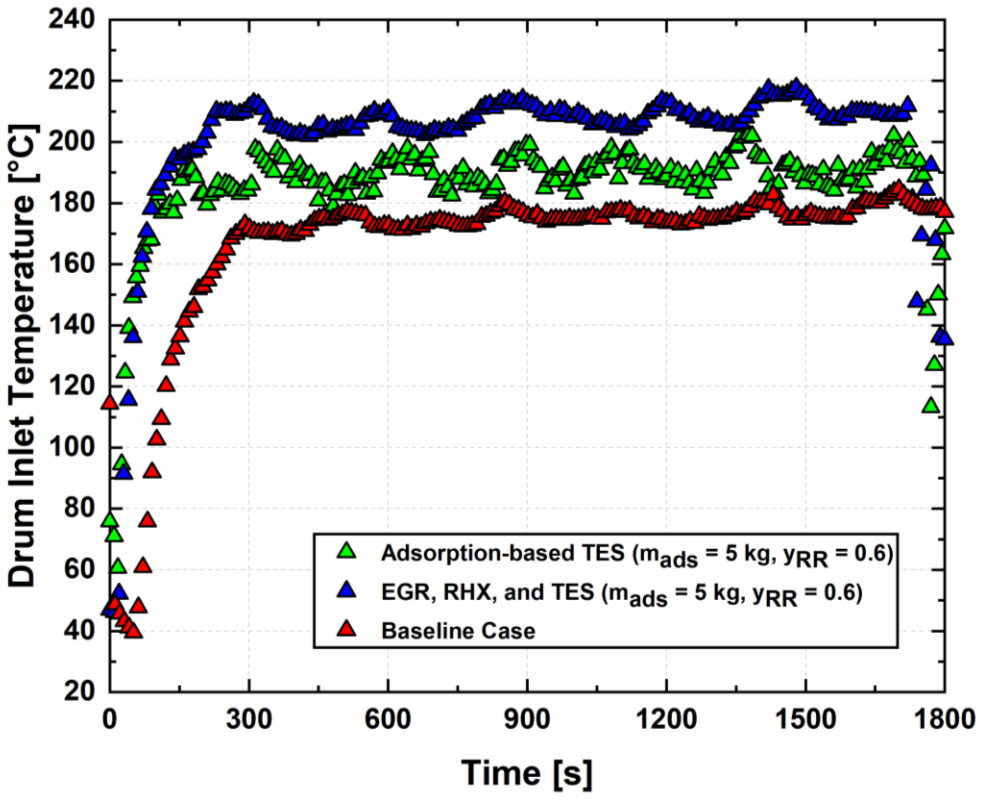

Figure 7.7: Variation of the drum inlet temperature as function of drying

Figure 7.7 shows that integrating the dryer with EGR, RHX, and adsorption-based TES increases the temperature of the air entering the drum to ~ 208°C compared to 172°C for the baseline case. When only the sorption bed is used without recuperation, the temperature of the air entering the drum is ~ 191°C. Thus, a recuperative heat exchanger increased the temperature at the inlet of the drum by ~ 17°C compared to the case with only the sorption bed. This is because the inlet air is preheated at two different locations. Initially the ambient air is sensibly heated by the exhaust air at State 8. The average temperature of the air leaving the RHX is ~ 38°C (from an ambient value of 24°C). the air stream is then mixed with the air leaving the sorption bed, which is typically at high temperature and low humidity ratio.

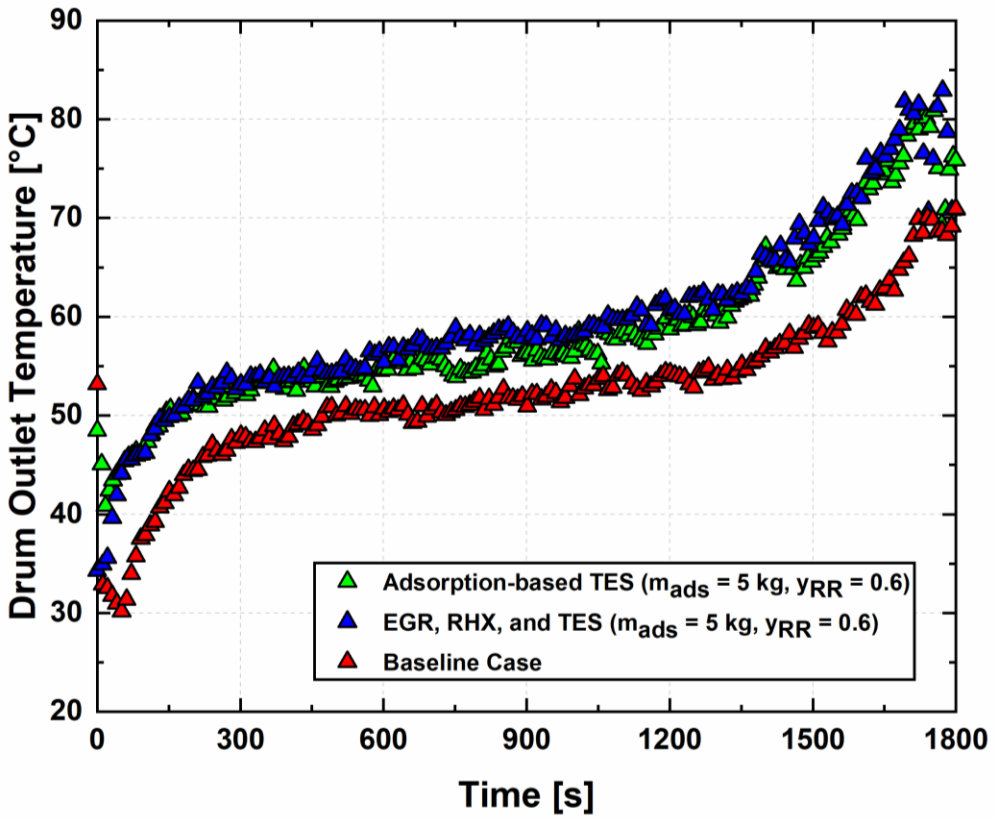

Figure 7.8: Variation of the drum exit temperature as function of drying

Figure 7.8 shows the variation of the drum outlet temperature as function of drying time. Integrating the dryer with EGR, RHX, and adsorption-based TES increases the temperature at the exit of the drum by ~ 11°C in the first and second drying phases, and by ~16°C during the last phase. An increased temperature at the inlet of the drum increases the exit temperature and therefore, also increases the evaporation rate. The temperature of the air leaving the drum in the case with EGR, RHX, and TES exceeds that of only TES by ~ 4°C, despite a larger increase in temperature (~ 13°C) at the inlet of the drum as shown in Figure 7.7. Despite almost similar exhaust temperatures for either the case of integrating EGR, RHX, and TES, or only a sorption bed, the drying performance increases

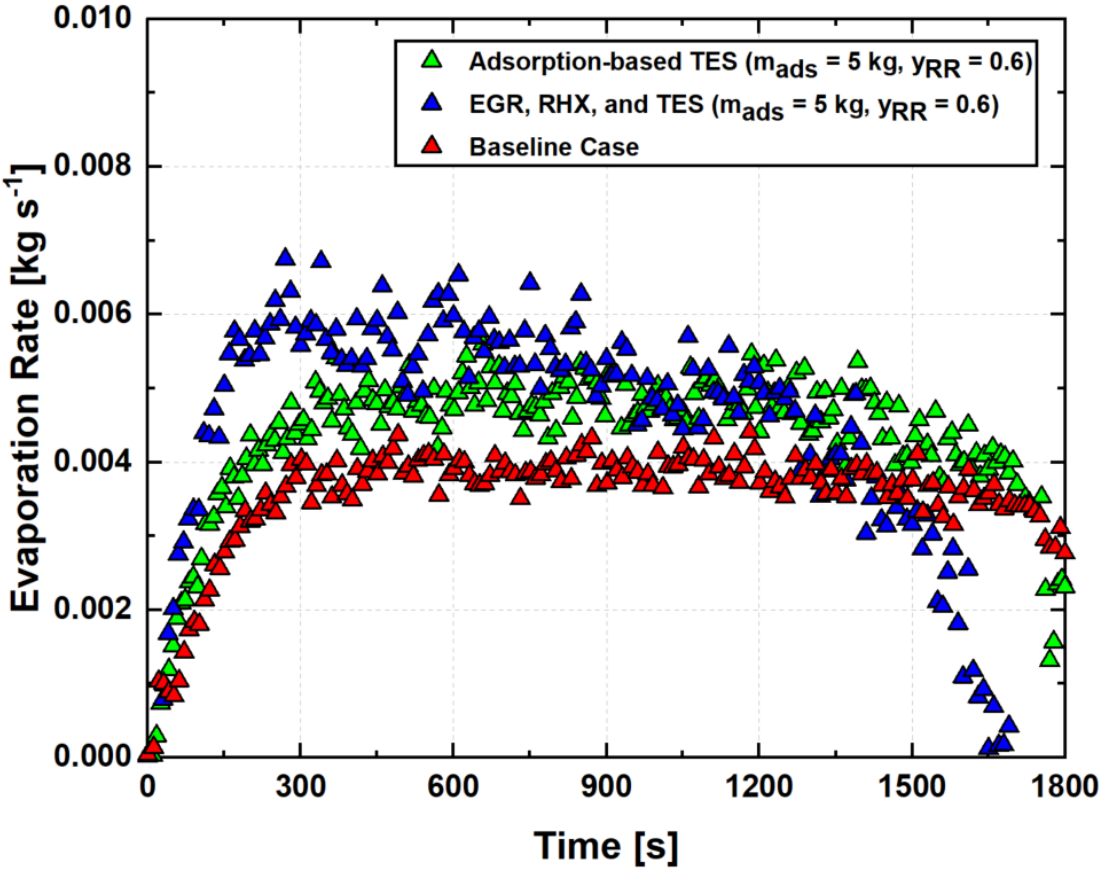

Figure 7.9: Evaporation rate as function of drying time

significantly when an RHX is added to the adsorbent bed. This, the TES alone, for m_{ads} = 8.5 kg can yield a 22% energy savings, while with m_{ads} = 5 kg, the energy savings is 13%. When an RHX is added to this m_{ads} = 5 kg case, the energy savings increase to 19%. This is mainly due to a significant increase in the temperature of the air entering the drum at the beginning of the drying period, thus evaporating most of the moisture content in the textile (Figure 7.9). To understand the effect of the increase in drum exhaust temperature on the drying performance, it is important to quantify the evaporation rate. Figure 7.9 depicts the evaporation rate measured during a single drying cycle for the three cases. The average evaporation rate for the baseline case is ~ 0.0038 kg s^{-1}, while the evaporation rate

increased to ~ 0.0044 kg s^{-1} with a sorption bed only. Additionally, when an RHX is also added to the sorption bed, the evaporation rate peaks to ~ 0.006 kg s^{-1} during the initial phase of the drying period and drops to 0.0047 kg s^{-1} towards the end of the drying cycle. Furthermore, the shape of the evaporation rate curve for EGR, RHX, and TES is different from the constant evaporation rate profile for $300 \le t \le 1500$ s. The evaporation rate (for EGR, RHX, and TES) is much higher at the beginning of the drying cycle due to an air inlet temperature that exceeds 205°C while the textile is still at a high moisture content. As the evaporation continues, the moisture content of the textile decreases significantly. As shown in Figure 7.9, the evaporation rate drops at $t = 1485$ s, which signifies that the textile has reached the desired moisture content of $\le 3.5\%$. Table 7.2 summarizes the drying performance for the experiments conducted to investigate the effect of combining the three energy saving techniques. The results show that a combination of EGR, RHX, and TES $(m_{ads} = 5 \text{ kg})$ results in a reduction energy consumption (SMER) and drying time by 18.2% and 14.2%, respectively.

Table 7.2: Energy saving techniques implemented in the gas-fired tumble dryer

	Description
High RPM	Fan motor speed of 3800 rpm compared to 3400 rpm for baseline case.
RHX	Dryer with an air-to-air aluminum plate-fin recuperative heat exchanger (plate spacing 8 mm, length 610 mm, width 203 mm.)
TES	A 5-kg silica gel type RD packed bed is integrated to the dryer. The recirculation ratio used in that experiment was 0.6.
RHX + TES	5-kg silica gel type RD packed bed and a RHX (Figure 5) installed in the dryer, with a recirculation ratio of 0.6.
RHX + TES + RPM	In addition to 5-kg silica gel packed bed and RHX, fan motor controlled up to 3600 rpm

7.4.3 Overall assessment of drying performance

An overall assessment of five energy saving techniques for gas-fired tumble dyers summarized in Table 7.3 is presented here. Figure 7.10 shows the experimentally measured drying efficiency for each of the energy saving techniques. The drying efficiency for the baseline case is measured to be 42.16 ± 2.13%. Increasing the mass flow rate of the air increased the drying efficiency to ~ 44.25%. The drying efficiency reflects the fraction of the total input energy used directly for evaporation. As the air flow rate increases, the evaporation rate increases (Equation (7.10)). When an RHX is incorporated into the dryer, the drying efficiency increases to 48.31% due to the elevated temperature at the inlet of the drum. When a sorption bed is incorporated into the dryer, the temperature of the air entering

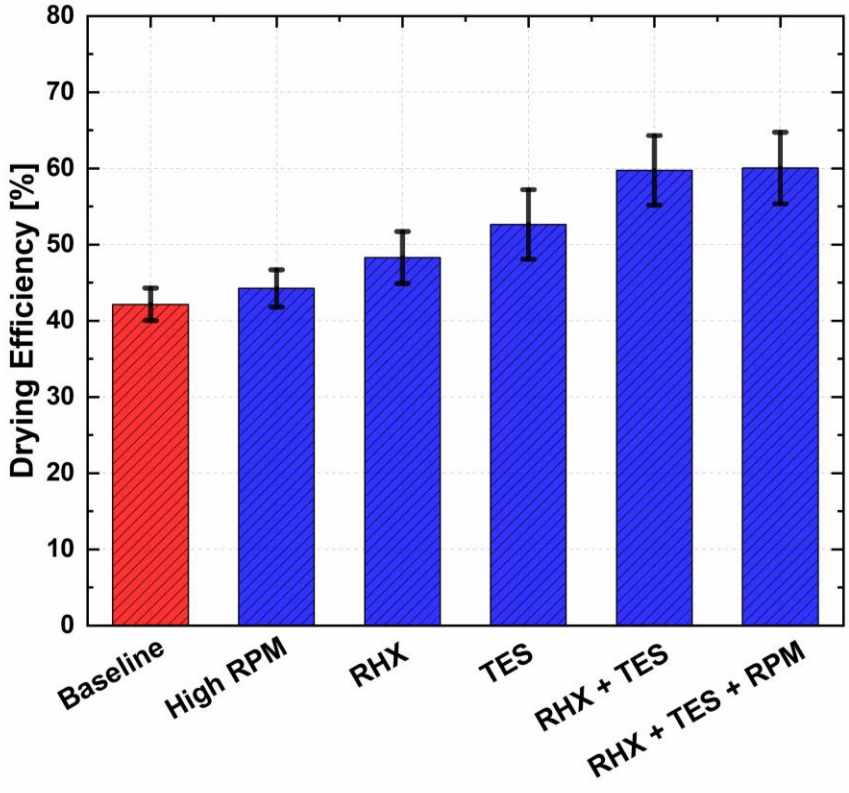

Figure 7.10: Measured drying efficiency for all energy saving techniques

the drum increases, in addition to a decrease in the air humidity ratio. The lower inlet humidity increases the difference in water vapor partial pressure, which is the driving force for drying. The drying efficiency improves appreciably with the use of a sorption bed. The combined effects of a higher mass flow rate, RHX, and a sorption bed increase the drying efficiency to 60.05%.

Figure 7.11 shows the measured drying time for each of the investigated techniques. The drying time was initially 1752 ± 14 s; however, increasing the mass flow rate of the air, adding an RHX, and adding a sorption bed decreased the drying time by 140 s, 186 s,

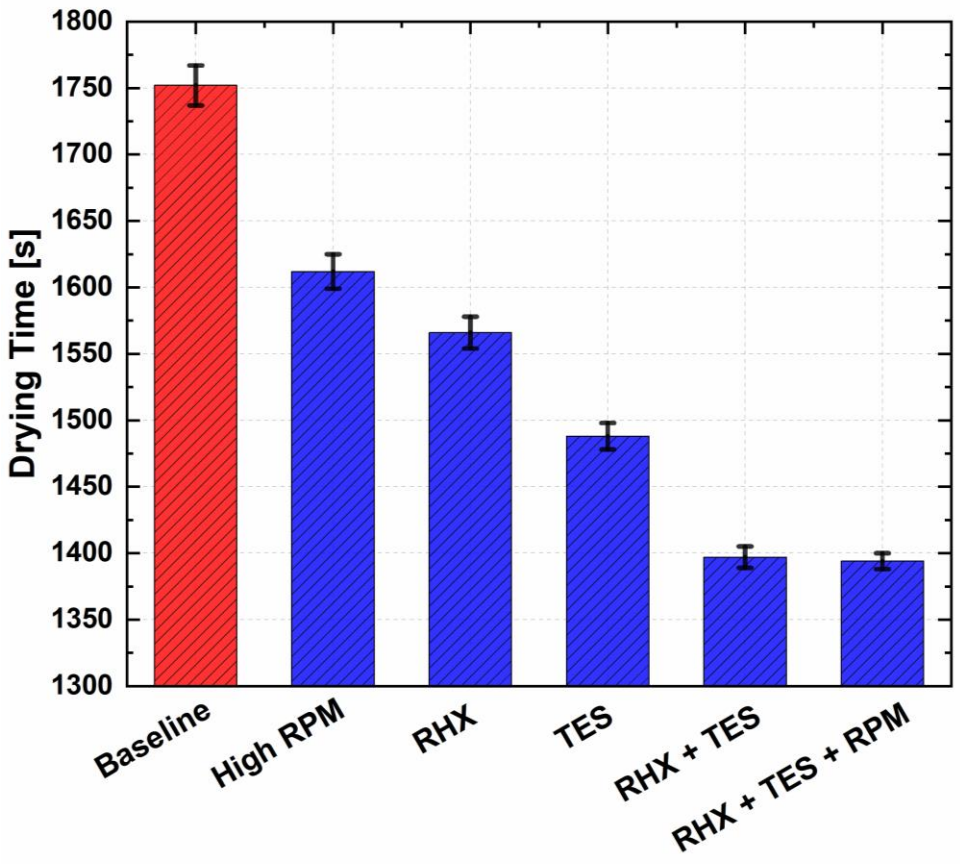

Figure 7.11: Measured drying time for all energy saving techniques

Table 7.3: Overall drying performance

y_{RR} = 0.6	Baseline case	Adsorption-based TES (m_{ads} = 5 kg)	EGR, RHX, and TES (m_{ads} = 5 kg)
$\dot{m}_{evap} \times 10^3$, kg s^{-1}	3.816	4.391	4.644
Drying time. s	1752	1503	1421
SMER, kWh kg_w^{-1}	1.456	1.268	1.191

and 264 s, respectively. With an RHX and a sorption bed, the drying time decreases to 1397 s, mainly due to the favorable conditions at the inlet of the dryer, i.e., the higher temperature and lower inlet humidity ratio, which helps to increase the evaporation rate by ~ 15% compared to the baseline case.

Figure 7.12 shows the measured specific moisture extraction ratio (SMER) for each of the energy saving technologies. An RHX decreases the energy consumption by ~ 7.34%. An adsorption-based TES increases the energy savings and results in an SMER of 1.245 kWh kg^{-1}. Combining the dryer with an RHX and TES decreases the SMER further to ~ 1.172 kWh kg^{-1}. This signifies a reduction in energy consumption by ~ 19.5% despite a slight increase in fan power (0.29 kW as compared to 0.2 kW for the baseline case) to overcome the additional pressure drop induced by the sorption bed and the RHX. The fan power represents 1.7% of the total power added to the dryer. However, with RHX and TES, an increase in mass flow rate of ~ 8% at a higher fan speed results in additional energy savings. As shown in Figure 7.12, the energy consumption with increased RPM, RHX, and TES decreases by 19.7% and results in an SMER of 1.168 kWh kg^{-1}. The increase in air mass flow rate increases evaporation, which results in a slightly shorter time than with only the RHX and TES.

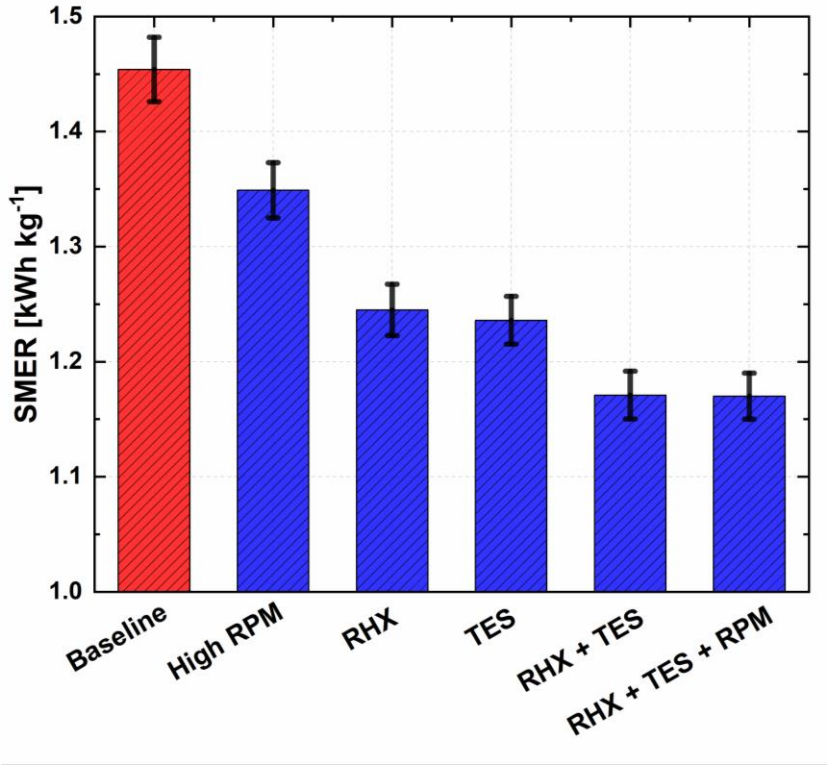

Figure 7.12: Measured specific moisture extraction ratio (SMER) for all energy saving techniques

7.5 Conclusion

Waste heat recovery, thermal energy storage, and heat pumping in a commercial gas-fired tumble dryer were investigated numerically and experimentally. Installing an adsorption heat pump in a single dryer showed that due to the air bleed required to drive the heat pump, i.e., the reduction in the air flow rate entering the drum, the evaporation rate actually decreases. However, integrating an adsorption heat pump into a bank of commercial dryers that can operate at high temperatures, i.e., $T_{in}^{drum} \geq 250°C$, can reduce the energy consumption and overall drying time. EGR, RHX, and TES were investigated individually with a focus in this study on the effect of combining these three technologies. Exhaust gas recirculation, waste heat recovery through recuperation, adsorption-based thermal energy

storage, and heat pumping were investigated to achieve a reduction in energy consumption and drying time. Combining the effects of exhaust gas recirculation with an air-to-air cross flow heat exchanger, and a 5-kg silica gel bed was able to experimentally demonstrate a specific moisture extraction ratio of 1.174 kWh kg_w^{-1} and reduce drying time by ~ 355 s. This is a reduction in energy consumption by 18.2% compared to the baseline gas-fired tumble dryer. The results from this study offer several paths for decreasing the energy consumption of dryers to provide vendors with a multitude of options with graduated improvements in efficiency and drying time for incremental feature additions.

CHAPTER 8. CONCLUSION

8.1 Overview

A comprehensive study on energy saving techniques for a commercial gas-fired tumble dryer is presented. Detailed investigations of the pore-level underlying heat and mass transfer phenomena, component-level design and analysis, and full system integration were performed. To understand the drying process and the corresponding complex transport phenomena, a lumped model as well as a 2-D transient model were developed. The models were experimentally validated on an 11.33-kg capacity commercial gas-fired tumble dryer. The effects of varying airflow $(0.165 \le \dot{V}_a \le 0.283\ \mathrm{m^3 s^{-1}})$, fuel flow rate $(33 \le y_{fuel} \le 100\%)$, mass of the bone-dry textile $(1.92 \le m_{cl,dry} \le 11.33\ \mathrm{kg})$, initial moisture content $(50 \le X \le 150\%)$, and drum rotational speed $(39 \le \Omega_d \le 64\ \mathrm{rpm})$ were explored. Waste heat recovery, thermal energy storage, and heat pumping energy saving techniques were investigated. In particular, exhaust gas recirculation (EGR), recuperation (RHX), adsorption-based thermal energy storage (TES) system, and adsorption heat pump (AHP) were considered. Additionally, the effect of combining EGR, RHX, and TES was explored.

The literature on drying theory and underlying transport transfer phenomena, identification of the most energy-consuming stages in the process, and assessment of the potential for energy savings was revised. The majority of the energy-saving methods applied to convective textile drying are based on heat recovery from the exhaust air, either by recirculating it or with the use of a heat exchanger. Other energy saving methods include

modifications to the main cycle operation to make better use of the available energy. For instance, heat modulation is a very common technique that tends to save a significant amount of energy; however, it extends the drying time significantly. Other methods include changing open-cycle, air-vented dryers to closed-cycle HPDs. “Not-in-kind” dryers including thermoelectric-powered, sorption-driven, and ultrasonic dryers have shown promising enhancement in energy performance.

Lumped-parameter and 2-D transient models for a commercial gas-fired tumble dryer were developed. The dryer was dived into four submodules: the combustor, the drum, the lint filter cabinet, and the exhaust fan. The lumped-parameter model was developed to analyze the effect of integrating several energy saving techniques with a gas-fired tumbler dryer. The 2-D transient model for the commercial gas-fired tumble dryer was developed to understand heat and moisture transfer within the textile based on the moving evaporation front approach. The model accounted for the heat and mass transfer processes in the drum without input from the experiments, and showed good agreement with experimental data and with the lumped-parameter model. The lumped-parameter and 2-D transient models predicted the drying performance (SMER) with AADs of 7.9% and 7.5%, respectively.

Two methods to recover the waste heat from the exhaust stream, typically at $T \leq 55°\mathrm{C}$, were investigated. They included recovery of waste heat from a commercial gas-fired tumble dryer through exhaust gas recirculation and recuperative heat exchange. The recirculation of the exhaust gas tends to increase the temperature in the drum while also increasing the moisture, which indicates the existence of an optimal recirculation ratio. A recirculation ratio of 51% was found to be optimal in reducing the specific moisture extraction ratio and drying time by 9% and 164 s, respectively. To avoid the rise in

humidity associated with recirculation, a compact plate-fin heat exchanger was used to recuperatively preheat the air entering the combustor. Energy savings of ~15% and reduction in drying time by 216 s over the baseline case were demonstrated.

An experimental study of textile drying in a commercial gas-fired tumble dryer was performed to analyze the influence of inlet conditions on energy consumption, drying efficiency, and drying time. The effects of varying airflow, fuel flow rate, mass of the bone-dry textile, initial moisture content, and drum rotational speed were investigated. Insights from the experiments show that varying the air flowrate had the strongest influence on the performance of the dryer. Additionally, the results from the experiments showed that the drying time can be reduced by up to 162 s from the baseline value of 1725 s while also decreasing the SMER to 1.31 kWh kg^{-1}, i.e., a 9.65% reduction compared to the baseline case. The data were used to develop correlations to predict dryer performance. Reduced-order models to predict the drying time, drying efficiency, and SMER were also developed. The results showed that the SMER is influenced by all the inlet parameters; however, there is a low dependence on the rotational speed of the drum. These correlations can be used as tools to optimize dryer performance and implement control algorithms in commercial gas-fired tumble dryers to reduce energy consumption and drying time.

A novel adsorption-based thermal energy storage system was also investigated. An adsorbent bed is used to capture waste heat from the exhaust stream, store, and reuse it in the current and subsequent drying cycles. The warm and humid exhaust stream from the dryer passes through the sorption bed. During the adsorption phase, the humidity from the exhaust stream is adsorbed onto the surface of the silica gel, releasing the heat of adsorption. Without the addition of any auxiliary energy source, the sorption bed is

regenerated from the same exhaust stream while taking advantage of the water vapor partial pressure swing that occurs as drying proceeds. A 1-D transient heat and mass transfer model is developed to capture the dynamics of the thermal storage system, and validated experimentally on a 11.33-kg capacity gas-fired tumble dryer. The sorption bed reduces the overall energy consumption by 22%, while increase the drying efficiency to 60.7%.

Waste heat recovery, thermal energy storage, and heat pumping were also considered individually and in combined installations. An adsorption heat pump applied to a single dryer with hot gas bleed driving the bed was not found to be very effective because the resulting reduced air flow entering the drum decreases the evaporation rate. However, an adsorption heat pump applied to a bank of dryers that operate at high temperatures, i.e., $T_{in}^{drum} \geq 250°C$ could reduce the energy consumption and overall drying time. The use of EGR with an air-to-air cross flow heat exchanger, and a 5-kg silica gel bed yields a specific moisture extraction ratio of 1.174 kWh kg_w^{-1} and reduces drying time by ~ 355 s. This is a reduction in energy consumption by 18.2% compared to the baseline gas-fired tumble dryer. Adoption of these energy saving techniques in gas-fired tumble dryers across the U. S. market could reduce primary energy consumption by ~ 4.17×10^7 GJ (11.6 billion kWh) annually, as shown in Figure 8.1.

Residential textile dryers typically have a dry load capacity that ranges between 2 – 8.1 kg, while that of commercial textile dryers ranges between 8.1 – 44.9 kg. The cycles are run back to back (~ 90 cycles/week) in most commercial dryers, while the frequency of drying cycles in residential dryers is low (~ 2 cycles/week). In this study, the energy savings were demonstrated on a commercial gas-fired tumble dryer with a maximum dry

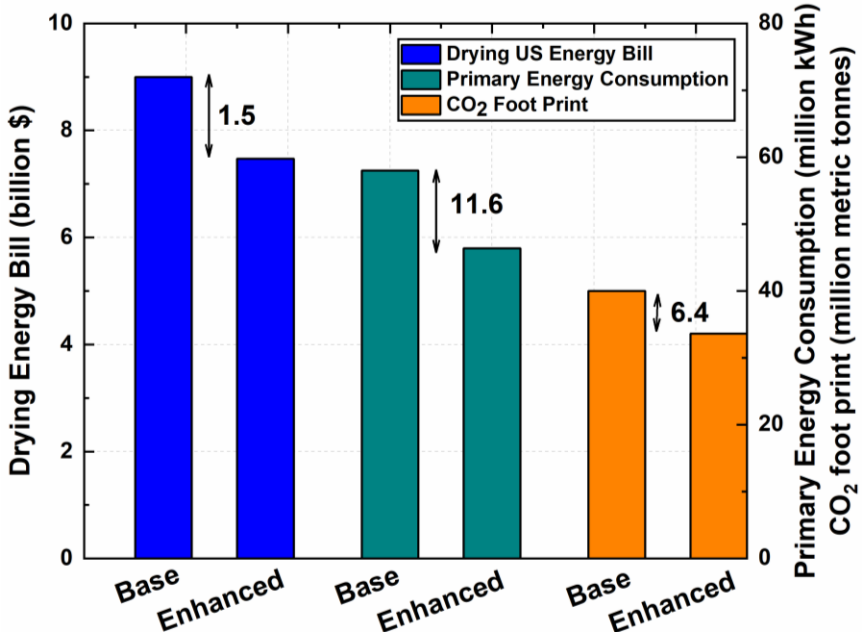

Figure 8.1: Impact of adopting the energy saving techniques on all the convective textile dryers in the US.

load capacity of 11.33 kg. Nonetheless, many of the demonstrated energy saving techniques (EGR, RHX, TES, and HP) can be adjusted and integrated into a residential dryer. Some additional considerations should be addressed while retrofitting these energy saving techniques into a residential dryer. Waste heat recovery methods such as exhaust gas recirculation and recuperation have been investigated in literature. In fact, a higher recirculation ratio is expected in residential dryers due to the humidity ratio of the air at the exit of the dryer being lower than that in commercial dryers. Implementing a recuperative heat exchanger in a residential textile dryer has been demonstrated in literature. It is essential to resize the heat exchanger based on the exit temperature and humidity ratio of the dryer, i.e., the inlet of the hot stream of the heat exchanger. Similarly, integrating an adsorption-based thermal energy storage system is feasible. Since the adsorption-based TES system is advantageous to the current cycle and the next drying cycles, this will make

it a viable option for residential dryers too, despite having drying cycles that are not running back to back. Thermal energy in the exhaust stream is stored in the adsorbent as chemical potential, thus charging it for the next cycle. Karmakar et al. (2020) showed that if the adsorbent is reasonably isolated from ambient air, water vapor uptake in the adsorbent layer would remain relatively unchanged between cycles. The worst case is that the adsorbent layer equilibrates with moisture in the quiescent ambient air, which will still leave substantial dehumidification capability using exhaust air that is typically at 40-55°C, with a relative humidity of ~ 50-60%. Commercial textile dryers are used more often than residential dryers, minimizing this concern. In commercial dryers, in addition to energy stored as chemical potential in the adsorbent, sensible energy reclaimed from hot adsorbent can also be used in more frequent cycles with minimal losses. Additional consideration in designing and sizing the adsorption beds to adjust the switching time between the adsorption and desorption phase, and also, the differences in the frequency of use of residential and commercial dryers, should be considered to determine the enhancement appropriate for each application.

8.2 Recommendations for Future work

The present study was successful in simulating, developing, and demonstrating energy saving techniques for gas-fired textile drying. The computational models developed to predict the performance of the dryer and the data can be used for further research as discussed below.

- The mathematical models were developed for a gas-fired tumble dryer at fixed capacity of 11.33 kg; however, in future investigations, a generic model that can

account to change in the dry mass load and drum dimensions should be developed. This can help in quantifying the effective heat and mass transfer area. A correlation relating the effective areas with drying performance can help in providing design guidelines to maximize evaporation.

- The models and experiments were conducted on the standardized 100% cotton load of terrycloth towels. In reality, the textile load is a combination of cotton, wool, nylon, silk, etc. Each of these materials exhibit difference surface and thermophysical properties. Therefore, different textile material would have different evaporation rates for the same moisture content. This due to the fact that the falling rate phase for each of these textiles starts at different drying times and moisture contents. The critical moisture content for each type of textile can be derived from Lambert et al. (1991)'s water activity correction. The critical moisture content is achieved when the correction factor is less than unity. The critical moisture content of wool and nylon are estimated to be 0.37 and 0.22, respectively. In future studies, the effect of different material should be taken into account to avoid under or over predicting the drying time or energy consumption.

- The experiments were conducted on a gas-fired tumble dryer with a self-controlled combustor that limited some of the experiments, specifically when the temperature of the air at the inlet of the drum exceeds 220°C. Additional energy savings can be demonstrated with high recirculation ratios and adsorbent masses if the combustor is able to function at temperatures ranging between 220 – 250°C without scorching of the textile.

- In the experiments and simulations, air leakage was quantified based on a correlation from the literature that takes the measured pressure difference between the inlet and the outlet of the dryer as inputs. Leakage has a significant effect on drying efficiency and drying time, and better characterization of leakage can enable optimal performance. A full accounting of leakage and air flow rates at various locations (not just in the drum) in the dryer air flow path is essential to achieving an accurate energy balance and, therefore, better agreement with data.

- Adding an adsorption heat pump to a single commercial dryer showed that the evaporation rate was reduced by ~7% due to the bleed of airflow rate used to drive the heat pump. In future investigations, an adsorption heat pump coupled to a bank of dryers at high temperature should be investigated to achieve additional energy savings.

- The present work has provided a suite of options for improving the energy efficiency and drying time in tumble dryers with implications on commercial and residential applications. Depending on the application under consideration, some or all of these options, such as insulation, drum rotation speed, recirculation, recuperation, thermal storage, and heat pumping can be implemented to significantly reduce energy consumption and CO_2 emissions in this ubiquitous energy intensive market.

APPENDIX A. EXPERIMENTAL DATA AND UNCERTAINTY PROPAGATION ANALYSIS

This appendix presents the approach used to analyze a representative data point to predict the performance of the gas-fired tumble dryer. The methods to calculate the SMER, drying efficiency, and drying time are presented below for the baseline case.

A.1 Baseline experiments

The instrumentation mounted to the experimental test facility is shown in Figure A.1.

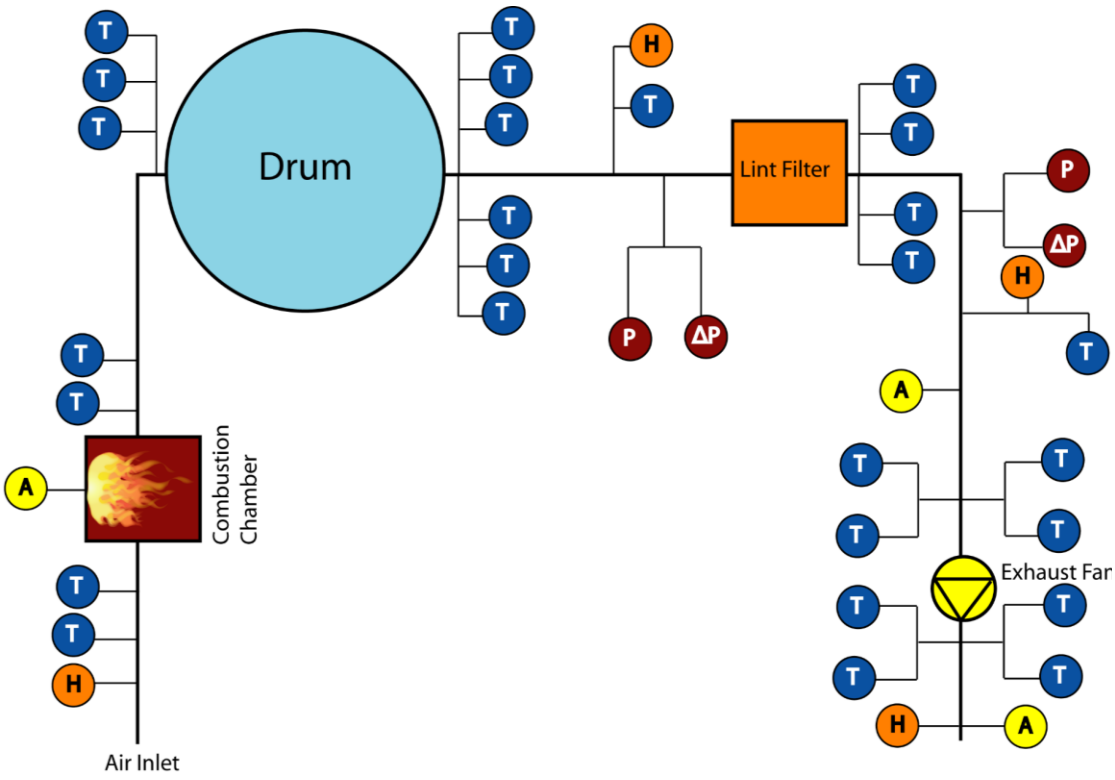

Figure A. 1: Schematic of the instrumentation installed on the dryer for the baseline experiments. *T*: Thermocouple, *H*: Humidity sensor, *A*: Anemometer, *P*: Absolute pressure, and *ΔP*: Differential pressure

Conditions: Baseline, 100% cotton terrycloth towels, $\dot{Q}_{comb} = 18.8$ kW, $m_{cl,dry}$ = 7.66 kg, $m_{cl,wet} = 14.16$ kg, $\Omega_d = 48$ rpm, $T_{amb} = 24°C$, $RH_{amb} = 0.5$, $t = 900$ s		
Inputs/Measurements	**Equations**	**Results**
Thermophysical properties		
T_{amb} = 24 ± 2 °C $RH_{amb} = 40 \pm 5\%$ $P_{amb} = 100.62 \pm 0.34$ kPa	$\omega = f(T_{amb}, RH_{amb}, P_{amb})$ $\rho = f(T_{amb}, RH_{amb}, P_{amb})$ $k = f(T_{amb}, RH_{amb}, P_{amb})$ $c_p = f(T_{amb}, RH_{amb}, P_{amb})$ $h = f(T_{amb}, RH_{amb}, P_{amb})$ $\Pr = f(T_{amb}, RH_{amb}, P_{amb})$	$\omega = 0.007092 \pm 0.000955$ kg kg^{-1} $\rho = 1.175 \pm 0.004$ kg m^{-3} $k = 0.02547 \pm 0.0003$ W m^{-1} K^{-1} $c_p = 1.018 \pm 0.002$ kJ kg^{-1} K^{-1} $h = 42.15 \pm 2.51$ kJ kg^{-1} $\Pr = 0.73110 \pm 0.00038$
Initial Moisture Content		
$m_{cl,dry}$ = 7.66 ± 0.23 kg $m_{cl,wet}$ = 14.16 ± 0.42 kg	$m_{cl,wet} = m_{cl,dry}(1 + X_{init})$	X_{init} = 0.8486 ± 0.08178
State 1: Inlet to dryer/combustor		
$D_{in} = 0.155 \pm 0.008$ m $\rho_{in} = 1.173 \pm 0.0235$ kg m^{-3} V_{in} = 5.46 ± 0.51 m s^{-1} $P_{in} = 100.62 \pm 0.34$ kPa $RH_{in} = 40 \pm 5\%$ T_{in} = 24 ± 2°C	$A_{inlet,duct} = \pi D_{in}^2 / 4$ $\dot{V}_{in} = V A_{inlet,duct}$ $\dot{m}_{in} = \rho_{in} \dot{V}_{in}$ $h_{in} = f(T_{in}, RH_{in}, P_{in})$ $\omega_{in} = f(T_{in}, RH_{in}, P_{in})$	$A_{inlet,duct} = 0.01887 \pm 0.00195$ m^2 $\dot{V}_{in} = 0.1032 \pm 0.0144$ m^3 s^{-1} $\dot{m}_{in} = 0.1210 \pm 0.0168$ kg s^{-1} $h_{in} = 42.15 \pm 2.51$ kJ kg^{-1} $\omega_{in} = 0.007092 \pm 0.000955$ kg kg^{-1}
State 2: Inlet to drum/ exit of combustor		
$\dot{V}_{fuel} = 21.22 \pm 0.31$ L min^{-1} $\rho_{fuel} = 0.8972$ kg m^{-3} $T_3 = 186.45 \pm 0.25$ °C $T_4 = 184.36 \pm 0.25$ °C $T_5 = 185.74 \pm 0.25$ °C $T_6 = 185.56 \pm 0.25$ °C $T_7 = 183.87 \pm 0.25$ °C $RH_{in}^{drum} = 0.133 \pm 0.040\%$	$\dot{m}_{fuel} = \rho_{fuel} \dot{V}_{fuel}$ $T_{in}^{drum} = \frac{1}{5} \sum_{i=3}^{7} T_i$ $h_{in}^{drum} = f(T_{in}^{drum}, RH_{in}^{drum}, P_{in})$ $\rho_{in}^{drum} = f(T_{in}^{drum}, RH_{in}^{drum}, P_{in})$ $\omega_{in}^{drum} = f(T_{in}^{drum}, RH_{in}^{drum}, P_{in})$	$\dot{m}_{fuel} = (3.173 \pm 0.046) \times 10^{-4}$ kg s^{-1} $T_{in}^{drum} = 185.20 \pm 0.11$°C $\omega_{in}^{drum} = 0.007983 \pm 0.002862$ kg kg^{-1} $\rho_{in}^{drum} = 0.7611 \pm 0.0029$ kg m^{-3} $h_{in}^{drum} = 209.98 \pm 8.16$ kJ kg^{-1}
State 3: Outlet of the drum		
$P_{out} = 98.46 \pm 0.29$ kPa $T_8 = 46.99 \pm 0.25$ °C $T_9 = 46.97 \pm 0.25$ °C	$T_{out}^{drum} = \frac{1}{7} \sum_{i=8}^{14} T_i$ $h_{out}^{drum} = f(T_{out}^{drum}, RH_{out}^{drum}, P_{out})$	$T_{out}^{drum} = 46.90 \pm 0.09$°C $h_{out}^{drum} = 160.10 \pm 5.01$ kJ kg^{-1}

$T_{10} = 47.15 \pm 0.25$ °C $T_{11} = 45.72 \pm 0.25$ °C $T_{12} = 46.34 \pm 0.25$ °C $T_{13} = 47.49 \pm 0.25$ °C $T_{14} = 47.64 \pm 0.25$ °C $RH_{out}^{drum} = 61.1 \pm 2.5\%$	$\rho_{out}^{drum} = f\left(T_{out}^{drum}, RH_{out}^{drum}, P_{out}\right)$ $\omega_{out}^{drum} = f\left(T_{out}^{drum}, RH_{out}^{drum}, P_{out}\right)$	$\rho_{out}^{drum} = 1.045 \pm 0.003$ kg m^{-3} $\omega_{out}^{drum} = 0.04367 \pm 0.00193$ kg kg^{-1}
State 4: Lint filter/Exhaust Fan/		
$P_{out} = 98.24 \pm 0.28$ kPa $V_{air} = 12.29 \pm 0.51$ m s^{-1} $D_{out} = 0.140 \pm 0.008$ m $T_{15} = 46.45 \pm 0.25$ °C $T_{16} = 46.12 \pm 0.25$ °C $T_{17} = 46.53 \pm 0.25$ °C $T_{18} = 44.99 \pm 0.25$ °C $T_{19} = 45.65 \pm 0.25$ °C $T_{20} = 47.13 \pm 0.25$ °C $T_{21} = 47.24 \pm 0.25$ °C $RH_{out}^{dryer} = 59.7 \pm 2.5\%$	$\Delta P_{LF} = P_{in} - P_{out}$ $A_{out,duct} = \pi D_{out}^2 / 4$ $\dot{V}_{out} = VA_{out,duct}$ $\dot{m}_{out} = \rho_{out}^{dryer} \dot{V}_{out}$ $T_{out}^{dryer} = \frac{1}{7}\sum_{i=15}^{21} T_i$ $h_{out}^{dryer} = f\left(T_{out}^{dryer}, RH_{out}^{dryer}, P_{out}\right)$ $\rho_{out}^{dryer} = f\left(T_{out}^{dryer}, RH_{out}^{dryer}, P_{out}\right)$ $\omega_{out}^{dryer} = f\left(T_{out}^{dryer}, RH_{out}^{dryer}, P_{out}\right)$	$A_{out,duct} = 0.01533 \pm 0.00175$ m^2 $\dot{V}_{out} = 0.1884 \pm 0.0229$ m^3 s^{-1} $\dot{m}_{out} = 0.1976 \pm 0.0241$ kg s^{-1} $T_{out}^{dryer} = 46.30 \pm 0.09$°C $h_{out}^{dryer} = 153.20 \pm 4.82$ kJ kg^{-1} $\rho_{out}^{dryer} = 1.049 \pm 0.003$ kg m^{-3} $\omega_{out}^{dryer} = 0.04363 \pm 0.00189$ kg kg^{-1}
Evaporation Rate		
$T_{in}^{drum} = 185.20 \pm 0.11$°C $RH_{in}^{drum} = 0.133 \pm 0.040\%$ $T_{out}^{drum} = 46.90 \pm 0.09$°C $RH_{out}^{drum} = 61.1 \pm 2.5\%$ $\dot{m}_{in} = 0.1210 \pm 0.0168$ kg s^{-1}	$\dot{m}_e = \dot{m}_{in}\left(\omega_{out}^{drum} - \omega_{in}^{drum}\right)$	$\dot{m}_e = 0.004318 \pm 0.000732$ kg s^{-1}

To quantify the total amount of water evaporated from the textile, the above procedure is repeated for each time step (1 s) in the drying cycle (1800 s).

$$m_{w,r} = \int_{t}^{t+dt} \dot{m}_e dt \tag{A.1}$$

$$X(t) = \frac{1}{m_{cl,dry}}\left(X_i m_{cl,dry} - \int_0^t \dot{m}_e dt\right) \tag{A.2}$$

A.2 Baseline Drying Performance

The time needed to reach the desired moisture content of < 3.5% is 1716 s; however, taking into account the upper and lower bounds of the uncertainty propagation the conservative time required to reach the desired moisture content is 1725 s.

Conditions: Baseline, 100% cotton terrycloth towels, $\dot{Q}_{comb} = 18.8$ kW, $m_{cl,dry}$ = 7.66 kg, $m_{cl,wet} = 14.16$ kg, $\Omega_d = 48$ rpm, $T_{amb} = 24°C$, $RH_{amb} = 0.5$, $t = 900$ s		
Inputs/Measurements	**Equations**	**Results**
Drying Efficiency		
$\dot{m}_e = 0.004318 \pm 0.000732$ kg s^{-1} $\dot{Q}_{comb} = 18.87 \pm 0.34$ kW $\dot{W}_{fan} = 0.176 \pm 0.012$ kW $\dot{W}_{drum} = 0.187 \pm 0.012$ kW $T_{cl} = 39.16 \pm 0.25°C$ $PEF = 2.66$ (calculated from EIA based on December 2019 – Monthly Report)	$\dot{E}_{in} = \dot{Q}_{comb} + PEF\left(\dot{W}_{fan} + \dot{W}_{drum}\right)$ $\dot{Q}_{evap} = \dot{m}_e h_{fg}\left(T_{cl}\right)$ $\eta_{d,i} = \dot{Q}_{evap} / \dot{E}_{in}$ $\overline{\eta}_d = \frac{1}{N}\sum_{i=1}^{1800} \eta_{d,i}$	$\dot{E}_{in} = 19.84 \pm 0.34$ kW $\dot{Q}_{evap} = 9.13 \pm 0.31$ kW $\eta_{d,i} = 0.4811 \pm 0.0837$ $\overline{\eta}_d = 0.4123 \pm 0.0746$
Specific Moisture Extraction Ratio (SMER)		
$t_{dry} = 1725 \pm 8$ s $\dot{E}_{in} = 19.84 \pm 0.34$ kW $m_{w,r} = 6.713 \pm 0.213$ kg	$E_{in} = \int_0^{t_{drt}} \dot{E}_{in} dt$ $SMER = \frac{E_{in}}{m_{w,r}}$	$E_{in} = 9.55 \pm 0.17$ kWh $SMER = 1.423 \pm 0.051$ kWh kg^{-1}

APPENDIX B. AIR GATE CALIBRATION

B.1 Exhaust Gas Recirculation

As mentioned previously, the procedure described in detail in A.1 is used to analyze the experimental data for the recirculation experiments. Figure B.2 shows a schematic of the LabVIEW interface with number of sensors and actuators indicated on each state.

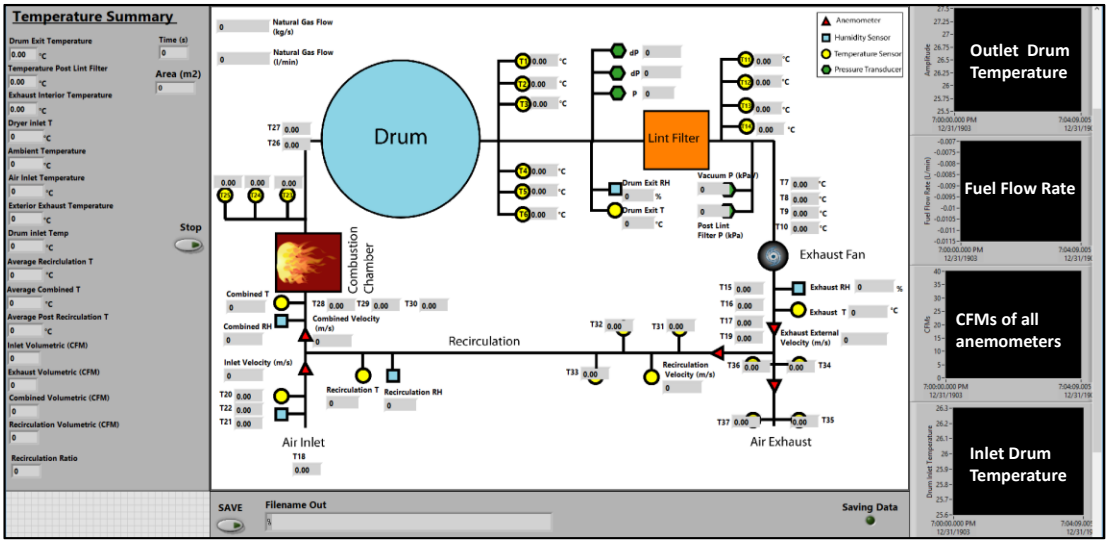

Figure B. 1: Schematic of the instrumentation installed on the dryer for the exhaust gas recirculation experiments.

The air gates used to control total airflow in the experiments are “self-cleaning” blast gates, as shown in Figure B.2. The configuration of the air gate minimizes the buildup of lint, but has an accessible slider that can be cleaned after each experiment. Additionally, a locking screw is available to hold the air gate at the desired opening fraction.

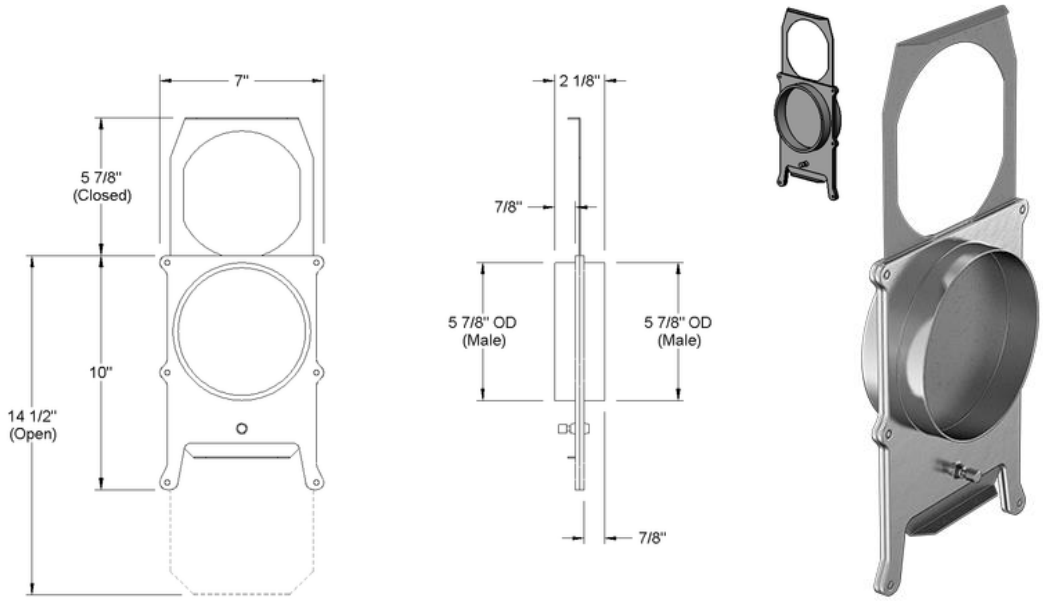

Figure B. 2: A schematic of the air gate used in the recirculation experiments.

To accurately quantify the required opening cross sectional area of the air gate to meet the desired recirculation ratio, a set of calibration experiments was performed. An additional air damper was installed for finer control of the flowrates. The results of the calibration experiments are tabulated in Table B.1. As shown in Figure B.3, the cross sectional area was varied from 0 to 100%, where 100% represents a fully opened gate.

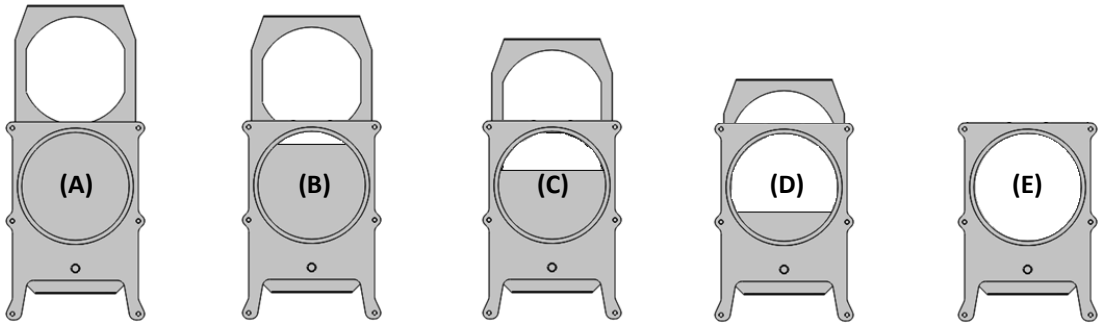

Figure B. 3: A schematic of the calibration experiments for the air gate.

Table B. 1: The results of the calibration experiments

	Case A	Case B	Case C	Case D	Case E
Opened area	0 m^2	0.0104 m^2	0.0279 m^2	0.0524 m^2	0.0699 m^2
Area fraction	0%	15%	40%	75%	100%
Recirculation Ratio	0	0.24	0.55	0.82	1.0

B.2 Exhaust Gas Recirculation Sample Calculation

Conditions: Exhaust gas recirculation calibration, y_{RR} = 0.5		
Inputs/Measurements	**Equations**	**Results**
State 4: Lint filter/Exhaust Fan/		
$V_1 = 12.54 \pm 0.51$ m s^{-1} $V_2 = 4.97 \pm 0.51$ m s^{-1} $D_1 = 0.140 \pm 0.008$ m $D_2 = 0.155 \pm 0.008$ m State 1: Exhaust of the dryer State 2: Recirculated air 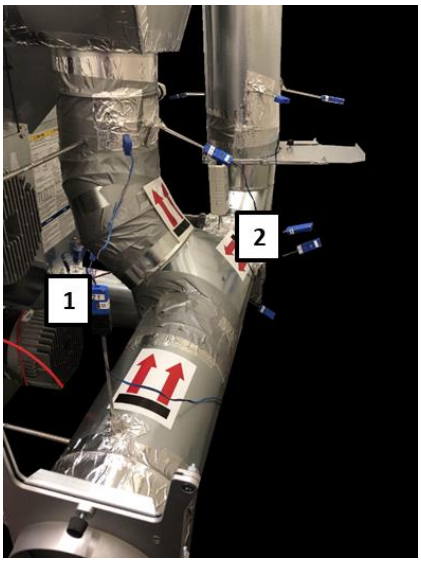 	$A_1 = \pi D_1^2 / 4$ $A_2 = \pi D_2^2 / 4$ $\dot{V}_1 = V_1 A_1$ $\dot{V}_2 = V_2 A_2$ $y_{RR} = \frac{\dot{V}_2}{\dot{V}_1}$	$A_1 = 0.01539 \pm 0.00176$ m^2 $A_1 = 0.01887 \pm 0.00195$ m^2 $\dot{V}_1 = 0.1931 \pm 0.0234$ m^3 s^{-1} $\dot{V}_1 = 0.09378 \pm 0.0136$ m^3 s^{-1} $y_{RR} = 0.486 \pm 0.092$

APPENDIX C. RECUPERATIVE HEAT EXCHANGER

C.1 Recuperation experiments

The procedure described follows the steps described in Appendix A.1. A schematic showing the instrumentation mounted to the test facility for the recuperation experiments is depicted in Figure C.1

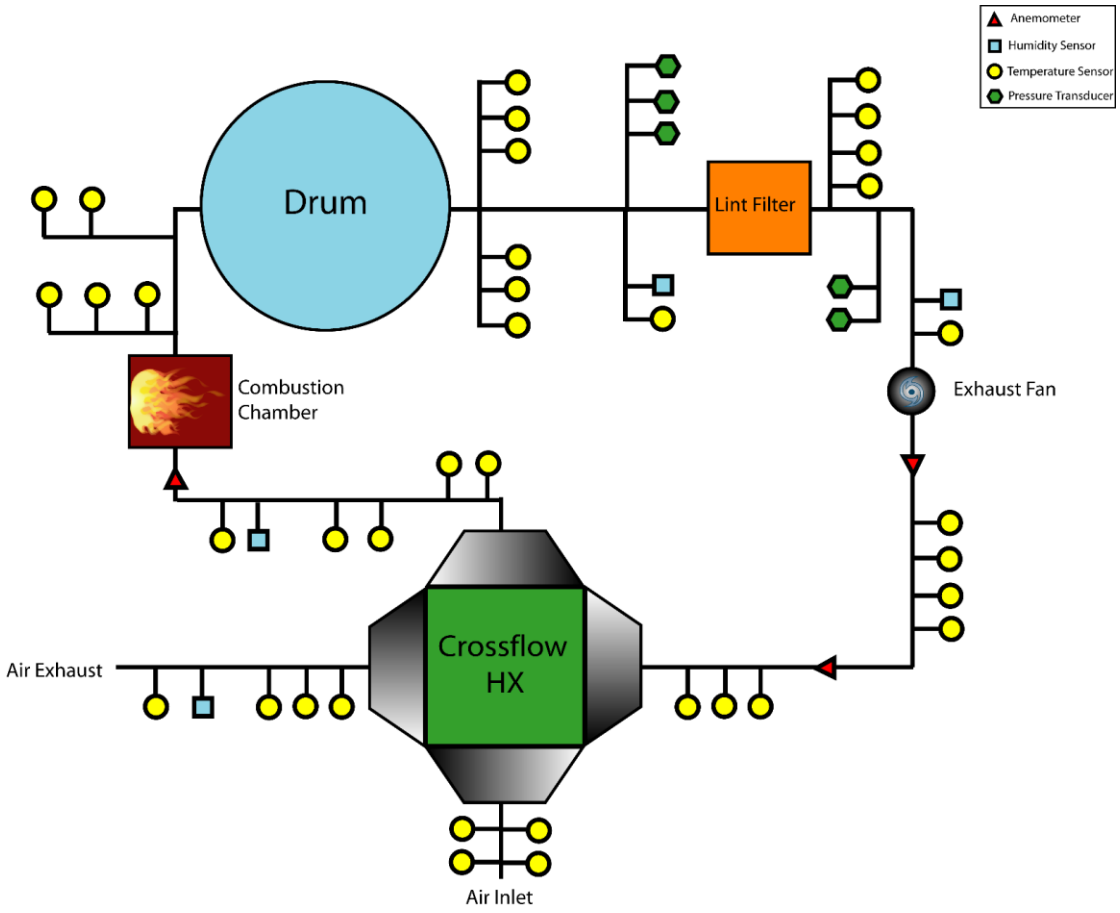

Figure C. 1: Schematic of the instrumentation installed on the dryer for the recuperation experiments

The details of the heat exchanger are shown in Table C.1.

Table C. 1:Recuperative heat exchanger parameters

Parameter	**Value**
Material	Aluminum
Length	610 mm
Width	203 mm
Plate Spacing	8 mm
Mass	6.3 kg

An energy balance was performed on the heat exchanger to ensure there is no internal leakage from one stream to another.

Conditions: Recuperative heat exchanger, $\dot{Q}_{comb} = 18.8$ kW , $m_{cl,dry} = 7.66$ kg, $\Omega_d = 48$ rpm $m_{cl,wet} = 14.16$ kg , $T_{amb} = 24$°C , $RH_{amb} = 0.5$, $t = 1500$ s		
Inputs/Measurements	**Equations**	**Results**
Energy Balance on the		
$T_{in}^{hot} = 55.43 \pm 0.15$ °C	$h_{in}^{hot} = f\left(T_{in}^{hot}, RH_{in}^{hot}, P_h\right)$	$h_{in}^{hot} = 167.90 \pm 7.42$ kJ kg^{-1}
$T_{out}^{hot} = 38.69 \pm 0.15$ °C	$h_{out}^{hot} = f\left(T_{out}^{hot}, RH_{out}^{hot}, P_h\right)$	$h_{out}^{hot} = 149.80 \pm 3.30$ kJ kg^{-1}
$T_{in}^{cold} = 24.16 \pm 0.15$ °C	$h_{in}^{cold} = f\left(T_{in}^{cold}, RH_{in}^{cold}, P_c\right)$	$h_{in}^{cold} = 42.82 \pm 1.25$ kJ kg^{-1}
$T_{out}^{cold} = 45.62 \pm 0.15$ °C	$h_{out}^{cold} = f\left(T_{out}^{cold}, RH_{out}^{cold}, P_c\right)$	$h_{out}^{cold} = 70.73 \pm 4.07$ kJ kg^{-1}
$RH_{in}^{hot} = 40.8 \pm 2.5\%$		
$RH_{out}^{hot} = 95.4 \pm 2.5\%$	$\dot{Q}_h = \dot{m}_h\left(h_{in}^{hot} - h_{out}^{hot}\right)$	$\dot{Q}_h = 3.402 \pm 0.641$ kW
$RH_{in}^{cold} = 39.1 \pm 2.5\%$	$\dot{Q}_c = \dot{m}_c\left(h_{out}^{cold} - h_{in}^{cold}\right)$	$\dot{Q}_c = 3.377 \pm 0.581$ kW
$RH_{out}^{cold} = 45.6 \pm 2.5$		
$\dot{m}_h = 0.1876 \pm 0.0113$ kg s^{-1}	$\varepsilon = \left\lvert \dot{Q}_h - \dot{Q}_c \right\rvert$	$\varepsilon = 0.0252$ kW (< 0.7% of the total duty of the heat exchanger)
$\dot{m}_c = 0.1210 \pm 0.0166$ kg s^{-1}		
$P_h = 97.66 \pm 0.32$ kPa		
$P_c = 99.47 \pm 0.36$ kPa		

APPENDIX D. ADSORBENT BED FOR THERMAL STORAGE EXPERIMENTS

D.1 Thermal energy storage experiments

The procedure described follows the steps described in Appendix A.1. A schematic showing the instrumentation mounted to the test facility for the thermal energy storage is depicted in Figure D.1

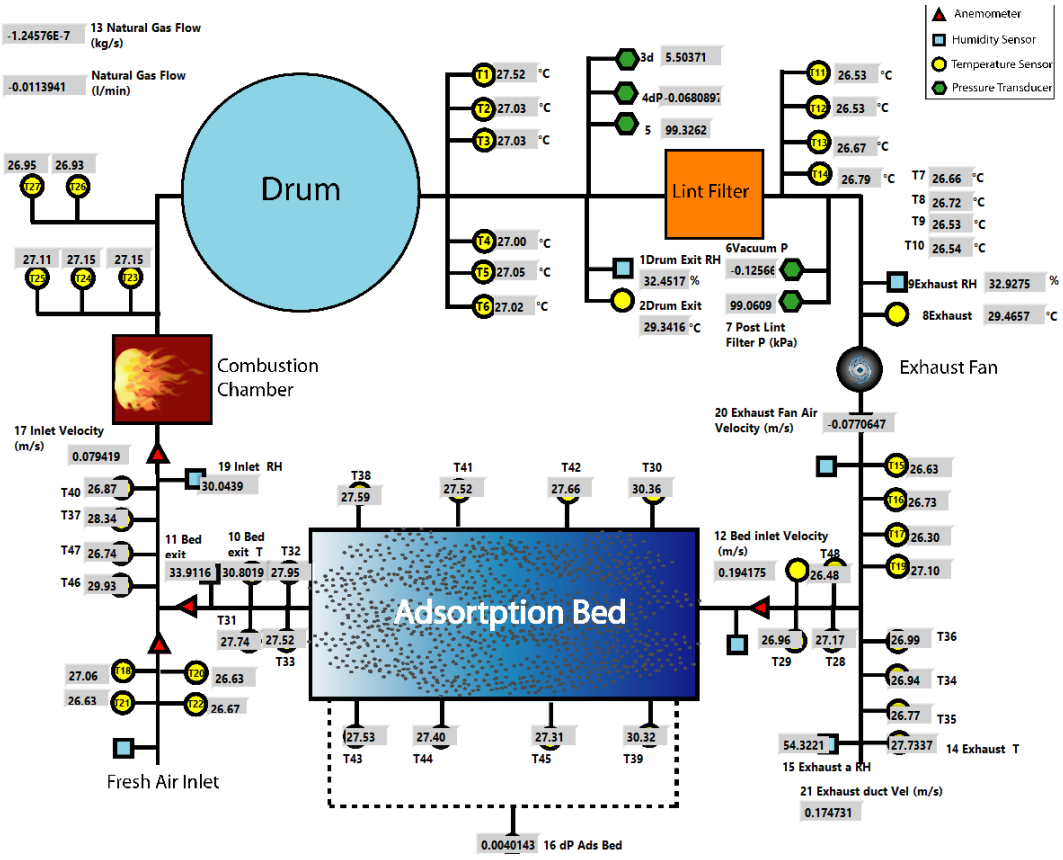

Figure D. 1:Schematic of the instrumentation installed on the dryer for the thermal energy storage experiments

For a fixed effective pellet diameter of 3.66 mm, which corresponds to a batch of 3 – 5 mm silica gel Type RD, it was important to investigate the effects of bed length and bed diameter. The main penalty function was to achieve the switching time in the adsorbent bed while minimizing the pressure drop. According to the Ergun's pressure drop:

$$\Delta P = \sum_{i=1}^{N} \Delta P_i = \sum_{i=1}^{N} \left\{ \left(\frac{150}{\mathrm{Re}_i} + \frac{7}{4} \right) \left(\frac{\rho_i U (1-\varepsilon_b)(x_i - x_{i-1})}{d_p \varepsilon_b^2} \right) \right\} \tag{D.1}$$

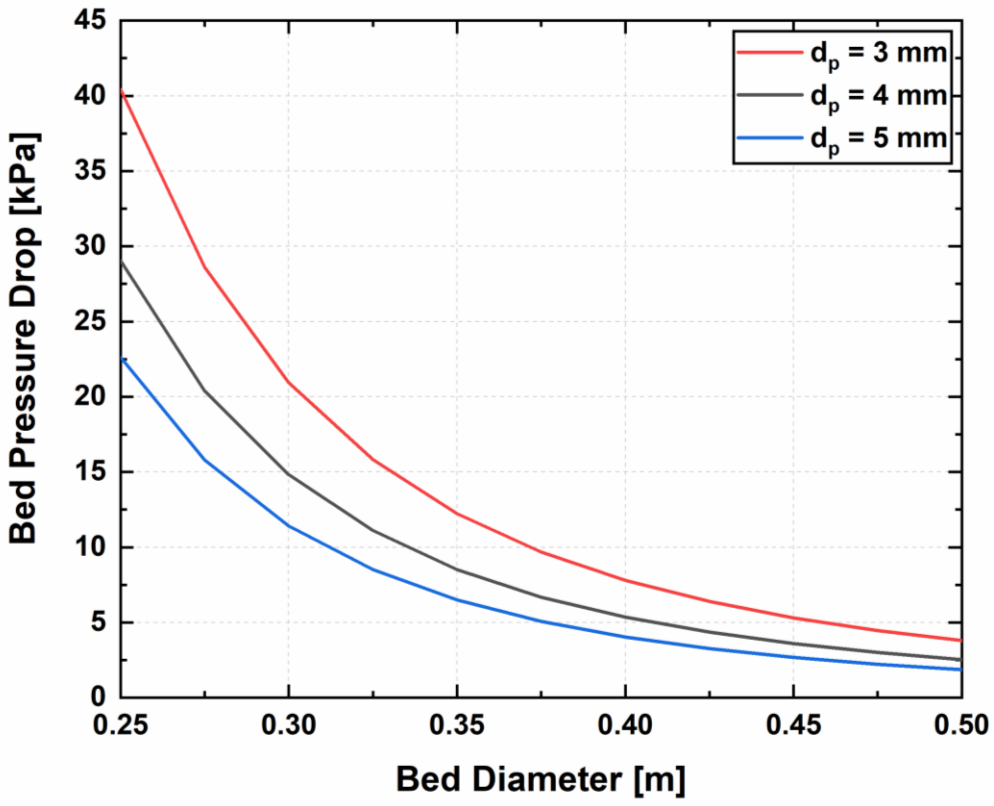

Figure D. 2: Pressure drop as function of bed diameter for different silica gel pellet diameters.

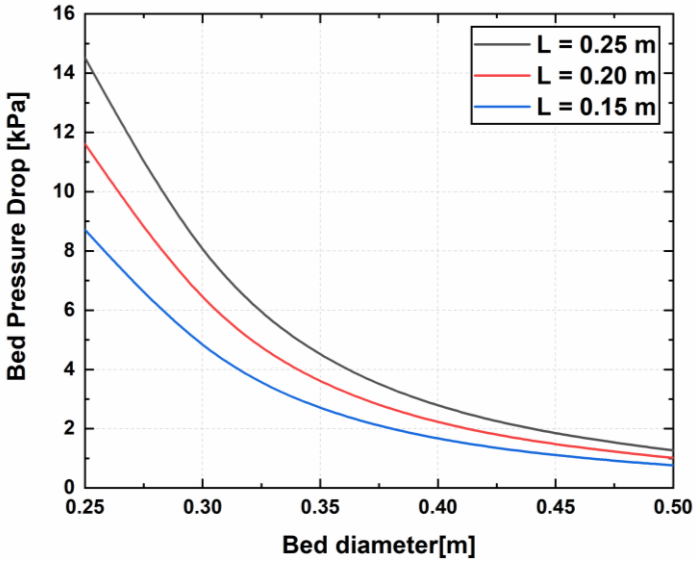

Figure D. 3: Pressure drop as function of bed diameter for different bed lengths.

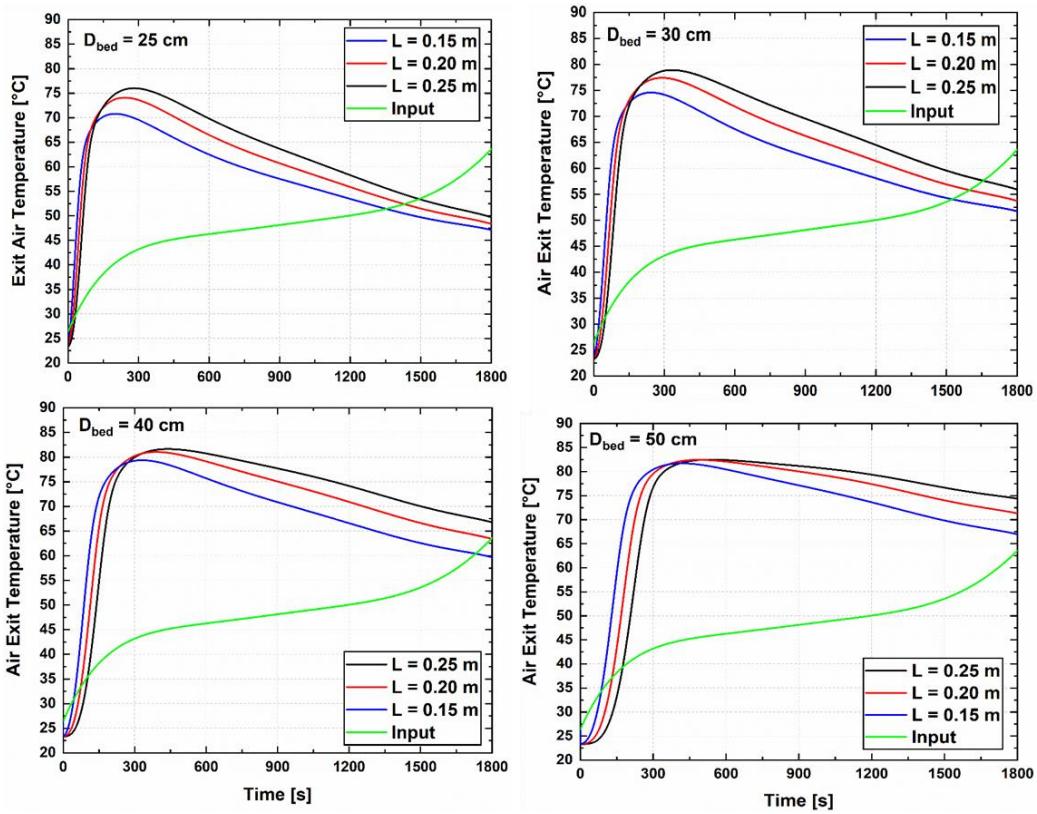

Figure D. 4: Temperature of air exiting the adsorbent bed for different beds

The final bed design consisted of a diameter of 0.381 m and a length that can be varied from 0 – 0.18 m. The maximum capacity of the bed is 11.8 kg. To connect the bed to the dryer, two headers were connected to each of the inlet and outlet of the bed. Figure D.5 shows a schematic the connecting headers.

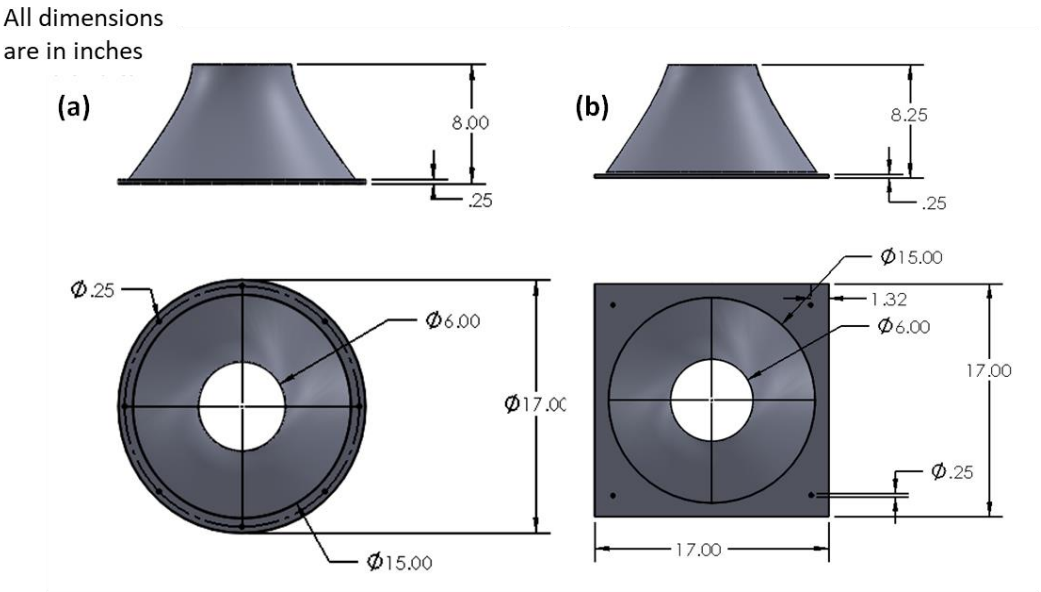

Figure D. 5: Dimensions of the inlet and exit headers used on the adsorbent bed for the thermal energy storage experiments

REFERENCES

Ackermann, G. (1937). "Heat Transfer and Molecular Mass Transfer in the Same Field at High Temperatures and Large Partial Pressure Differences," *Vdi-forschungsheft*. Vol. 8(382), pp. 1-10.

Ahmadi, M., K. R. Gluesenkamp and S. Bigham (2021). "Energy-Efficient Sorption-Based Gas Clothes Dryer Systems," *Energy Conversion and Management*. Vol. 230, p. 113763 DOI: https://doi.org/10.1016/j.enconman.2020.113763.

Ahn, S. P., S. H. Kim, Y. G. Park and M. Y. Ha (2019). "Experimental Study on Drying Time and Energy Consumption of a Vented Dryer," *Journal of Mechanical Science and Technology*. Vol. 33(5), pp. 2471-2480 DOI: 10.1007/s12206-019-0444-5.

Akyol, U., A. Erhan Akan and A. Durak (2015). "Simulation and Thermodynamic Analysis of a Hot-Air Textile Drying Process," *The Journal of The Textile Institute*. Vol. 106(3), pp. 260-274 DOI: 10.1080/00405000.2014.916062.

Ameen, A. and S. Bari (2004). "Investigation into the Effectiveness of Heat Pump Assisted Clothes Dryer for Humid Tropics," *Energy Conversion and Management*. Vol. 45(9), pp. 1397-1405 DOI: https://doi.org/10.1016/j.enconman.2003.09.001.

Avvaru, B., M. N. Patil, P. R. Gogate and A. B. Pandit (2006). "Ultrasonic Atomization: Effect of Liquid Phase Properties," *Ultrasonics*. Vol. 44(2), pp. 146-158 DOI: https://doi.org/10.1016/j.ultras.2005.09.003.

Bansal, P., S. Islam and K. Sharma (2010a). "A Novel Design of a Household Clothes Tumbler Dryer," *Applied Thermal Engineering*. Vol. 30(4), pp. 277-285 DOI: https://doi.org/10.1016/j.applthermaleng.2009.09.002.

Bansal, P., A. Mohabir and W. Miller (2016). "A Novel Method to Determine Air Leakage in Heat Pump Clothes Dryers," *Energy*. Vol. 96, pp. 1-7 DOI: 10.1016/j.energy.2015.12.051.

Bansal, P., K. Sharma and S. Islam (2010b). "Thermal Analysis of a New Concept in a Household Clothes Tumbler Dryer," *Applied Energy*. Vol. 87(5), pp. 1562-1571 DOI: https://doi.org/10.1016/j.apenergy.2009.10.029.

Bansal, P. K., J. E. Braun and E. A. Groll (2001). "Improving the Energy Efficiency of Conventional Tumbler Clothes Drying Systems," *International Journal of Energy Research*. Vol. 25(15), pp. 1315-1332 DOI: 10.1002/er.752.

Bassily, A. M. and G. M. Colver (2003a). "Correlation of the Area-Mass Transfer Coefficient inside the Drum of a Clothes Dryer," *Drying Technology*. Vol. 21(5), pp. 919-944 DOI: 10.1081/DRT-120021692.

Bassily, A. M. and G. M. Colver (2003b). "Performance Analysis of an Electric Clothes Dryer," *Drying Technology*. Vol. 21(3), pp. 499-524 DOI: 10.1081/DRT-120018459.

Bengtsson, P., J. Berghel and R. Renström (2014). "Performance Study of a Closed-Type Heat Pump Tumble Dryer Using a Simulation Model and an Experimental Set-Up," *Drying Technology*. Vol. 32(8), pp. 891-901 DOI: 10.1080/07373937.2013.875035.

Bergman, T. L., F. P. Incropera, D. P. DeWitt and A. S. Lavine (2011). *Fundamentals of Heat and Mass Transfer*. John Wiley & Sons.

Bhandari, B. (2015). "Handbook of Industrial Drying, Fourth Edition Edited by A. S. Mujumdar," *Drying Technology*. Vol. 33(1), pp. 128-129 DOI: 10.1080/07373937.2014.983704.

Bird, R. B., W. E. Stewart and E. N. Lightfoot (2006). *Transport Phenomena*. John Wiley & Sons.

Bjurström, H., E. Karawacki and B. Carlsson (1984). "Thermal Conductivity of a Microporous Particulate Medium: Moist Silica Gel," *International Journal of Heat and Mass Transfer*. Vol. 27(11), pp. 2025-2036 DOI: https://doi.org/10.1016/0017-9310(84)90189-3.

Boudreaux, P., K. R. Gluesenkamp, V. K. Patel and B. Shen (2020). "Measurement and Analysis of Clothes Dryer Air Leakage," *Drying Technology*. pp. 1-13 DOI: 10.1080/07373937.2020.1753765.

Büyükakıncı, B. Y. (2012). "Usage of Microwave Energy in Turkish Textile Production Sector," *Energy Procedia*. Vol. 14, pp. 424-431 DOI: https://doi.org/10.1016/j.egypro.2011.12.953.

Cabeza, L. F., A. Solé and C. Barreneche (2017). "Review on Sorption Materials and Technologies for Heat Pumps and Thermal Energy Storage," *Renewable Energy*. Vol. 110, pp. 3-39 DOI: https://doi.org/10.1016/j.renene.2016.09.059.

Calabrese, L., L. Bonaccorsi, P. Bruzzaniti, A. Frazzica, A. Freni and E. Proverbio (2018). "Adsorption Performance and Thermodynamic Analysis of Sapo-34 Silicone Composite Foams for Adsorption Heat Pump Applications," *Materials for Renewable and Sustainable Energy*. Vol. 7(4), p. 24 DOI: 10.1007/s40243-018-0131-y.

Cao, T., J. Ling, Y. Hwang and R. Radermacher (2014a). "Development of a Novel Two-Stage Heat Pump Clothes Dryer," *Proceedings of ASME 2014 International Mechanical Engineering Congress and Exposition*.

Cao, T., J. Ling, Y. Hwang and R. Radermacher (2014b). "Development of a Novel Two-Stage Heat Pump Clothes Dryer," *Proceedings of ASME International Mechanical Engineering Congress and Exposition*.

Chandrasekaran, S., S. Ramanathan and T. Basak (2013). "Microwave Food Processing—a Review," *Food Research International*. Vol. 52(1), pp. 243-261 DOI: https://doi.org/10.1016/j.foodres.2013.02.033.

Chen, G., W. Wang and A. S. Mujumdar (2001). "Theoretical Study of Microwave Heating Patterns on Batch Fluidized Bed Drying of Porous Material," *Chemical Engineering Science*. Vol. 56(24), pp. 6823-6835 DOI: https://doi.org/10.1016/S0009-2509(01)00320-7.

Chen, P. and P. S. Schmidt (1990). "An Integral Model for Drying of Hygroscopic and Nonhygroscopic Materials with Dielectric Heating," *Drying Technology*. Vol. 8(5), pp. 907-930 DOI: 10.1080/07373939008959928.

Chi, C. W. and D. T. Wasan (1970). "Fixed Bed Adsorption Drying," *AIChE Journal*. Vol. 16(1), pp. 23-31 DOI: 10.1002/aic.690160107.

China Energy, G. and A. Hasanbeigi (2010). "Energy-Efficiency Improvement Opportunities for the Textile Industry," United States.

Cochran, M., J. Goodnight, B. Babin and S. Eckels (2009). "Condensing Dryers with Enhanced Dehumidification Using Surface Tension Elements," *Applied Thermal Engineering*. Vol. 29(4), pp. 723-731 DOI: https://doi.org/10.1016/j.applthermaleng.2008.03.050.

Colak, N. and A. Hepbasli (2009). "A Review of Heat Pump Drying: Part 1 – Systems, Models and Studies," *Energy Conversion and Management*. Vol. 50(9), pp. 2180-2186 DOI: https://doi.org/10.1016/j.enconman.2009.04.031.

Conde, M. R. (1997). "Energy Conservation with Tumbler Drying in Laundries," *Applied Thermal Engineering*. Vol. 17(12), pp. 1163-1172 DOI: https://doi.org/10.1016/S1359-4311(97)00031-8.

Cranston, J., A. Askalany and G. Santori (2019). "Efficient Drying in Washer Dryers by Combining Sorption and Heat Pumping," *Energy*. Vol. 183, pp. 683-692 DOI: https://doi.org/10.1016/j.energy.2019.06.141.

Deans, J. (2001). "The Modelling of a Domestic Tumbler Dryer," *Applied Thermal Engineering*. Vol. 21(9), pp. 977-990 DOI: https://doi.org/10.1016/S1359-4311(00)00092-2.

Deans, J. and D. Tranxaun (1992). "A Computer Simulation of a Tumbler Dryer," *Transport Phenomena in Heat and Mass Transfer*. Vol. 2.

Demir, H., M. Mobedi and S. Ülkü (2008). "A Review on Adsorption Heat Pump: Problems and Solutions," *Renewable and Sustainable Energy Reviews*. Vol. 12(9), pp. 2381-2403 DOI: https://doi.org/10.1016/j.rser.2007.06.005.

Ding, M. and A. Kantzas (2007). "Capillary Number Correlations for Gas-Liquid Systems," *Journal of Canadian Petroleum Technology*. Vol. 46(02) DOI: 10.2118/07-02-03 %J Journal of Canadian Petroleum Technology.

Do, Y., M. Kim, T. Kim, S. Jeong, S. Park, S. Woo, Y. Kwon, Y. Jung, J. Lee and Y. Ahn (2013). "An Experimental Study on the Performance of a Condensing Tumbler Dryer with an Air-to-Air Heat Exchanger," *Korean Journal of Chemical Engineering*. Vol. 30(6), pp. 1195-1200 DOI: 10.1007/s11814-013-0037-4.

Du, G., S. Wang and Z. Cai (2005). "Microwave Drying of Wood Strands," *Drying Technology*. Vol. 23(12), pp. 2421-2436 DOI: 10.1080/07373930500340494.

Dunn, D. R. (2020). "December 2019 Monthly Energy Report," U.S. Energy Information Administration, Washington, D.C.

Durur, G. and E. Öner (2013). "The Comfort Properties of the Terry Towels Made of Cotton and Polypropylene Yarns," *Journal of Engineered Fibers and Fabrics*. Vol. 8(2), p. 155892501300800201 DOI: 10.1177/155892501300800201.

EIA (2015). "U.S. Energy Information Adminstration. Residential Energy Consumption Survey - 2015 Recs Survey Data."

EIA (2019). United States Energy Information Administration: U.S. Energy Facts Explained, Access Date: September 23, 2019, DOI: https://www.eia.gov/energyexplained/us-energy-facts/.

EIA (2020). "United States Energy Information Administration: U.S. Energy Facts Explained, Accessed on July 8, 2020." DOI: https://www.eia.gov/energyexplained/us-energy-facts/.

El Fil, B. and S. Garimella (2021). "Waste Heat Recovery in Commercial Gas-Fired Tumble Dryers," *Energy*. Vol. 218, p. 119407 DOI: https://doi.org/10.1016/j.energy.2020.119407.

Electronics, S. (2020). Speedqueen St025 Dryer Id:10904, Access Date: DOI.

Feldman, B. and R. Ganesan (2019). "U.S. Appliance Repair Affordability, Realiability and Seansonality ", San Francisco, CA.

Feng, H., Y. Yin and J. Tang (2012). "Microwave Drying of Food and Agricultural Materials: Basics and Heat and Mass Transfer Modeling," *Food Engineering Reviews*. Vol. 4(2), pp. 89-106 DOI: 10.1007/s12393-012-9048-x.

Fiaschi, D., G. Manfrida, L. Russo and L. Talluri (2017). "Improvement of Waste Heat Recuperation on an Industrial Textile Dryer: Redesign of Heat Exchangers Network and Components," *Energy Conversion and Management*. Vol. 150, pp. 924-940 DOI: 10.1016/j.enconman.2017.05.053.

Fiaschi, D. and L. Talluri (2019). "Assessment of the Thermoelectric Conversion Potential of Low-Temperature Waste Heat from Textile Dry-Cleaning Processes," *E3S Web Conf.* Vol. 113, p. 03019 DOI: 10.1051/e3sconf/201911303019.

Fontana, É., R. Donca, E. Mancusi, A. A. Ulson de Souza and S. M. A. Guelli Ulson de Souza (2016). "Mathematical Modeling and Numerical Simulation of Heat and Moisture Transfer in a Porous Textile Medium," *The Journal of The Textile Institute*. Vol. 107(5), pp. 672-682 DOI: 10.1080/00405000.2015.1061324.

Franke, T., D. Görges and M. G. Arend (2019). "The Energy Interface Challenge. Towards Designing Effective Energy Efficiency Interfaces for Electric Vehicles," *Proceedings of Proceedings of the 11th International Conference on Automotive User Interfaces and Interactive Vehicular Applications*.

Gatarić, P., B. Širok, M. Hočevar and L. Novak (2019). "Modeling of Heat Pump Tumble Dryer Energy Consumption and Drying Time," *Drying Technology*. Vol. 37(11), pp. 1396-1404 DOI: 10.1080/07373937.2018.1502778.

Ghali, K., B. Jones and J. Tracy (1994). "Experimental Techniques for Measuring Parameters Describing Wetting and Wicking in Fabrics," *Textile Research Journal*. Vol. 64(2), pp. 106-111 DOI: 10.1177/004051759406400206.

Gibson, P. W. and M. Charmchi (1997). "Modeling Convection/Diffusion Processes in Porous Textiles with Inclusion of Humidity-Dependent Air Permeability," *International Communications in Heat and Mass Transfer*. Vol. 24(5), pp. 709-724 DOI: https://doi.org/10.1016/S0735-1933(97)00056-0.

Gluesenkamp, K. R., P. Boudreaux, V. K. Patel, D. Goodman and B. Shen (2019). "An Efficient Correlation for Heat and Mass Transfer Effectiveness in Tumble-Type Clothes Dryer Drums," *Energy*. Vol. 172, pp. 1225-1242 DOI: https://doi.org/10.1016/j.energy.2019.01.146.

Gluesenkamp, K. R., V. K. Patel and A. M. Momen (2020). "Efficiency Limits of Evaporative Fabric Drying Methods," *Drying Technology*. pp. 1-21 DOI: 10.1080/07373937.2020.1839486.

Goh, L. J., M. Y. Othman, S. Mat, H. Ruslan and K. Sopian (2011). "Review of Heat Pump Systems for Drying Application," *Renewable and Sustainable Energy Reviews*. Vol. 15(9), pp. 4788-4796 DOI: https://doi.org/10.1016/j.rser.2011.07.072.

Goodman, D., V. K. Patel and K. R. Gluesenkamp (2017). *Thermoelectric Heat Pump Clothes Dryer Design Optimization*. ; Oak Ridge National Lab. (ORNL), Oak Ridge, TN (United States).

Hadley, G. R. (1982). "Theoretical Treatment of Evaporation Front Drying," *International Journal of Heat and Mass Transfer*. Vol. 25(10), pp. 1511-1522 DOI: https://doi.org/10.1016/0017-9310(82)90030-8.

Haghi, A. (2001). "A Mathematical Model of Thedrying Process," *Acta Polytechnica*. Vol. 41(3).

Haghi, A. K. and N. Amanifard (2008). "Analysis of Heat and Mass Transfer During Microwave Drying of Food Products," *Brazilian Journal of Chemical Engineering*. Vol. 25, pp. 491-501.

Hall, R. L., M. Shows, J. L. Douglas, E. S. Anderson, B. T. Beck, P. E. Collins, L. A. Damiano, M. A. Kedziersk, O. Kurtulus, A. Leyderman, H. Liang, J. L. Neel, M. Perevozchikov, J. Schaefer, J. P. Scott, F. J. Spevak, C. G. Stone, R. C. Tharp, S. L. J. Wage and M. A. Wegenka (2018). "Ansi/Ashrae Standard 41.2-2018 Standard Methods for Air Velocity and Airflow Measurement," Tullie Circle, NE, Atlanta, GA.

Hauer, A. and W. Dallmayer (1996). "Open Gas Fired Adsorption Heat Pump for Space Heating in Conjunction with Solar Collectors," *Proceedings of International absorption heat pump conference,*, Montreal, Canada.

Hauer, A. and F. Fischer (2011). "Open Adsorption System for an Energy Efficient Dishwasher," *Chemie Ingenieur Technik*. Vol. 83(1-2), pp. 61-66 DOI: https://doi.org/10.1002/cite.201000197.

Hekmat, D. and W. J. Fisk (1984a). "Improving the Energy Performance of Residential Clothe Dryers," Ernest Orlando Lawrence Berkeley National Laboratory, Berkeley, USA, LBL-17501.

Hekmat, D. and W. J. Fisk (1984b). "Improving the Energy Performance of Residential Clothesdryers," Ernest Orlando Lawrence Berkeley National Laboratory, Berkeley, USA, LBL-17501.

Horowitz, N. (2011). "Residential Clothes Dryers: A Closer Look at Energy Efficiency Test Procedures and Savings Opportunities."

Hougen, O. and W. Marshall (1947). "Adsorption from a Fluid Stream Flowing through a Stationary Granular Bed," *Chemical Engineering Progress*. Vol. 43(4), pp. 197-208.

Huang, X.-M., L.-S. Xiong, Y.-W. Zheng, H.-Q. Liu, Y.-Z. Xu and Y.-C. Li (2020). "Comparative Investigation of Performance of Gas Dryer and Two Other Types of Domestic Clothes Dryers," *International Journal of Low-Carbon Technologies*. DOI: 10.1093/ijlct/ctaa064.

Huelsz, G., L. Urbiola-Soto, F. López-Alquicira, R. Rechtman and G. Hernández-Cruz (2013). "Total Energy Balance Method for Venting Electric Clothes Dryers,"

Drying Technology. Vol. 31(5), pp. 576-586 DOI: 10.1080/07373937.2012.746977.

Instruments, N. (2019). *Labtoratory Virtual Instrument Engineering Workbench (Labview)*.

Intertreck (2020). Silica Gel Packets - Desiccant Packets, Access Date: DOI.

James, A. J., B. Vukasinovic, M. K. Smith and A. Glezer (2003). "Vibration-Induced Drop Atomization and Bursting," *Journal of Fluid Mechanics*. Vol. 476, pp. 1-28 DOI: 10.1017/S0022112002002835.

Jian, Q. and J. Zhao (2017). "Drying Performance Analysis of a Condensing Tumbler Clothes Dryer with a Unique Water Cooled Heat Exchanger," *Applied Thermal Engineering*. Vol. 113, pp. 601-608 DOI: https://doi.org/10.1016/j.applthermaleng.2016.11.086.

Junior, C., G. Chen and J. Koehler (2012). "Modeling of a New Recuperative Thermoelectric Cycle for a Tumble Dryer," *International Journal of Heat and Mass Transfer*. Vol. 55(5), pp. 1536-1543 DOI: https://doi.org/10.1016/j.ijheatmasstransfer.2011.11.008.

Kabir, E., P. Kumar, S. Kumar, A. A. Adelodun and K.-H. Kim (2018). "Solar Energy: Potential and Future Prospects," *Renewable and Sustainable Energy Reviews*. Vol. 82, pp. 894-900 DOI: https://doi.org/10.1016/j.rser.2017.09.094.

Kafui, K. D. (1994). "Transient Heat and Moisture Transfer in Thin Silica Gel Beds," *Journal of Heat Transfer*. Vol. 116(4), pp. 946-953 DOI: 10.1115/1.2911470.

Kahveci, K. and A. Cihan (2007). *Transport Phenomena During Drying of Food Materials*. Nova Science, New York, USA.

Kandilli, C. and A. Koclu (2011). "Assessment of the Optimum Operation Conditions of a Plate Heat Exchanger for Waste Heat Recovery in Textile Industry," *Renewable and Sustainable Energy Reviews*. Vol. 15(9), pp. 4424-4431 DOI: 10.1016/j.rser.2011.07.110.

Karmakar, A., V. Prabakaran, D. Zhao and K. J. Chua (2020). "A Review of Metal-Organic Frameworks (Mofs) as Energy-Efficient Desiccants for Adsorption Driven Heat-Transformation Applications," *Applied Energy*. Vol. 269, p. 115070 DOI: https://doi.org/10.1016/j.apenergy.2020.115070.

Kerkhof, P. J. A. M. and W. J. Coumans (2002). "Drying: A Fascinating Unit Operation," *Chemical Engineering Journal*. Vol. 86(1), pp. 1-2 DOI: https://doi.org/10.1016/S1385-8947(01)00264-9.

Kim, H.-S., Y.-B. Chae, S.-B. Jung and Y.-N. Jang (2008). "Drying of by-Product Gypsum by Microwave Heating," *Journal of the Mineralogical Society of Korea*. Vol. 21(2), pp. 193-200.

Klein, S. (2020a). *Engineering Equation Solver F-Chart Software [Online]*.

Klein, S. A. (2020b). *Engineering Equation Solver*, Version Academic Professional V10.644-3D. F-Chart Software.

Koekemoer, A. and A. Luckos (2015). "Effect of Material Type and Particle Size Distribution on Pressure Drop in Packed Beds of Large Particles: Extending the Ergun Equation," *Fuel*. Vol. 158, pp. 232-238 DOI: https://doi.org/10.1016/j.fuel.2015.05.036.

Krokida, M. K. and G. I. Bisharat (2004). "Heat Recovery from Dryer Exhaust Air," *Drying Technology*. Vol. 22(7), pp. 1661-1674 DOI: 10.1081/DRT-200025626.

Krönauer, A., E. Lävemann, S. Brückner and A. Hauer (2015). "Mobile Sorption Heat Storage in Industrial Waste Heat Recovery," *Energy Procedia*. Vol. 73, pp. 272-280 DOI: https://doi.org/10.1016/j.egypro.2015.07.688.

Kudra, T. (2004). "Energy Aspects in Drying," *Drying Technology*. Vol. 22(5), pp. 917-932 DOI: 10.1081/DRT-120038572.

Kumar, C., M. U. H. Joardder, T. W. Farrell and M. A. Karim (2016). "Multiphase Porous Media Model for Intermittent Microwave Convective Drying (Imcd) of Food," *International Journal of Thermal Sciences*. Vol. 104, pp. 304-314 DOI: https://doi.org/10.1016/j.ijthermalsci.2016.01.018.

Kumar, C. and M. A. Karim (2019). "Microwave-Convective Drying of Food Materials: A Critical Review," *Critical Reviews in Food Science and Nutrition*. Vol. 59(3), pp. 379-394 DOI: 10.1080/10408398.2017.1373269.

Lambert, A. J. D., F. P. M. Spruit and J. Claus (1991). "Modelling as a Tool for Evaluating the Effects of Energy-Saving Measures. Case Study: A Tumbler Drier," *Applied Energy*. Vol. 38(1), pp. 33-47 DOI: 10.1016/0306-2619(91)90040-5.

Law, R., A. Harvey and D. Reay (2013). "Opportunities for Low-Grade Heat Recovery in the Uk Food Processing Industry," *Applied Thermal Engineering*. Vol. 53(2), pp. 188-196 DOI: 10.1016/j.applthermaleng.2012.03.024.

Lee, B.-H., R. A. Sian and C.-C. Wang (2019). "A Rationally Based Model Applicable for Heat Pump Tumble Dryer," *Drying Technology*. Vol. 37(6), pp. 691-706 DOI: 10.1080/07373937.2018.1454940.

Lee, H. S., W. W. Carr, H. W. Beckham and J. Leisen (2002). "A Model of through-Air Drying of Tufted Textile Materials," *International Journal of Heat and Mass*

Transfer. Vol. 45(2), pp. 357-366 DOI: https://doi.org/10.1016/S0017-9310(01)00130-2.

Lee, J.-G., K. J. Bae and O. K. Kwon (2020). "Performance Investigation of a Two-Bed Type Adsorption Chiller with Various Adsorbents," *Energies*. Vol. 13(10), p. 2553.

Lefebvre, D. and F. H. Tezel (2017). "A Review of Energy Storage Technologies with a Focus on Adsorption Thermal Energy Storage Processes for Heating Applications," *Renewable and Sustainable Energy Reviews*. Vol. 67, pp. 116-125 DOI: https://doi.org/10.1016/j.rser.2016.08.019.

Li, H., Q. Chen, X. Zhang, K. N. Finney, V. N. Sharifi and J. Swithenbank (2012). "Evaluation of a Biomass Drying Process Using Waste Heat from Process Industries: A Case Study," *Applied Thermal Engineering*. Vol. 35, pp. 71-80 DOI: https://doi.org/10.1016/j.applthermaleng.2011.10.009.

Li, X.-J., B.-G. Zhang and W.-J. Li (2008). "Microwave-Vacuum Drying of Wood: Model Formulation and Verification," *Drying Technology*. Vol. 26(11), pp. 1382-1387 DOI: 10.1080/07373930802333551.

Little, A. B. and S. Garimella (2011). "Comparative Assessment of Alternative Cycles for Waste Heat Recovery and Upgrade," *Energy*. Vol. 36(7), pp. 4492-4504 DOI: https://doi.org/10.1016/j.energy.2011.03.069.

Liu, D., F.-Y. Zhao and G.-F. Tang (2008). "Modeling and Performance Investigation of a Closed-Type Thermoelectric Clothes Dryer," *Drying Technology*. Vol. 26(10), pp. 1208-1216 DOI: 10.1080/07373930802306995.

Ma, S.-S., C.-Y. Tseng, Y.-R. Jian, T.-H. Yang and S.-L. Chen (2018). "Utilization of Waste Heat for Energy Conservation in Domestic Dryers," *Energy*. Vol. 162, pp. 185-199 DOI: https://doi.org/10.1016/j.energy.2018.08.011.

Mancini, F., S. Minetto and E. Fornasieri (2011). "Thermodynamic Analysis and Experimental Investigation of a Co2 Household Heat Pump Dryer," *International Journal of Refrigeration*. Vol. 34(4), pp. 851-858 DOI: https://doi.org/10.1016/j.ijrefrig.2010.12.012.

Maskan, M. (2001). "Drying, Shrinkage and Rehydration Characteristics of Kiwifruits During Hot Air and Microwave Drying," *Journal of Food Engineering*. Vol. 48(2), pp. 177-182 DOI: https://doi.org/10.1016/S0260-8774(00)00155-2.

Masud, M. H., A. A. Ananno, N. Ahmed, P. Dabnichki and K. N. Salehin (2020). "Experimental Investigation of a Novel Waste Heat Based Food Drying System," *Journal of Food Engineering*. Vol. 281, p. 110002 DOI: 10.1016/j.jfoodeng.2020.110002.

McAllister, S., J.-Y. Chen and A. C. Fernandez-Pello (2011). *Fundamentals of Combustion Processes*. Springer.

Mokhtari Yazdi, M., M. Sheikhzadeh and S. Borhani (2015). "Modeling the Heat Transfer in a Pcm Cooling Vest," *The Journal of The Textile Institute*. Vol. 106(9), pp. 1003-1012 DOI: 10.1080/00405000.2014.959800.

Moraitis, C. S. and C. B. Akritidis (1997). "Energy Saving in Industrial Drying Plants by Partial Recovery of the Latent Heat of the Exhaust Air," *Drying Technology*. Vol. 15(6-8), pp. 1931-1940 DOI: 10.1080/07373939708917338.

Mujumdar, A. S. (2014). *Handbook of Industrial Drying*. 3rd Ed. CRC press, Boca Raton, USA.

Nemec, D. and J. Levec (2005). "Flow through Packed Bed Reactors: 1. Single-Phase Flow," *Chemical Engineering Science*. Vol. 60(24), pp. 6947-6957 DOI: https://doi.org/10.1016/j.ces.2005.05.068.

Ng, A. B. and S. Deng (2008). "A New Termination Control Method for a Clothes Drying Process in a Clothes Dryer," *Applied Energy*. Vol. 85(9), pp. 818-829 DOI: https://doi.org/10.1016/j.apenergy.2007.10.016.

NI (2019). *Laboratory Virtual Instrument Engineering Workbench (Labview) Sp 2018*. National Instruments, Austin, USA.

Nissan, A. H., W. G. Kaye and J. R. Bell (1959). "Mechanism of Drying Thick Porous Bodies During the Falling Rate Period: I. The Pseudo-Wet-Bulb Temperature," *AIChE Journal*. Vol. 5(1), pp. 103-110 DOI: https://doi.org/10.1002/aic.690050122.

Nordon, P. and H. G. David (1967). "Coupled Diffusion of Moisture and Heat in Hygroscopic Textile Materials," *International Journal of Heat and Mass Transfer*. Vol. 10(7), pp. 853-866 DOI: https://doi.org/10.1016/0017-9310(67)90065-8.

Novak, L., P. Gatarić and B. Širok (2019). "Influence of Drum Inlet Air Conditions on Drying Process in a Domestic Tumble Dryer," *Drying Technology*. Vol. 37(6), pp. 781-792 DOI: 10.1080/07373937.2018.1461111.

Novak, L., B. Širok, M. Hočevar and P. Gatarić (2020). "Influence of Load Mass and Drum Speed on Fabric Motion and Performance of a Heat Pump Tumble Dryer," *Drying Technology*. pp. 1-15 DOI: 10.1080/07373937.2020.1734608.

Núñez, T., W. Mittelbach and H.-M. Henning (2007). "Development of an Adsorption Chiller and Heat Pump for Domestic Heating and Air-Conditioning Applications," *Applied Thermal Engineering*. Vol. 27(13), pp. 2205-2212 DOI: https://doi.org/10.1016/j.applthermaleng.2005.07.024.

Orfeuil, M. (1987). *Electric Process Heating*. Columbus, OH (USA); Battelle Press.

Paksoy, H. Ö. (2007). *Thermal Energy Storage for Sustainable Energy Consumption: Fundamentals, Case Studies and Design*. Springer Science & Business Media.

Panwar, N. L., S. C. Kaushik and S. Kothari (2011). "Role of Renewable Energy Sources in Environmental Protection: A Review," *Renewable and Sustainable Energy Reviews*. Vol. 15(3), pp. 1513-1524 DOI: https://doi.org/10.1016/j.rser.2010.11.037.

Park, S., C. Yun, J. Kim and C. H. Park (2013). "The Effects of the Fabric Properties on Fabric Movement and the Prediction of the Fabric Movements in a Front-Loading Washer," *Textile Research Journal*. Vol. 83(11), pp. 1201-1212 DOI: 10.1177/0040517512468810.

Patel, V. and K. R. Gluesenkamp (2018). "Thermoelectric Heat Pump Clothes Dryer Using Secondary Loop Heat Exchangers: Experimental Evaluation and System Modeling."

Patel, V. K., P. R. Boudreaux and K. R. Gluesenkamp (2021). "Validated Model of a Thermoelectric Heat Pump Clothes Dryer Using Secondary Pumped Loops," *Applied Thermal Engineering*. Vol. 184, p. 116345 DOI: https://doi.org/10.1016/j.applthermaleng.2020.116345.

Patel, V. K., K. R. Gluesenkamp, D. Goodman and A. Gehl (2018). "Experimental Evaluation and Thermodynamic System Modeling of Thermoelectric Heat Pump Clothes Dryer," *Applied Energy*. Vol. 217, pp. 221-232 DOI: https://doi.org/10.1016/j.apenergy.2018.02.055.

Peishi, C. and D. C. T. Pei (1989). "A Mathematical Model of Drying Processes," *International Journal of Heat and Mass Transfer*. Vol. 32(2), pp. 297-310 DOI: https://doi.org/10.1016/0017-9310(89)90177-4.

Peng, C., S. Ravi, V. K. Patel, A. M. Momen and S. Moghaddam (2017). "Physics of Direct-Contact Ultrasonic Cloth Drying Process," *Energy*. Vol. 125, pp. 498-508 DOI: https://doi.org/10.1016/j.energy.2017.02.138.

Pesaran, A. A. and A. F. Mills (1987a). "Moisture Transport in Silica Gel Packed Beds-I. Theoretical Study," *International Journal of Heat and Mass Transfer*. Vol. 30, pp. 1037-1049.

Pesaran, A. A. and A. F. Mills (1987b). "Moisture Transport in Silica Gel Packed Beds—Ii. Experimental Study," *International Journal of Heat and Mass Transfer*. Vol. 30(6), pp. 1051-1060.

Pescatore, P. and P. Carbone (2005). "High Efficiency, High Performance Clothes Dryer," TIAX LLC.

Pourová, M., J. Vrba and O. Žák (2006). "Microwave System for Drying of Textile: Design, Model and Evaluation," *Proceedings of 2006 68th ARFTG Conference: Microwave Measurement*.

Prat, M. (2002). "Recent Advances in Pore-Scale Models for Drying of Porous Media," *Chemical Engineering Journal*. Vol. 86(1), pp. 153-164 DOI: https://doi.org/10.1016/S1385-8947(01)00283-2.

Pulat, E., A. B. Etemoglu and M. Can (2009). "Waste-Heat Recovery Potential in Turkish Textile Industry: Case Study for City of Bursa," *Renewable and Sustainable Energy Reviews*. Vol. 13(3), pp. 663-672 DOI: 10.1016/j.rser.2007.10.002.

Rakib, M. I., R. Saidur, E. N. Mohamad and A. M. Afifi (2017). "Waste-Heat Utilization – the Sustainable Technologies to Minimize Energy Consumption in Bangladesh Textile Sector," *Journal of Cleaner Production*. Vol. 142, pp. 1867-1876 DOI: 10.1016/j.jclepro.2016.11.098.

Rasti, M., J. H. Jeong and S.-I. Park (2020). "A Review of Models for Estimation of Moisture Evaporation Rate from Clothes inside Clothes Dryer," *International Journal of Air-Conditioning and Refrigeration*.

Rattanadecho, P. and N. Makul (2016). "Microwave-Assisted Drying: A Review of the State-of-the-Art," *Drying Technology*. Vol. 34(1), pp. 1-38 DOI: 10.1080/07373937.2014.957764.

Rattner, A. S. and S. Garimella (2011). "Energy Harvesting, Reuse and Upgrade to Reduce Primary Energy Usage in the USA," *Energy*. Vol. 36(10), pp. 6172-6183 DOI: https://doi.org/10.1016/j.energy.2011.07.047.

Raymond, A. and S. Garimella (2011). "Intraparticle Mass Transfer in Adsorption Heat Pumps: Limitations of the Linear Driving Force Approximation," *Journal of Heat Transfer*. Vol. 133(4) DOI: 10.1115/1.4001310.

Raymond, A. W. and S. Garimella (2021). "Distributed Parameter Simulation of Annular-Finned Tube Sorption Bed," *International Journal of Heat and Mass Transfer*. Vol. 166, p. 120755 DOI: https://doi.org/10.1016/j.ijheatmasstransfer.2020.120755.

Sadeghiamirshahidi, M. and S. J. Vitton (2019). "Analysis of Drying and Saturating Natural Gypsum Samples for Mechanical Testing," *Journal of Rock Mechanics and Geotechnical Engineering*. Vol. 11(2), pp. 219-227 DOI: https://doi.org/10.1016/j.jrmge.2018.08.007.

Santori, G., A. Frazzica, A. Freni, M. Galieni, L. Bonaccorsi, F. Polonara and G. Restuccia (2013). "Optimization and Testing on an Adsorption Dishwasher," *Energy*. Vol. 50, pp. 170-176 DOI: https://doi.org/10.1016/j.energy.2012.11.031.

Sarkar, J., S. Bhattacharyya and M. R. Gopal (2006). "Transcritical Co2 Heat Pump Dryer: Part 1. Mathematical Model and Simulation," *Drying Technology*. Vol. 24(12), pp. 1583-1591 DOI: 10.1080/07373930601030903.

Shaik, A. R. A., S. L. Caskey and E. A. Groll (2018). *Waste Heat Recovery from a Vented Electric Clothes Dryer Utilizing a Finned-Tube Heat Exchanger*. The Summer

Undergraduate Research Fellowship (SURF) Symposium. Purdue University West Lafayette, USA p. 43.

Shampine, L. F. and M. W. Reichelt (1997). "The MATLAB Ode Suite," *SIAM Journal on Scientific Computing*. Vol. 18(1), pp. 1-22 DOI: 10.1137/s1064827594276424.

Shelton, S. V. and P. J. Christiansen (1999). "Analysis of a Nozzle Condensation Drying Cycle," *Applied Thermal Engineering*. Vol. 19(8), pp. 831-845 DOI: 10.1016/S1359-4311(98)00072-6.

Shen, B., K. Gluesenkamp, P. Bansal and D. Beers (2016). "Heat Pump Clothes Dryer Model Development."

Somdalen, R. and J. Köhler (2018). "Theoretical Investigation of a Novel Thermoelectric Laundry Dryer Concept," *Materials Today: Proceedings*. Vol. 5(4, Part 1), pp. 10323-10332 DOI: https://doi.org/10.1016/j.matpr.2017.12.280.

Stawreberg, L. and L. Nilsson (2010). "Modelling of Specific Moisture Extraction Rate and Leakage Ratio in a Condensing Tumble Dryer," *Applied Thermal Engineering*. Vol. 30(14), pp. 2173-2179 DOI: https://doi.org/10.1016/j.applthermaleng.2010.05.030.

Stawreberg, L. and L. Nilsson (2013). "Potential Energy Savings Made by Using a Specific Control Strategy When Tumble Drying Small Loads," *Applied Energy*. Vol. 102, pp. 484-491 DOI: https://doi.org/10.1016/j.apenergy.2012.07.045.

Sultan, M., I. I. El-Sharkawy, T. Miyazaki, B. B. Saha and S. Koyama (2015). "An Overview of Solid Desiccant Dehumidification and Air Conditioning Systems," *Renewable and Sustainable Energy Reviews*. Vol. 46, pp. 16-29 DOI: https://doi.org/10.1016/j.rser.2015.02.038.

T'Jollyn, I., S. Lecompte, B. Vanslambrouck and M. De Paepe (2019). "Energetic and Financial Assessment of the Implementation of an Absorption Heat Pump in an Industrial Drying System," *Drying Technology*. Vol. 37(15), pp. 1939-1953 DOI: 10.1080/07373937.2018.1546190.

TeGrotenhuis, W., A. Butterfield, D. Caldwell, A. Crook and A. Winkelman (2017). "Modeling and Design of a High Efficiency Hybrid Heat Pump Clothes Dryer," *Applied Thermal Engineering*. Vol. 124, pp. 170-177 DOI: https://doi.org/10.1016/j.applthermaleng.2017.05.048.

Tuğrul Oğulata, R. (2004). "Utilization of Waste-Heat Recovery in Textile Drying," *Applied Energy*. Vol. 79(1), pp. 41-49 DOI: https://doi.org/10.1016/j.apenergy.2003.12.002.

Tuncer, N., H. B. Tufekç¸ioglu and S. Ç¸alikkocaoglu (1993). "Investigation on the Compressive Strength of Several Gypsum Products Dried by Microwave Oven with

Different Programs," *The Journal of Prosthetic Dentistry*. Vol. 69(3), pp. 333-339 DOI: https://doi.org/10.1016/0022-3913(93)90116-6.

Turner, I. and A. S. Mujumdar (1996). *Mathematical Modeling and Numerical Techniques in Drying Technology*. 1st Ed. CRC Press, Boca Raton, USA.

Turns, S. R. (2000). *An Introduction to Combustion: Concepts and Applications*. McGraw-Hill, Boston, USA.

Ulloa, C., J. L. Míguez, J. Porteiro, P. Eguía and A. Cacabelos (2013). "Development of a Transient Model of a Stirling-Based Chp System," *Energies*. Vol. 6(7), pp. 3115-3133 DOI: https://doi.org/10.3390/en6073115.

Van Den Brekel, L. D. M. and E. J. De Jong (1989). "Hydrodynamics in Packed Textile Beds," *Textile Research Journal*. Vol. 59(8), pp. 433-440 DOI: 10.1177/004051758905900801.

Vasta, S., V. Brancato, D. La Rosa, V. Palomba, G. Restuccia, A. Sapienza and A. Frazzica (2018). "Adsorption Heat Storage: State-of-the-Art and Future Perspectives," *Nanomaterials (Basel, Switzerland)*. Vol. 8(7), p. 522 DOI: 10.3390/nano8070522.

Vongpradubchai, S. and P. Rattanadecho (2011). "Microwave and Hot Air Drying of Wood Using a Rectangular Waveguide," *Drying Technology*. Vol. 29(4), pp. 451-460 DOI: 10.1080/07373937.2010.505312.

Vrba, J., M. Stejskal, R. Klepl, A. Richter, M. Pourova, O. Zak, J. Herza and L. Oppl (2005). "Microwave Drying Machine for Textile Materials," *Proceedings of 2005 European Microwave Conference*.

Vu, H. T. and E. Tsotsas (2018). "Mass and Heat Transport Models for Analysis of the Drying Process in Porous Media: A Review and Numerical Implementation," *International Journal of Chemical Engineering*. Vol. 2018, p. 9456418 DOI: 10.1155/2018/9456418.

Walmsley, T. G., J. J. Klemeš, M. R. Walmsley, M. J. Atkins and P. S. Varbanov (2017). "Innovative Hybrid Heat Pump for Dryer Process Integration."

Walmsley, T. G., M. R. W. Walmsley, M. J. Atkins, J. R. Neale and A. H. Tarighaleslami (2015). "Thermo-Economic Optimisation of Industrial Milk Spray Dryer Exhaust to Inlet Air Heat Recovery," *Energy*. Vol. 90, pp. 95-104 DOI: https://doi.org/10.1016/j.energy.2015.03.102.

Weaver, S. (2017). "Energy Efficient Clothes Dryer with Ir Heating and Electrostatic Precipitator,"; GE Global Research, Niskayuna, NY (United States), DOE-GE-06720 United States 10.2172/1412657 GFO English.

Wei, Y., R. H. Gong, L. Ning and X. Ding (2018a). "Enhancing the Energy Efficiency of Domestic Dryer by Drying Process Optimization," *Drying Technology*. Vol. 36(7), pp. 790-803 DOI: 10.1080/07373937.2017.1356329.

Wei, Y., R. H. Gong, Z. Su, X. Wang and X. Ding (2018b). "Optimization and Performance Evaluation of Silk Fabrics Dried in the Domestic Dryer," *The Journal of The Textile Institute*. Vol. 109(6), pp. 703-712 DOI: 10.1080/00405000.2017.1365579.

Wei, Y., J. Hua and X. Ding (2017). "A Mathematical Model for Simulating Heat and Moisture Transfer within Porous Cotton Fabric Drying inside the Domestic Air-Vented Drum Dryer," *The Journal of The Textile Institute*. Vol. 108(6), pp. 1074-1084 DOI: 10.1080/00405000.2016.1219450.

Wei, Y., Z. Su, Y. Zhang, P. Li and H. Yuan (2019). "The Effect of Fabric Movement on Drying Performance of the Domestic Drum Dryer," *The Journal of The Textile Institute*. Vol. 110(7), pp. 1059-1071 DOI: 10.1080/00405000.2018.1537104.

Whitaker, S. (1977). Simultaneous Heat, Mass, and Momentum Transfer in Porous Media: A Theory of Drying. *Advances in Heat Transfer*. J. P. Hartnett and T. F. Irvine. Elsevier, Vol. 13 pp. 119-203.

Whitaker, S. (1980). "Heat and Mass Transfer in Granular Porous Media," *Adv. Drying*. Vol. 1, pp. 23-61.

Wiberg, R. and N. Lior (2005). "Heat Transfer from a Cylinder in Axial Turbulent Flows," *International Journal of Heat and Mass Transfer*. Vol. 48(8), pp. 1505-1517 DOI: https://doi.org/10.1016/j.ijheatmasstransfer.2004.10.015.

Williamson, N. and P. K. Bansal (2004). "Experimental Investigation of the Energy Efficiency of Gas Commercial Laundry Dryers," *Proceedings of the Institution of Mechanical Engineers, Part E: Journal of Process Mechanical Engineering*. Vol. 218(3), pp. 143-152 DOI: 10.1243/0954408041323421.

Yadav, V. and C. G. Moon (2008a). "Fabric-Drying Process in Domestic Dryers," *Applied Energy*. Vol. 85(2), pp. 143-158 DOI: https://doi.org/10.1016/j.apenergy.2007.06.007.

Yadav, V. and C. G. Moon (2008b). "Modelling and Experimentation for the Fabric-Drying Process in Domestic Dryers," *Applied Energy*. Vol. 85(5), pp. 404-419 DOI: https://doi.org/10.1016/j.apenergy.2007.06.014.

Yi, T., J. C. Dye, M. E. Shircliff and F. Ashrafzadeh (2016). "A New Physics-Based Drying Model of Thin Clothes in Air-Vented Clothes Dryers," *IEEE/ASME Transactions on Mechatronics*. Vol. 21(2), pp. 872-878 DOI: 10.1109/TMECH.2015.2506179.

Yu, X., Y. Li and X. Ding (2020). "Dynamics of Cotton Textile Motion in a Domestic Tumble Dryer and Its Effect on Drying Performance," *Textile Research Journal*. p. 0040517520960751 DOI: 10.1177/0040517520960751.

Zhou, G., Y. Ye, J. Wang, W. Zuo, Y. Fu and X. Zhou (2018). "Modeling Air-to-Air Plate-Fin Heat Exchanger without Dehumidification," *Applied Thermal Engineering*. Vol. 143, pp. 137-148 DOI: 10.1016/j.applthermaleng.2018.07.064.